NAME A. M. AINDOW DEPARTMENT APPLIED PHYSICS DEGREE Ph.D.

THE UNIVERSITY OF HULL

Deposit of thesis in accordance with
Senate Minutes 131, 1955/56
and 141, 1970/71

I A. M. AINDOW hereby give my

consent that the copy of my thesis CHARACTERISTICS OF

A LASER-GENERATED ACOUSTIC SOURCE IN SOLIDS

if accepted for the degree of Ph.D in the

University of Hull and thereafter deposited in the University

Library shall be available for consultation, inter-library

loan and photocopying at the discretion of the University

Librarian from the following date 15.12.86

Signature _____

If by reason of special circumstances the author wishes to withhold for a period of not more than 5 years from the date of the degree being awarded the consent required by the Senate, application should immediately be made in writing to the University Librarian, giving a full statement of the circumstances involved.

IN THE EVENT OF THIS FORM NOT BEING RETURNED TO THE HIGHER DEGREES OFFICE WITH THE THESIS IT WILL BE ASSUMED THAT THE AUTHOR CONSENTS TO THE THESIS BEING MADE AVAILABLE AS INDICATED ABOVE.

THE UNIVERSITY OF HULL

CHARACTERISTICS OF A LASER-GENERATED ACOUSTIC SOURCE IN SOLIDS

being a thesis submitted for the Degree of

Doctor of Philosophy

in the University of Hull

by

Alan Michael Aindow, B.Sc. (Hull)

November 1986

SUMMARY

SUMMARY OF THESIS SUBMITTED FOR Phd DEGREE

by Alan Michael Aindow

on

CHARACTERISTICS OF A LASER-GENERATED ACOUSTIC SOURCE IN SOLIDS

This thesis describes a combined experimental and theoretical study of acoustic generation in solids by laser irradiation.

Two basic types of laser acoustic source are identified, namely, the thermoelastic and the ablation source. Both sources are described in detail in metals and to a lesser extent in non-metals. The emphasis is on generation in the ultrasonic region. The thermoelastic source operates at comparatively low incident laser intensities, typically $< 3 \times 10^{12}$ Wm^{-2}, and is driven by dynamic thermal expansion due to transient surface heating. The second source takes over at higher intensities, and results from the effects of surface vaporisation and plasma formation. The resultant acoustic waveforms (bulk and surface) have been studied over a wide range of experimental conditions using a pulsed Nd:YAG laser and both resonant and broad bandwidth detection probes. The surface forces produced under these various conditions are discussed in detail, and using acoustic theory, are related to the acoustic waveforms.

In a wider context, thermoelastic generation is related to the photoacoustic effect in a generalised 1D model.

To my parents

Acknowledgements

I am indebted to my supervisors Dr. R.J. Dewhurst and Dr. S.B. Palmer for their guidance and continual encouragement. Of all my colleagues, I would like to extend special thanks to Dave Hutchins, Chris Edwards and Jerry Cooper who have helped over the years in ways too numerous to mention. I am also obliged to Judy for her patient typing, and the technical staff in mechanical workshops for constructing the capacitance probes. On a personal level, my heartfelt thanks go to Sandy for somehow managing to tolerate me whilst completing the work. The necessary finance was provided in the first instance by the SERC under a Quota Award studentship and subsequently for one year by Harwell UKAEA.

C O N T E N T S

CHAPTER 1

Introduction

" .....sonorousness, under the influence of intermittent light,
is a property common to all matter"

A.G. Bell 1881

The thermal generation of sound by light, the photoacoustic effect, was discovered over a century ago by A.G. Bell. In his pioneering study, he found that many different gases, liquids and solids emitted sound when exposed to a chopped beam of sunlight. The intensity of the sound varied considerably, following the trend of being greatest in substances which absorb light strongly; for example, a deeply coloured gas such as NO_2 produced much louder sounds than dry air; similarly, discolouring clear water with ink, or, dulling the surfaces of polished metal plates, enhanced the effect. This direct dependence on optical absorptivity firmly supported Lord Rayleigh's view that the effect was thermal in origin, the sounds being produced as a result of expansion due to heating associated with the absorption of light.

Interest in the effect though intense was short lived, and Bell's work gradually faded into obscurity. The recent revival has been mainly due to two quite different developments; first, photoacoustic spectroscopy, the application of the effect to the study of absorption spectra; and secondly, in a strictly modern context, the thermal generation of ultrasound by pulsed laser irradiation. In the latter case, the use of laser pulses has lifted the main energy content of the acoustic source out

of the audio spectrum and planted it firmly in the ultrasonic region, an area of keen practical interest. It is towards this high frequency, complimentary aspect of the photoacoustic effect, usually termed thermoelastic generation, that the present work is directed. In particular, the main aim of this thesis is to characterise the laser ultrasonic source in solids.

Chapters 2 and 3 review the relevant aspects of acoustic theory and previous work on laser ultrasonics, respectively. Chapter 4 gives a theoretical introduction to thermoelastic generation, offering a generalised view of the thermal generation of acoustic waves at the interface between a light absorbing target medium and an overlying transparent medium through which laser radiation is incident. The remaining chapters combining experimental and theoretical studies, are divided into two sections; the first comprising Chapters 5, 6 and 7, describes various aspects of ultrasonic generation in metals, while the second, Chapter 8, considers in less detail the same processes in non-metals. The results indicate that there are two distinct laser ultrasonic sources operating either side of the incident intensity for plasma formation. Below this threshold, typically $< 3 \times 10^{12} Wm^{-2}$, the source is thermoelastic, being driven by thermal expansion due to transient surface heating. Above the threshold, the second source rapidly takes over, and is dominated by the effects of ablation processes. The surface forces produced by both source types are discussed in detail and are related to the resultant ultrasonic waveforms. The results are summarised in Chapter 9 where suggestions for future areas of study are also made.

CHAPTER 2

Review of Acoustic Theory

2.0 Introduction

Fundamental to the theory of rigid dynamics is the assumption that a body reacts to applied forces without shape or volume change. Elastic theory, in contrast, considers bodies under applied stresses to be reversibly deformable, but implicitly assumes that the resultant stress-strain distributions are established instantaneously. If the applied forces vary comparatively slowly with time, these two theories often adequately describe the mechanical response of solid bodies. Rigid dynamics describes inertial aspects of gross body motion while elastic theory gives details of internal stress-strain distributions. If the forces are transient, however, they may not be directly applicable as the body may not have had sufficient time to maintain its internal equilibrium. Instead, it will respond in a reverberant jelly-like fashion. Under these conditions of dynamic loading, body response must be considered in terms of the propagation of acoustic waves or vibrations which transmit the effects of an applied force in a progressive elastic shunting action. These waves propagate throughout the body until all regions have been reached and internal mechanical equilibrium eventually returns. The propagation of acoustic waves may therefore be viewed as the process through which gross body response occurs and the ordinary theories of rigid dynamics and elasticity as the long time scale (steady-state) or time-averaged approximations.

As an order of magnitude guide, acoustic theory is required when the time scale, Δt, over which significant changes in the applied force occur, is less than the time taken by acoustic waves to propagate across the relevant body dimension, ie when

$$\Delta t < \frac{d}{C} \qquad 2.1$$

where d = relevant body dimension

C = propagation velocity of acoustic waves

Over longer time scales,

$$\Delta t > \frac{d}{C} \qquad 2.2$$

steady-state mechanics may be directly applicable as sufficient time is available for internal mechanical equilibrium to be continuously maintained.

As an example, consider a rod, length ℓ, one end of which is uniformly applied a sinusoidally time-varying stress. From equation 2.2 it follows that steady state theory is applicable if

$$\tau >> \frac{\ell}{C}$$

where τ = period of applied stress

or, in terms of the acoustic wavelength, λ, when

$$\lambda >> \ell \qquad 2.3$$

Under this condition, if the far end were, for example, free, the rod would remain unstrained and oscillate rigidly in response to the stress as described by Newton's second law of motion (rigid dynamics). Alternatively, if the far end were clamped, it would at any instant be uniformly axially stressed and strained as related to the applied stress simply by Young's modulus (elastic theory).

Over shorter time scales when the acoustic wavelength becomes comparable or shorter than the rod length,

$$\lambda \lesssim \ell \qquad 2.4$$

there will exist appreciable phase delays along the rod length. The free-ended rod will start to loose its rigidity and begin to behave elastically as regions of compression and rarefraction start to form and propagate along its length. Similarly, the clamped rod will simultaneously possess propagating regions of both extension and compression. The inertial and elastic aspects of the mechanical response have become intertwined in this, the realm of acoustic theory.

Subject to certain boundary conditions relating to the effect of body surfaces, the propagation velocity of acoustic waves is determined by the medium's density and elastic strength. A dense body medium tends to slow a wave down by presenting more inertia to its motion while an increase in the appropriate elastic modulus speeds it up by providing a greater driving force.

2.1 Acoustic wave propagation in isotropic solids

To analyse the propagation of acoustic waves, the equations of motion for the body medium are derived, the travelling wave solutions of which correspond to propagating acoustic waves. These equations are obtained by considering the motion of an infinitesimal volume element of an elastic continuum in terms of its mass and the stress-strain gradients acting across it.

2.2 Stress-strain distributions

The relationship between stress and strain within a solid has been analysed by Officer 1958. Stress acting within a body can be generally resolved into two sets of orthogonal components, those acting in normal directions to a given area, the compressional or tensile stresses, and the shear stresses which act tangentially. From Figure 2.1, three independent components of each can be defined, σ_{xx}, σ_{yy} and σ_{zz}, the compressional stresses, and $\sigma_{xy} = \sigma_{yx}$, $\sigma_{yz} = \sigma_{zy}$ and $\sigma_{zx} = \sigma_{xz}$, the shear stresses. (The first index refers to the stress direction and the second the plane in which it acts).

Strain, the spatial derivative of displacement, may likewise be resolved into components. If u,v and w are the components of displacement in the x,y and z directions respectively, these can be seen to be

$$\varepsilon_{xx} = \frac{\partial u}{\partial x} ; \quad \varepsilon_{yy} = \frac{\partial v}{\partial y} ; \quad \varepsilon_{zz} = \frac{\partial w}{\partial z}$$

$$\varepsilon_{xy} = \varepsilon_{yx} = \frac{\partial v}{\partial x} + \frac{\partial u}{\partial y} ; \quad \varepsilon_{yz} = \varepsilon_{zy} = \frac{\partial w}{\partial y} + \frac{\partial v}{\partial z} ; \quad \varepsilon_{zx} = \varepsilon_{xz} = \frac{\partial u}{\partial z} + \frac{\partial w}{\partial x}$$

For a linear elastic medium, the stress and strain components are directly related through the elastic constants (Hooke's Law). For an

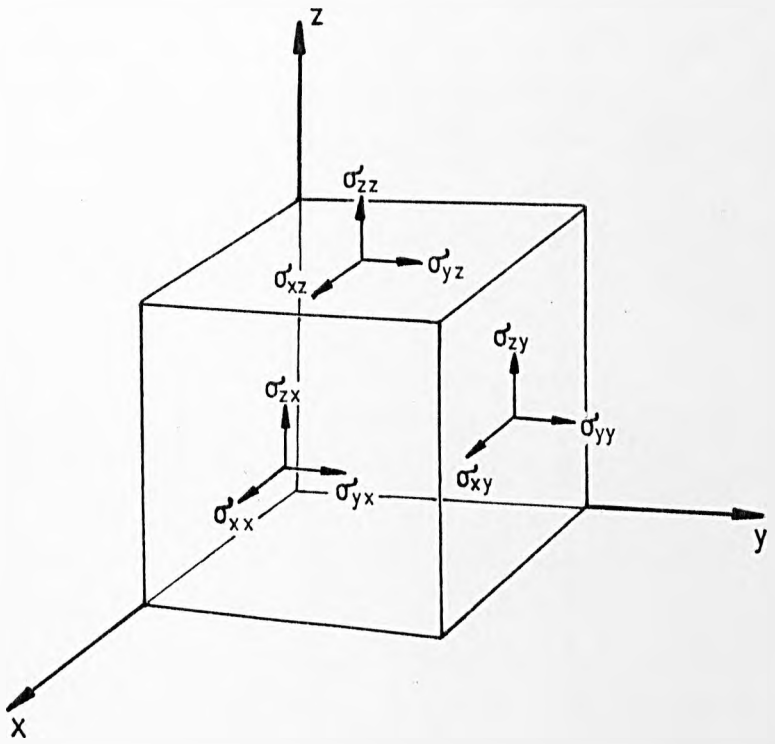

FIGURE 2.1: Definition of stress components. From equilibrium considerations, it follows that $\sigma'_{xy}=\sigma'_{yx}$ $\sigma'_{yz}=\sigma'_{zy}$ $\sigma'_{zx}=\sigma'_{xz}$.

After Officer 1958.

isotropic linear elastic medium or one that is effectively so, such as metal in a fine, randomly-orientated polycrystalline state, it is necessary to define at least two elastic constants, one ultimately relating to the characterisation of isotropic (hydrostatic) stress and isotropic strain (dialatation or volume change), and the other, to shear stress and strain (shape change) (Condon and Odishaw 1958a).

There are a variety of ways of expressing this two constant relationship, the one due to Lamé being

$$\sigma_{xx} = (\lambda+2\mu)\,\varepsilon_{xx} + \lambda\varepsilon_{yy} + \lambda\varepsilon_{zz} = \lambda\Delta + 2\mu\varepsilon_{xx}$$

$$\sigma_{yy} = \lambda\varepsilon_{xx} + (\lambda+2\mu)\varepsilon_{yy} + \lambda\varepsilon_{zz} = \lambda\Delta + 2\mu\varepsilon_{yy}$$

$$\sigma_{zz} = \lambda\varepsilon_{xx} + \lambda\varepsilon_{yy} + (\lambda+2\mu)\varepsilon_{zz} = \lambda\Delta + 2\mu\varepsilon_{zz}$$

$$\sigma_{xy} = \mu\varepsilon_{xy}$$

$$\sigma_{yz} = \mu\varepsilon_{yz}$$

$$\sigma_{zx} = \mu\varepsilon_{zx} \qquad 2.5$$

where λ and μ are the Lamé constants

$\Delta = \varepsilon_{xx} + \varepsilon_{yy} + \varepsilon_{zz}$ ie. the change in volume per unit cube.

Other commonly used elastic constants may be expressed in terms of λ and μ as (Condon and Odishaw 1958a)

G = shear modulus = μ

$$K = \text{bulk modulus} = \lambda + \frac{2}{3}\mu \qquad 2.6$$

$$\nu = \text{Poisson's ratio} = \frac{\lambda}{2(\lambda+\mu)}$$

2.3 Equations of motion

Consider an infinitesimal parallelepiped of body medium dimensions δx, δy, δz across which act stress gradients; Figure 2.2. The total force in, for example, the x direction is given by (Officer 1958)

$$F_{xx} = \left(\sigma_{xx} + \frac{\partial \sigma_{xx}}{\partial x}.\delta x\right)\delta y\delta z - \sigma_{xx}\delta y\delta z$$

$$+ \left(\sigma_{xy} + \frac{\partial \sigma_{xy}}{\partial y}.\delta y\right)\delta x\delta z - \sigma_{xy}\delta x\delta z$$

$$+ \left(\sigma_{xz} + \frac{\partial \sigma_{xz}}{\partial z}.\delta z\right)\delta x\delta y - \sigma_{xz}\delta x\delta y$$

$$= \left(\frac{\partial \sigma_{xx}}{\partial x} + \frac{\partial \sigma_{xy}}{\partial y} + \frac{\partial \sigma_{xz}}{\partial z}\right).\delta x\delta y\delta z \qquad 2.7$$

This force will accelerate the parallelepiped in the x direction so

$$F_{xx} = \rho.\delta x\delta y\delta z \frac{\partial^2 u}{\partial t^2} \qquad 2.8$$

where ρ = medium density

Hence, by equating 2.7 and 2.8

$$\rho \frac{\partial^2 u}{\partial t^2} = \frac{\partial \sigma_{xx}}{\partial x} + \frac{\partial \sigma_{xy}}{\partial y} + \frac{\partial \sigma_{xz}}{\partial z} \qquad 2.9$$

Substituting for stresses in terms of strains and displacements, allows this to be rewritten as

$$\rho \frac{\partial^2 u}{\partial t^2} = \frac{\partial}{\partial x}\left(\lambda\Delta + 2\mu \frac{\partial u}{\partial x}\right) + \frac{\partial}{\partial y}\left[\mu\left(\frac{\partial v}{\partial x} + \frac{\partial u}{\partial y}\right)\right] + \frac{\partial}{\partial z}\left[\mu\left(\frac{\partial w}{\partial x} + \frac{\partial u}{\partial z}\right)\right]$$

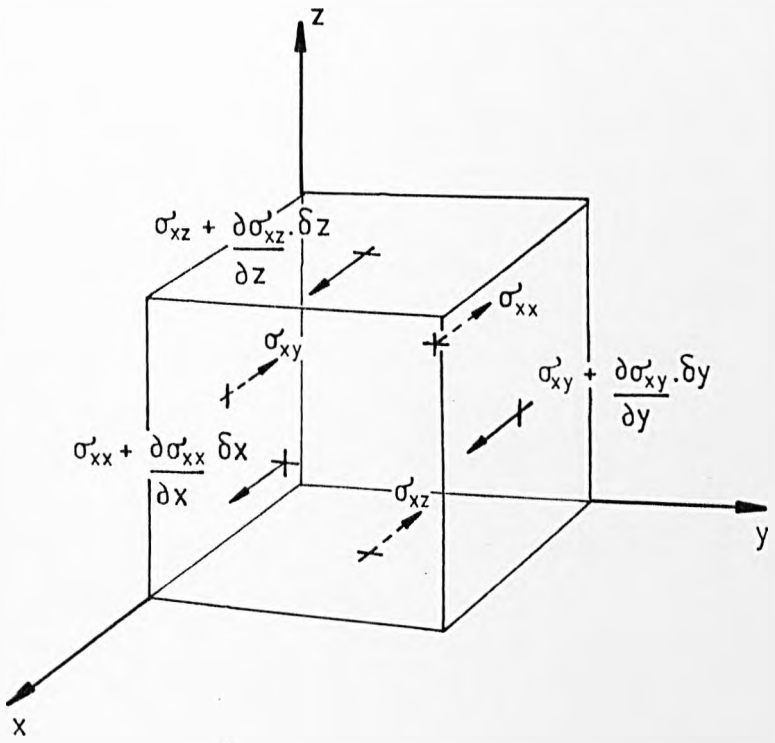

FIGURE 2.2: Variation in stress components in the x direction acting across an infinitesimal parallelpiped, dimensions $\delta x, \delta y, \delta z$, due to stress gradients.

After Officer 1958.

$$= (\lambda+\mu)\frac{\partial \Delta}{\partial x} + \mu\nabla^2 u \qquad 2.10$$

and similarly for the y and z directions:

$$\rho\frac{\partial^2 v}{\partial t^2} = (\lambda+\mu)\frac{\partial \Delta}{\partial y} + \mu\nabla^2 v \qquad 2.11$$

$$\rho\frac{\partial^2 w}{\partial t^2} = (\lambda+\mu)\frac{\partial \Delta}{\partial z} + \mu\nabla^2 w \qquad 2.12$$

where $\nabla^2 = \frac{\partial^2}{\partial x^2} + \frac{\partial^2}{\partial y^2} + \frac{\partial^2}{\partial z^2}$

Equations 2.10 - 2.12 are the equations of motion for an isotropic medium. There are two independent solutions corresponding to two different bulk modes of acoustic propagation. For example, consider propagation in the x direction only, in which case the displacements u, v and w become functions of x and t only, reducing the equations to

$$\rho\frac{\partial^2 u}{\partial t^2} = (\lambda+\mu)\frac{\partial^2 u}{\partial x^2} + \mu\frac{\partial^2 u}{\partial x^2} = (\lambda+2\mu)\frac{\partial^2 u}{\partial x^2}$$

$$\rho\frac{\partial^2 v}{\partial t^2} = \mu\frac{\partial^2 v}{\partial x^2}$$

$$\rho\frac{\partial^2 w}{\partial t^2} = \mu\frac{\partial^2 w}{\partial x^2}$$

The solution to the first equation indicates that displacements in the x direction propagate at a velocity

$$C_L = \sqrt{\frac{(\lambda+2\mu)}{\rho}} \qquad 2.13$$

This is the longitudinal wave in which the displacement is in the propagation direction.

The remaining two equations have a different solution for which displacements in the perpendicular directions propagate at a velocity

$$C_S = \sqrt{\frac{\mu}{\rho}} \qquad 2.14$$

This is the slower propagating shear wave.

These waves are the only two that can propagate in a bulk, homogeneous medium.

2.4 Reflection of longitudinal waves

Reflection of longitudinal waves at a boundary has been considered by Tilley 1974. Consider a longitudinal wave normally incident on a plane interface between two media; Figure 2.3. Suppose the displacements u_i, u_r and u_t in the incident, reflected and transmitted waves are written as

$$u_i = a_i \exp[j(\omega t - k_1 x)]$$

$$u_r = a_r \exp[j(\omega t + k_1 x)] \qquad 2.15$$

$$u_t = a_t \exp[j(\omega t - k_2 x)]$$

where $k_1 = \omega/C_{1L}$ and $k_2 = \omega/C_{2L}$ are the wave numbers in the first and second medium respectively

ω = angular frequency.

Two boundary conditions apply; first, the displacement at the interface is the same in both media, in other words, they stand in contact

$$u_i + u_r = u_t \qquad 2.16$$

and, secondly, the stress is continuous across the interface

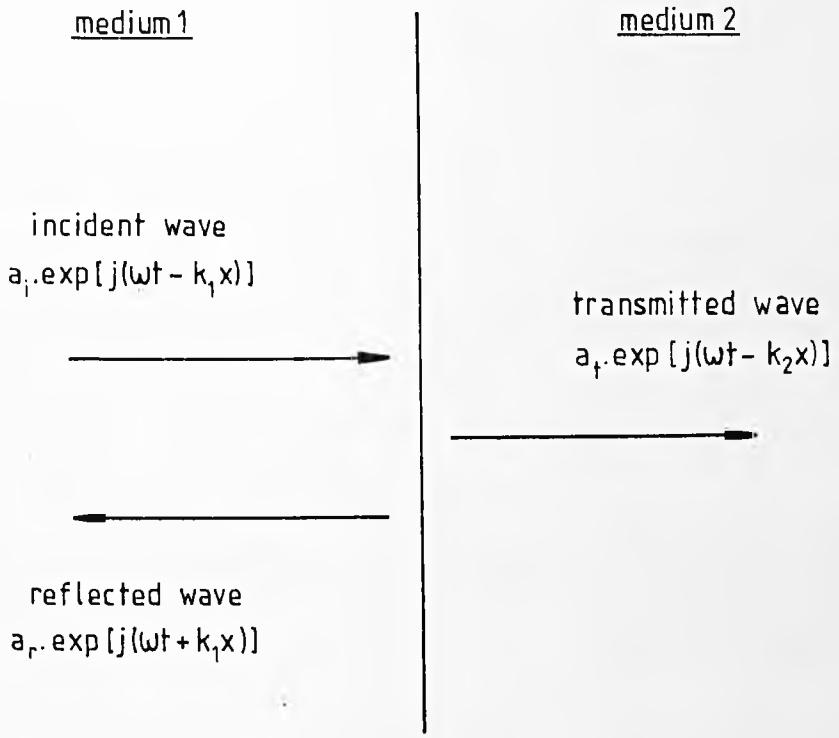

FIGURE 2.3: Reflection and transmission of longitudinal waves normally incident upon a plane interface.

After Tilley 1974.

$$E_1 \frac{\partial(u_i+u_r)}{\partial x} = E_2 \frac{\partial u_t}{\partial x} \qquad 2.17$$

where $E_1 = (\lambda_1+2\mu_1)$, $E_2 = (\lambda_2+2\mu_2)$ are the longitudinal elastic moduli.

By substituting equation 2.15 into equations 2.16 and 2.17 and solving to give a_r and a_t in terms of a_i, yields

$$\frac{a_r}{a_i} = \frac{E_2k_2 - E_1k_1}{E_1k_1 + E_2k_2}$$

$$\frac{a_t}{a_i} = \frac{2\,E_1k_1}{E_1k_1 + E_2k_2}$$

which may be more conveniently expressed in terms of acoustic impedance, $z = \sqrt{E\rho}$, as

$$\frac{a_r}{a_i} = R_{12} = \frac{z_2 - z_1}{z_2 + z_1} \qquad 2.18$$

$$\frac{a_t}{a_i} = T_{12} = \frac{2z_1}{z_2 + z_1} \qquad 2.19$$

where R_{12} = amplitude reflection coefficient

T_{12} = amplitude transmission coefficient

Modified expressions for the case of oblique incidence and also shear reflection have been derived by Achenbach 1980.

2.5 Rayleigh surface waves

When body surfaces are present, additional types of wave may propagate due to boundary stress-strain modifications.

The primary wave of this kind, the Rayleigh surface wave, has been discussed by Achenbach 1980. This wave will propagate in the immediate neighbourhood of a free surface. It has both longitudinal and shear

components, giving particles at the surface of a retrograde elliptical trajectory; Figure 2.4. As an example, consider a sinusoidal plane wave propagating in the x direction, where the xy plane defines the surface of a body occupying the space $z > 0$. The Rayleigh wave corresponds to the solution of the equations of motion (satisfying the boundary conditions that no net stress acts normally across the surface) of the form

$$u = A(z) \sin(\omega t - kx)$$

$$v = B(z) \cos(\omega t - kx)$$

where u = longitudinal component of displacement

v = shear component of displacement

$$A(z) = Ak \left(e^{-qz} - \frac{2qs}{s^2 + k^2} \cdot e^{sz}\right)$$

$$B(z) = Aq \left(e^{-qz} - \frac{2k^2}{s^2 + k^2} \cdot e^{-sz}\right)$$

$$q^2 = k^2 - \left(\frac{\omega}{C_L}\right)^2$$

$$s^2 = k^2 - \left(\frac{\omega}{C_S}\right)^2$$

The two functions, A(z) and B(z), illustrated in Figure 2.5, describe the depth variation in the amplitude of the longitudinal and shear components of displacement. Both scale linearly with wavelength and decrease rapidly with depth becoming insignificant within a few free surface wavelengths.

The propagation velocity is less than either longitudinal or shear bulk waves. The appropriate solution to the equation of motion indicates a value of

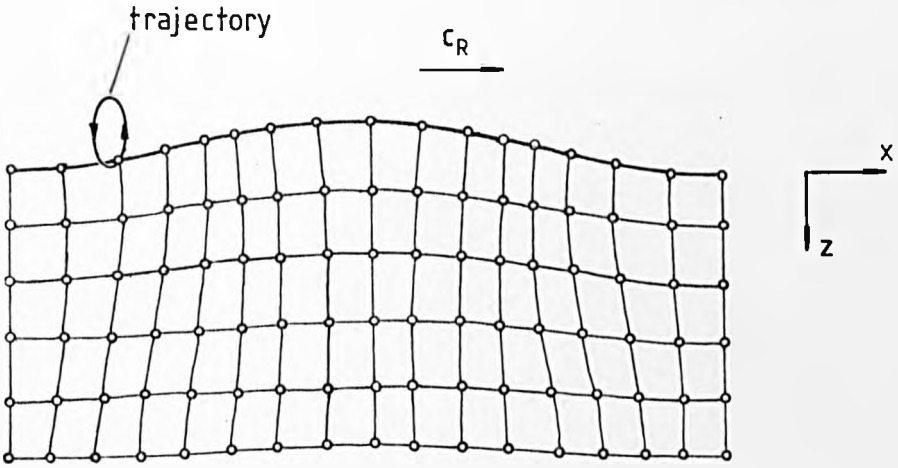

FIGURE 2.4: Pattern of displacements within a Rayleigh wave.

After Achenbach 1980.

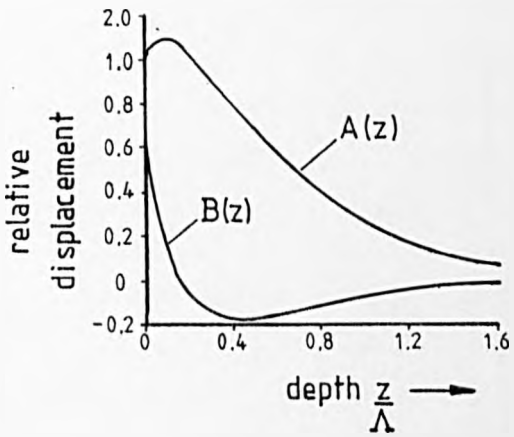

FIGURE 2.5: Depth variation of the longitudinal displacement amplitude, A(z), and shear displacement amplitude, B(z), within a Rayleigh wave.

Λ = free surface wavelength

After Achenbach 1980, assuming $\lambda = \mu$.

$$C_R = a\, C_S$$

where a is approximately given by (Viktorov 1967)

$$a \approx \frac{1.74\mu + 2.86\lambda}{2\lambda + 3\mu}$$

For most common solids, C_R lies in the range 0.86 - 0.96 C_S.

2.6 Other propagation modes and bulk resonances

When more complicated body geometries are considered, many more types of wave may propagate. In plates, for example (Viktorov 1967), a wide range of flexural modes may occur resulting in the propagation of so-called Lamb waves in which opposite faces of a plate may flex in either phase or antiphase as the wave passes in between. Furthermore if two or more body surfaces are present, there is the possibility of standing waves being set up in what are termed bulk resonances. In a real body enclosed on all sides, standing waves may be set up throughout its entire medium, so that it resonates or rings at its own characteristic frequencies (normal modes).

2.7 Response of a body to an applied force

The relationship between the various types of waves can be illustrated by considering an elastic body suddenly subjected to a fast-rising force which remains constant thereafter. Immediately from the point of application, longitudinal and shear waves will be launched into the bulk together with Rayleigh waves out across the surfaces. When other body surfaces are reached, they will begin to loose their identity as other generally lower-energy modes, possibly Lamb waves, build up. Eventually, all the acoustic energy will be reflected back on itself and fed into standing waves, finally leaving the body resonating. Moreover, if the

body was originally free, it would have now acquired a translational motion and, in general, a rotational motion also (rigid dynamics). Alternatively, if it was clamped, the time-averaged stress-strain distribution would now be tending towards its steady-state value (elastic theory).

2.8 Transient acoustic waveforms

To determine the precise motion within a body subjected to specified forces, it is necessary to include an additional driving term in the equations of motion. If a generalised displacement $\underline{r} = \underline{u} + \underline{v} + \underline{w}$ is introduced, the previous three equations 2.10 -2.12 can be combined and recast as (Burridge and Knopoff 1964)

$$\rho \frac{\partial^2 \underline{r}}{\partial t^2} = (\lambda+\mu)\ \nabla\nabla.\ \underline{r} + \mu\ \nabla^2\ \underline{r} + \underline{F}(x,y,z,t) \qquad 2.20$$

where $\underline{F}(x,y,z,t)$ = force per unit volume acting at some position, x, y, z and time t.

Some selected solutions for forced body motion of later relevance to this thesis, will now be discussed for the case of a point force applied to the otherwise stress-free surface of a uniform elastic half-space.

2.9 Surface motion of the uniform elastic half-space due to a point vertical surface force

The forced motion of the elastic half-space was first analysed by Lamb 1904. He determined the surface motion due to a vertical surface impulse by synthesis from the periodic solution. A less intricate analysis was subsequently carried out by Pekeris 1955 who solved the equation of motion directly for the case of a force with a step time dependence acting vertically at a point on the surface. Assuming the Lamé constants are

equal, $\mu = \lambda$, a fair approximation for many metals μ lying typically in the range $0.5 - 1.4\lambda$, Pekeris' solution for the vertical component of displacement, $W(r,t)$, produced at a distance, r, is

$$W(r,t) = 0 \qquad \ldots\ldots \tau < \frac{1}{\sqrt{3}}$$

$$= \frac{-F}{32\pi\mu r}\left\{6 - \frac{\sqrt{3}}{\sqrt{\tau^2 - \frac{1}{4}}} - \frac{\sqrt{3\sqrt{3}+5}}{\sqrt{\frac{3}{4} + \frac{\sqrt{3}}{4} - \tau^2}}\right.$$

$$\left. + \frac{\sqrt{3\sqrt{3}-5}}{\sqrt{\tau^2 + \frac{\sqrt{3}}{4} - \frac{3}{4}}}\right\} \qquad \ldots\ldots \frac{1}{\sqrt{3}} < \tau < 1$$

$$= \frac{-F}{16\pi\mu r}\left\{6 - \frac{\sqrt{3\sqrt{3}+5}}{\sqrt{\frac{3}{4} + \frac{\sqrt{3}}{4} - \tau^2}}\right\} \qquad \ldots\ldots 1 < \tau < \frac{1}{2}\sqrt{3+\sqrt{3}}$$

$$= \frac{-3F}{8\pi\mu r} \qquad \ldots\ldots \tau > \frac{1}{2}\sqrt{3+\sqrt{3}}$$

2.21

where F = magnitude of force

$\tau = \frac{C_S t}{r}$ ie dimensionless time normalised to shear arrival

This expression, plotted in Figure 2.6, indicates that the surface remains at rest until the first acoustic disturbance arrives producing a small rise in the surface (SL). This precursor is associated with the arrival of the longitudinal wave. The main disturbance comprising a large surface rise arrives subsequently, propagating at the Rayleigh wave velocity (R). The arrival associated with the shear wave (S) is marked only by a change in the gradient of the waveform prior to the Rayleigh arrival. After the Rayleigh arrival, the surface remains displaced downwards, this being the expected steady-state depression.

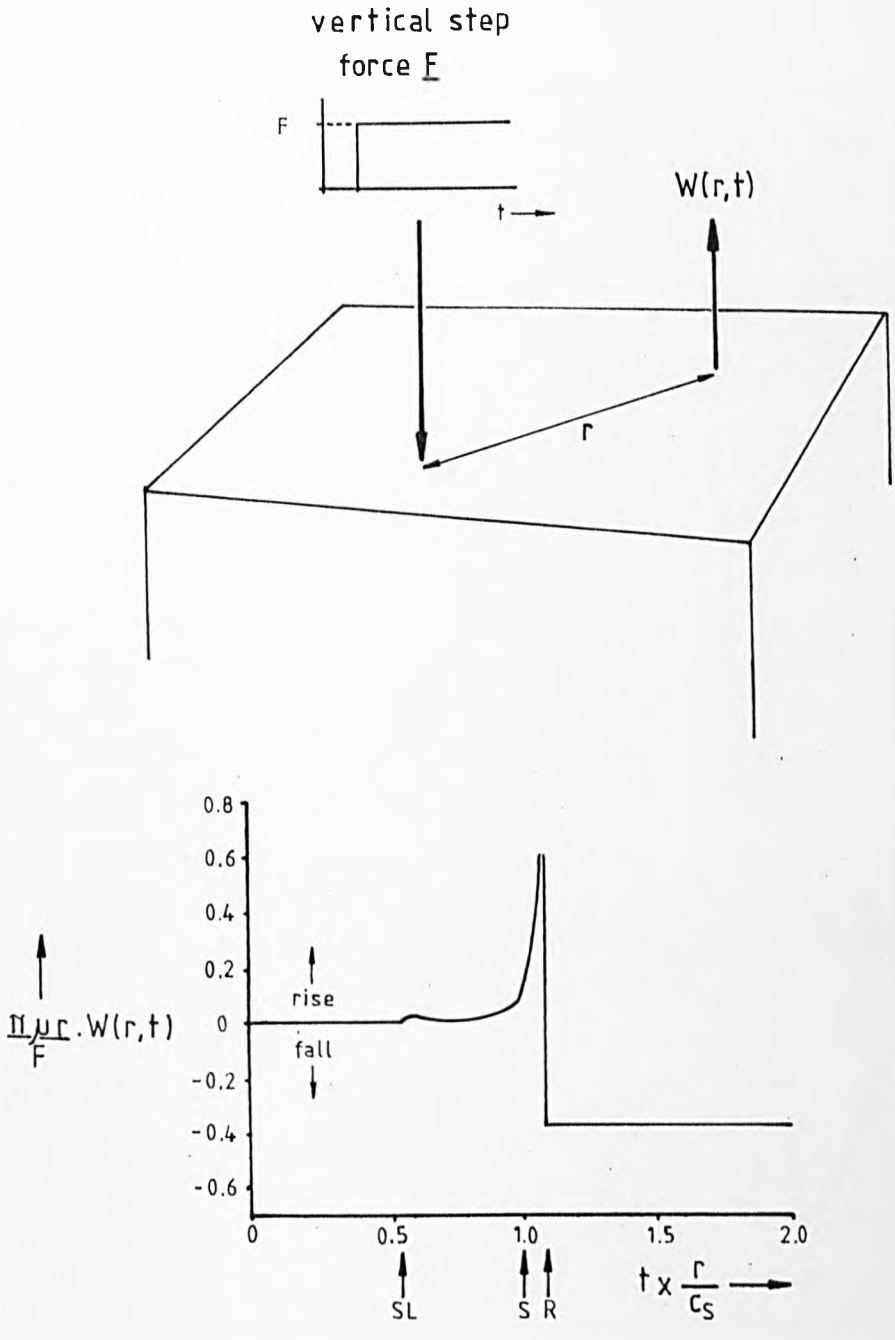

FIGURE 2.6: Vertical component of surface displacement, W(r,t), produced on the uniform elastic half-space by a step force acting vertically at a point on the surface.

After Pekeris 1955.

2.10 Surface motion of the uniform elastic half-space due to a point tangential surface force

The surface motion due to a step force acting at a point and tangentially to the surface, has been determined by Chao 1960 taking a similar approach to Pekeris. His result for the vertical component of displacement, $Q(r,t)$, produced at angle θ to the force direction, is given by

$$Q(r,t) = q(r,t)\cos\theta$$

where

$$q(r,t) = 0 \qquad \ldots\ldots \tau < \frac{1}{\sqrt{3}}$$

$$= \frac{\sqrt{\frac{3}{2}}\,\tau F}{16\pi^2\mu r}\left\{ 6K(k) - 18\pi(8k^2,k) + (6-4\sqrt{3})\Pi[-(12\sqrt{3}-20)k^2,k]\right.$$

$$\left. + (6+4\sqrt{3})\Pi[(12\sqrt{3}+20)k^2,k]\right\} \qquad \ldots\ldots \frac{1}{\sqrt{3}} < \tau < 1$$

$$= \frac{\sqrt{\frac{3}{2}}\,\tau\kappa F}{16\pi^2\mu r}\{6K(\kappa) - 18\Pi(8,\kappa) + (6-4\sqrt{3})\Pi[-(12\sqrt{3}-20),\kappa]$$

$$+ (6+4\sqrt{3})\Pi[(12\sqrt{3}+20),\kappa]\} \qquad \ldots\ldots 1 < \tau < \frac{1}{2}\sqrt{3+\sqrt{3}}$$

$$= \frac{\sqrt{\frac{3}{2}}\,\tau\kappa F}{16\pi^2\mu r}\left\{ 6K(\kappa) - 18\Pi(8,\kappa) + (6-4\sqrt{3})\Pi[-(12\sqrt{3}-20),\kappa]\right.$$

$$\left. + (6+4\sqrt{3})\pi[(12\sqrt{3}+20),\kappa]\right\} + \frac{F\tau}{8\pi\mu r\sqrt{\tau^2 - \frac{1}{4}(3+\sqrt{3})}}$$

$$\ldots\ldots \tau > \frac{1}{2}\sqrt{3+\sqrt{3}}$$

2.22

where $k = \frac{1}{2}(3\tau^2 - 1)$

$$\kappa = \frac{1}{k^2}$$

$$K(k) = \int_0^{\pi/2} \frac{d\theta}{\sqrt{1 - k^2\sin^2\theta}}$$

$$\Pi(n,k) = \int_0^{\pi/2} \frac{d\theta}{(1+n\sin^2\theta)\sqrt{1 - k^2\sin^2\theta}}$$

The expression for $Q(r,t)$ is plotted in Figure 2.7. It is notably different in two respects; first, the Rayleigh wave disturbance in the force direction, $3\pi/2 < \theta < \pi/2$, is a fall in the surface, and secondly, the surface eventually rises back to its original vertical position rather than being permanently displaced. At $\cos\theta = \pi/2$ and $3\pi/2$, $Q(r,t) = 0$, and so no vertical motion is experienced in directions perpendicular to the force line.

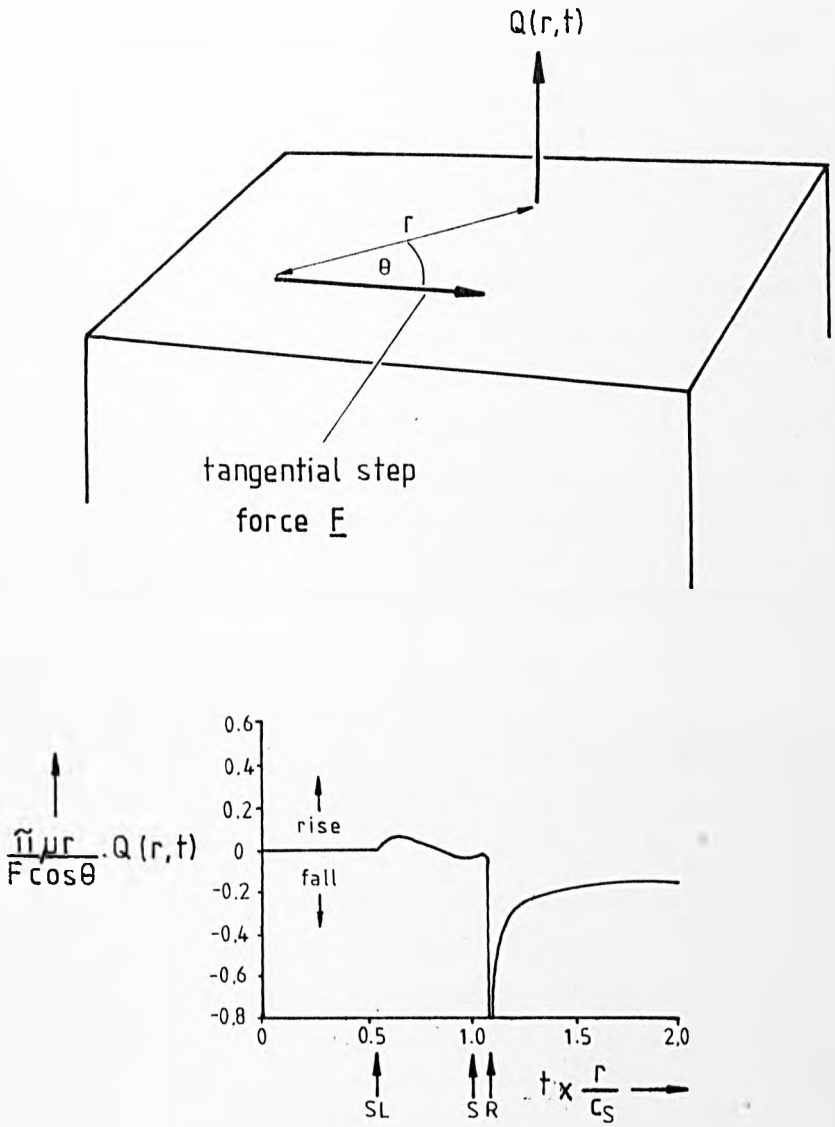

FIGURE 2.7: Vertical componenent of displacement, Q(r,t), produced on the uniform elastic half-space by a step force acting tangentially at a point on the surface.

After Chao 1960.

CHAPTER 3

Review of Laser-Generated Ultrasound in Solids

3.0 The beginning

The use of lasers to generate acoustic waves began with the work of Askar'yan 1963 and White 1963. Askar'yan noted that during the focused irradiation of liquids, sound was generated due to local vaporisation and bubble formation. White, whose main interest lay in solids, demonstrated that acoustic waves could also be generated at comparatively low laser intensities purely as a result of rapid thermal expansion. These two authors thus identified two basic acoustic generation mechanisms. In both, the waves are generated by transient forces due to some form of laser-induced expansion, but in one case, the large-scale abrupt expansion accompanying a change of state (high intensity source), and in the other, the weaker near-linear effect of ordinary thermal expansion (thermoelastic generation).

Subsequently, both source types have been studied in gases, liquids and solids. The high intensity source has also been extended to include the effects of ionisation and plasma formation.

3.1 White's thermoelastic analysis for solids

In White's original paper, he presented a detailed thermoelastic theory. It laid the foundations for subsequent work, and for a long time remained the only approach applicable to metals. In particular, he analysed a number of cases relating to harmonic (single frequency) generation in solids, namely, the uniformly-irradiated semi-infinite body, the uniformly-irradiated rod, and the locally-irradiated thermally-thin

laminar; see Figure 3.1. In the first two cases, acoustic waves are launched in the direction of absorption due to normal thermal expansion; in the latter case, in perpendicular directions as a result of lateral expansion. The case of the semi-infinite body is typical and may be summarised as follows.

As a result of the uniform absorption of energy at the surface, there is a temperature rise at and near the surface, $\theta(x,t)$, and with it an associated strain

$$\varepsilon_{xx} = \frac{\partial u(x,t)}{\partial x} = \alpha\theta(x,t)$$

where $u(x,t)$ = component of displacement in the x direction

α = coefficient of linear thermal expansion

The stress, σ_{xx}, which would have been required in the absence of heating to produce the same strain is equal to $-K\alpha\theta$, where K = bulk elastic modulus. In the presence of both heating and actual stresses, the usual 1D stress-strain relationship,

$$\sigma_{xx} = (\lambda + 2\mu)\,\varepsilon_{xx}$$

(obtainable from the first line of equation 2.5 by setting $\varepsilon_{yy} = \varepsilon_{zz} = 0$) becomes

$$\sigma_{xx} = (\lambda + 2\mu)\,\varepsilon_{xx} - K\alpha\theta$$

Upon substitution into the 1D equation of motion (equation 2.9), this gives

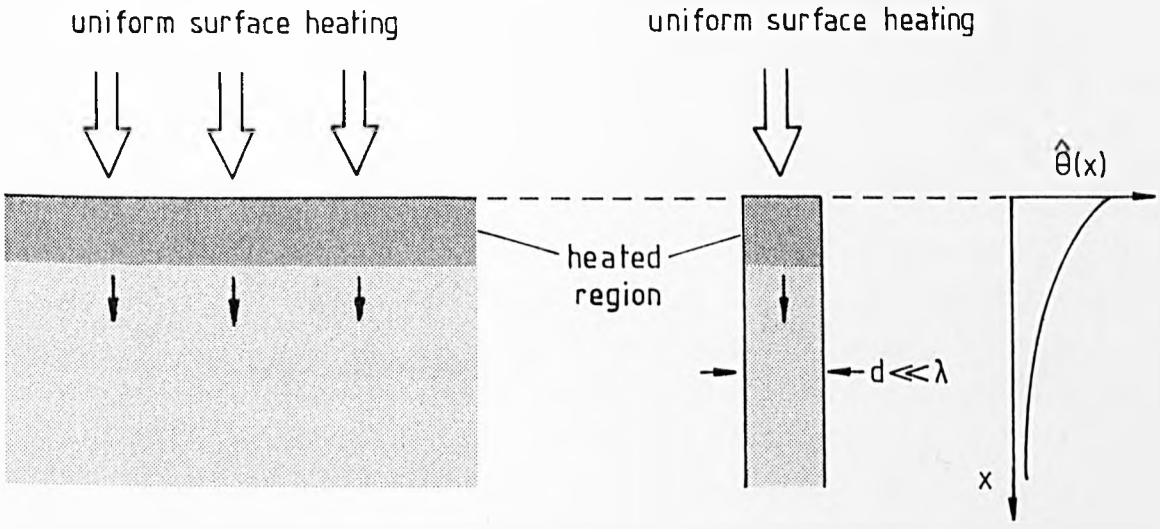

(a). semi-infinite body

(b). acoustically-thin rod

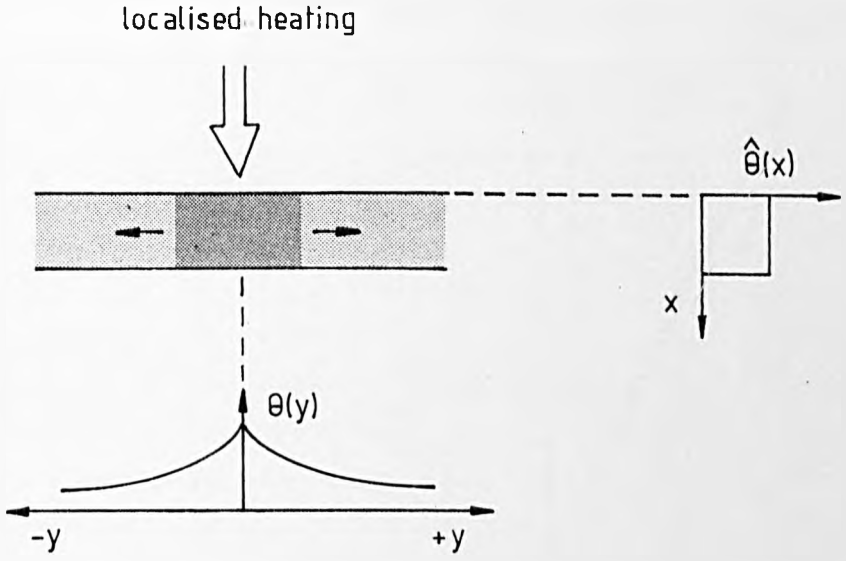

(c). thermally-thin laminar

FIGURE 3.1: The three cases of thermoelastic generation analysed by White 1963.

In cases (a) and (b) acoustic waves are launched in the x-direction as a result of normal thermal expansion; in case (c) in the y-direction due to lateral expansion.

$\hat{\theta}$ = peak temperature rise

$$\rho \frac{\partial^2 u}{\partial t^2} = \frac{\partial \sigma_{xx}}{\partial x} = (\lambda + 2\mu) \frac{\partial^2 u}{\partial x^2} - K\alpha \frac{\partial \theta}{\partial x} \qquad 3.1$$

where the term $K\alpha \frac{\partial \theta}{\partial x}$ relating to temperature gradients, is the driving term ($\underline{F}$ in equation 2.20).

White proceeded to solve this equation for the case of the harmonic component of heating due to a modulated cw heat input. The solution for displacements in the x-direction, is

$$u(x) = Ae^{-jkx} - \frac{\tau \beta \theta_o}{k^2 + \tau^2} \cdot e^{-\tau x} \qquad 3.2$$

where $u(x)$ = peak displacement (time dependence omitted)

A = constant to be evaluated from boundary conditions

k = wave number

$\tau = (1+j)/\delta_{TH}$

$\beta = K\alpha/\rho C_L^2$

θ_o = maximum (surface) temperature

δ_{TH} = harmonic thermal skin depth

K = bulk modulus

ρ = density

C_L = propagation of longitudinal waves

The constant A was evaluated for two sets of boundary conditions corresponding to the cases of the free surface (no normal component of surface stress) and the rigidly clamped surface (zero component of surface displacement). In metals in particular at comparatively low frequencies, typically << 1GHz, the expected travelling wave stress amplitude ($x \to \infty$) produced at these extremes, may be shown to approximate to

$$\frac{\sigma_{xx}}{\rho C_L^2} \approx \frac{k^2}{\tau^2}\,\beta\theta_o \qquad \text{(stress-free surface)} \qquad 3.3$$

$$\approx \frac{k}{\tau}\,\beta\theta_o \qquad \text{(constrained surface)} \qquad 3.4$$

These results are to be compared with that for the locally-heated thermal-thin laminar for which an acoustic wave is launched sidewards with an amplitude

$$\frac{\sigma_{yy}}{\rho C_L^2} \approx \beta\theta_o \qquad \text{(locally-irradiated, thermally-thin laminar)} \qquad 3.5$$

The results for the uniformly-irradiated acoustic-thin rod are essentially the same as the semi-infinite body except $\beta \equiv \alpha$.

The relative amplitudes generated in these various cases, are controlled by the two parameters k and τ. Typically, τ is a magnitude or more greater than k; for example, in aluminium at 10MHz, $\tau \approx 10k$. This implies $k/\tau \ll 1$. By comparing equations 3.3, 3.4 and 3.5, it is clear therefore that the strongest acoustic source is the thermally-thin laminar, and the weakest, the stress-free surface. In the former case, the generation efficiency may be shown to approach several % under favourable conditions. In all cases, the acoustic amplitudes are many magnitudes greater than those expected as a result of radiation pressure.

White compared these results with experimental data obtained using a variety of transient heat sources including electron beam bombardment, microwave radiation and a pulsed ruby laser. Although few experimental details were given, he asserted the results supported his theory in two ways. First, under low intensity conditions, the acoustic amplitudes

varied linearly with incident energy, as his model with its simple dependence on temperature rises (θ_o) indicated. Secondly, for different materials, acoustic amplitudes followed closely the expected functional dependence on the physical properties of the target medium.

This original analysis is important for a number of reasons; it

(1) emphasises the dynamic nature of the generation processes as a result of transient stresses due to temperature gradients ie. a non-uniform component of heating.

(2) indicates the dependence of the resultant acoustic amplitudes upon laser intensity and the thermal, optical and elastic properties of the target medium as contained in the parameters, τ, β and θ_o.

(3) gives the frequency dependence through τ and k.

(4) recognises both normal and lateral thermal expansion as potential acoustic sources.

(5) notes the importance of boundary conditions in determining the resultant amplitudes.

(6) distinguishes between the effect of constraint imposed by some external agency (constrained surface) and that internally provided by the inertia of surrounding cooler material (locally-irradiated laminar).

It does, however, have some limitations, namely, that it

(1) considers only harmonic generation.

(2) gives no simple, physical explanation for the frequency dependences or the control of boundary conditions.

(3) implicitly considers only longitudinal waves and none of the other propagation modes supported by solids.

(4) does not consider any 2 or 3D problems, only pseudo-1D source geometries.

As will be seen later, the last two points are intimately linked, the imposing of 1D source geometry immediately confining the generation to longitudinal waves.

3.2 Other Early Thermoelastic Studies

A number of thermoelastic experiments followed White's, usually pulsed. Some generated directly in bulk materials (Penner and Sharma 1966, Percival 1967, Bushnell and McCloskey 1968), but most relied on absorbing target films to launch ultrasonic waves into a variety of non-metal substrates (Brienza and De Maria 1967, Cachier 1971, Fox 1974, Von Gutfield and Melcher 1977).

The absorbing film experiments are typified by the work of Von Gutfield and Melcher 1977. They irradiated vacuum deposited Mo and W on quartz or sapphire slabs with 5ns pulses from a rhodamine 6G dye laser; Figure 3.2. A narrow-bandwidth resonant detector was employed, thereby approximating the experiment to single frequency conditions. The metalised slabs could be coupled to sample surfaces either way up, so providing a convenient

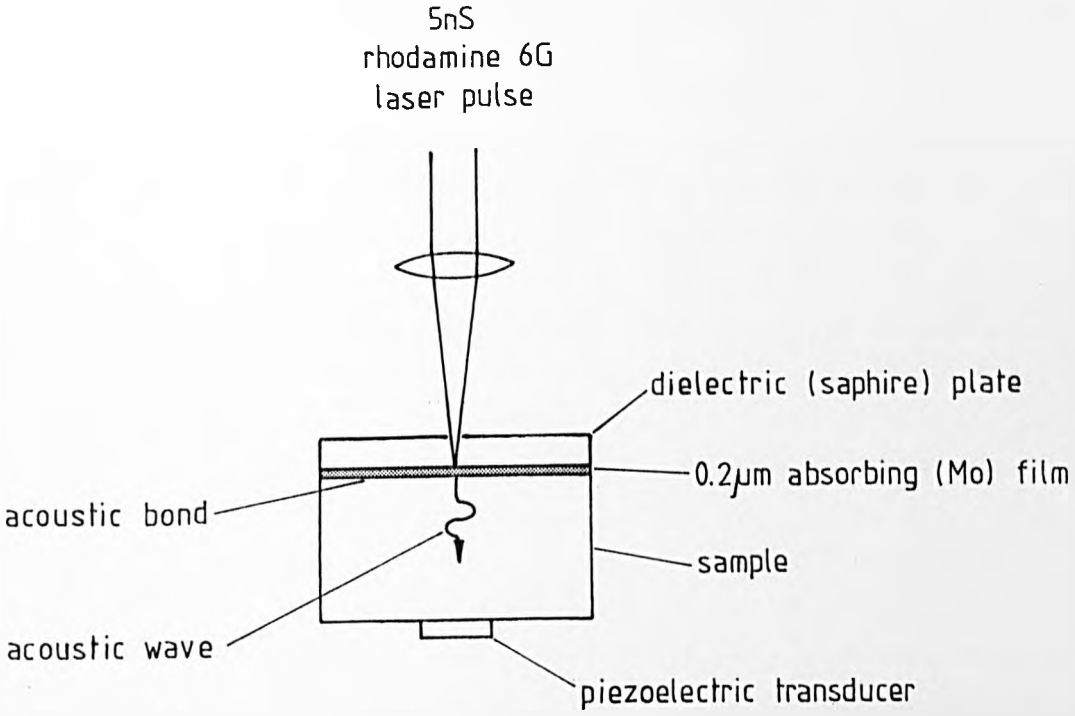

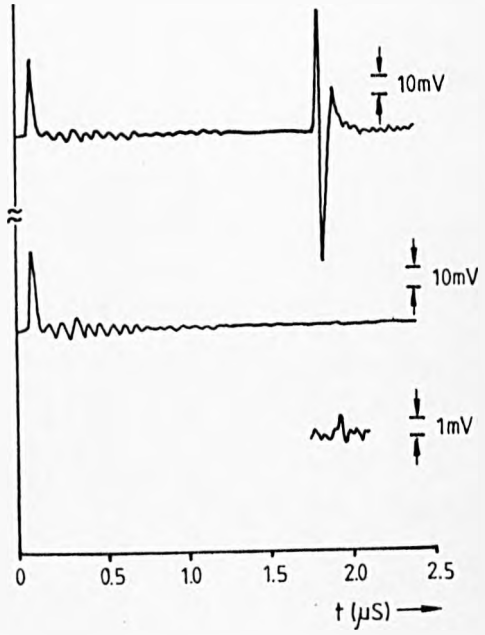

(a). absorbing film face down
(constrained surface)

(b). absorbing film face up
(free surface)

FIGURE 3.2: Von Gutfield and Melcher's 1977 experiment on thermoelastic generation at absorbing thin films.

means of simulating a free surface (metalised surface up) or a constrained surface (face down). With a 20MHz piezoelectric probe, the detected waveform at a constrained surface, in the form of a dipolar pulse, had an amplitude ×95 the free surface value. The expected enhancement obtained by division of equations 3.3 and 3.4, is

$$R = \frac{\tau}{k} = \frac{C_L}{\sqrt{2\pi\kappa f}} \qquad 3.6$$

where R = amplitude enhanced provided by total constraint

κ = thermal diffusivity

and f may be taken as the resonant frequency of the transducer

Substituting for the various parameters, indicates R = 75, a value which Von Gutfield and Melcher thought in reasonable agreement with experiment considering the approximations made and the estimated values for κ. However, this result is not entirely satisfactory, the problem being that the theoretical value is the lower of the two, and yet it represents the maximum possible having been derived assuming total constraint. The reason for this discrepancy lies in an arbitrary choice of a metal film with a thickness, d = 0.2μm. This value is to be compared with the expected thermal skin depth in M_O at 20MHz as given by $1/\tau$, of ≈ 1μm. In other words, they used a film which was thermally thin. This would have limited the effective thermal skin depth to the film thickness. Under these conditions, the relevant parameter is not $1/\tau$ but d, ie.

$$R = \frac{1}{kd} \qquad \text{thermal thin film}$$

Substituting for d, gives R = 263, making Von Gutfield and Melcher's measured value ×95 for the real case of partial constraint, seem, in retrospect, more reasonable.

Direct bulk generation in plain media was confined to non-metals, and absorbing glass in particular. Samples were examined in both rod (Percival 1967) and plate form (Bushnell and McCloskey 1968). The latter authors approximated their experimental conditions to the uniformly-irradiated semi-infinite body. They did not, however, use White's solution but rather by means of Laplace transforms showed there was an alternative solution to equation 3.1 appropriate to their conditions, of the form,

$$V(\xi,\tau) = \frac{1}{2}\int_0^{\infty} \theta(x,\tau-\xi+x)\,dx + \frac{1}{2} R_{12} \int_0^{\tau-\xi} \theta(x,\tau-\xi-x)\,dx \qquad 3.7$$

where $V(\xi,\tau) = \rho C_L^2 u/\nu Q$ = dimensionless displacement produced deep within bulk

$\theta = \rho c\lambda/Q$ = dimensionless temperature rise

$\xi = x/\lambda$ = dimensionless distance

$\tau = C_L t/\lambda$ = dimensionless time

λ = optical penetration depth

c = specific heat

Q = total absorbed energy density

u = displacement

ν = Grüneisen constant

R_{12} = acoustic (amplitude) reflection coefficient at sample surface

By substituting for θ and solving the integrals, Bushnell and McCloskey obtained the series of waveforms in Figure 3.3(a) which shows the expected acoustic stress profiles produced in a pulse-irradiated non-metal over a range of surface constraints.

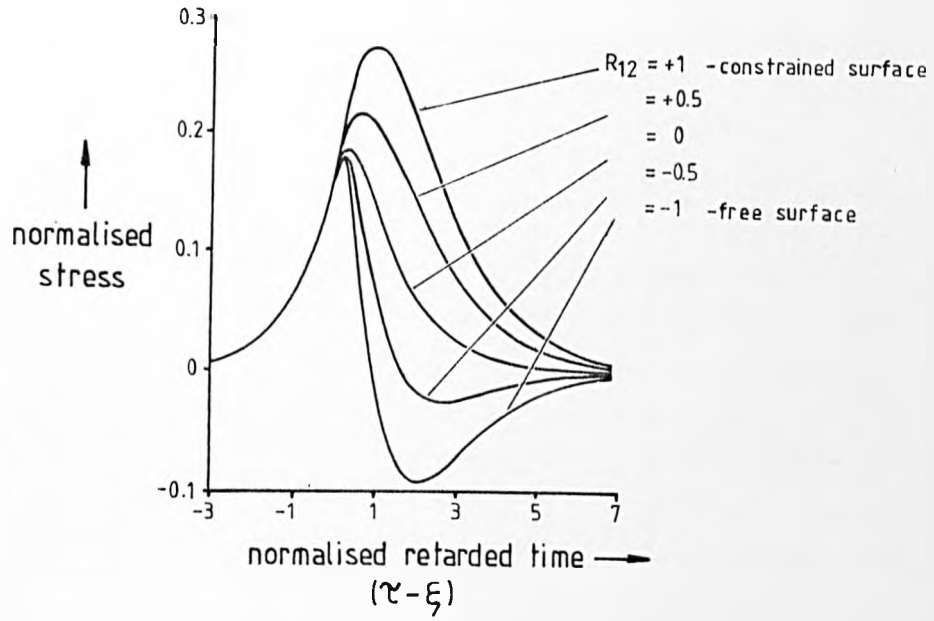

(a).

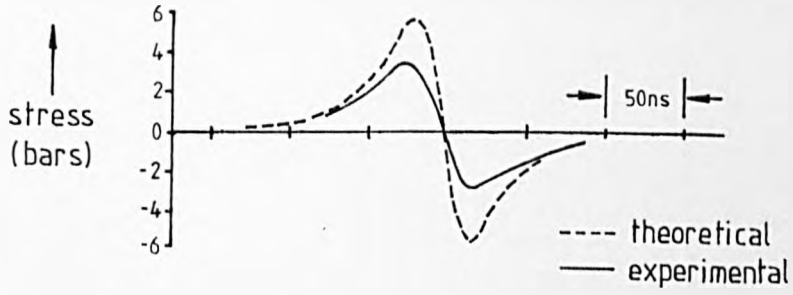

(b).

FIGURE 3.3: Results of Bushnell and McCloskey's 1968 study of pulsed thermoelastic generation in non-metals.

(a). Variation of theoretical acoustic waveform with acoustic reflection coefficient, R_{12}.

(b). Comparison of theoretical and typical experimental waveforms generated in absorbing glass by Q-switched 2J ruby laser irradiation. Fused quartz constraint and X-cut "thick" quartz detector. Free surface.

Figure 3.3(b) gives a comparison between theory and one of a number of experimental waveforms produced in a range of absorbing glass plates by pulsed ruby laser irradiation. The agreement is reasonable in terms of both pulse profile and amplitude. The calibration of the experimental waveform was achieved by operating the piezoelectric probe in "thick" mode whereby measurements of stress are made at the front electrode face before the waves have reached the back. In this configuration, it may be shown that the resultant signal when fed in a low impedance (50Ω) load, is directly proportional to the local front-face stress (Graham et al 1965). It is interesting to note from the family of theoretical waveforms, that the expected peak-to-peak amplitudes at the free and totally constrained surfaces, are approximately the same, a feature confirmed by experiment. Such a result is in contrast to Von Gutfield and Melcher's study in metals which indicated a considerable enhancement under constraint. The origin of this difference is explained in Chapter 8, and is ultimately due to differences in the optical and thermal properties between metals and non-metals.

3.3 Early studies of high intensity generation

At the other extreme to these early thermoelastic studies was an almost unrelated group of high intensity experiments. These studies used high energy laser pulses focused onto targets so as to vaporise surface material and form an intense plasma.

The experimental arrangements were all very similar, comprising a thin metal target either bonded or vaporised directly onto a quartz gauge. The choice of laser was generally high-energy Nd:glass delivering between 7-500J in pulses 2ps - 60ns long. During focused irradiation, ablation drove an intense shock wave into the gauges through surface recoil, the

usual result of which was damaged or shattered targets and transducers. The gauges were usually operated in "thick" mode, measurements being taken in the brief time before shattering presumably due to tensile reflection of the shock waves off the back surface.

A variety of surface conditions were investigated including the free surface (Skeen and York 1968, Peercy et al 1970, Jones 1971, Fox 1974), constrained surface (Anderholm 1970, Peercy et al 1970, Fairand et al 1974, Fox 1974, Yang 1974, Fairand and Clauer 1979), and surfaces covered with various volatile coats, liquids or paints (Peercy et al 1970, O'Keefe and Skeen 1972, Fox 1974). Of the differing arrangements, the free surface produced the weakest shock waves with typical amplitudes of 0.5 - 10kbar. Impeding the plasma expansion by using a transparent liquid or solid overlay increased the peak stresses by roughly an order of magnitude to typically 20-40kbar. Similar enhancements were obtained using volatile coats and paints. In the case of volatile coats, this was thought to be due to partial decomposition or vaporisation of the coating nearest to the metal surface, reacting against the constraint of remaining outer layers. Paints were considered to both increase the initial optical absorptivity and present different boil-off characteristics.

The profile of the resultant stress pulses is typified by the free-surface waveform in Figure 3.4 recorded by Peercy et al 1970 by irradiating an aluminised X-cut quartz transducer with 10-20J pulses from a Nd:glass laser. It has a comparatively fast, detector-limited rise time of $\leq$ 1ns but an extended $\approx$ 20ns tail well outlasting the original laser pulse. This tail was thought to be due to prolonged evaporation of metal due to the lingering presence of a hot plasma.

Such waveforms are not strictly dynamic. With the detectors

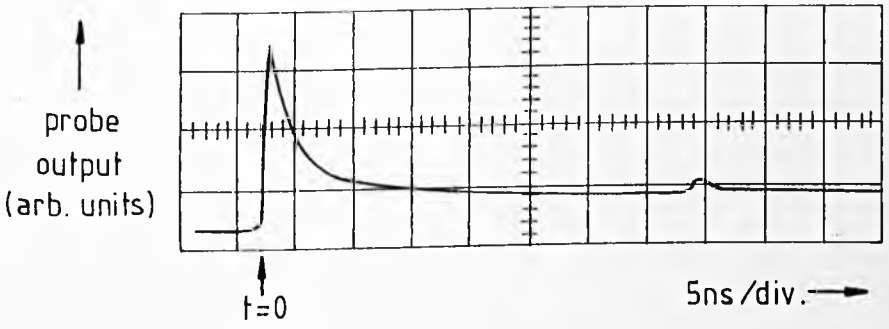

FIGURE 3.4: The stress waveform obtained by Peercy et al. 1970 by irradiating an aluminium-coated X-cut quartz transducer with a plasma-forming 3ps 10-20J Nd:glass laser pulse.

effectively positioned directly underneath the source, they simply recorded the vertical component of the surface forces. In terms of equation 2.2, the targets were acoustically thin ($d << C \Delta t$), the experiments being essentially quasi-static. This explains why either very brief or no propagation delays were observed. However, these experiments are interesting because they reveal directly the forces acting at the high intensity source. In this respect, a number of models of the vaporisation and plasma processes have been suggested. Jones 1970, for example, presented a simple 1D model of the vaporisation and impulse imparting processes. He assumed all the incident energy was absorbed within the electromagnetic skin depth, δ_{em}, producing an instantaneous absorbed energy density

$$E(x) = E_o \, e^{-x/\delta_{em}}$$

where E_o = maximum (surface) absorbed energy density.

Up to a certain critical depth, there is sufficient energy release to vaporise metal with any excess energy being transformed into kinetic energy of the vapour. In 1D geometry, all this kinetic energy will appear as vertical vapour motion. For a thin laminar of this super-heated material, thickness Δx, the energy balance may therefore be approximately written as

$$E(x)\Delta x = \rho \, \Delta x \, E_v + \frac{1}{2} \rho \, \Delta x \, V(x)^2 \qquad 3.8$$

where E_v = latent heat of vaporisation

ρ = solid density

$V(x)$ = ablation velocity

$\frac{1}{2} \rho \, \Delta x \, V(x)^2$ = kinetic energy of vapour

The contribution to the impluse imparted to the metal surface is thus

$$\Delta I = \rho \, \Delta x \, V(x)$$

which by substituting for V(x) and integrating back to the surface, gives the total imparted momentum as

$$I = 2\sqrt{(2\rho \, \delta_{em} \, E_o)} \left\{ \sqrt{1 - X} - \sqrt{X} \tan^{-1} \sqrt{\left(\frac{1-X}{X}\right)} \right\} \qquad 3.9$$

where $X = \dfrac{\rho \, \delta_{em} \, E_v}{E_o}$

Jones obtained good agreement between this expression and a wide range of experimental estimates of impulse obtained by integrating under observed stress waveforms with respect to time ($I = \int F \, dt$). This model, however, did not yield any information about the profile of the stress pulses. Similarly simple expressions have also been derived for the pressure exerted by the plasma by considering it as a hot ideal gas, notably in the case of the constrained surface (eg. Anderholm 1970, Yang 1974).

Unfortunately, the alternative to simplistic expressions such as the above, is usually sophisticated computer codes which give a frame-to-frame picture of the plasma-ablation processes. Typical examples of such codes are to be found in the work of Fairand and Clauer 1979, Fairand et al 1984. Excellent agreement in terms of both stress pulse profile and amplitude may be obtained though only after lengthy numerical computations.

There was a limited number of high intensity studies which displayed significant propagation delays due to appreciable distances between source and detector. This includes the work of Palmer and Asmus 1970 who obtained the waveform reproduced in Figure 3.5 by irradiating in air a sample of porous carbon with focused Nd:glass laser pulses. It reveals a clear delay and what is probably the first cross-sample reflection. There

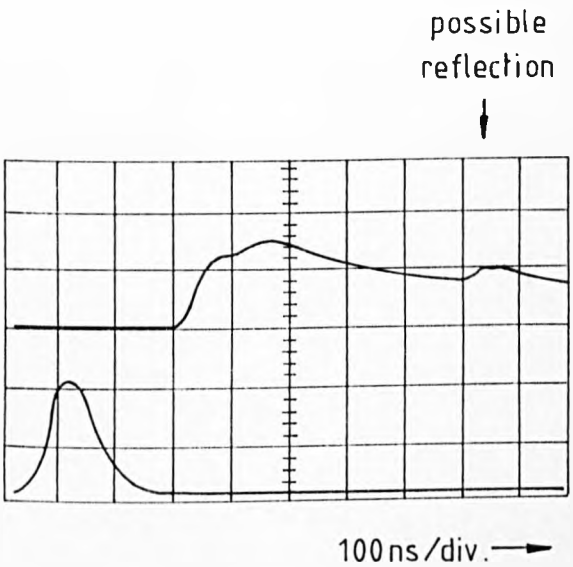

FIGURE 3.5: The waveform obtained by Palmer and Asmus 1970 in a porous carbon material by focused irradiation with a 20J Nd:glass laser pulse.

Sample thickness: 2.5mm.

Both vertical scales in arbitary units.

is also some sub-structure unrelated to the original smoothly profiled laser pulse. Although no explanation of the waveform was offered at the time, it is shown in Chapter 8 that such sub-structure develops only in the acoustic far-field, and is characteristic of non-metals under certain generating conditions.

3.4 Distinction of source type and acoustic mode

A common failing in these early studies was a lack of any real distinction between the various acoustic modes a solid body can support. The low intensity studies in particular often referred loosely to acoustic waves as "stress" waves, whereas, in retrospect, longitudinal waves were implied.

As long ago as 1968, however, Lee and White clearly identified Rayleigh surface waves generated under thermoelastic conditions in a thin metal film experiment. In 1972, Kubota and Nakatoni recognised the generation of shear waves in a variety of metals and non-metals. It was not until 1979, however, with the work of Ledbetter and Moulder came the report of the simultaneous generation of all three principle waves associated with semi-infinite solid body, namely, longitudinal and shear bulk waves, and Rayleigh surface waves. In this case, generation took place in aluminium under conditions of plasma-ablation. It was suggested that the resultant removal of surface material may have enhanced thermoelastic processes by surface recoil through momentum transfer.

Although such studies distinguished different acoustic modes, none analysed the pulse profiles nor described in detail possible generation mechanisms.

3.5 Quantitative studies

In more recent years, attempts have been made to quantify the generation processes under certain specialised conditions. This work is epitomised by the work of Scruby et al 1980 who provided an almost complete quantitative description of the thermoelastic bulk acoustic waveform produced on epicentre by pulsed localised irradiation of a free metal surface. They compared calibrated experimental waveforms obtained with a broad bandwidth capacitance probe, with an unpublished solution to the 3D equation of motion; Figure 3.6. The agreement is excellent, revealing both longitudinal and shear arrivals in the form of step-like displacements. In this study, the laser source was represented as an expanding point volume of surface metal.

Further studies have included modelling the epicentral bulk waveforms produced by plasma-ablation, surface coat ablation and transitional sources (Hutchins et al 1981c, Dewhurst et al 1982). In the case of ablation, the source is characteristic of a point vertical surface force, for which solutions are readily available from standard acoustic theory. Corresponding surface wave responses in metals have been given by Aindow et al 1983a.

Certain aspects of the surface response have also been described in non-metals by Ash et al 1980. By using masks, these authors irradiated ink-covered $LiNbO_3$ with a series of parallel lines from a chopped cw Ar laser thereby producing an array of harmonic thermoelastic sources. The resultant Rayleigh waves were launched in normal directions as collimated, rectilinear beams. This allowed relatively simple expressions to be derived from essentially 1D considerations. Similar work has been subsequently carried out by Royer and Dieulesaint 1983.

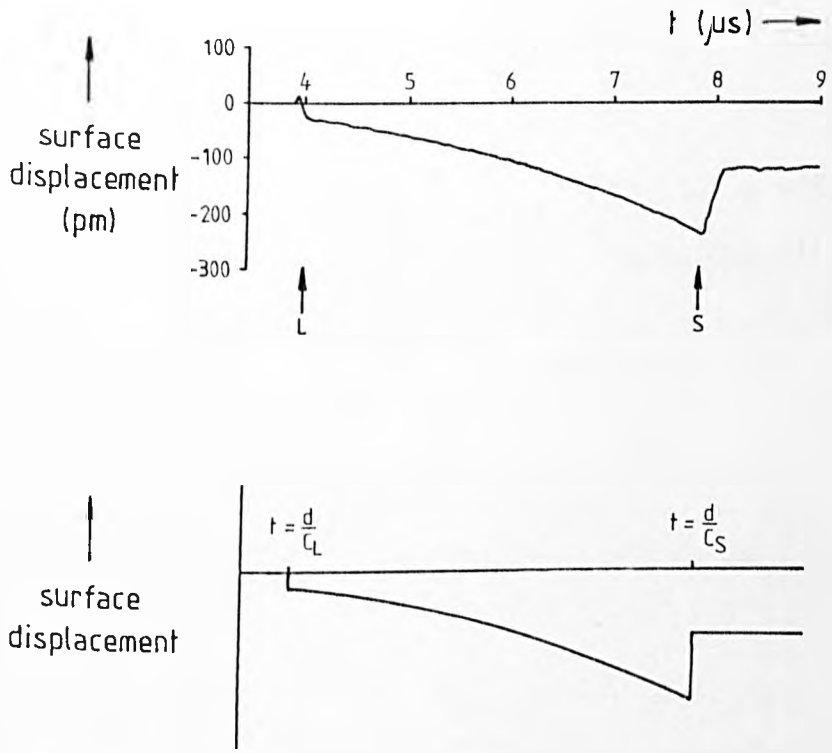

FIGURE 3.6: Scruby et al.'s 1980 comparison of experimental and theoretical bulk acoustic waveforms produced by pulsed thermoelastic irradiation of a free metal surface.

(a). Experimental waveform produced by a 31mJ Q-switched Nd:YAG pulse incident on a 25mm thick aluminium sample. Broad bandwidth capacitance detector.

(b). Theoretical waveform obtained from an unpublished solution to the equation of motion. Source represented as an expanding point-volume of surface metal.

The understanding of the thermoelastic source in metals has been recently improved by Rose 1984 who extended the theory of Scruby et al 1980 to include the effects of surface constraint. He formulated the problem for both the epicentral bulk wave and surface wave sources though waveforms were presented only in the former case. Cooper 1985 has also considered the free surface source, and also described off-epicentre plate waveforms.

Other quantitative or broad bandwidth studies include Wadley et al 1982, Tam and Coufal 1983, Hutchins and Nandeau 1983, Nandeau and Hutchins 1984, Scruby 1985, Hutchins and Wilkins 1985, Hutchins et al 1985.

In metals, the laser acoustic source is now comparatively well understood particularly in relation to bulk waveforms. In non-metals, some effort has been made to understand electrostrictive generation in suitably optically-active media eg. Chiao et al 1964, Garmire and Townes 1964, Cachier 1971 and Nelson 1982. Non-metals generally, however, have received comparatively little attention.

3.6 Practical applications

Laser ultrasonics has aroused considerable interest as a means of generating ultrasound remote from a test piece. For example, when coupled with a non-contact detector such as a laser interferometer, it opens up the possibility of remote non-destructive testing, potentially useful in hostile environments or where fast scanning is required. A number of such systems have been developed including Bondarenko et al 1976, Kaule 1978, Calder and Wilcox 1980, Wellman 1980, Nadeau and Hutchins 1984. However, the systems suffer from a general lack of sensitivity particularly when relying on the non-ablating thermoelastic source to minimise target damage. This is mainly due to the interferometer detectors which are not only

comparatively insensitive but usually also require a flat and polished surface. To help overcome some of these limitations, attempts have been made to increase the initial ultrasonic amplitudes by focusing with axicon lenses (Jen et al 1980, Cielo 1984). Perhaps laser ultrasonic testing is better performed in conjunction with non-contact electro-magnetic acoustic transducers (EMATs) (Budenkov and Kaunov 1979, Hutchins et al 1985, Hutchins and Wilkins 1985). Alternatively, it has proved useful in static or small-scale precision NDT (Bar-Cohen 1979, Aindow et al 1983b, 1983c, 1984, Cooper 1985). The problem of increasing ultrasonic amplitudes without causing damage is discussed towards the end of Chapter 9. Other non-destructive ultrasonic measurements possible with laser ultrasound include the estimation of propagation velocities and elastic constants (Bonderenko 1976, Calder and Wilcox 1978 and 1980, Ledbetter and Moulder 1979). Additionally, otherwise difficult or impossible measurements can be made on thin films, ribbons or rods (Krautkramer 1979, Rosen et al 1981, Smith et al 1983, Sessler 1983, Tam 1984).

Another application to solids is as a standard acoustic source for calibration purposes where the well-characterised, reproducible nature of the laser source is unsurpassed (Davidson et al 1976, Egle and Brown 1976, Hutchins et al 1981c, Scruby et al 1981).

The laser source has also been successfully applied to various forms of microscopy. In the conventional acoustic microscope, lasers have been used to generate hypersound directly in samples replacing the usual liquid-coupled ZnO transducers (Wickramasinghe et al 1978, Petts and Wickramasinghe 1980). Other arrangements have variously exploited associated thermal or acoustic effects, eg. Luukkata and Penttinem 1979, Favro et al 1980, Rosencwaig 1980, Ameri et al 1981, Martin and Ash 1984.

Laser acoustics has also proved valuable in the development of photoacoustic spectroscopy, a useful compliment to conventional spectroscopic techniques. Several reviews of this particular subject have been published including Pao 1977, Rosencwaig 1978, Patel and Tam 1981. Other aspects of laser ultrasonics have been reviewed by Scruby et al 1981 (metals only), Birnbaum and White 1984 (applications to NDT) and Hutchins 1986 (general review in gases, liquids and solids).

CHAPTER 4

Theory of the Thermal Generation of Acoustic Waves by Laser Irradiation

4.0 Introduction

The purpose of this chapter is twofold. First, it describes thermoelastic generation in metals, analysing a number of different cases. Secondly, and in a broader perspective, it offers a general view of acoustic wave generation at the interface between a light absorbing target medium and an overlying transparent medium. In the latter respect, consideration is given to groups of waves propagating simultaneously into both media, thereby combining into a single model the thermoelastic and photoacoustic effects as complimentary aspects of the same basic mechanism.

Two basic assumptions are made. First, the heating due to the absorption of laser energy changes neither the physical state nor properties of the media. Secondly, only a small proportion of the absorbed energy is actually carried off in the form of acoustic waves. This implies that the temperature rises are not significantly moderated by the acoustic processes, thereby allowing the thermal and acoustic aspects of the generation processes to be satisfactorily considered consecutively as though uncoupled.

The emphasis is on generation in the ultrasonic region. This directs the discussion towards generation by either a rapidly-modulated continuous wave laser, or, brief pulsed irradiation.

4.1 Temperature rises in metals

When laser radiation is incident on a metal surface, most of it is

reflected whilst the transmitted remainder is absorbed and almost instantaneously converted into heat within a short distance usually taken as the electromagnetic skin depth, δ_{em}. Classical electromagnetic theory indicates that this is due to the induction of eddy currents within the metal surface which reradiate most of the energy while dissipating the rest as resistive losses. On this basis (Bleaney and Bleaney 1976), the absorptivity of a metal surface, T_{op}, and δ_{em} are given by

$$T_{op} = \frac{4}{\mu_o \sigma_e c_{em} \delta_{em}} \approx 2.1 \times 10^{-s} \sqrt{\left(\frac{\mu_r \nu}{\sigma_e}\right)} \qquad 4.1$$

$$\delta_{em} = \sqrt{\frac{1}{\pi \sigma \nu \mu_r \mu_o}}$$

where μ_o = permeability of free space

μ_r = relative permeability

σ_e = electrical conductivity

c_{em} = velocity of light in free space

ν = frequency

In practice, these expressions are not generally applicable to short wavelengths especially towards the visible and UV end of the spectrum. This is due to selective absorption by bound electrons (Longhurst 1970). At a wavelength of 1.06μm (Nd:YAG laser wavelength) in the near infra-red, T_{op} indicates an absorptivity of 7% for a typical metal such as aluminium, which compares favourably with the measured value of 8% (Kaye and Laby 1973).

For most common metals, δ_{em} lies in the 2-5nm range over the visible and near infra-red spectra. Though this defines the depth to which heat is generated, it rapidly diffuses to much greater depths. This can be demonstrated by comparing δ_{em} with values for the thermal skin depth, δ_T,

which will give an estimate of the distance heat will flow away from a suddenly heated region in a given time, t. From heat flow theory (Condon and Odishaw 1958b), the thermal skin depth for a half-space impulsively heated at its surface is given by

$$\delta_{TP} = \sqrt{4\kappa t} \qquad \text{(pulsed)} \qquad 4.2$$

where κ = thermal diffusivity

Alternatively, if the heating is periodic, the equivalent harmonic thermal skin depth is

$$\delta_{TH} = \sqrt{\frac{2\kappa}{\omega}} \qquad \text{(harmonic)} \qquad 4.3$$

where ω = angular frequency of heat source

The time (frequency) variation of both forms of δ_T are shown in Figure 4.1 for a number of different metals. It is clear that provided $t >> 10^{-12}$s ($\omega << 10^{12}$ rads^{-1})

$$\delta_T >> \delta_{em}$$

This implies that for all but exceptionally brief pulses or high frequencies, heat is being conducted as it is being generated to very considerable depths. To a good approximation therefore, heat production within metal, A(x,y,z,t), may be taken as being purely superficial, and so may be simply equated to the instantaneous laser intensity absorbed at the surface, as given by

$$I(x,y,t) = I_o\, S(x,y)\, P(t)$$

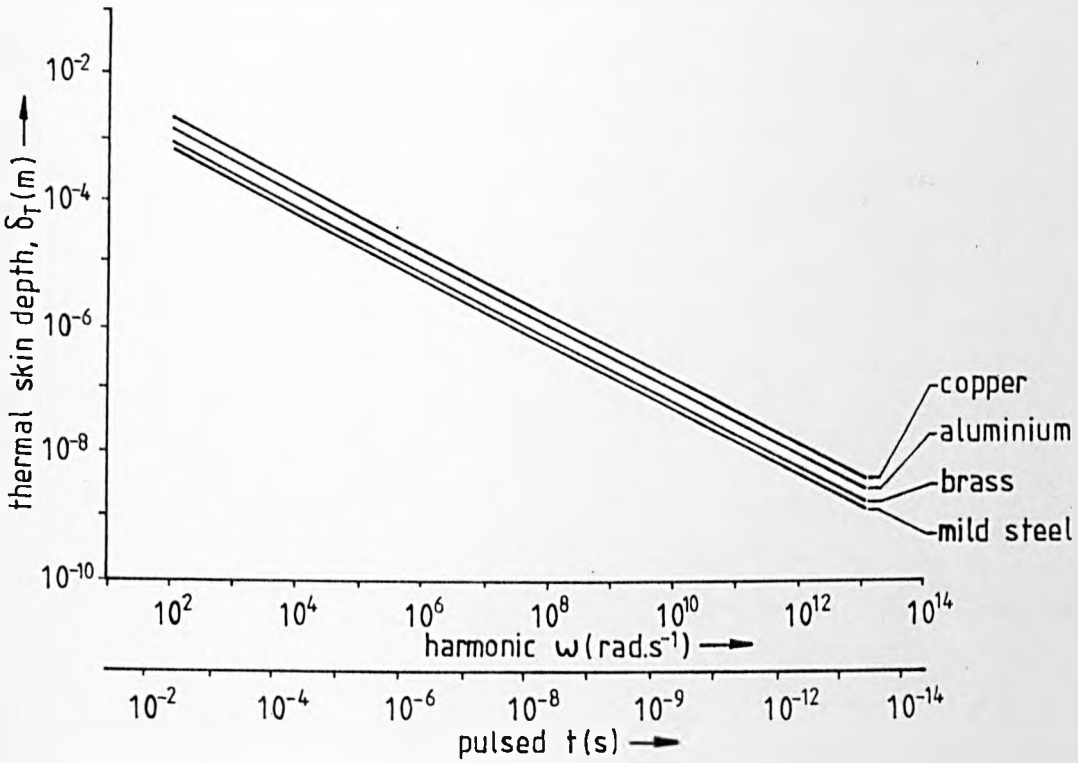

FIGURE 4.1: The time (frequency) variation of the pulsed (harmonic) thermal skin depth for a variety of metals.

This is to be compared with δ_{em}=2-5nm over the visible and near infra-red spectra.

where I_o = peak absorbed laser intensity

$S(x,y)$ = normalised laser spatial profile

$P(t)$ = normalised laser temporal profile

These quantities are related to the total absorbed pulse energy, E_T, as

$$I_o \int_o^\infty P(t)dt. \iint S(x,y)\, dxdy = E_T \qquad 4.4$$

Under these conditions, the differential equation of heat flow, namely, (Ready 1971)

$$\nabla^2\theta(x,y,z,t) - \frac{1}{\kappa}\frac{\partial\theta(x,y,z,t)}{\partial t} = -\frac{A(x,y,z,t)}{K} \qquad 4.5$$

where c = specific heat

ρ = density

$\theta(x,y,z,t)$ = temperature rise

K = thermal conductivity

may be solved subject to the boundary condition of no back flow of heat across the surface, to give the resultant temperature rises.

The appropriate solutions in cases of interest will now be either derived by adaptation from standard heat flow theory (Condon and Odishaw 1958b, Carslaw 1921) or quoted from previously worked examples (Ready 1971).

Uniform laser irradiation

In the case of spatially uniform irradiation, $S(x,y) = 1$, the heat flow is totally normal to the surface, and the 1D form of equation 4.5 may be solved as follows.

Instantaneous laser pulse

If the laser pulse is sufficiently brief that it may be considered to vary in time as a delta function, the resultant temperature rise will be simply twice that produced by the equivalent impulsive planar heat source in the infinite medium, and hence from Condon and Odishaw (1958b),

$$\theta(z,t) = \frac{E_T}{c\rho\sqrt{\pi}\,\delta_{TP}} \exp\left\{-\frac{z^2}{\delta_{TP}^2}\right\} \qquad 4.6$$

where $E_T = I_o \int P(t)dt$ = absorbed laser energy density

Prolonged laser pulse

The temperature rise due to a laser pulse with an arbitary temporal profile may be obtained by convolving equation 4.6 with the laser temporal profile so

$$\theta(z,t) = \frac{I_o}{c\rho\sqrt{\kappa\pi}} \int_o^t \frac{e^{-\frac{z^2}{4\kappa t'}}}{\sqrt{t'}} P(t-t')dt' \qquad 4.7$$

Sinusoidally modulated laser irradiation

If a continuous laser beam is modulated, it produces two components of heating. The first, related to the time-averaged absorbed laser intensity, is continuous and leads to a steady heating up of the metal. The associated thermal expansion is likewise gradual and so generates no acoustic waves. The other component - the one of interest - is due to the modulation and superimposes a harmonic variation in the temperature rise near the surface with an amplitude that decreases exponentially with depth to a characteristic distance directly related to the harmonic thermal skin depth, δ_{TH}. If the absorbed laser intensity is expressed as

$$I(t) = I_o\left(1 + \cos\left(\omega t + \frac{\pi}{4}\right)\right)$$

where ω = angular frequency of modulation

then the harmonic component of temperature rise is given by (Carslaw 1921),

$$\theta(z,t) = \theta_o\, e^{-\frac{z}{\delta_{TH}}} \cos\left(\omega t - \frac{z}{\delta_{TH}}\right) \qquad 4.8$$

where $\theta_o = \dfrac{I_o\, \delta_{TH}}{\sqrt{2}\, K}$ = maximum (surface) temperature rise

This may be alternatively expressed as the real part of

$$\theta(z,t) = \theta_o\, e^{-\tau z}\, e^{j\omega t} \qquad 4.9$$

where $\tau = \dfrac{(1+j)}{\delta_{TH}}$

The variation of $\theta(z,t)$ with depth is illustrated in Figure 4.2 to show how the surface is effectively heated and cooled alternately so producing successive hot and cold temperature fronts which travel with rapidly decreasing amplitude into the bulk.

Non-uniform irradiation

If the surface is not uniformly irradiated, then strictly a full 3D solution to equation 4.5 should be sought. However, provided that the characteristic width or diameter of the laser beam, d, is much greater than the thermal skin depth, the heat flow will be approximately normal to the surface. For example, it can be seen from Figure 4.1 that for a d = 100μm beam, this is the case provided t << 0.1ms. Therefore unless either the

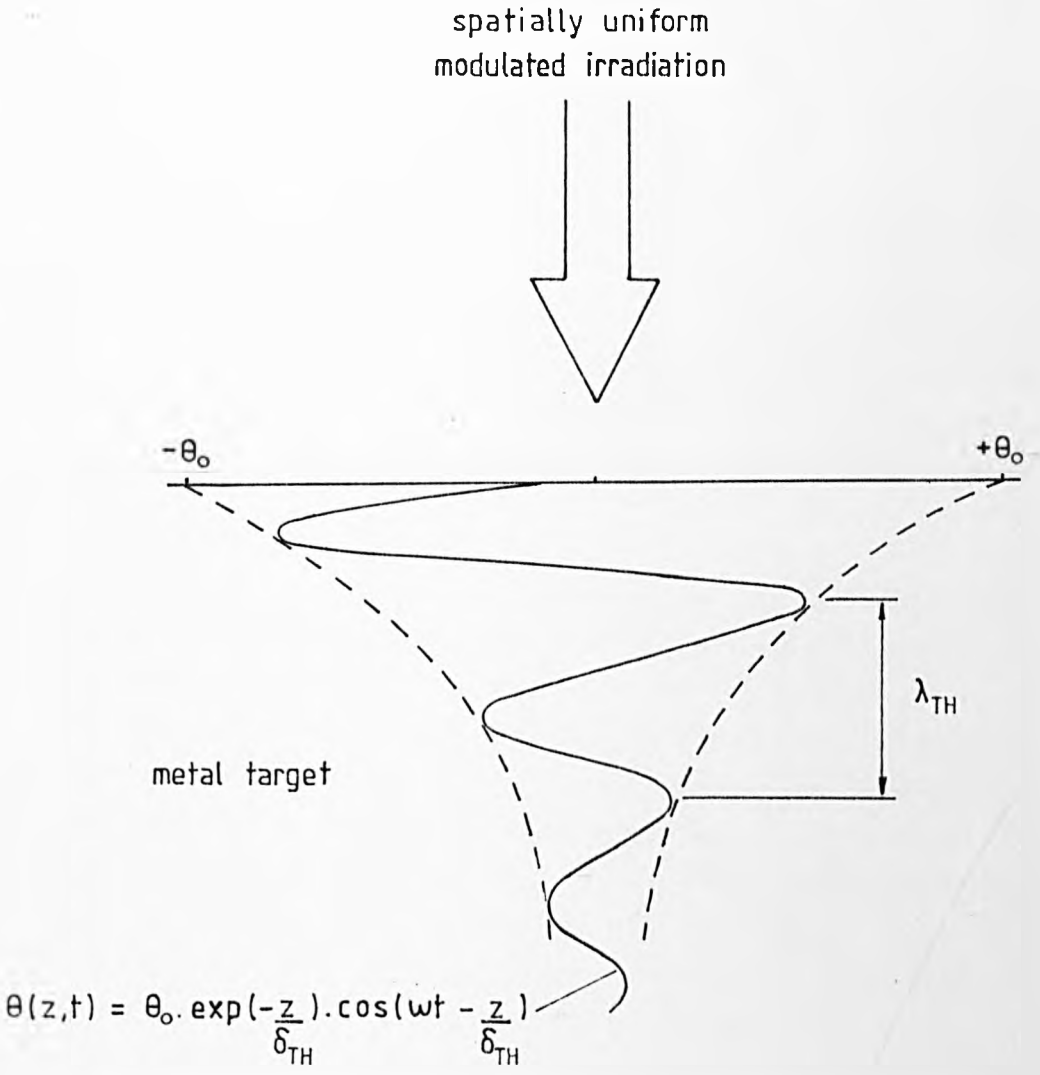

FIGURE 4.2: Temperature rise produced by the harmonic intensity component of a continuous laser beam moduated at an angular frequency, ω.

Adapted from Carslaw 1921.

laser pulse is focused or long time scales are of interest, the above 1D results will hold for each vertical column of metal.

Under these conditions, it may be seen from equation 4.7 that the temperature rise due to a laser pulse with both arbitrary temporal and spatial profiles is

$$\theta(x,y,z,t) = I_o \frac{S(x,y)}{c\rho\sqrt{\kappa\pi}} \int_o^t \frac{e^{-\frac{z^2}{4\kappa t'}}}{\sqrt{t'}} P(t-t')dt' \qquad 4.10$$

For a single mode (TEM_{oo}) laser pulse which has the special property of having a gaussian axi-symmetric spatial profile

$$S(x,y) = e^{-\frac{x^2+y^2}{a^2}}$$

where a = gaussian radius

this can be rewritten in cylindrical coordinates as

$$\theta(r,z,t) = \frac{I_o e^{-\frac{r^2}{a^2}}}{c\rho\sqrt{\kappa\pi}} \int_o^t \frac{e^{-\frac{z^2}{4\kappa t'}}}{\sqrt{t'}} P(t-t')dt' \qquad 4.11$$

where r = radial position

This expression has been evaluated for the case of an aluminium surface irradiated by a 30ns single mode pulse from a Nd:YAG laser with an incident energy of 2.5mJ and a gaussian radius of 0.3mm. Details of the assumed laser temporal profile are given in Figure 4.3(a). These conditions correspond to those met in the experimental work described in Chapter 5 onwards. The results for the on-axis temperature rise, $\theta(0,z,t)$, are presented in two forms; first, in Figure 4.4(b) as a function of time for various depths, and secondly, as a function of depth at selected times

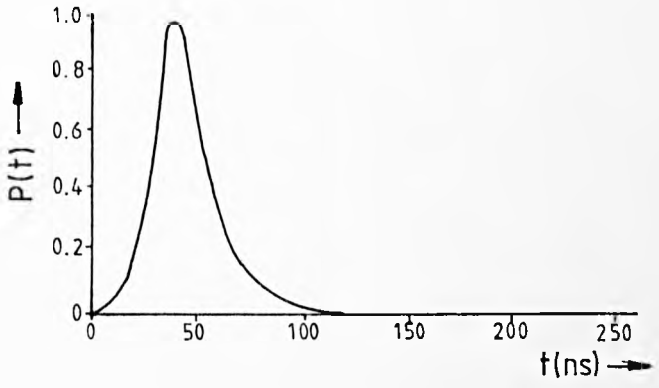

(a). Normalised temporal profile

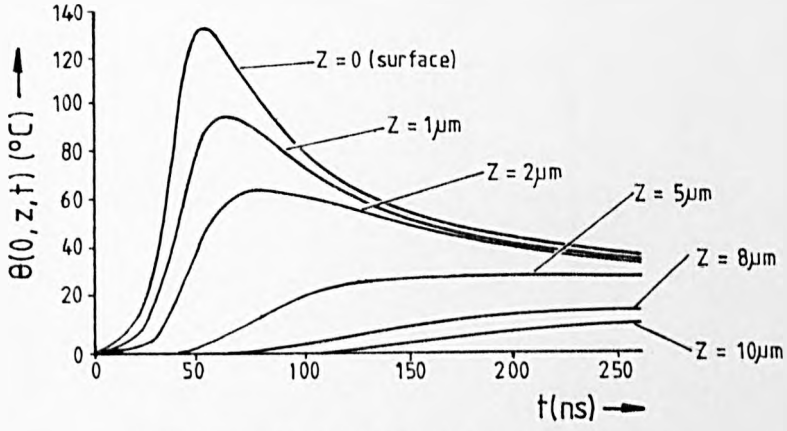

(b). Time variation at different depths.

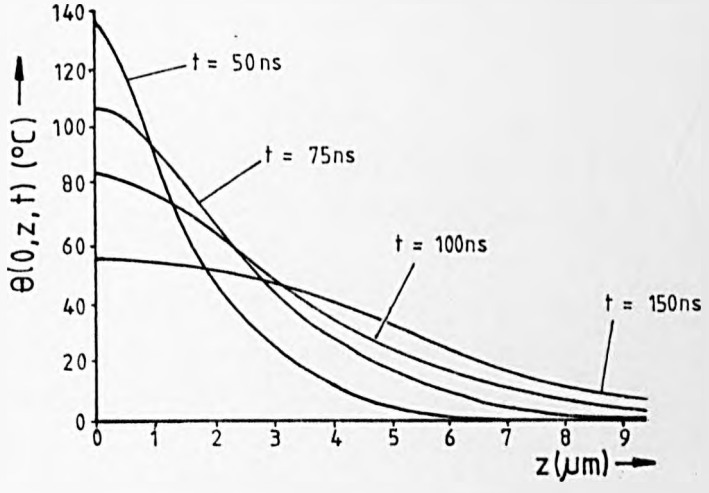

(c). Depth variation at different times.

FIGURE 4.3: Calculated temperature rises produced in aluminium by irradiation with a 2.5mJ single mode Nd:YAG laser pulse. Evaluated from equation 4.11 for a guassian radius, a=0.3mm.

after the onset of irradiation in Figure 4.3(c). The off-axis temperature rises may be obtained from these two figures by noting

$$\theta(r,z,t) = S(x,y)\ \theta(o,z,t) = e^{-\frac{r^2}{a^2}}\ \theta(0,z,t)$$

The maximum (surface) temperature rise which occurs immediately after the peak in the laser temporal profile, is ≈ 140°C. Furthermore, the region of significant heating as defined by the depth to which the maximum temperature rise is 1/e of the surface value, is ≈ 5μm. This is in reasonable agreement with an estimate of ≈ 4μm made from equation 4.2 for the thermal skin depth at t = 30ns. The heating is therefore both moderate and superficial.

Similar calculations for different metals indicate maximum temperature rises ranging from 35°C for a good thermal conductor such as copper to 700°C for mild steel which is a poor thermal conductor with a relatively high optical absorptivity.

If the laser pulse is finely focused or longer time scales are being considered, equations 4.10 and 4.11 will be in error due to significant lateral flow of heat. However, if interest lies in transient process such as acoustic wave generation by unfocused laser pulses, such diffusion is unimportant. Full 3D solutions for a single mode pulse may be found elsewhere (Ready 1971).

4.2 Stress-strain relationship in the presence of thermal stresses

The laser-induced temperature rises will produce associated stresses due to thermal expansion. If an elemental cube of heated material (Figure 4.4) were unconstrained, it would expand from a volume V to V + ΔV,

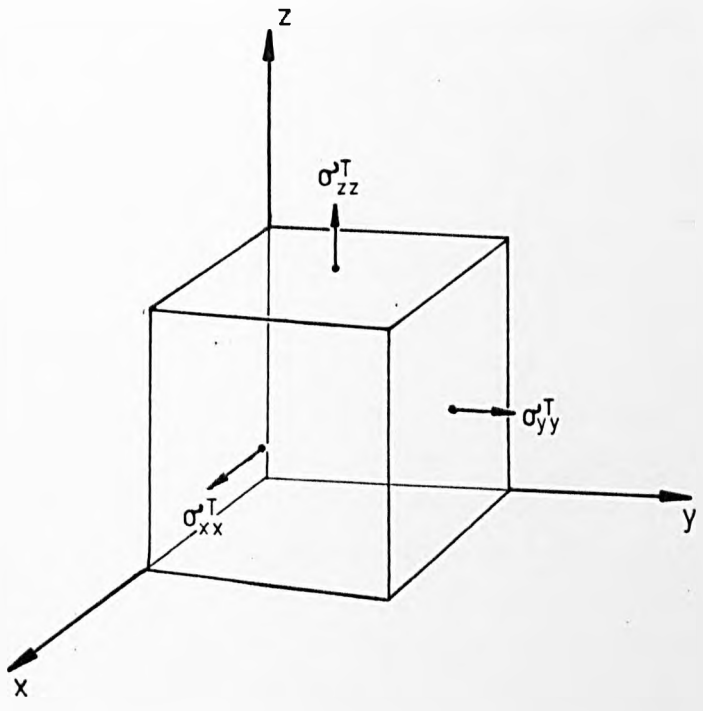

$$\sigma'^{T}_{xx} = \sigma'^{T}_{yy} = \sigma'^{T}_{zz} = -K.\frac{\Delta V}{V} = -\alpha(3\lambda + 2\mu).\theta(x,y,z,t)$$

FIGURE 4.4: The stresses effective at an elemental cube of laser-heated material as a result of thermal expansion.

K = bulk elastic modulus

$\frac{\Delta V}{V}$ = volume strain

where

$$\frac{\Delta V}{V} = 3\alpha\ \theta(x,y,z,t) \qquad 4.12$$

where α = linear expansivity

The same expansion would also be produced without heating by stresses acting on each of its faces

$$\sigma^T_{xx} = \sigma^T_{yy} = \sigma^T_{zz} = -K\frac{\Delta V}{V} \qquad 4.13$$

where K = bulk modulus

which by substitution from 4.12 and 2.6 can be rewritten as

$$\sigma^T_{xx} = \sigma^T_{yy} = \sigma^T_{zz} = -\alpha(3\lambda+2\mu)\ \theta(x,y,z,t) \qquad 4.14$$

These additional stresses may be summed with the usual elastic stresses described by equation 2.5 to give the stress-strain relationship in the presence of thermal stresses as

$$\begin{aligned}
\sigma_{xx} &= (\lambda+2\mu)\ \varepsilon_{xx} + \lambda(\varepsilon_{yy}+\varepsilon_{zz}) - \alpha(3\lambda+2\mu)\ \theta(x,y,z,t)\\
\sigma_{yy} &= (\lambda+2\mu)\ \varepsilon_{yy} + \lambda(\varepsilon_{zz}+\varepsilon_{xx}) - \alpha(3\lambda+2\mu)\ \theta(x,y,z,t)\\
\sigma_{zz} &= (\lambda+2\mu)\ \varepsilon_{zz} + \lambda(\varepsilon_{xx}+\varepsilon_{yy}) - \alpha(3\lambda+2\mu)\ \theta(x,y,z,t)\\
\sigma_{xy} &= \mu\varepsilon_{xy}\ ;\ \sigma_{yz} = \mu\varepsilon_{yz}\ ;\ \sigma_{zx} = \mu\varepsilon_{zx}
\end{aligned} \qquad 4.15$$

These are standard thermoelastic expressions (Johns 1965). The shear stresses σ_{xy}, σ_{yz} and σ_{zx} can be seen to remain unaltered as thermal expansion in acting uniformly in all directions, produces no pure shear

strains.

4.3 Equation of motion

These thermal stresses can now be incorporated as a driving term in the equation of motion for the target medium by substituting equation 4.15 for 2.5 ultimately yielding (see Section 2.3)

$$\rho \frac{\partial^2 \underline{r}}{\partial t^2} = (\lambda+\mu)\ \nabla\nabla.\underline{r} + \mu\nabla^2\underline{r} - \alpha(3\lambda+2\mu)\nabla\theta(x,y,z,t) \qquad 4.16$$

This is the equation of motion due to thermal stresses resulting from laser irradiation. If the left hand side were set to zero, it could be recognised as a form of the quasi-static thermoelastic equation (Johns 1965) describing the steady-state stress-strain distributions due to slowly varying temperature variations where inertial effects are negligible. In the present case, the dynamic problem of acoustic wave generation is being considered and so the essential inertial term, $\rho\partial^2\underline{r}/\partial t^2$, is included. It is essentially the 3D version of the various 1D equations proposed by White 1963, Penner and Sharma 1966, and Bushnell and McCloskey 1968 (see Sections 3.1 and 3.2).

Two solutions to this equation will be discussed. The first, to which the remainder of this chapter is devoted, is a generalised integral solution for the case of longitudinal bulk wave generation at a uniformly irradiated surface. The second, considered in detail in Chapter 8, is for the other physically extreme case of the point source.

4.4 Generalised uniform irradiation model

Consider the case of a light absorbing surface overlayed by a second transparent medium through which laser radiation is incident; Figure 4.5.

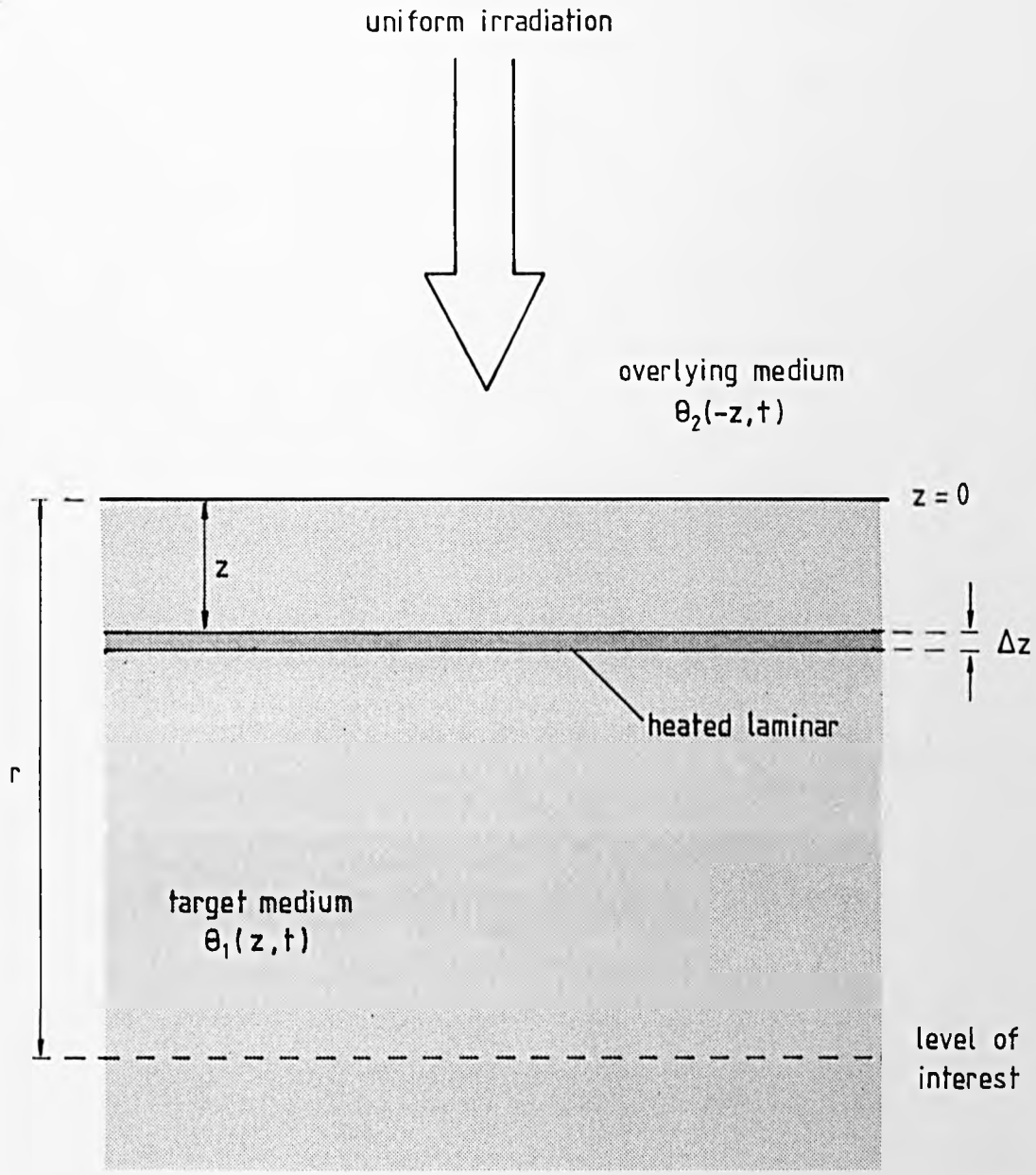

FIGURE 4.5: 1D model of longitudinal wave generation by spatially uniform laser irradiation.

By virtue of 1D geometry only longitudinal bulk waves will be generated, planar and normal to the interface.

First, consider an isolated elemental laminar of heated target material thickness, Δz. As a result of being raised by a temperature $\theta_1(z,t)$, it will expand normal to the surface by an amount

$$\gamma_1 \, \theta_1(z,t) \, \Delta z$$

where γ_1 = laminar coefficient of thermal expansion

Parameters with the suffix $_1$ refer to the target medium, those with $_2$ to the overlying medium.

For an isotropic solid, γ_1 may be found by subjecting the third line of equation 4.15 to the boundary conditions $\varepsilon_{xx} = \varepsilon_{yy} = 0$ and $\sigma_{zz} = 0$, yielding

$$0 = (\lambda+2\mu)\varepsilon_{zz} - \alpha(3\lambda+2\mu) \, \theta_1(z,t)$$

ie.

$$\gamma_1 \equiv \frac{\varepsilon_{zz}}{\theta_1(z,t)} = \alpha \frac{(3\lambda+2\mu)}{(\lambda+2\mu)}$$

In this case, γ_1 may be viewed as the coefficient of linear expansion, α, enhanced by constraint in lateral directions.

If the target medium were continuous rather than a half-space, this expansion would be accommodated equally in both directions normal to the laminar so displacing points at a greater depth inwards by half this amount but experienced after an acoustic propagation delay, ie.

$$\Delta u(r,t) = \frac{\gamma_1}{2}\,\theta_1\left(z,t - \frac{r-z}{C_{1L}}\right)\Delta z$$

where $\Delta u(r,t)$ = acoustic displacement at a depth r due to heated laminar

$(r-z)/C_{1L}$ = acoustic delay in propagating between heated laminar and point of interest

C_{1L} = propagation velocity of longitudinal bulk waves in target medium

The resultant displacement due to all such heated laminae above the point of interest, u_1 say, may now be found by letting this equation tend to the limits of integration and summing. In a real target of finite extent, this summation must be made from the point of interest to the surface ie.

$$u_1 = \frac{\gamma_1}{2}\int_0^r \theta_1\left(z,t - \frac{r-z}{C_{1L}}\right) dz \qquad 4.17$$

However, this component, which is the direct wave from above, is not the only one. There are in total three others; Figure 4.6(a). First, if the heated region extends beyond the point of interest, a direct wave will arrive from below, u_2, acting in the opposite direction due to the expansion of deeper heated laminae

$$u_2 = -\frac{\gamma_1}{2}\int_r^\infty \theta_1\left(z,t - \frac{z-r}{C_{1L}}\right) dz \qquad 4.18$$

where $\frac{z-r}{C_{1L}}$ = acoustic delay in propagating from deeper laminae

Secondly, displacements propagating towards the surface will return as a reflected wave

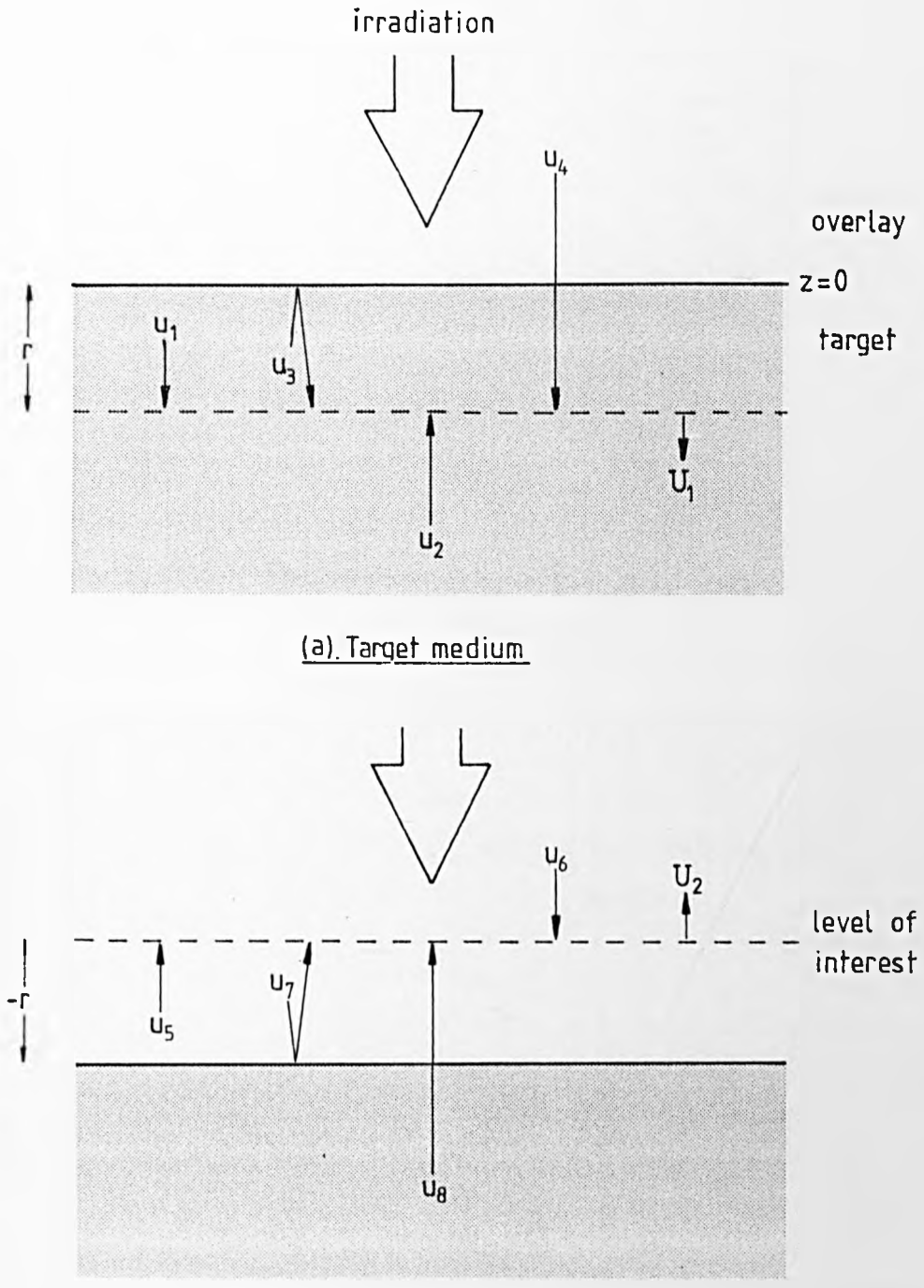

FIGURE 4.6: Component wave groups contributing to acoustic displacement as viewed in either medium.

$$u_3 = \frac{\gamma_1}{2} R_{12} \int_0^{\infty} \theta_1\left(z, t - \frac{r+z}{C_{1L}}\right) dz \qquad 4.19$$

where $(r+z)/C_{1L}$ = acoustic delay in propagating from heated laminae to surface and back to point of interest

R_{12} = acoustic reflection coefficient at metal/overlay interface

And, thirdly, any conduction-heated overlying medium will launch a wave back across the interface

$$u_4 = \frac{\gamma_2}{2} \cdot T_{21} \int_0^{-\infty} \theta_2\left(z, t-\left(\frac{r}{C_{1L}} + \frac{|z|}{C_{2L}}\right)\right) dz \qquad 4.20$$

where T_{21} = acoustic transmission coefficient across overlay/target interface

r/C_{1L} = acoustic delay in target medium

$|z|/C_{2L}$ = acoustic delay in overlying medium

θ_2 = temperature rise in overlying medium

C_{2L} = propagation velocity of longitudinal bulk waves in overlying medium

Thus, the resultant displacement anywhere within the target may be expressed as the superposition of the four components,

$$U_1 = u_1 + u_2 + u_3 + u_4 \qquad 4.21$$

Similarly, the displacement in the overlying medium is composed of four complimentary wave groups; Figure 4.6(b),

$$U_2 = u_5 + u_6 + u_7 + u_8 \qquad 4.22$$

where $u_5 = \frac{\gamma_2}{2} \int_0^{-r} \theta_2 \left(z, t - \frac{z-r}{C_{2L}}\right) dz$

$$u_6 = -\frac{\gamma_2}{2} \int_{-r}^{-\infty} \theta_2 \left(z, t - \frac{r-z}{C_{2L}}\right) dz$$

$$u_7 = \frac{\gamma_2}{2} R_{21} \int_0^{-\infty} \theta_2 \left(z, t - \frac{|z+r|}{C_{2L}}\right) dz$$

$$u_8 = \frac{\gamma_2}{2} T_{12} \int_0^{\infty} \theta_1 \left(z, t - \frac{|r|}{C_{2L}} + \frac{z}{C_{1L}}\right)\right) dz$$

Well away from the interface, the u_2 and u_6 terms which only apply if the point of interest lies within the heating region, become insignificant, giving a boundary-distant displacement of

$$U_1 = u_1 + u_3 + u_4 \qquad 4.23$$

$$U_2 = u_5 + u_7 + u_8 \qquad 4.24$$

If the u_4 term is omitted from equation 4.23, it can be seen to be essentially the same as equation 3.7 obtained by Bushnell and McCloskey 1968. These authors only considered the specific case of the pulsed irradiation of a non-metal, and arrived at their solution using Laplace

transforms. The above equations remain, however, entirely general.

The resultant acoustic waveforms may now be found by substituting for $\theta_1(z,t)$ and $\theta_2(z,t)$ and evaluating the integrals. It is not always necessary to evaluate every integral since some wave terms may be insignificant depending on the physical circumstances. In this respect, it is useful to examine the relative source strengths.

Relative source strengths

An accurate guide to the strength of a thermally driven source is the total amount of expansion associated with it. On this basis, the strength of the sources in the target and overlying medium, S_1 and S_2 respectively, are

$$S_1 = \Upsilon_1 \int_0^{\infty} \theta_1(z,t)\, dz = \frac{\Upsilon_1 E_1}{c_1 \rho_1}$$

$$S_2 = \Upsilon_2 \int_0^{-\infty} \theta_2(z,t)\, dz = \frac{\Upsilon_2 E_2}{c_2 \rho_2}$$

4.25

where c = specific heat

ρ = density

E_1 = thermal energy contained in target medium

E_2 = thermal energy contained in overlying medium

In order to relate E_1 and E_2, it can be noted that at a heated interface between two media, the relative heat flow in each direction is given by the ratio of the thermal capacities of the respective thermal skin depths, ie.

$$\frac{E_2}{E_1} = \frac{\delta_{2T}\, c_2\rho_2}{\delta_{1T}\, c_1\rho_1} \quad \text{ie.} \quad E_2 = \frac{\delta_{2T}\, c_2\rho_2}{\delta_{1T}\, c_1\rho_2} E_1 \qquad 4.26$$

which by substitution for δ_{1T} and δ_{2T} from either equation 4.2 or 4.3, gives

$$E_2 = \sqrt{\frac{\kappa_2}{\kappa_1}}\ \frac{c_2\rho_2}{c_1\rho_1}\ E_1$$

The strength of the sources as viewed in their own medium and in the other across the impedance mismatch of the interface, may therefore be expressed in terms of E_1 as

$$\frac{S_{11}}{E_1} = \frac{\gamma_1}{c_1\rho_1}$$

$$\frac{S_{12}}{E_1} = \frac{\gamma_1}{c_1\rho_1}\ T_{12}$$

$$\frac{S_{21}}{E_1} = \frac{\gamma_2}{c_2\rho_2}\ T_{21}\ \sqrt{\frac{\kappa_2}{\kappa_1}}\ \frac{c_2\rho_2}{c_1\rho_1} = \frac{\gamma_2}{c_1\rho_1}\ \sqrt{\frac{\kappa_2}{\kappa_1}}\ T_{21}$$

$$\frac{S_{22}}{E_1} = \frac{\gamma_2}{c_2\rho_2}\ \sqrt{\frac{\kappa_2}{\kappa_1}}\ \frac{c_2\rho_2}{c_1\rho_1} = \frac{\gamma_2}{c_1\rho_1}\ \sqrt{\frac{\kappa_2}{\kappa_1}}$$

where the first suffix after S indicates the source medium, the second, the viewing medium, and T_{ij} is the acoustic transmission coefficient from medium i to j.

Table 4.1 shows which of the wave terms these sources govern.

4.5 Photoacoustic effect

Consider the specific case of a metal target in a gaseous environment. Substituting typical material parameters of

		Viewing Medium	
	Source	Target	Overlay
S_1	S_{11}	u_1, u_2, u_3	-
	S_{12}	-	u_8
S_2	S_{22}	-	u_5, u_6, u_7
	S_{21}	u_4	-
		Thermoelastic terms	Photoacoustic terms

TABLE 4.1 : Sources, images and dependent wave terms.

S_{ij} - source in medium i as viewed from medium j.

$$\gamma_1 = 2 \times 10^{-5}\ ^\circ C^{-1}$$

$$c_1 = 400\ J\ kg^{-1}\ ^\circ C^{-1}$$

$$\rho_1 = 6000\ kg\ m^{-3}$$

$$\gamma_2 = 3.7 \times 10^{-3}\ ^\circ C^{-1}$$

$$c_2\rho_2 = 1.5 \times 10^{3}\ J\ m^{-3}\ ^\circ C^{-1}$$

$$T_{12} \simeq 2$$

$$T_{21} = 2 \times 10^{-5}$$

$$\frac{\delta_{T2}}{\delta_{T1}} = \frac{\kappa_2}{\kappa_1} = 0.12$$

yields

$$\frac{S_{11}}{E_1} = 8 \times 10^{-12}\ m^3J^{-1}$$

$$\frac{S_{12}}{E_1} = 1.6 \times 10^{-11}\ m^3J^{-1}$$

$$\frac{S_{21}}{E_1} = 3.6 \times 10^{-15}\ m^3J^{-1}$$

$$\frac{S_{22}}{E_1} = 1.8 \times 10^{-10}\ m^3J^{-1}$$

If the interest is in the waves launched into the gas, that is in the photoacoustic signal, the two relevant terms are S_{12} and S_{22}. By comparison, it can be seen that the source associated with the expansion of conduction heated gas (S_{22}) is roughly 11× stronger than that due to the displacements from expanding target metal being transmitted across the interface (S_{12}). This result shows that the dominant source is expanding conduction-heated gas, as emphasised in some work on the photoacoustic effect (eg. Parker 1973, Rosencwaig and Gersho 1975). It also supports

later authors (eg. McDonald and Wetsel 1977) who have suggested that expansion of target material can make a significant though generally secondary contribution.

4.6 Thermoelastic effect

If the interest lies in the signal generated in the target medium, ie. in the thermoelastic effect, the relevant terms are S_{11} and S_{21} of which the strongest by far is S_{11}. In other words, expansion of metal dominates the generation processes, displacements due to expanding gas being negligible. The same holds true for a transparent solid or liquid overlay; for example, substituting material parameters for glass on aluminium indicates $S_{21} = 3 \times 10^{-3}\ S_{11}$. This dominance of S_{11} is largely due to the differences in acoustic impedances which ensure that the transmission coefficient across the interface is lower in the reverse direction. For example, in the case of a metal in a gaseous environment, typically $T_{21} = 2 \times 10^{-5}$ as compared with $T_{12} \simeq 2$.

Thus, of the thermoelastic terms (Table 4.1), S_{21} and hence u_4 are generally insignificant and so may be omitted, giving a target signal of

$$U_1 \simeq u_1 + u_2 + u_3 \quad \text{(heated region)} \qquad 4.27$$

$$\simeq u_1 + u_3 \quad \text{(boundary distant)} \qquad 4.28$$

4.7 Thermoelastic generation under a finite thickness overlay

If the overlying medium is a finite thickness solid or liquid, it may be necessary to include some further wave terms. While u_4 can still be ignored, u_8, which did not return in the case of the infinite overlay, will

be reflected off the overlay's upper surface and so may eventually re-enter the target medium; Figure 4.7. Since this term is relatively strong in being driven by S_1, it may produce significant additional displacements especially if the acoustic impedances of the target and overlay medium are comparable. This can be demonstrated by comparing S_1 with its strength as imaged through the appropriate transmission and reflection coefficients,

$$S_1^* = S_1 . T_{12} . R_{23} . T_{21}$$

where R_{23} = reflection coefficient at overlay/third medium interface

Substituting into equations 2.18 and 2.19 typical values for a solid dielectric ($z_2 = 12 \times 10^6$ Pasm^{-1}) overlying a metal surface ($z_1 = 17 \times 10^6$ Pasm^{-1}) taking free space as the third medium, gives

$$T_{12} = 1.17; \quad R_{23} = -1; \quad T_{21} = 0.83$$

ie. $S_1^* = - 0.97 S_1$

The same calculation for a liquid overlay ($z_2 = 2 \times 10^6$Pasm^{-1}) indicates

$$S_1^* = - 0.38 S_1$$

In more exact terms, this comparatively strong imaged source will produce a first reflected wave

$$u_9^1 = \frac{\gamma_1}{2} T_{12} . R_{23} . T_{21} \int_0^\infty \theta_1(z, t - (\frac{2D}{C_{2L}} + \frac{r+z}{C_{1L}})) \, dz \qquad 4.29$$

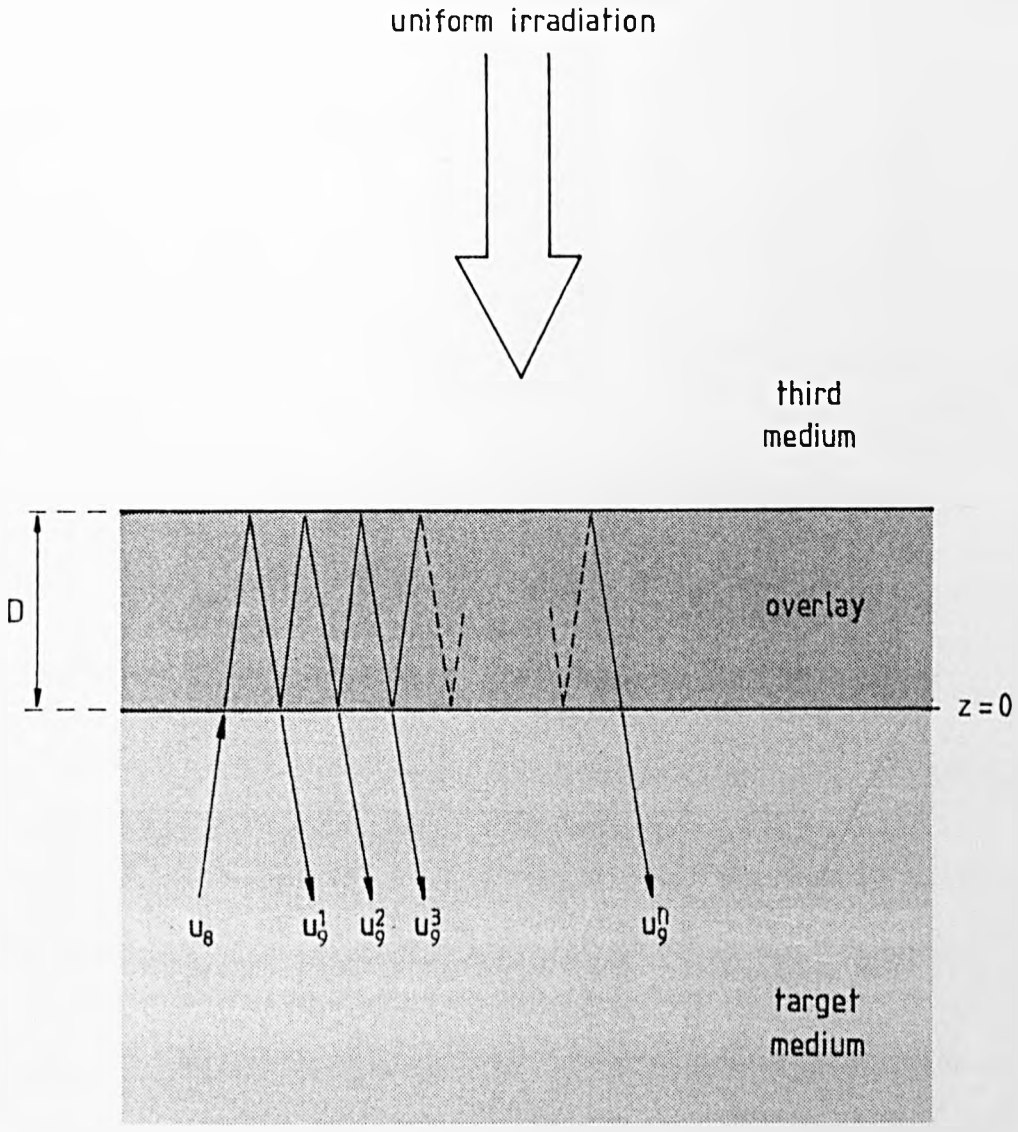

FIGURE 4.7: Additional wave terms introduced by multiple reflections within a finite thickness overlay.

Waves shown off-normal for clarity only.

where D = overlay thickness

$2D/C_{2L}$ = round trip acoustic delay within overlay

and subsequently, a complete series of multiply-reflected signals, the n^{th} one of which will be

$$u_g^n = \frac{\gamma_1}{2} T_{12} . (R_{23})^n . (R_{21})^{n-1} T_{21} \int_0^\infty \theta_1(z, t - (\frac{2nD}{C_{2L}} + \frac{r+z}{C_{1L}})) \, dz \quad 4.30$$

Thus, the displacement produced within a target with a finite thickness overlay may be written as

$$U_1 = u_1 + u_2 + u_3 + u_g^1 + u_g^2 + ... u_g^n \text{ (heated region)} \quad 4.31$$

$$= u_1 + u_3 + u_g^1 + u_g^2 + ...u_g^n \quad \text{(boundary distant)} \quad 4.32$$

4.8 Thermoelastic generation in metals by a uniform modulated continuous laser beam

For periodic irradiation, the interface-distant equation 4.28 may be rewritten in terms of phase delays rather than time delays as

$$U_1 \approx u_1 + u_3$$

$$= \frac{\gamma_1}{2} \int_0^\infty \theta_1(z, \omega t - k_1(r-z)) \, dz$$

$$+ \frac{\gamma_1}{2} R_{12} \int_0^\infty \theta_1(z, \omega t - k_1(r+z) \, dz$$

where k_1 = wave number

$k_1(r-z)$ = phase delay in propagating directly to point of interest

$k_1(r+z)$ = phase delay in propagating via reflection off surface

In strict terms, θ_1 does not correspond precisely to $\theta(z,t)$ in equation 4.9 since this was derived assuming no flow of heat into any overlying medium. However, substituting typical material values into equation 4.26 indicates that such back heat flow is usually negligible. For example, in the case of glass overlying an aluminium surface, $E_2 = 0.004\ E_1$, ie. the aluminium contains $\simeq 99.6\%$ of the heat. Under such conditions, equation 4.9 may be substituted directly with minimal error, giving

$$U_1 = \frac{\gamma}{2} \int_0^\infty \frac{I_o\ \delta_{TH}}{\sqrt{2}\,K}\ e^{-\tau z}\ e^{j(\omega t - k(r-z))}\ dz$$

$$+ \frac{\gamma}{2}\ R_{12} \int_0^\infty \frac{I_o\ \delta_{TH}}{\sqrt{2}\,K}\ e^{-\tau z}\ e^{j(\omega t - k(r+z))}\ dz$$

where, for simplicity, the suffix$_1$ has been dropped from parameters relating to the target medium.

The integrals are readily evaluated to give

$$U_1 = \frac{\gamma}{2}\ \frac{I_o\ \delta_{TH}}{\sqrt{2}\,K}\ \left[\frac{1}{\tau - jk} + R_{12}\ \frac{1}{\tau + jk}\right] e^{j(\omega t - kr)}$$

$$= \frac{\gamma}{2}\ \frac{I_o\ \delta_{TH}}{\sqrt{2}\,K}\ \frac{1}{\tau^2 + k^2}\ \left[(\tau + jk) + R_{12}(\tau - jk)\right] e^{j(\omega t - kr)} \qquad 4.33$$

This is the expression for the displacement produced deep within a metal target. The first term within square brackets ($\tau+jk$) relates to u_1, the wave propagating directly from the heated region, the second $R_{12}(\tau-jk)$ to u_3, the wave reflected off the interface. The resultant amplitude is determined by the way these two waves interfere with each other. The effect is most marked at the extreme cases of the free surface and the fully constrained surface. For the free surface, the reflection coefficient at the metal/overlay interface, $R_{12} = -1$, ($z_2 = 0$ in equation 2.18) and so the waves tend to subtract so

$$U_1 = \frac{\gamma}{2} \frac{I_o \delta_{TH}}{\sqrt{2}\, K} \frac{1}{\tau^2+k^2} \left[\tau+jk - \tau+jk\right] e^{j(\omega t-kr)}$$

$$= j\, \gamma \frac{I_o \delta_{TH}}{\sqrt{2}\, K} \frac{k}{\tau^2+k^2} e^{j(\omega t-kr)} \qquad 4.34$$

while for the fully constrained surface, $R_{12} = +1$ ($z_2 >> z_1$), and they tend to sum

$$U_1 = \frac{\gamma}{2} \frac{I_o \delta_{TH}}{\sqrt{2}\, K} \frac{1}{\tau^2+k^2} \left[\tau+jk + \tau-jk\right] e^{j(\omega t-kr)}$$

$$= \frac{\gamma\, I_o \delta_{TH}}{\sqrt{2}\, K} \frac{\tau}{\tau^2+k^2} e^{j(\omega t-kr)} \qquad 4.35$$

In this form, these two results are equivalent to those finally derived by White 1963 by direct solution of the equation of motion (see Section 3.1). However, they are still in complex form. Only the real parts are required. Taking the constrained surface as an example, these may be separated out by substituting $\tau = (1+j)/\delta_{TH}$ from equation 4.9 and $e^{j(\omega t-kr)} = \cos(\omega t-kr) + j\sin(\omega t-kr)$, giving

$$U_1 = \frac{\gamma I_o}{\sqrt{2}\,K} \frac{\delta_{TH}^2}{(4 + \delta_{TH}^4 k^4)} \left[(2+\delta_{TH}^2 k^2) \cos(\omega t - kr) + (2-\delta_{TH}^2 k^2) \sin(\omega t - kr) \right]$$

By summing the $\cos(\omega t-kr)$ and $\sin(\omega t-kr)$ wave terms, this may be written as

$$U_1 = \frac{\gamma I_o}{K} \cdot \frac{\delta_{TH}^2}{\sqrt{4+\delta_{TH}^4 k^4}} \cdot \cos\left(\omega t - kr - \tan^{-1}\left(\frac{2-\delta_{TH}^2 k^2}{2+\delta_{TH}^2 k^2}\right)\right) \qquad 4.36$$

The final expression for the displacement produced deep within free surface metal, can be similarly shown to be

$$U_1 = \frac{\gamma I_o}{\sqrt{2}\,K} \frac{k\delta_{TH}^3}{\sqrt{4 + \delta_{TH}^4 k^4}} \cos\left(\omega t - kr - \tan^{-1}\left(\frac{\delta_{TH}^2 k^2}{2}\right)\right) \qquad 4.37$$

These equations can be simplified by approximation since heat diffuses into the bulk at a speed that for all but the highest frequencies, is considerably less than the acoustic wave propagation velocity. In other words, the laser-generated acoustic waves propagating into the bulk, rapidly out-distance the heat fronts from which they originate. This implies that the thermal wavelength is much less than the acoustic wavelength, ie.

$$\lambda_{TH} << \lambda_{AC} \quad \text{or} \quad \delta_{TH} k << 1 \qquad 4.38$$

From Figure 4.8 this can be seen to be true for typical metals providing the modulation frequency, $\omega << 10^{12}$ rad s^{-1}.

Under these conditions, equations 4.36 and 4.37 may be satisfactorily approximated to show that the displacement amplitudes produced deep within a uniformly irradiated metal are

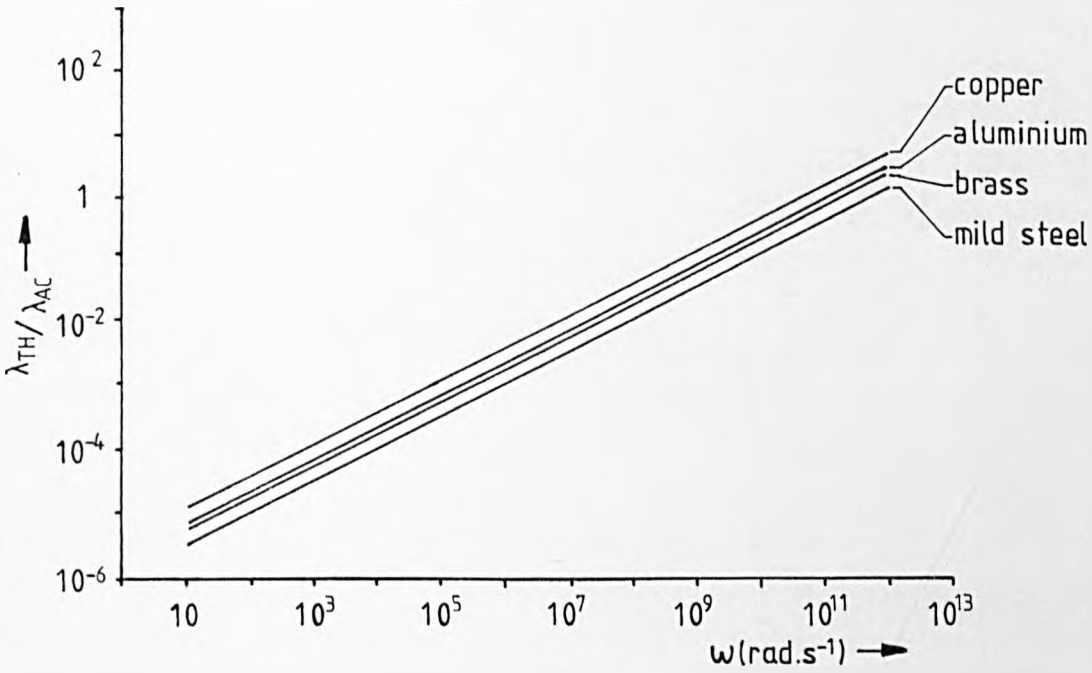

FIGURE 4.8: The increase of $\lambda_{TH}/\lambda_{AC}$ with frequency.

λ_{TH} = thermal wavelength = $2\pi\delta_{TH}$

λ_{AC} = acoustic wavelength = $\frac{c_L}{f}$

(This may be viewed as an estimate of the acoustic thickness of the laser source)

$$\hat{U}_1 \approx \frac{\gamma I_o \delta_{TH}^2}{2K} \qquad \text{constrained surface}$$

$$\approx \frac{\gamma I_o k \delta_{TH}^3}{2\sqrt{2} K} \qquad \text{free surface}$$

These expressions may be concisely expressed in terms of the source strength (equation 4.25)

$$S_1 = \gamma \int_o^\infty \theta(z,t)\, dz$$

or, from equation 4.8,

$$S_1 = \frac{\gamma I_o \delta_{TH}}{\sqrt{2} K} \int_o^\infty e^{-z/\delta_{TH}} \cos\left(\omega t - \frac{z}{\delta_{TH}}\right) dz$$

$$= \frac{\gamma I_o \delta_{TH}^2}{2K} \cos\left(\omega t - \frac{\pi}{4}\right)$$

$$= \hat{S}_1 \cdot \cos\left(\omega t - \frac{\pi}{4}\right)$$

where $\hat{S}_1 = \frac{\gamma I_o \delta_{TH}^2}{2K}$ = peak source strength

Hence

$$\hat{U}_1 \approx \hat{S}_1 \qquad \text{constrained surface} \qquad 4.39$$

$$\approx \hat{S}_1 \cdot \frac{k\delta_{TH}}{\sqrt{2}} \qquad \text{free surface} \qquad 4.40$$

Applying the same procedure to the general case, shows

$$\hat{U}_1 \approx \frac{\hat{S}_1}{Z_2+Z_1} \sqrt{Z_2^2 + \frac{(k\delta_{TH} Z_1)^2}{2} + Z_2 Z_1 \delta_{TH} k} \quad \text{partial constraint}$$

Dividing equation 4.39 by 4.40, immediately gives the ratio of constrained to free surface amplitudes as

$$R = \frac{\sqrt{2}}{k\delta_{TH}} = \frac{C_L}{\sqrt{\omega k}} \qquad 4.41$$

This is equivalent to Von Gutfield and Melcher's 1977 expression (equation 3.6) derived from White's 1963 analysis. Taking an aluminium surface as an example and substituting $\delta_{TH} = 6.9\mu m$, $k = 2160\ m^{-1}$ and $\omega = 2\pi \times 10^6$ rad s^{-1} (f = 1MHz), gives R = 130. Constraint clearly enhances the generation processes considerably. The physical reason for this enhancement, not obvious from previous work, lies in the $\lambda_{TH}/\lambda_{AC} << 1$ ($\delta_{TH}k << 1$) inequality. Since δ_{TH} also appears in the exponent of the temperature distribution (equation 4.8), this may be alternatively interpreted as implying the laser source is acoustically thin. In this respect, Figure 4.8 may be viewed as a plot of acoustic thickness against frequency.

In the case of the free surface, it can now be seen that u_3, the wave initially propagating towards the surface, is not only inverted by reflection ($R_{12} = -1$) but also returns having incurred only a very small additional phase delay. It consequently superimposes itself in almost perfect antiphase on u_1, the wave propagating directly into the bulk. The destruction is almost total; the result is a very weak acoustic wave.

Similarly, but with the opposite effect, u_3 reflected off a constrained surface likewise suffers little delay but is not inverted ($R_{12} = +1$) and so reinforces the direct wave almost perfectly; the result is relatively

strong generation.

Alternatively, in terms of the basic equations 2.2 and 2.3, the source being acoustically thin implies it possesses negligible longitudinal inertia ie. mechanical equilibrium is maintained at all times across its thickness. Consequently, no acoustic waves will be generated within the source as such, only by dynamic reaction against some outside constraint. This ensures strong generation at a constrained surface where, as equation 4.39 indicates, all the expansion is forced to occur in the one direction, ie. into the bulk. At a free surface where no external constraint is provided, the result is that the heated region is almost free to rise and fall in response to the periodic heat input without exerting any significant stresses against the bulk. Any acoustic generation under these conditions arises solely from the limited inertial constraint provided by the source's minimal, though not entirely insignificant, acoustic thickness. Such across-thickness generation is represented by the $k\delta_{TH}/\sqrt{2}$ term in equation 4.40.

The control exerted by surface boundary conditions is further emphasised in Figures 4.9 and 4.10 which give the displacement amplitude across the heated region for the free surface and constrained surface respectively. The plotted functions which may be obtained by solution of the full three term expression (equation 4.27) are

$$\hat{U}_1 = \frac{\hat{S}_1}{\sqrt{2}} \sqrt{2e^{-2r/\delta_{TH}} - 2\sqrt{2}\, k\, \delta_{TH}\, e^{-r/\delta_{TH}} \cos\left(kr - \frac{r}{\delta_{TH}} + \frac{\pi}{4}\right) + k^2 \delta_{TH}^2}$$

free surface 4.42

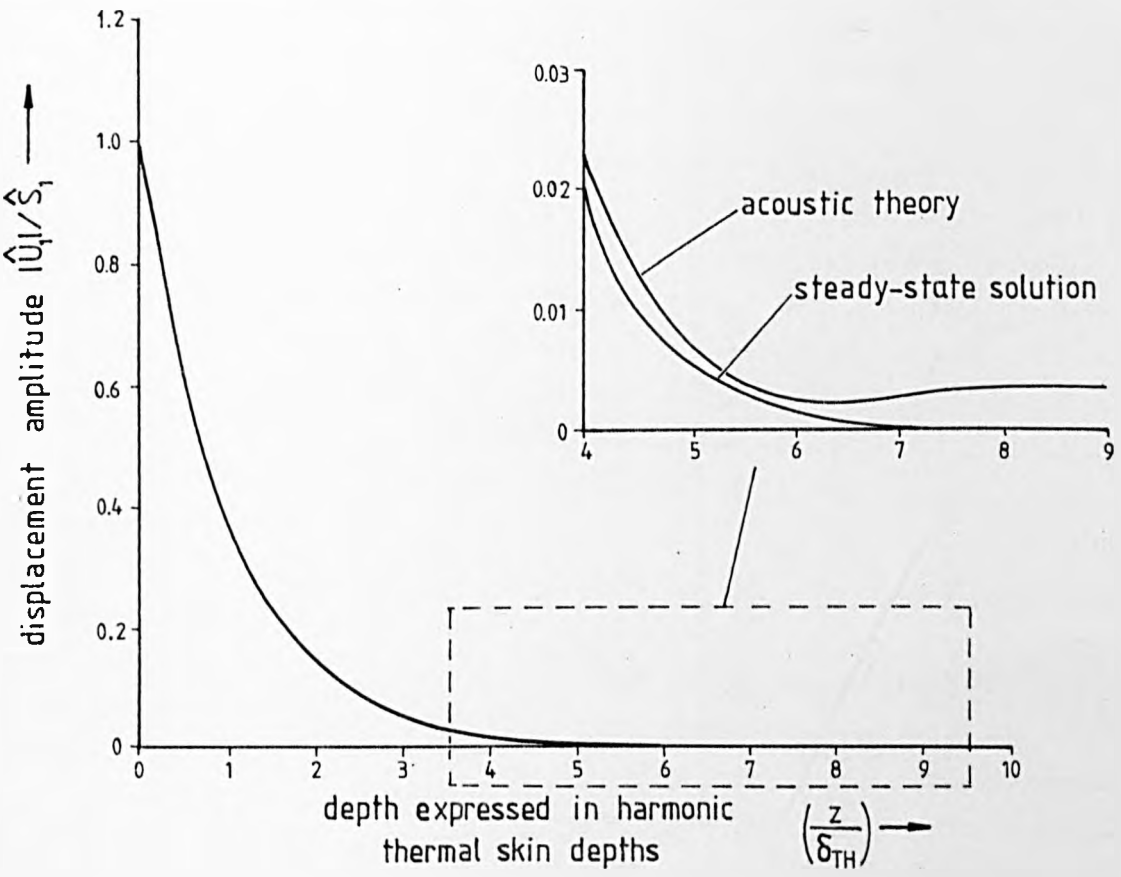

FIGURE 4.9 : The displacement amplitude produced near a free aluminium surface by uniform irradiation with a laser beam modulated at f = 1MHz.

Acoustic and steady-state solutions plotted from equations 4.42 and 4.44 respectively.

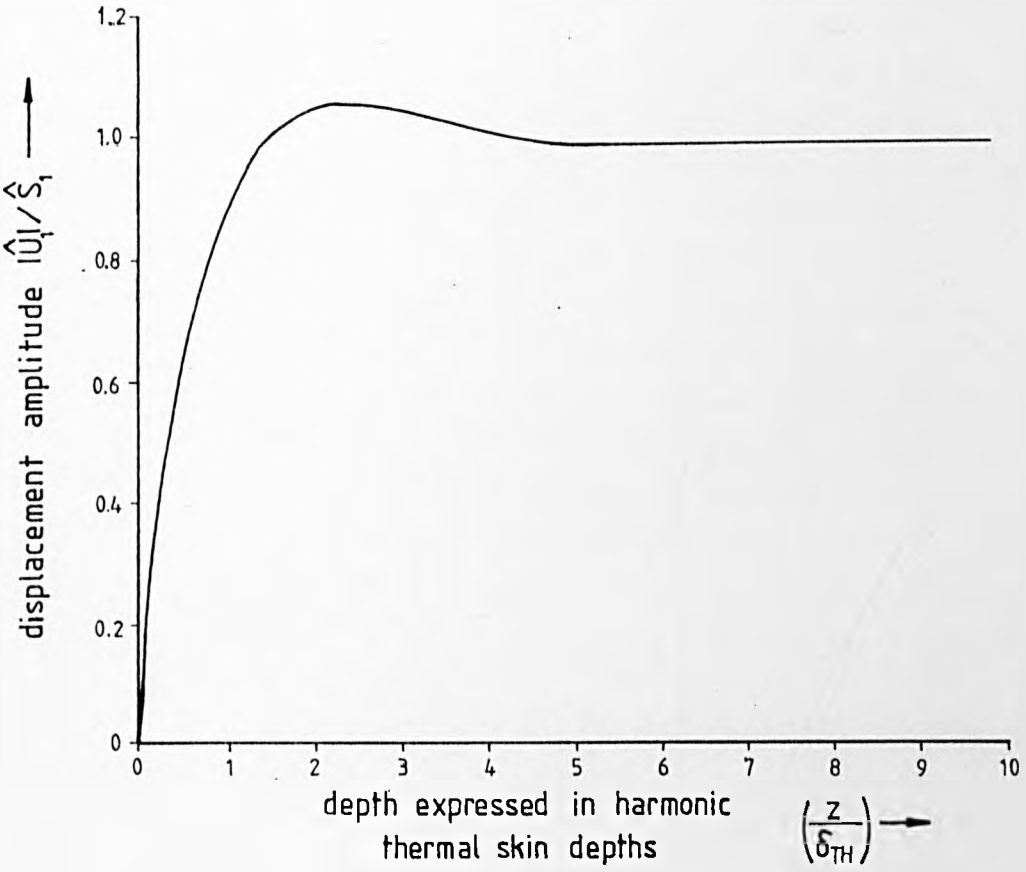

FIGURE 4.10: The displacement amplitude produced near a fully constrained aluminium surface by a laser beam modulated at f = 1MHz. Plotted from equation 4.43.

$$= \hat{S}_1 \sqrt{1 + e^{-2r/\delta_{TH}} - 2e^{-r/\delta_{TH}} \cos\left(k - \frac{1}{\delta_{TH}}\right)r}$$

fully constrained surface

4.43

In the case of free surface, the motion is largely confined to the surface in a rigid piston-like response. This is emphasised by comparison with the quasi steady-state expression,

$$\hat{U}_1 = \frac{\gamma I_o \delta_{TH}^2}{2K} e^{-r/\delta_{TH}} = \hat{S}_1 e^{-r/\delta_{TH}} \qquad \text{free surface (equilibrium)}$$

4.44

which may be obtained either directly from the simple depth integral of thermal expansion, or, from the above acoustic expression by letting $k \to 0$, ie. $C_L \to \infty$. A close inspection deep within the bulk does, however, reveal the small difference of a weak acoustic wave propagating out of the heated region and on into the bulk. In the constrained case, the surface is immobilised while the displacement amplitude increases with depth as expanding metal displaces all the underlying metal by means of launching a relatively strong acoustic wave. The maximum prior to the expected travelling wave amplitude as defined by equation 4.39, is mechanical in origin, being an exaggerated push-pull motion occurring within the heated region between successive hot and cold temperature fronts.

From equation 4.41, the enhancement due to constraint can be seen to decrease with frequency as $\omega^{-1/2}$. The reason for this is that while the thermal skin, a diffusion controlled parameter, decreases with frequency as $\omega^{-1/2}$ (Figure 4.1), the acoustic wavelength does so more markedly as ω^{-1}. Consequently, the laser acoustic source though thinner in absolute terms at

higher frequencies, becomes acoustically thicker as $\omega^{+1/2}$ (Figure 4.8). The phase difference between the direct and reflected waves though generally small, therefore increases with frequency. This will not significantly reduce the constrained surface amplitude where the waves are tending to sum, but will considerably enhance the free surface amplitude where they are tending to subtract. This emphasises that if acoustic waves are to be generated efficiently by uniform irradiation of a metal surface, it is important either to apply a constraint, preferably one acoustic wavelength thick or more, or, to rapidly modulate the laser beam.

4.9 Thermoelastic generation in metals by uniform pulsed irradiation

The acoustic generation processes are essentially the same in the pulsed case. Surface boundary conditions, for example, still play a dominant role. At a free surface, significant amplitudes are generated only by brief pulses which have an appreciable high frequency content whilst the constrained surface source is relatively strong irrespective of pulse duration.

The mathematics of the pulsed case, however, is not so amenable. In particular, direct substitution of equation 4.6 into 4.28, gives a solution containing intractable delay-adjusted temperature integrals, namely,

$$U_1 = \frac{\gamma E_T}{c\rho\sqrt{\pi}} \left[\int_0^\infty \frac{\exp\left[\frac{-z^2}{4\kappa\left(t - \frac{r-z}{C_L}\right)}\right]}{\sqrt{4\kappa\left(t - \frac{r-z}{C_L}\right)}}\, dz \right.$$

$$\left. + R_{12} \int_0^\infty \frac{\exp\left[\frac{-z^2}{4\kappa\left(t - \frac{r+z}{C_L}\right)}\right]}{\sqrt{4\kappa\left(t - \frac{r+z}{C_L}\right)}}\, dz \right] \qquad 4.45$$

A physically revealing alternative to this solution may be found by considering the source in terms of its movement. Specifically, the source may be approximated as a centre of expansion (Figure 4.11) moving into the bulk due to diffusion with a net associated expansion (strength) of

$$S_1 = \gamma \int_0^\infty \theta\,(z,t)\,dz$$

For an instantaneous laser pulse, this reduces to

$$S_1 = \frac{\gamma}{c\rho} \int_0^t I_o\,\delta(t)\,dt$$

$$\frac{\gamma\, I_o}{c\rho} \int_0^t \delta(t)\,dt$$

$$= \frac{\gamma E_T}{c\rho} H(t) \qquad 4.46$$

where I_o = peak absorbed intensity

$\delta(t)$ = Dirac's delta function

E_T = absorbed energy density

$H(t)$ = unit step function

If this expansion were within an extended medium and stationary, it would be accommodated equally in both directions, so displacing points at a distance r by

$$\frac{\gamma E_T}{2c\rho} H\left(t - \frac{r}{C_L}\right) \qquad 4.47$$

Due to diffusion, the velocity of the heat front will be approximately given by (equation 4.2)

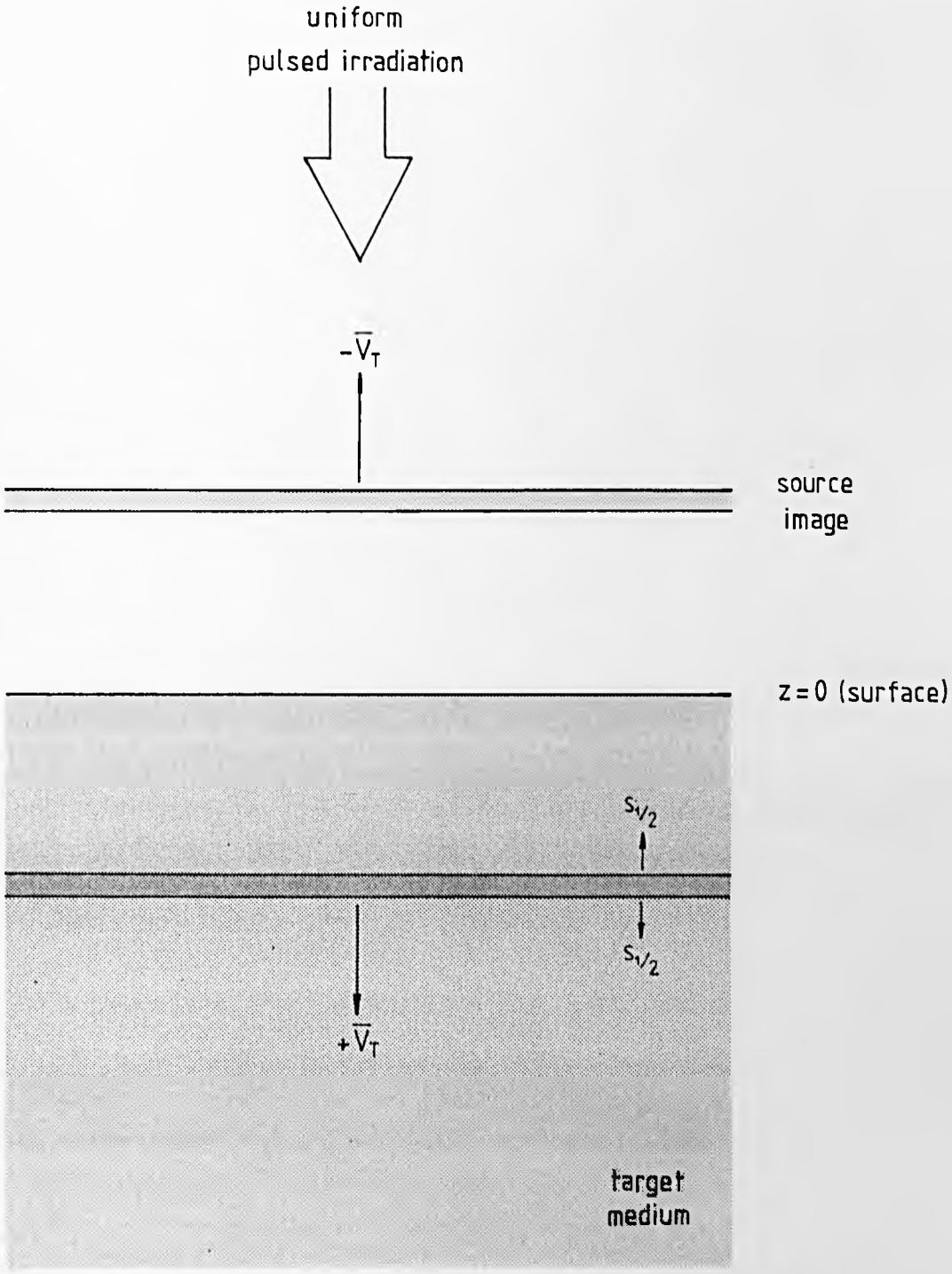

FIGURE 4.11: Source approximation for pulsed irradiation of a metal surface. A centre of expansion, strength $S_1 = \gamma E_T H(t)/c\varrho$, diffuses into the bulk at a velocity $+\bar{V}_T$ whilst a surface-reflected image travels in the opposite direction.

$$V_T = \frac{d\delta_{TP}}{dt} = \frac{d\sqrt{4\kappa t}}{dt} = \sqrt{\frac{\kappa}{t}}$$

while the mean thermal velocity will be

$$\bar{V}_T = \frac{d\bar{z}}{dt} \qquad 4.48$$

where $\bar{z}$ is the mean temperature rise position as defined by

$$\int_0^{\bar{z}} \theta(z,t)dz = \int_{\bar{z}}^{\infty} \theta(z,t)dz$$

ie. from equation 4.6, where

$$\int_0^{\bar{z}} e^{-\left(\frac{z}{\delta_{TP}}\right)^2} dz = \int_{\bar{z}}^{\infty} e^{-\left(\frac{z}{\delta_{TP}}\right)^2} dz$$

From standard statistical tables of the area under a normal distribution, this point occurs at

$$\bar{z} = 0.68\delta_{TP} = 0.68\sqrt{4\kappa t} \qquad 4.49$$

ie.

$$\bar{V}_T = 0.68\sqrt{\frac{\kappa}{t}} \qquad 4.50$$

This movement will alter the resultant acoustic displacement due to Doppler related effects. This can be demonstrated by first considering the case of a source of displacement D/2 in each direction, moving at a constant velocity, V_c. This is equivalent to a sequence of brief top-hat sources duration, Δt, each producing momentarily the same displacement but at spaced distances of

$$\Delta d = V_c . \Delta t$$

From Figure 4.12, it can be seen that in the direction of movement, there is an overlap in the component displacements observed at the detection point, p, given by

$$t_1 - t_2 = \left(\frac{r}{C_L} + \Delta t\right) - \left(\frac{r-\Delta d}{C_L} + \Delta t\right)$$

$$= \frac{\Delta d}{C_L} = \frac{V_c}{C_L} \Delta t$$

Upon summation, this overlap will appear as an increase in the mean amplitude, which in the limit $\Delta t \to 0$ becomes continuous, so producing a resultant displacement of

$$U_p = \frac{D}{2} \quad \frac{\Delta t}{\Delta t - \frac{V_c}{C_L} \Delta t} \cdot H\left(t - \frac{r}{C_L}\right)$$

$$= \frac{D}{2} \quad \frac{C_L}{C_L - V_c} \cdot H\left(t - \frac{r}{C_L}\right)$$

The resultant amplitude may be loosely described as Doppler-enhanced. A source or surface image propagating in the opposite direction would be amplitude-reduced.

If it is assumed that the total distance moved by the laser source is negligible, S_1 may be directly substituted for D (equation 4.46), and $\bar{V}_T$ for V_c (equation 4.50). Thus from equation 4.28, the boundary-distant displacement may be written as

$$U_1 \approx u_1 + u_3$$

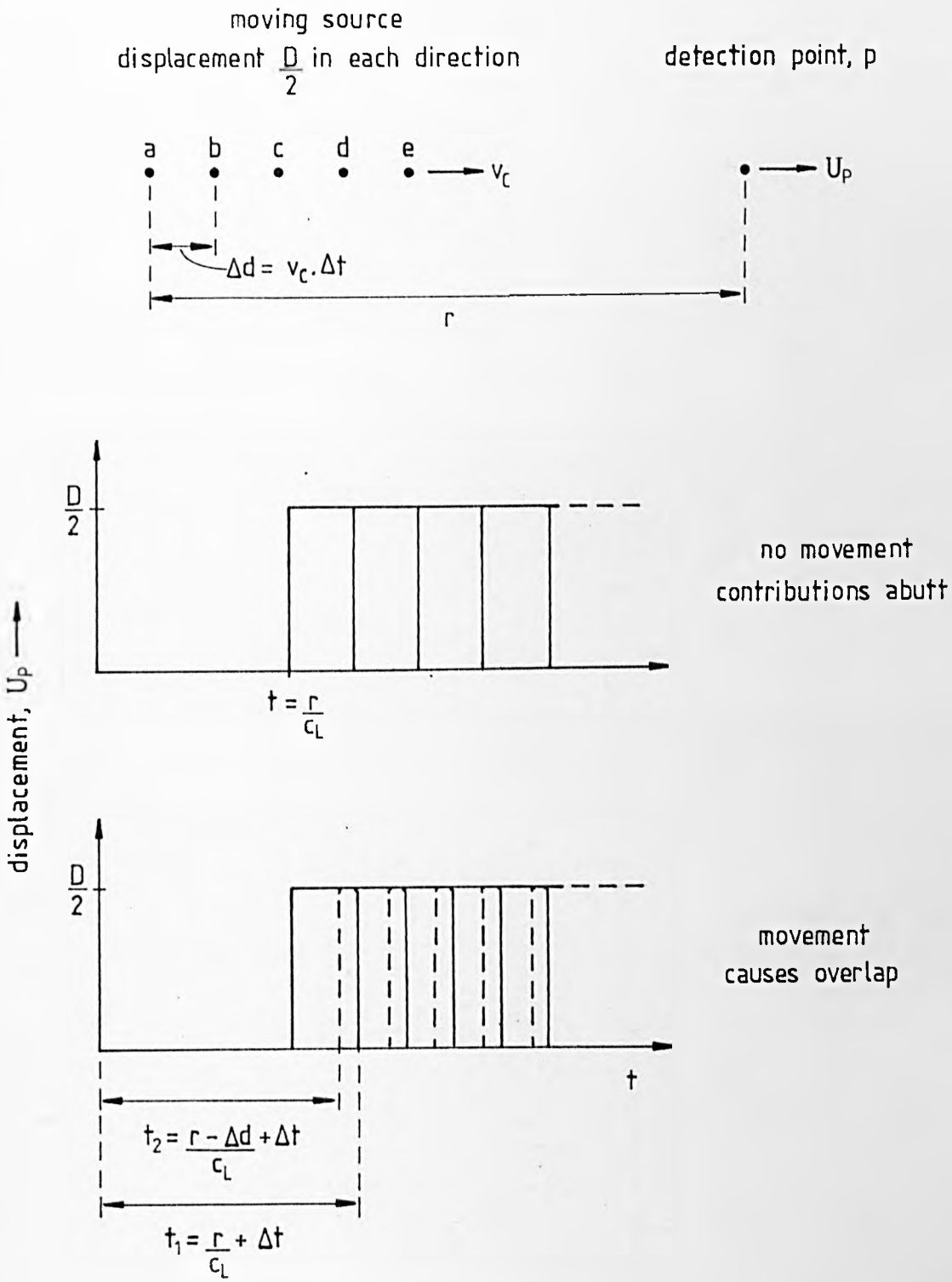

FIGURE 4.12: The effect of source movement upon resultant displacement waveform.

The source may be represented as a series of momentary sources, say a, b, c, d, e..., duration Δt, at spaced distances of $\Delta d = v_c . \Delta t$.

$$= \frac{\gamma E_T}{2c\rho} \quad \frac{C_L}{C_L - \bar{V}_T(t - \frac{r}{C_L})} \quad . H(t - \frac{r}{C_L})$$

$$+ R_{12} \quad \frac{\gamma E_T}{2c\rho} \quad \frac{C_L}{C_L + \bar{V}_T(t - \frac{r}{C_L})} \quad . H(t - \frac{r}{C_L}) \qquad 4.51$$

where u_1 = amplitude-enhanced direct wave

u_2 = amplitude-reduced surface-reflected wave

Taking the extreme case of the constrained surface ($R_{12} = +1$), this gives

$$U_1 = \frac{\gamma E_T}{2c\rho} \left[\frac{C_L}{C_L - \bar{V}_T(t - \frac{r}{C_L})} + \frac{C_L}{C_L + \bar{V}_T(t - \frac{r}{C_L})} \right] . H(t - \frac{r}{C_L})$$

$$= \frac{\gamma E_T}{c\rho} \left[\frac{C_L^2}{C_L^2 - \bar{V}_T(t - \frac{r}{C_L})^2} . H(t - \frac{r}{C_L}) \right] \qquad 4.52$$

This summation of wave terms is shown in graphical form in Figure 4.13(a), (b) and (c) for the typical case of an aluminium surface. A non-dispersive propagation velocity of $C_L = 6374 ms^{-1}$ (Kaye and Laby 1973) has been assumed. The displacement is initially enhanced above the stationary source value.

In the limit of the source becoming acoustically thin, the distance propagated by the acoustic wavefront becomes much greater than the thermal skin depth

$$\frac{\delta_{TP}}{C_L t} << 1 \qquad 4.53$$

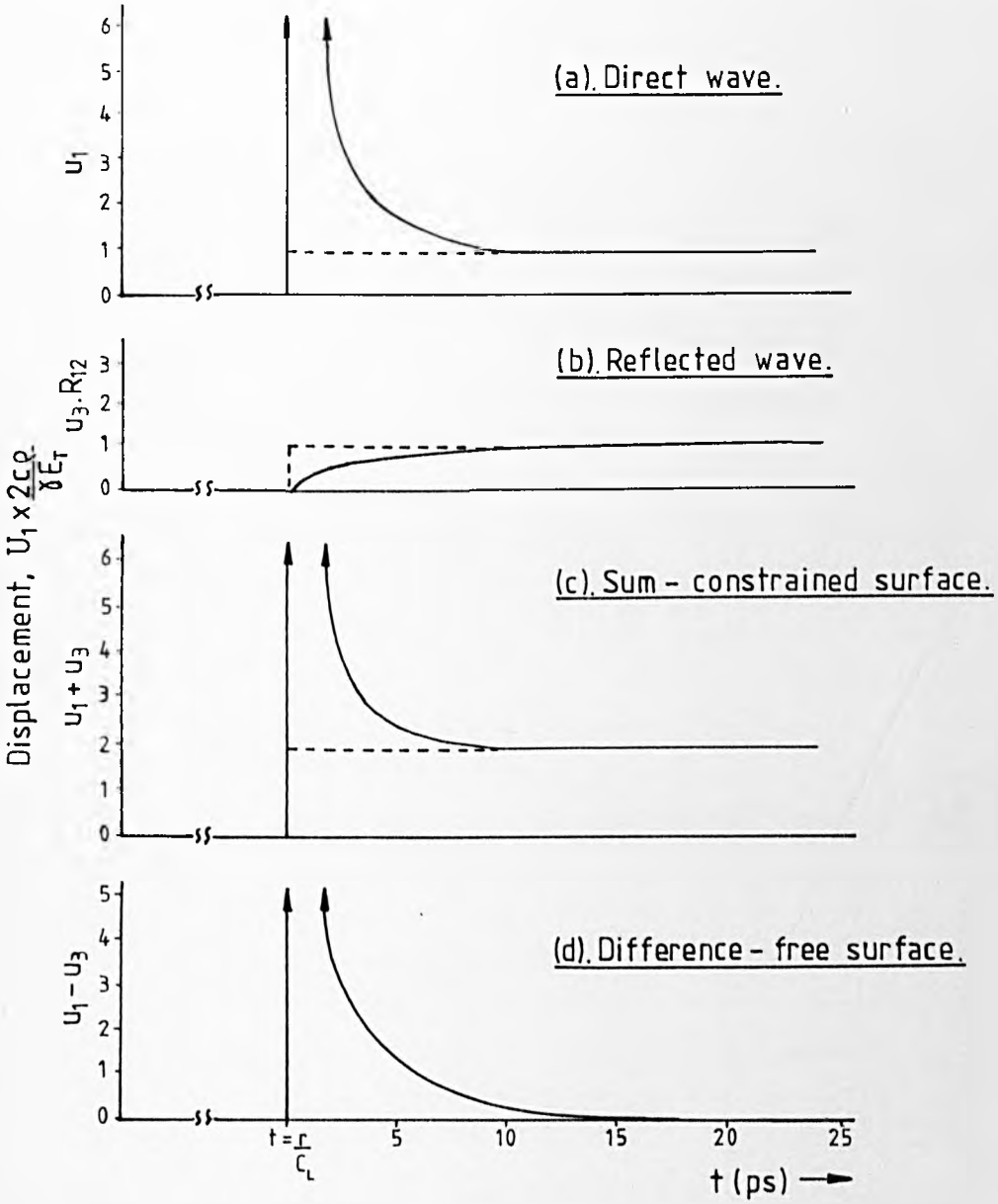

FIGURE 4.13: The longitudinal displacement produced by $\delta(t)$-pulsed, spatially uniform irradiation of an aluminium surface. Evaluated from equation 4.51.

During the brief initial period that the thermal velocity is comparable to the acoustic velocity, the direct wave is amplitude-enhanced and the reflected wave amplitude-reduced.

----- indicates stationary source displacement.

ie. by rearrangement of equations 4.2 and 4.50 when

$$\bar{V}_T << 0.34\ C_L$$

From Figure 4.14, this occurs typically at t >> 15ps.

Under these limiting conditions, equation 4.52 approximates to

$$U_1 = \frac{\gamma E_T}{c\rho} \cdot H\left(t - \frac{r}{C_L}\right) \qquad 4.54$$

This is simply twice the displacement produced by the stationary source (equation 4.47). In this case, the rigidly held surface has forced all the expansion to occur in the one direction, so doubling the resultant displacement.

In the case of the free surface ($R_{12} = -1$),

$$U_1 = \frac{\gamma E_T}{2c\rho} \left[\frac{C_L}{C_L - \bar{V}_T\left(t - \frac{r}{C_L}\right)} - \frac{C_L}{C_L + \bar{V}_T\left(t - \frac{r}{C_L}\right)} \right] \cdot H\left(t - \frac{r}{C_L}\right)$$

$$= \frac{\gamma E_T}{c\rho} \left[\frac{\bar{V}_T\left(t - \frac{r}{C_L}\right) \quad C_L}{C_L^2 + \bar{V}_T^2\left(t - \frac{r}{C_L}\right)} \right] H\left(t - \frac{r}{C_L}\right) \qquad 4.55$$

which in the $\bar{V}_T << 0.34\ C_L$ limit yields

$$U_1 = \frac{\gamma E_T}{c\rho} \frac{\bar{V}_T\left(t - \frac{r}{C_L}\right)}{C_L} \cdot H\left(t - \frac{r}{C_L}\right) \qquad 4.56$$

or, substituting for $\bar{V}_T$ from equation 4.50

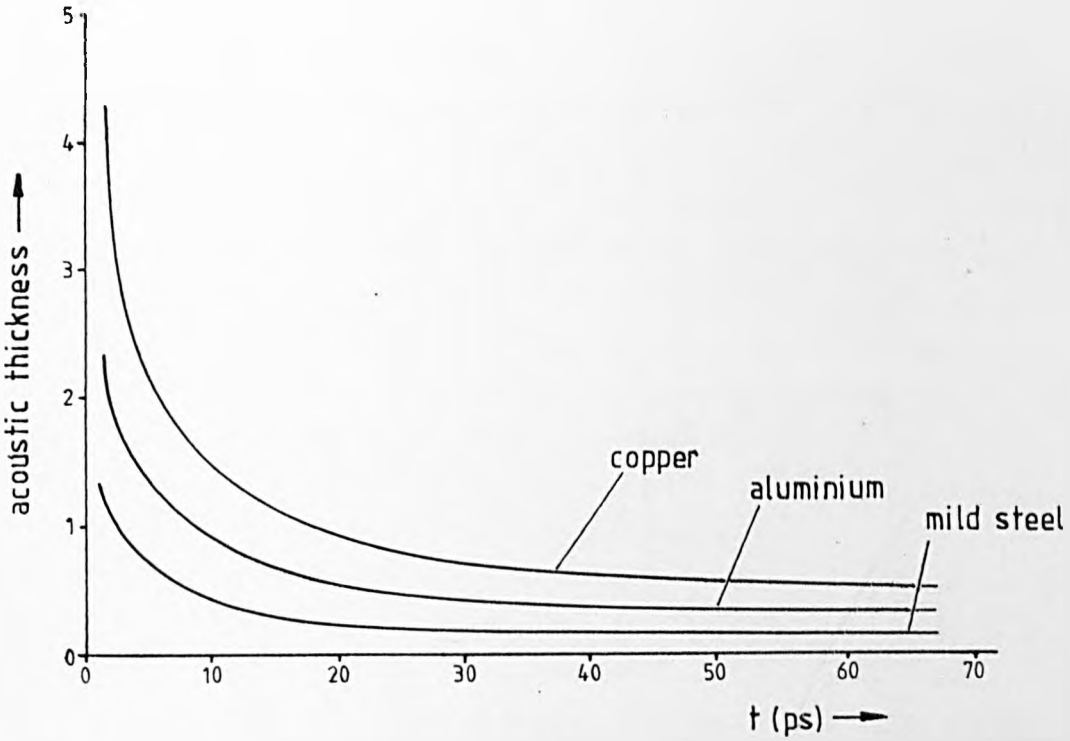

FIGURE 4.14: The decrease of the acoustic thickness of the pulsed laser source with time.

$$\text{Acoustic thickness} = \frac{\text{thermal thickness}}{\text{distance propagated by acoustic waves}}$$

$$= \frac{\delta_{tp}}{C_L t}$$

$$U_1 = 0.68 \frac{\gamma E_T}{c\rho} \cdot \frac{1}{C_L} \cdot \sqrt{\frac{\kappa}{t - \frac{r}{C_L}}} \cdot H\left(t - \frac{r}{C_L}\right) \qquad 4.57$$

In this case, it is clear that the acoustic pulses are produced solely as a result of source diffusion into the bulk. Without such movement $\bar{V}_T = 0$ ($\kappa = 0$), the source could not bury itself and hence find some overlying constraint against which to react.

This self-burying mechanism is, however, an extremely transient process, significant amplitudes being generated only when $\bar{V}_T$ is comparable to C_L and the source remains acoustically thick. This is graphically depicted in Figures 4.13 (a), (b) and (d) which show how the wave-term subtraction virtually eliminates all displacement except for the brief initial period that u_1 is velocity-enhanced and u_3 velocity-reduced. An important consequence of this is that laser pulses with comparatively long durations, typically $t_p >> 15ps$, will produce acoustically thin sources. As such, they will not generate significant acoustic waves as they feed the energy in too slowly. Rather, the surface will relieve itself by rising smoothly upwards as mechanical equilibrium is, in effect, continuously maintained. Under these quasi steady-state conditions, the bulk will remain stationary while the upward displacement within the heated region may be simply equated to the depth integral of thermal expansion below the point of interest, ie.

$$U_1 = \gamma \int_r^\infty \theta(z,t)dz \qquad 4.58$$

or, at the surface

$$U_1(0,t) = \gamma \int_0^\infty \theta(z,t)\,dz$$

$$= \frac{\gamma}{c\rho} \int_0^t E(t)\,dt \qquad 4.59$$

where $\int_0^t E(t)\,dt$ = time-integrated absorbed energy density.

No such effects will occur in the constrained case where providing the overlay remains acoustically thick, the acoustic thinning of the source with time will only serve to reduce any incoherence across the heated region. This re-emphasises that to generate significant amplitudes of compressive longitudinal acoustic waves at free metal surfaces, it is essential to employ extremely brief laser pulses, or, to provide some form of surface constraint. This does not means, however, that rarefractive-longitudinal and other types of acoustic waves may not be generated as will be explained at greater length in Chapters 5 and 7.

CHAPTER 5

Resonant Probe Study of Thermoelastic Generation in Metals

5.0 Introduction

This chapter describes an experimental study of thermoelastic generation of ultrasound in metals by pulsed, unfocused laser irradiation. It is essentially qualitative due to the use of resonant detection probes. The physical conditions vary significantly from those described in Sections 4.4 - 4.9 in that the irradiation was over a finite area rather than being spatially uniform.

5.1 The laser

A conventional Q-switched Nd:YAG laser (J.K. Lasers Ltd., 2000 series) was used throughout the study, delivering radiation pulses in the near infra-red (λ = 1.06μm). Depending on the size of an aperture within the laser cavity, it could be operated in two different modes producing different beam (spatial) profiles and pulse energies. With a large aperture, the entire laser rod width could participate in laser action, generating relatively high energy ≃ 30mJ pulses contained in a broad multimode beam measuring 3.5mm across the full-width half-height points (1024 point linear photodiode array, Integrated Photomatrix Ltd.) With a small aperture, the off-axis modes of cavity resonance were minimised, and the laser produced a lower energy 2.5mJ, single transverse mode (TEM_{oo}) pulse with a narrower, near-gaussian beam profile 0.6mm across at the 1/e intensity points. The temporal profile of the pulses is shown by the trace in Figure 5.1 obtained using a fast photodiode with a rise-time of ≃ 1ns

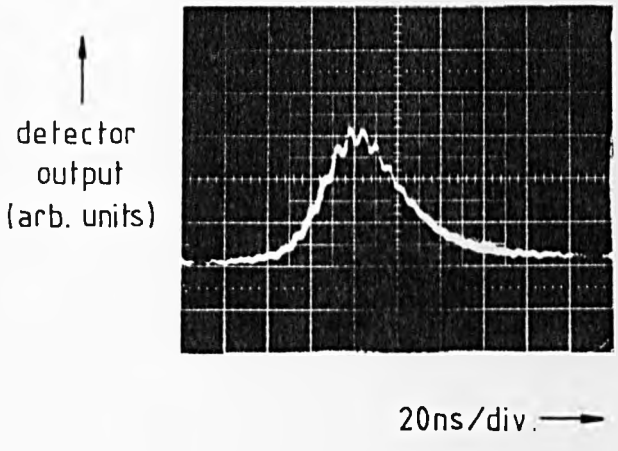

FIGURE 5.1: Temporal profile of the laser pulses (HP4200 photodiode).

(Hewlett-Packard type 4200). The profile, typical of both single and multimode operation, has a full-width half-height of ≃ 30ns.

The peak incident intensities of the raw (unfocused) beams, I_o, calculated from equation 4.4, were 3.2×10^{11} Wm^{-2} multimode and 1.4×10^{12} Wm^{-2} single mode. Evaluation of equations 4.10 and 4.11 indicates such pulses would produce maximum (surface) temperature rises of ≃ 35, 140 and 700°C single mode and ≃ 15, 60 and 310°C multimode in copper, aluminium and steel respectively, with thermal penetration depths ranging from 3 - 6μm.

5.2 Samples and detectors

A variety of different metal targets were examined all of which were machined prior to irradiation. The standard shape was a short cylinder 30mm in radius × 25mm thick.

For bulk wave studies, the ultrasonic detectors comprised small silvered 2 × 2mm squares of the piezoelectric ceramic, PZT (lead zirconium titanate, Unilater (UK) Ltd.), bonded on axis at the rear surface with cyanoacrylate adhesive; Figure 5.2(a). No backing material was employed, the transducers being allowed to resonate about their centre frequencies in the range 3-10MHz. Both longitudinally (L) and shear (S) polarised PZT were used, the former being sensitive to motion perpendicular to the back surface, the latter in lateral directions.

For surface wave studies, a number of PZT detectors were employed; Figure 5.2(b):

(1) Heavily damped conventional 3MHz wedge probe (Nortec Ltd.) with a perspex shoe at the critical angle for Rayleigh wave detection on a steel or aluminium surface.

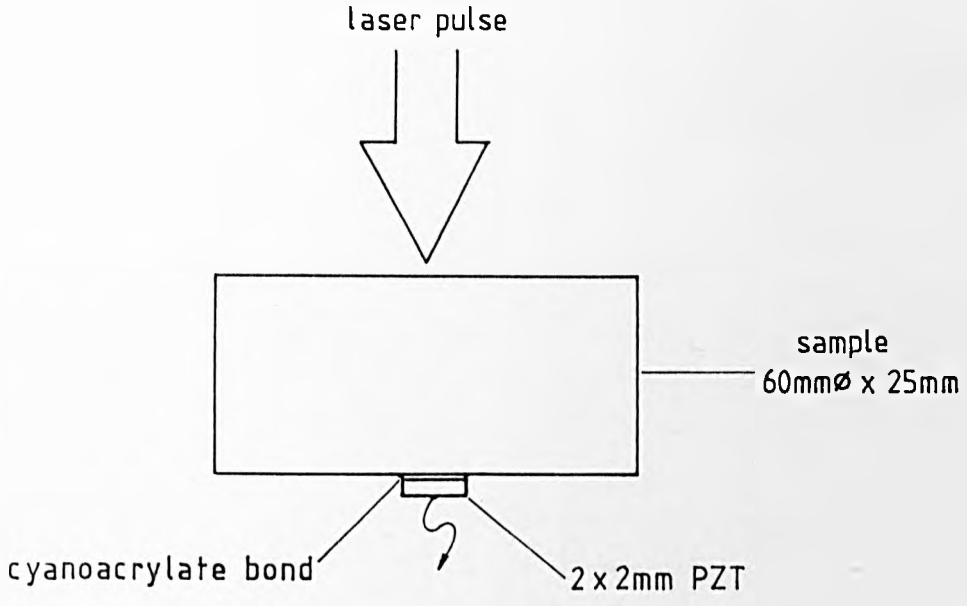

(a). Bulk wave studies

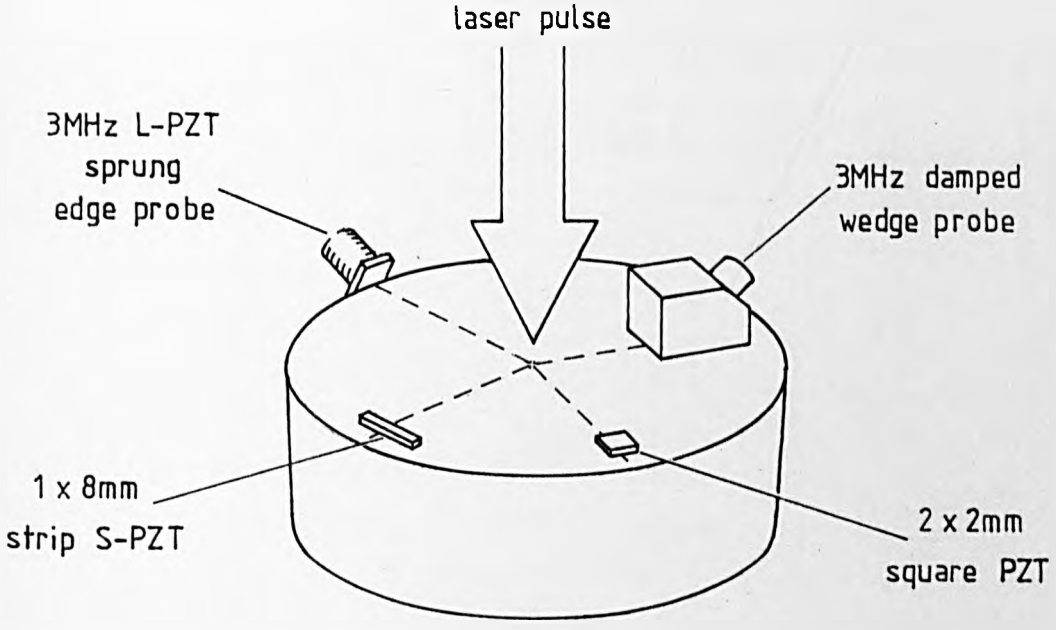

(b). Surface wave studies

wedge and edge probes coupled with oil
strip and square probes bonded with cyanoacrylate adhesive

FIGURE 5.2: Samples and detectors.

(2) 3MHz edge probe constructed from L-PZT held by a light spring mechanism at 45° to the sample's edge.

(3) Square probes of the same construction as the bulk wave detectors.

(4) Strip detectors comprising 1 × 8mm sections of S-PZT bonded normal to laser axis.

Design (4) gave better resolution for a given sensitivity than (3) as it minimised phase incoherence across emergent ultrasonic wavefronts though at the expense of requiring source/detector alignment.

5.3 Experimental arrangement

Figure 5.3 gives a typical experimental arrangement. The fast photodiode served as a trigger via a glass-slide beam splitter, feeding into either a storage oscilloscope (Tektronix 466) or a digitizer (Tektronix 7912AD) for subsequent signal analysis on a LSI II computer (Tektronix CP4165).

Neutral density filters could be inserted into the beam to reduce the intensity in accurate 1.5dB steps down to -30dB. Together with focusing lenses, this allowed a wide range of incident intensities to be generated, resulting in calculated maximum (surface) temperature rises ranging from a fraction of °C up to the point where surface material was melted, vaporised and ionised in rapid succession so as to form a hot expanding surface plasma. Estimates of the total pulse energy were made using a ceramic pyroelectric detector calibrated against a NPL standard.

5.4 Low intensity (unfocused) ultrasonic waveforms

Without focusing, both single and multimode laser operation produced well-defined ultrasonic pulses. The bulk waveforms, typified by the multimode waveform in Figure 5.4(a), showed two distinct arrivals (L and S)

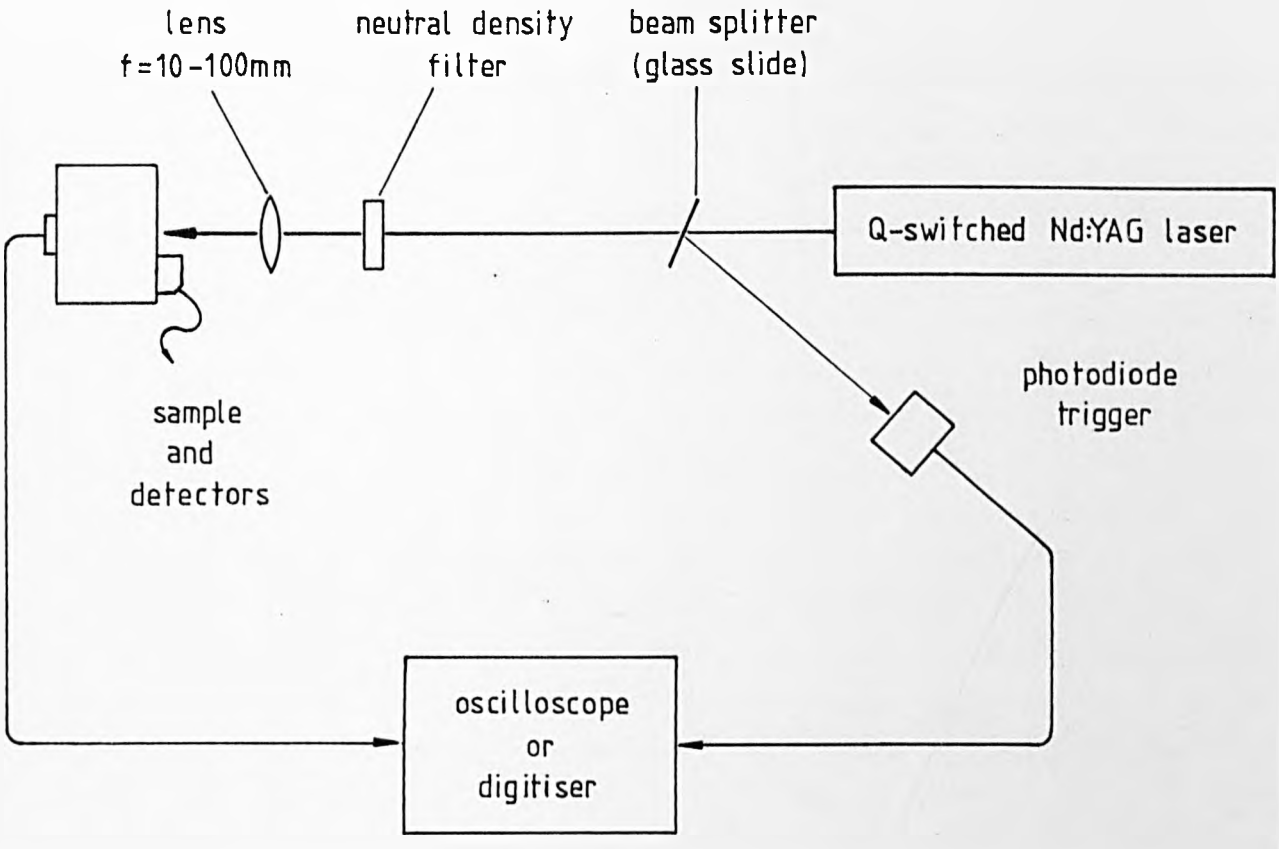

FIGURE 5.3: Typical experimental arrangement. The combination of focusing lens and neutral density filters allowed the incident intensity to be varied from approximately $10^9 - 10^{14}$ Wm^{-2}.

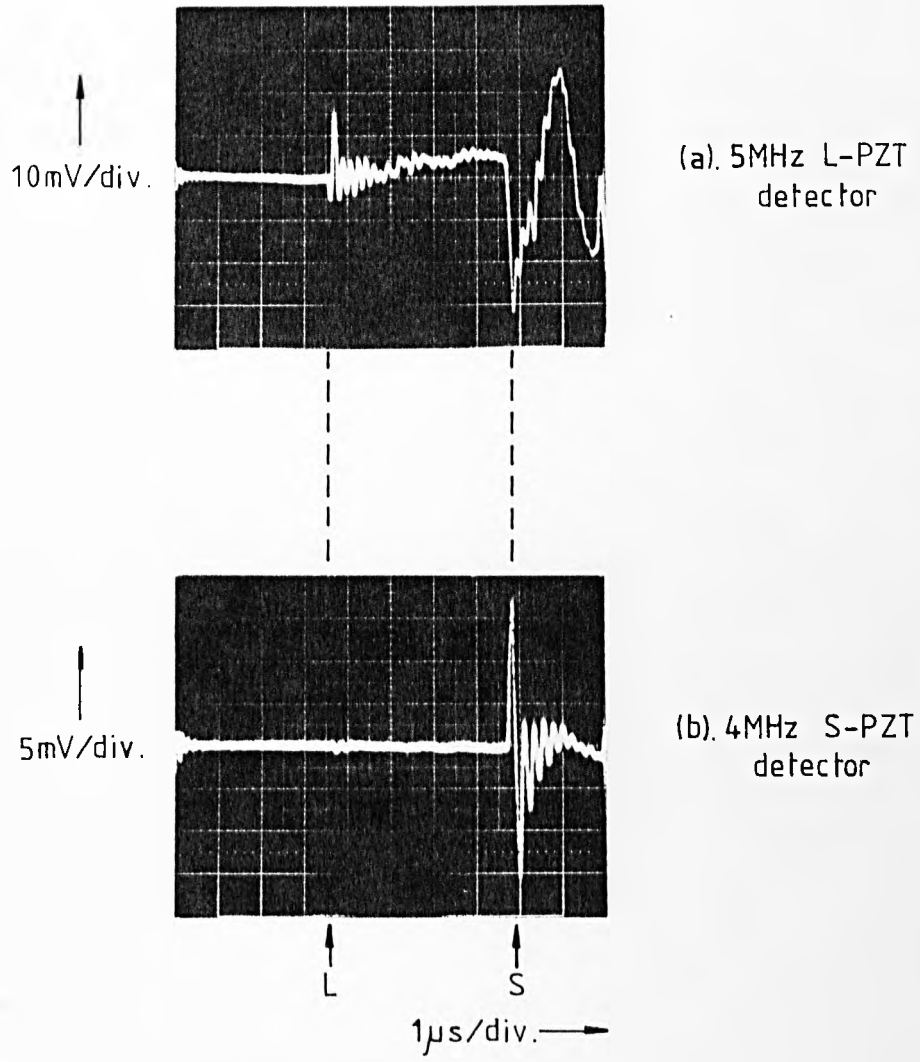

FIGURE 5.4: Typical unfocused bulk ultrasonic waveforms showing two distinct arrivals. Multimode laser pulses incident on a standard (25mm thick) aluminium alloy sample.

prior to multiple reflections and the build up of bulk resonances. The sample in this case was aluminium alloy (British Aerospace Ltd., type DTD 50/20 95% aluminium, 4% copper, 1% other elements), and the detector, 5MHz L-PZT. Measurement of the acoustic delay indicated a propagation velocity of 6250 ± 100 ms^{-1} for the initial arrival and 3050 ± 40ms^{-1} for the subsequent larger signal. This identified them as longitudinal and shear bulk wave pulses respectively for which the accepted (Kaye and Laby 1973) propagation velocities in pure aluminium are C_L = 6374ms^{-1} and C_S = 3111ms^{-1}.

The shear pulse is clearly the strongest of the two signals even though the detector being L-PZT, favoured longitudinal detection. This is further emphasised by waveform (b) detected with 4MHz S-PZT. Clearly, the unfocused laser source through generating both types of bulk wave, is characteristically shear.

That a laser should generate shear waves at all is perhaps surprising since thermal expansion, the presumed source mechanism, is essentially a volumetric phenomena.

The surface waveforms likewise showed two distinct ultrasonic arrivals comprising a main, high amplitude disturbance (R) preceded by a lower amplitude pulse (SL) propagating at roughly twice the velocity; Figure 5.5(a). In this case, it was possible to obtain more accurate differential velocity estimates by backing the laser source away from the detector using a micrometer sample bed, so obtaining a series of propagation delay measurements. The results shown in graphical form in Figure 5.6, indicated a propagation velocity of 3026 ± 25ms^{-1} for the main disturbance and 6440 ± 40ms^{-1} for the lower amplitude precursor. This identified them as the Rayleigh surface wave, accepted propagation velocity in pure aluminium of C_R = 2906ms^{-1} (Kaye and Laby 1973), and the so-called

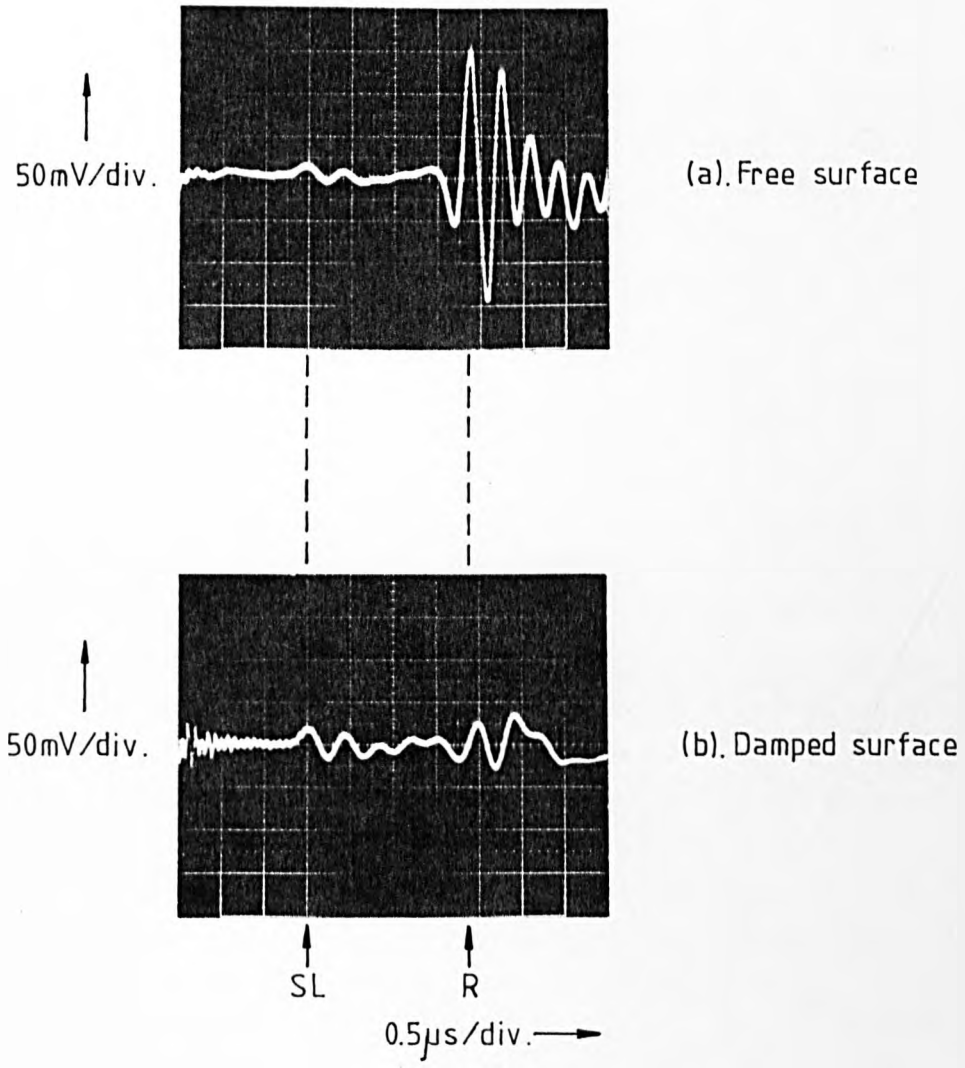

FIGURE 5.5: Typical unfocused surface ultrasonic waveforms produced by multimode pulses in aluminium alloy. Detected by 3MHz edge probe at a distance of ≈11mm.

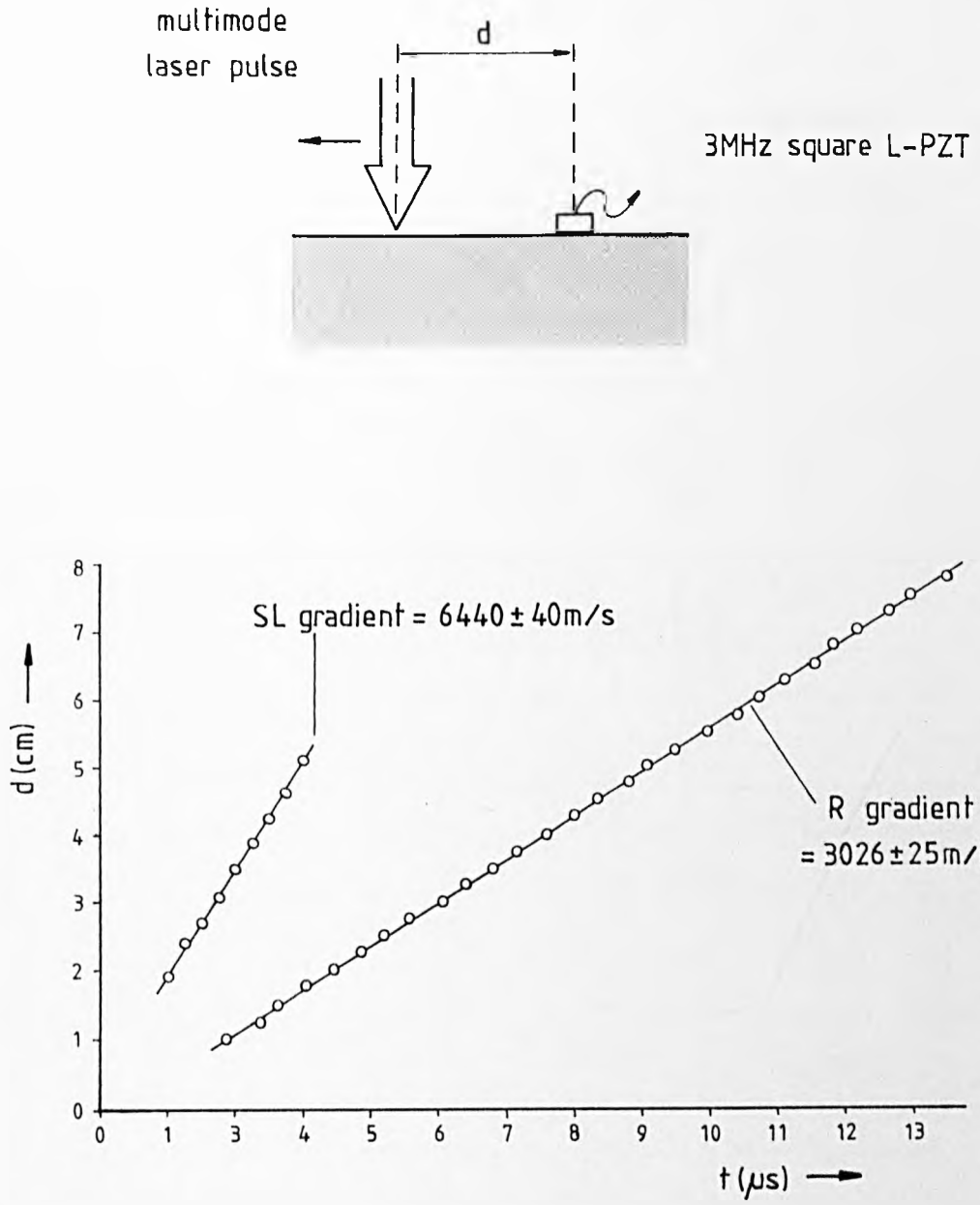

FIGURE 5.6: Differential measurent of surface wave propagation velocities in aluminium.

fast surface wave, accepted propagation velocity, C_L = 6374ms^{-1}. This fast surface wave is essentially a longitudinal bulk wave propagating sub-surface, as has been observed using conventional techniques by Couchman and Bell 1978. An interesting difference between the two types of surface waves could be demonstrated by the application of plasticine to the surface causing the waves to propagate under ≈ 8mm of surface damping. The result, apparent in waveform 5.5(b), was an almost unaffected longitudinal pulse but a highly attenuated Rayleigh pulse, indicating the latter unlike the former, is a true surface-guided wave.

A range of such propagation velocity estimates of both bulk and surface waves are presented in Table 5.1 for a variety of metal targets. They were all obtained by simple time-of-flight techniques over distances in the order of cms only, and yet yielded accurate results. This supports previous suggestions that the laser in producing brief, well-defined ultrasonic pulses, could prove useful in primary measurements of this kind (see Section 3.6).

The laser-produced ultrasonic pulses were also remarkably reproducible. The variation in amplitudes upon repeated irradiation of the same area of metal surface, appeared to be largely determined by small variations in the laser output energy; Table 5.2. This supports the view that the laser may be used as a standard acoustic source.

5.5 Effect of surface roughness

It has been asserted (White 1963) that radiation pressure is an insignificant source mechanism compared with thermal expansion. As a test, the absorptivity of a standard aluminium sample newly-polished to an optical quality finish, was progressively enhanced by systematic roughening with carborundum grits of increasing size. If radiation pressure was the

	C_L	C_S	C_R	C_{SL}
Aluminium Alloy *	6250	3050	3030	6440
type DTD 50/20	(6374)	(3111)	(2906)	(6374)
Mild Steel	5940	3195	2910	5665
	(4994-5957)	(2809-3224)	(2590-2986)	(4994-5957)
Brass	4310	2020	1950	4340
	(4372)	(2100)	(1964)	(4372)

TABLE 5.1 : Estimates of propagation velocities in ms^{-1} using the laser ultrasonic source. Typical accuracy ± 3%.

Accepted values in brackets (Kaye and Laby 1973).

* Accepted values quoted for pure aluminium.

	% variation $(\frac{\sigma}{\bar{x}} \times 100)$
laser energy	4.9
L - pulse	6.0
S - pulse	3.7
R - pulse	4.9
SL - pulse	7.7

TABLE 5.2 : Shot-to-shot variation in laser energy and resultant ultrasonic amplitudes in an aluminium sample.

Values expressed as normalised standard deviations

$$\frac{\sigma}{\bar{x}}$$

$\bar{x}$ = mean, σ = standard deviation.

Approximately 15 data points per sample.

chief source, this process would have decreased the generation efficiency since absorbed radiation exerts only half the pressure of that which is reflected. If thermal expansion was dominant, the acoustic amplitude would have increased in direct proportion to the absorptivity.

The results in Figure 5.7 give the peak-to-peak output produced from square 5MHz L—PZT detectors by unfocused multimode pulses for grits in the size range 3 - 74μm. All the pulse-types, surface and bulk alike, show an amplitude enhancement reaching a maximum of +60% to +95% at the 9μm grit size.

The appearance of an enhancement of any form favours the thermal explanation. The origin of the maxima, however, is not understood.

5.6 Ultrasonic output versus laser wavelength

Further evidence for the thermal model can be found by varying the laser wavelength and correlating the ultrasonic output with the spectral absorptivity or reflectivity. This was achieved in practice by using two additional lasers having comparable pulse durations and energies but operating at different wavelengths; first, a TEA CO_2 laser (R. Winfield 1980) producing 20ns 4.2mJ pulses in the infra-red(λ = 10.3μm) with a beam width of ≈ 4.0mm; and secondly, a KrF excimer laser (O. Bourne 1980) providing 20ns 2.6mJ pulses in a 1.6mm diameter beam in the ultra-violet (λ = 0.249μm). Together with the Nd:YAG laser acting as a cross-reference, this provided a means of studying the generation processes over a spectral region where the reflectivity of metal surfaces drops markedly from high values in the IR to comparatively low values in the UV (see Longhurst 1970).

The samples were standard aluminium, mild steel and brass cylinders onto the back of which were bonded square 3MHz L-PZT for bulk wave

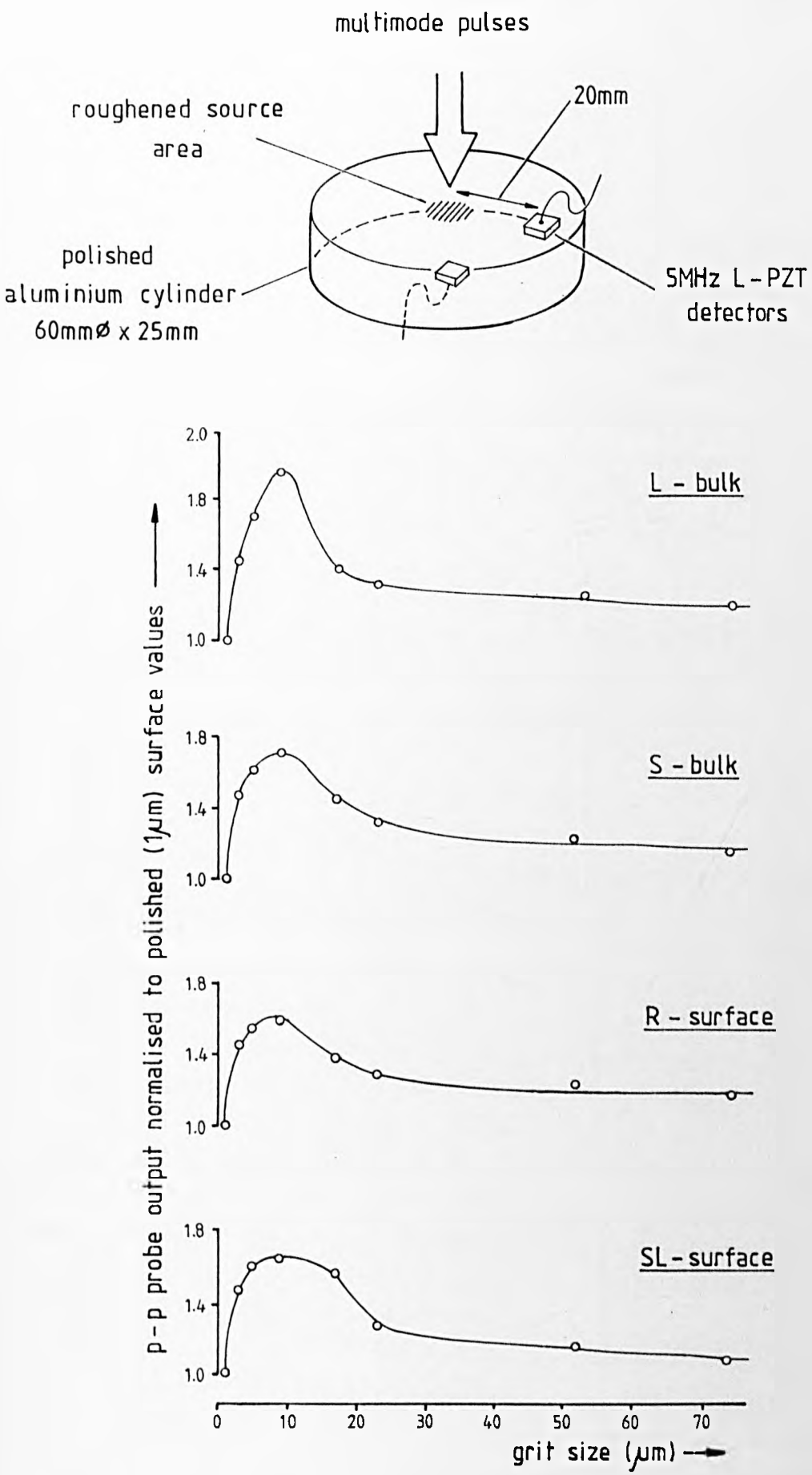

FIGURE 5.7: The effect of surface (source) roughness on acoustic amplitudes.

detection and 2MHz S-PZT strip probes for the surface waves. The ultrasonic output at the CO_2 and KrF laser wavelengths is given in Table 5.3 in terms of the peak-to-peak probe signals. The results are averages of all the wave-types and have been normalised to Nd:YAG multimode results apertured (iris) and attenuated (neutral density filters) to match beam diameters and incident pulse energies.

It is immediately obvious that radiation pressure cannot possibly be the dominant acoustic source since at most radiation pressure can vary by a factor of two, doubling between the perfect absorber and perfect reflector. Instead, the amplitudes are seen to range over an order of magnitude.

The accompanying figures in brackets are theoretical values for first the optical absorptivity relative to the Nd:YAG wavelength

$$(T_{op})_{rel} = \frac{T_{op}\ (\lambda)}{T_{op}\ (1.06\mu m)}$$

where T_{op}, the optical absorptivity, can be calculated from equation 4.1, and secondly, the relative radiation pressure

$$(P_{rad})_{rel} = \frac{1 + R_{op}\ (\lambda)}{1 + R_{op}\ (1.06\mu m)} = \frac{2 - T_{op}\ (\lambda)}{2 - T_{op}\ (1.06\mu m)}$$

where R_{op} = optical reflectivity

The calculated values for $(T_{op})_{rel}$ not only show an increase with decreasing wavelength as observed experimentally but also give the correct order of magnitude. The origin of the ultrasonic pulses appears to be the absorbed laser radiation.

5.7 Scaling with laser intensity (energy)

On a number of different metal surfaces, the scaling of ultrasonic amplitude with laser energy was found to be linear; Figures 5.8 (bulk

	CO_2 laser (λ = 10.3μm)	KrF laser (λ = 0.249μm)
Aluminium	0.25	2.3
	(0.32, 1.02)	(2.06, 0.97)
Mild steel	0.26	2.2
	(0.32, 1.16)	(2.06, 0.75)
Brass	0.47	4.3
	(0.32, 1.03)	(2.06, 0.95)

TABLE 5.3 : Peak-to-peak acoustic amplitudes produced at different laser wavelengths. Results normalised to Nd:YAG (λ = 1.06μm) values.

The figures in brackets are theoretical estimates of

(a) relative optical absorptivity, $\frac{T_{op}(\lambda)}{T_{op}(1.06\mu m)}$

(b) relative radiation pressure, $\frac{2 - T_{op}(\lambda)}{2 - T_{op}(1.06\mu m)}$

waves), Figure 5.9 (surface waves). Samples were irradiated with a multimode beam progressively attenuated by neutral density filters. No direct comparison should be made between the results for different metals as the detectors though nominally the same, varied considerably in sensitivity often by a factor of two or more due to differences in bond thickness and quality, and also to minor variations in surface finish.

These results are consistent with the uncoupled thermoelastic model for which thermal strains and hence acoustic stresses and displacements are directly proportional to the absorbed laser intensity.

5.8 Rayleigh pulse profile

The 3MHz wedge probe being heavily damped, revealed details of the Rayleigh pulse which were hidden in the resonance of the discrete element surface wave transducers. The profile took the form of a roughly symmetrical dipolar pulse as is shown by the multimode waveform in Figure 5.10. The longitudinal surface pulse is not obvious in this trace since the probe shoe was critically angled for Rayleigh wave detection.

The duration of the Rayleigh pulse as defined by the delay between the two opposed peaks, remained constant for different source/detector distances. However, it could be decreased by reducing the beam diameter using circular apertures cut from metal shim; Figure 5.11. This is demonstrated in Figure 5.12 which gives expanded time based traces in aluminium for a variety of apertured and unapertured multimode beams. As a further comparison, an unapertured single mode waveform is also included. For a given beam diameter, however, different metals produced slightly differing pulse durations; Figure 5.13.

This variation of pulse duration with both spot diameter and material, can be understood by considering the Rayleigh pulses in terms of their

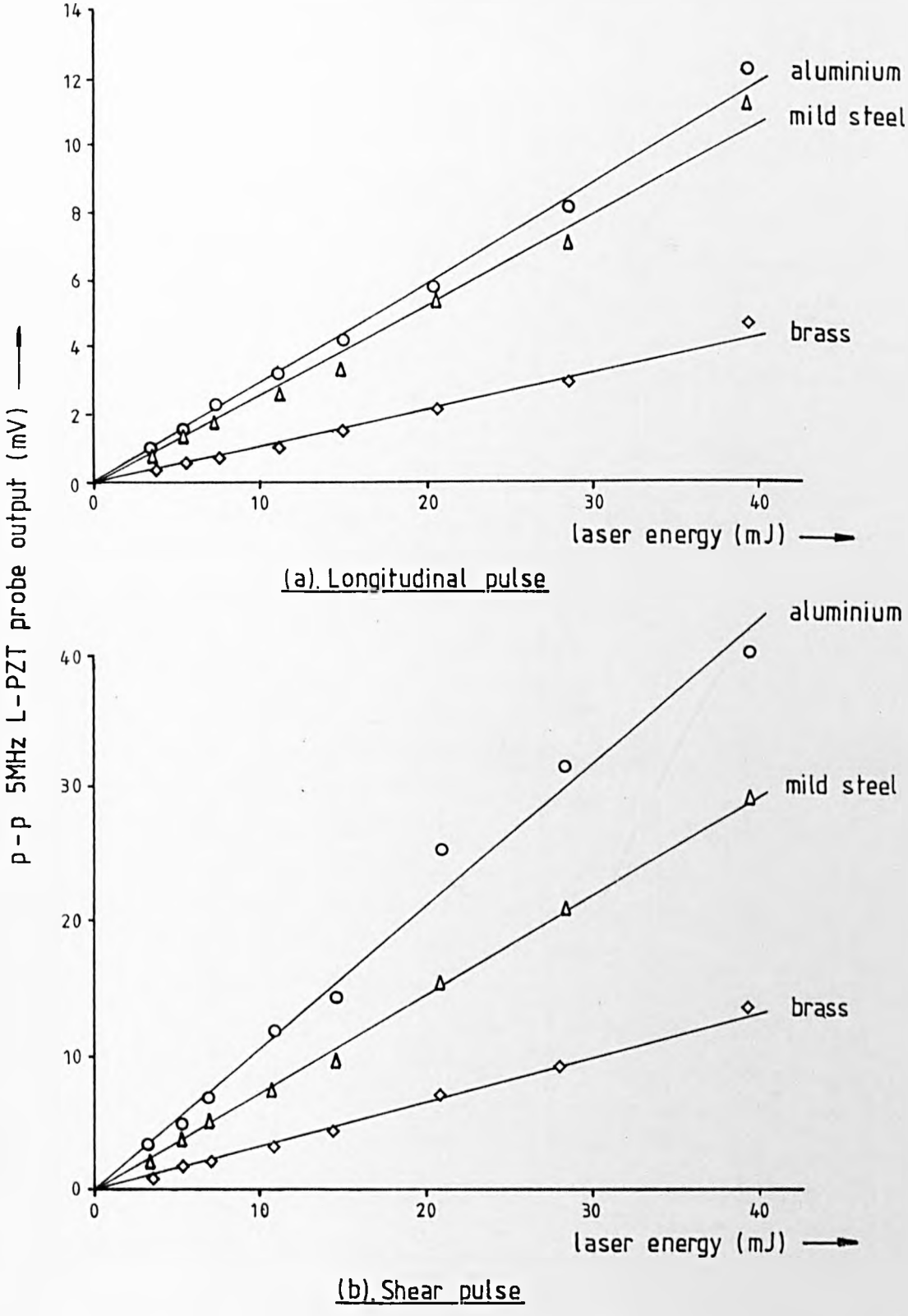

FIGURE 5.8: The variation of bulk wave amplitudes with laser energy. Filter -reduced unfocused multimode pulses incident on standard (25mm thick) samples.

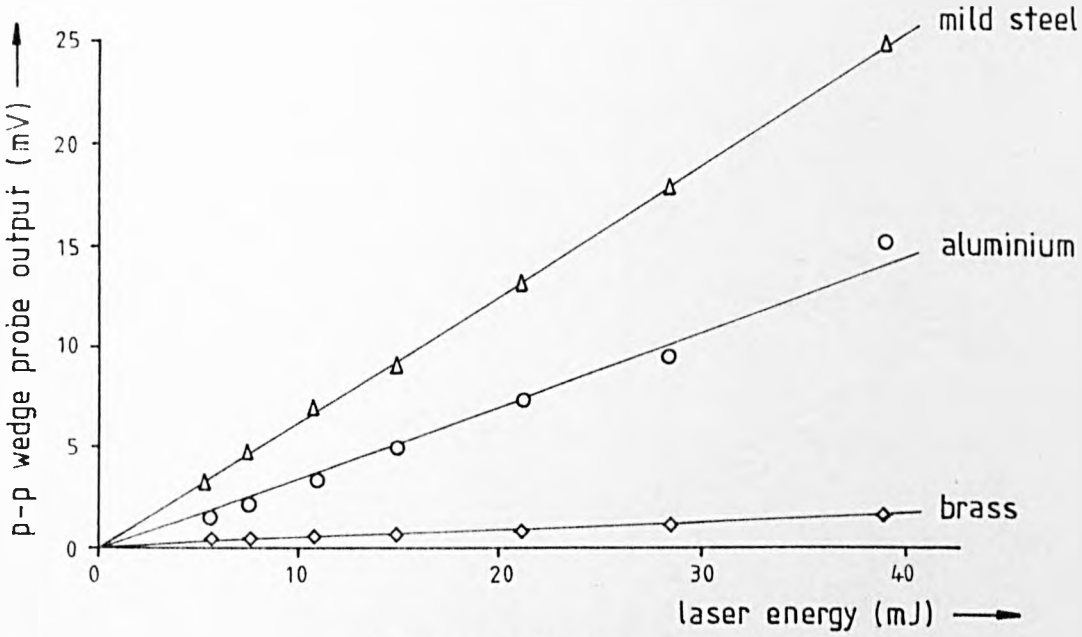

(a). Rayleigh pulse

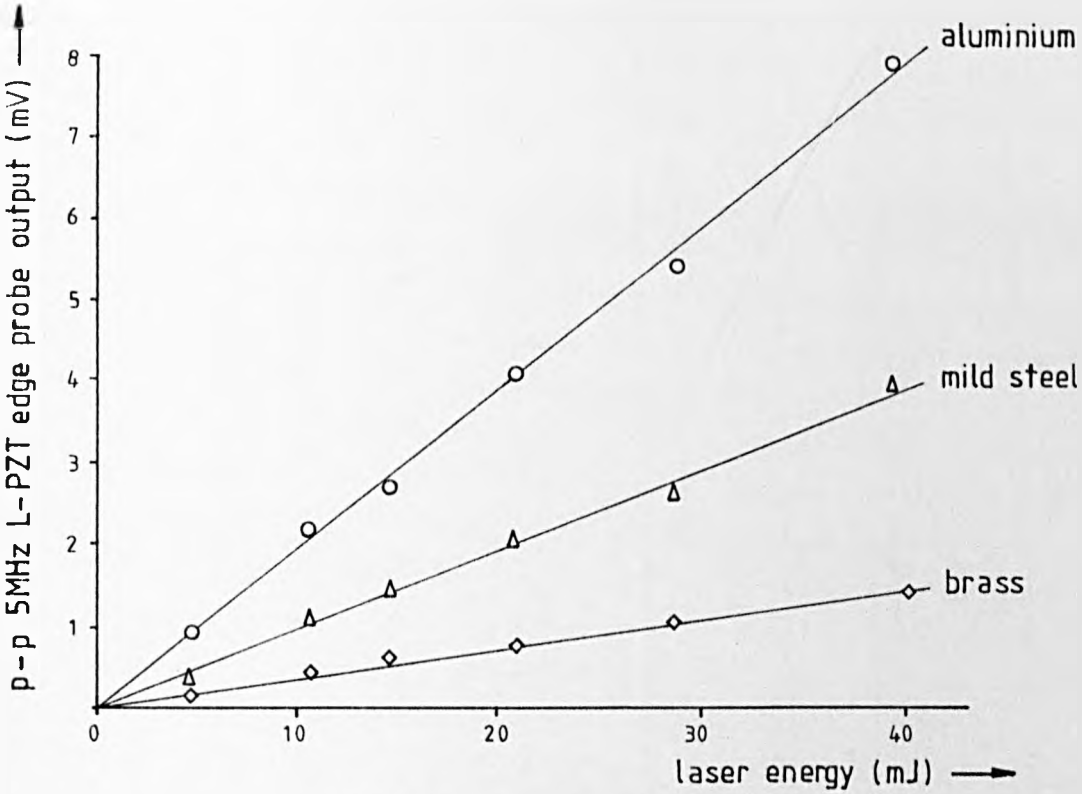

(b). Longitudinal pulse

FIGURE 5.9: The variation of surface wave amplitudes with laser energy. Unfocused multimode pulses at a source/detector distance of ≈ 10mm.

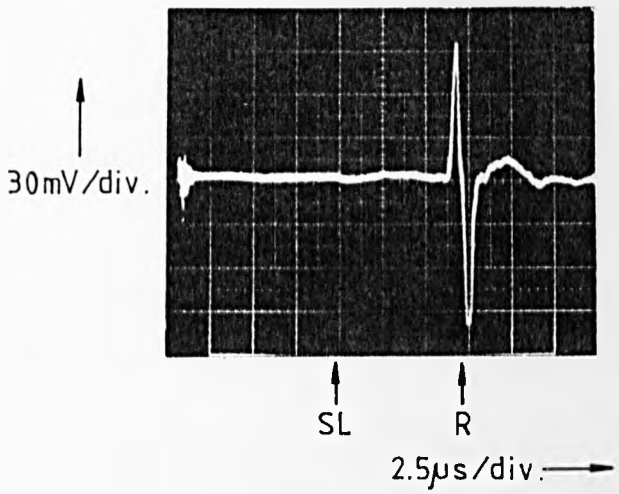

FIGURE 5.10: Surface waveform obtained with heavily damped, 3MHz wedge probe, revealing the Rayleigh pulse profile. Unfocused multimode pulse at a distance of ≈10mm from probe shoe.

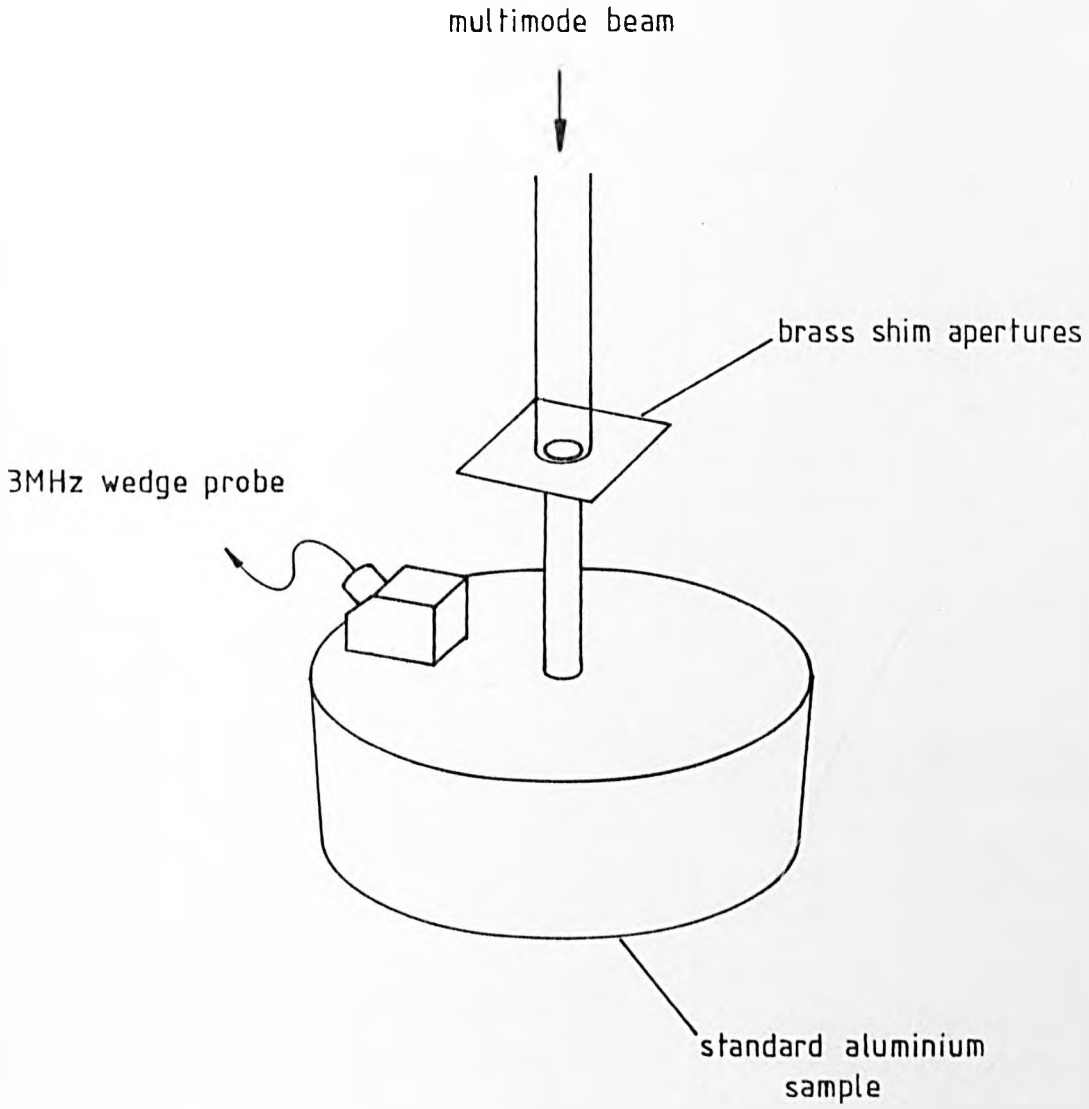

FIGURE 5.11: Arrangement for examining the variation of Rayleigh wave profile with spot diameter.

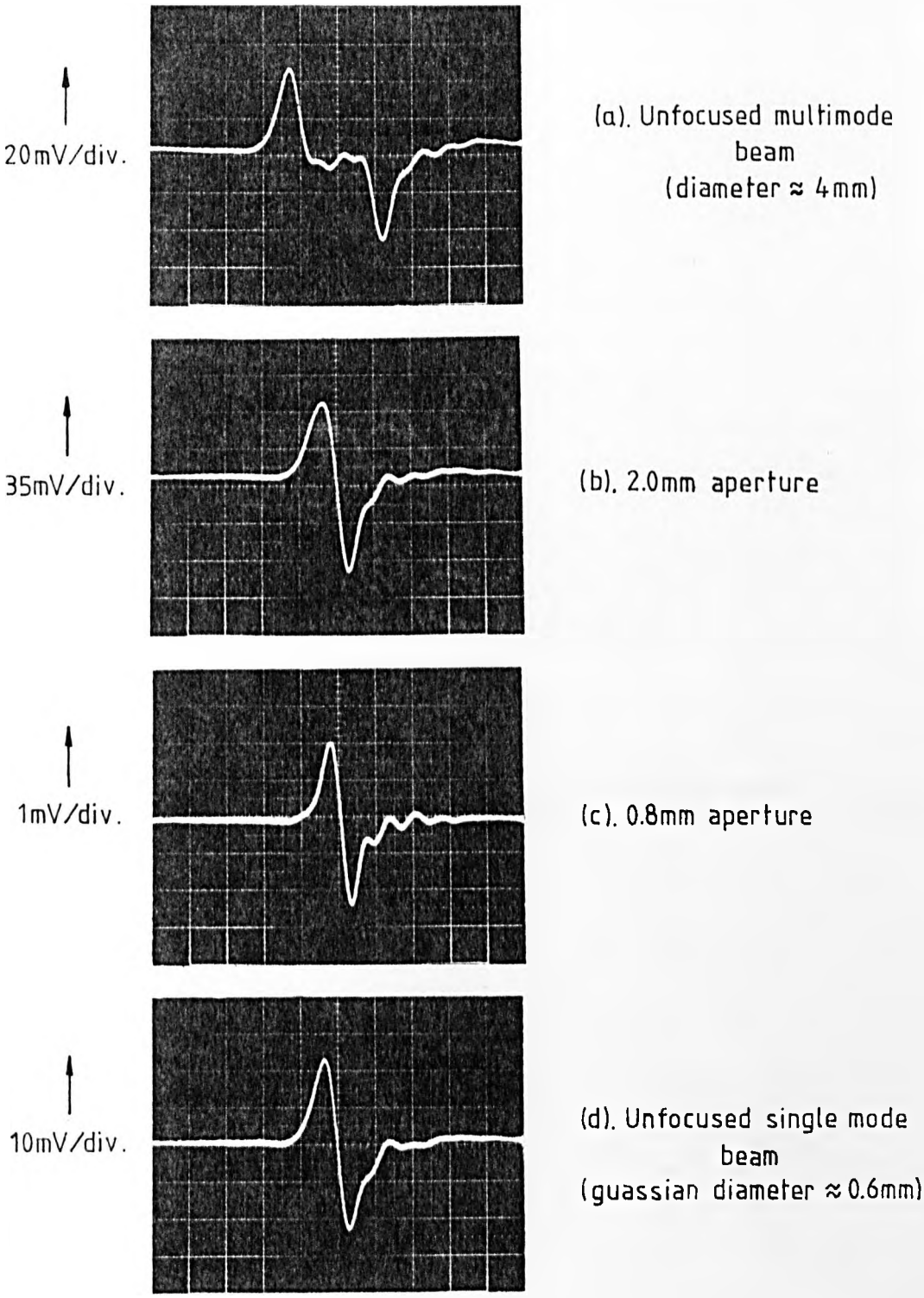

FIGURE 5.12: Reduction of Rayleigh pulse duration with laser beam diameter.

Expanded time base at 0.5μs/div.

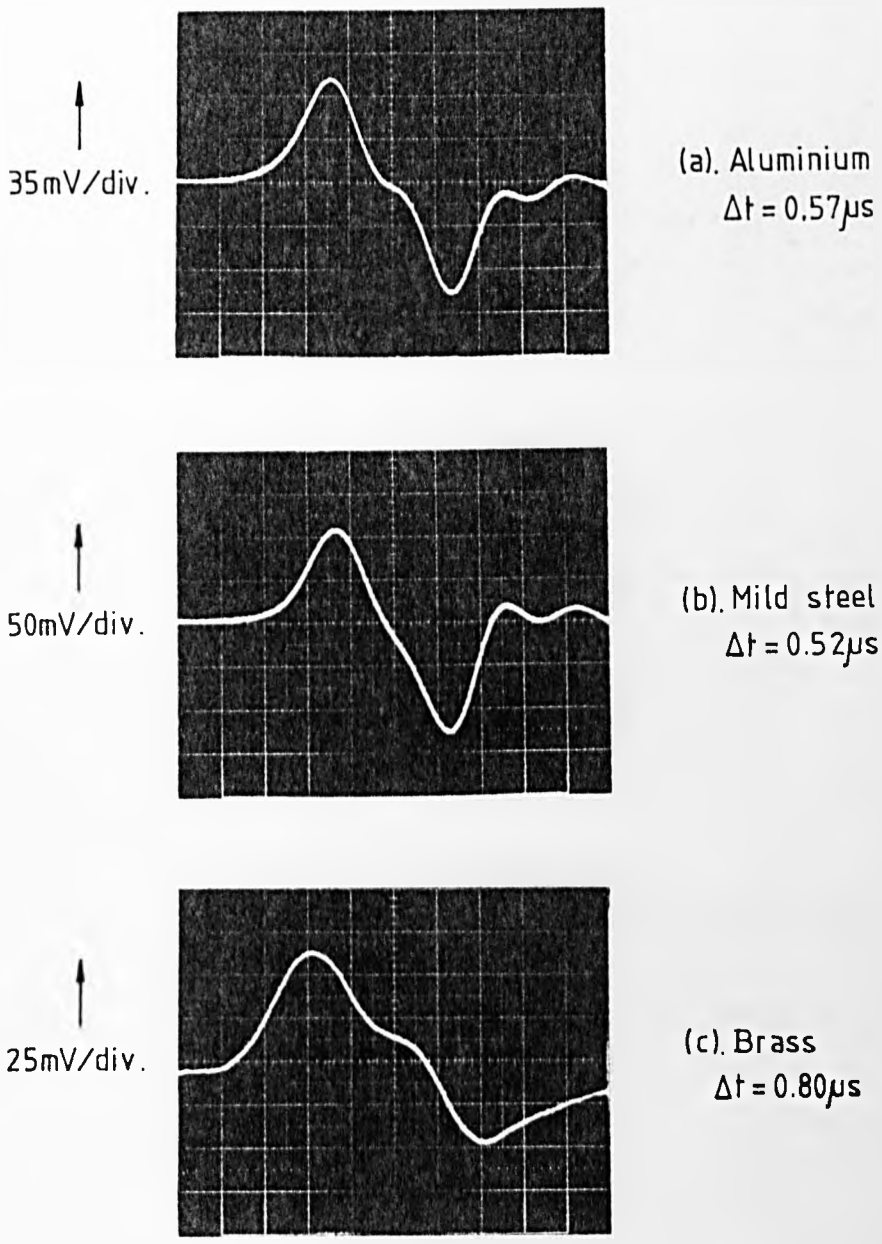

FIGURE 5.13: Details of the Rayleigh pulse for different metals at constant (1.8mm) laser beam diameter.

Expanded time base at 0.2μs/div.

physical length

$$\Delta d_R = \Delta t . C_R$$

where Δt = temporal duration of pulse (peak to peak)

C_R = propagation velocity

Substituting for Δt from Figure 5.13 for the aluminium, steel and brass waveforms, gives Δd_R = 1.7, 1.5 and 1.6 ± 0.1mm respectively. These values are remarkably close to the aperture diameter of 1.8mm. Indeed, a complete plot of Δd_R versus aperture diameter, D, for all three different metals reveals an almost direct and quite general spatial correspondence with Δd_R lying in the range 0.78 - 0.97D in the region where the probe may be expected to have sufficient spatial resolution; Figure 5.14. Clearly, the duration of the Rayleigh pulses is determined by the acoustic transit time across the source diameter.

The bulk waveforms showed no such beam diameter variation, the profile remaining essentially the same as Figure 5.4.

5.9 The effect of surface constraint

A fundamental change occurs in the laser acoustic source when any kind of transparent overlay is applied to the surface. This is shown in Figure 5.15 which gives the waveform produced at an aluminium surface submerged under ≈ 1cm of water. The experimental conditions were otherwise identical to those under which the waveform in Figure 5.4(a) was obtained. The amplitude of the longitudinal pulse has been enhanced by ×20 and the shear pulse slightly reduced by ×0.74. The laser source has all but lost its previously dominant shear character and become

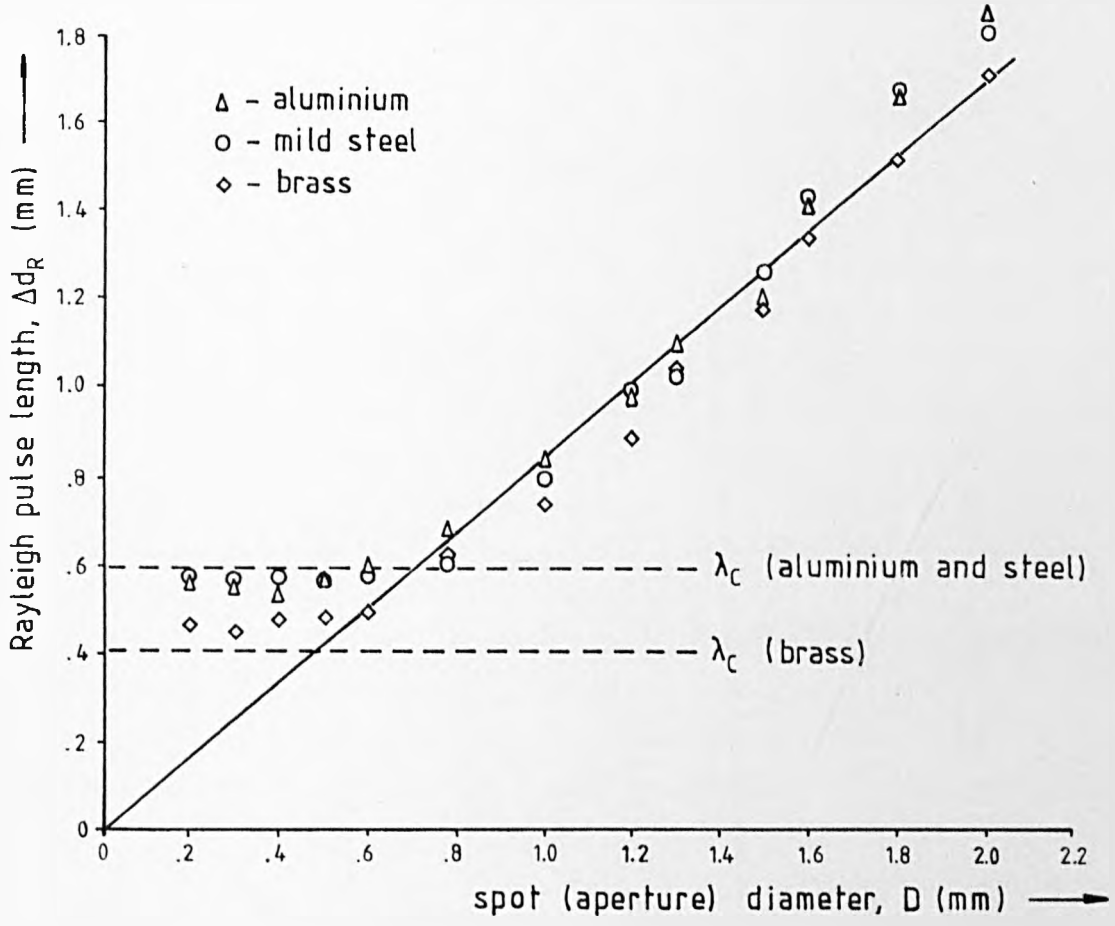

FIGURE 5.14: The direct dependence of Rayleigh pulse length, $\Delta d_R = \Delta t . C_R$, upon laser beam diameter, D.

λ_c indicates limit of detector's spatial resolution due to an upper cut-off frequency of ≈ 5MHz.

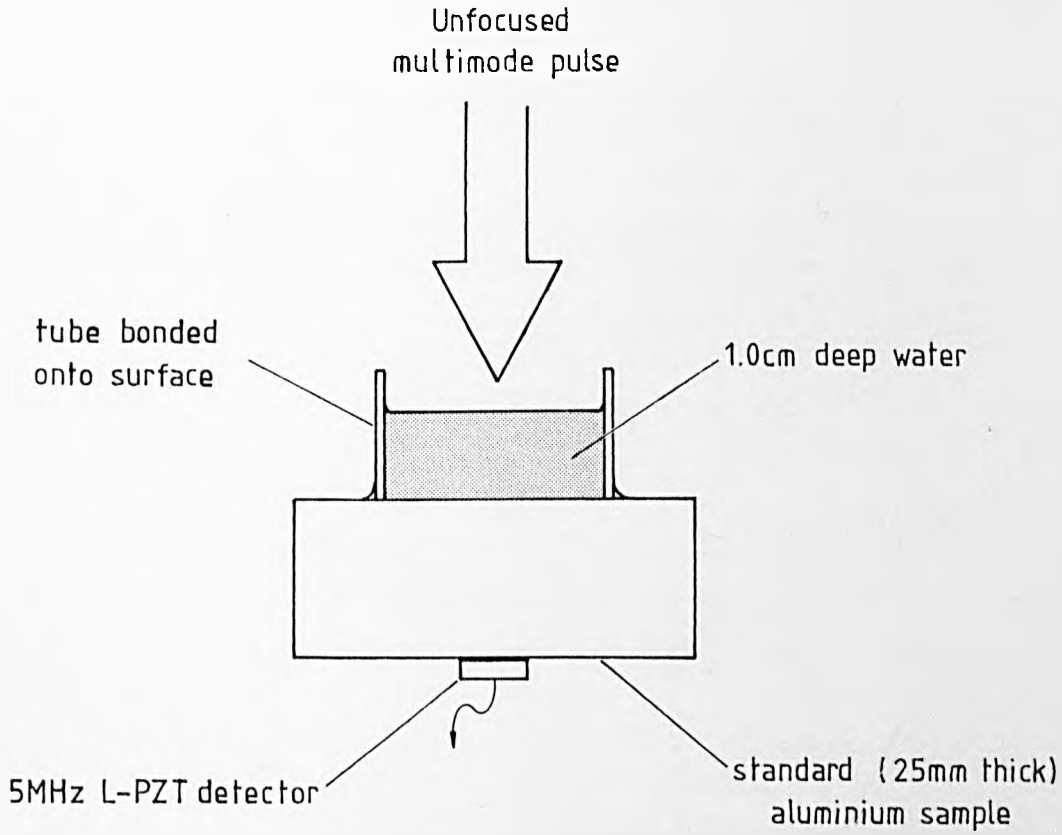

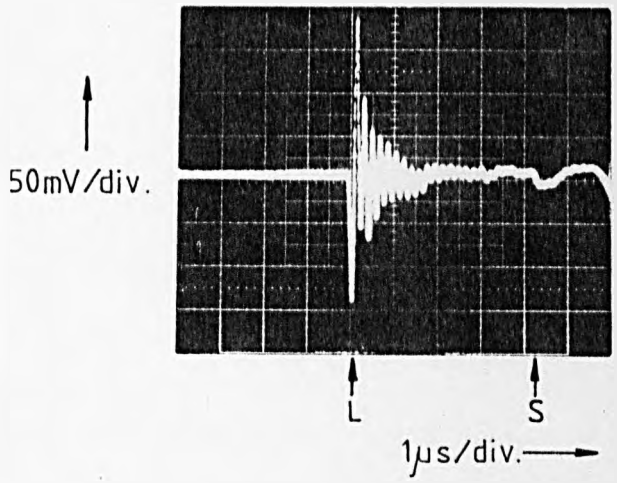

FIGURE 5.15: Bulk waveform produced at a constrained surface showing enhanced longitudinal generation.

overwhelmingly longitudinal.

The generation process remains, however, linear. This is demonstrated in Figure 5.16 which gives the laser energy scaling for an aluminium target.

In Sections 4.8 and 4.9, which discussed the effect of surface constraint, longitudinal enhancement was shown to be a direct consequence of the acoustic thinness of the laser acoustic source. This ensures weak generation at a free surface where expansion can take place almost stress-free outwards from the surface, but also results in relatively strong compressive - longitudinal pulse under the constraining presence of an overlay which causes some of the expansion to take place against the metal bulk.

The degree of enhancement provided by the water expressed in dB (20 log A_1/A_0), is given for a variety of metals in Table 5.4. The accompanying theoretical values were calculated from equation 4.41 which gives an enhancement for a fully constrained surface of

$$R = \frac{C_L}{\sqrt{2\pi\kappa f}}$$

where f may be taken as the resonant frequency of the transducer

κ = thermal diffusivity

The experimental results though of comparable magnitude are somewhat lower. This is to be expected since the theoretical results assume total surface constraint whereas the water only provided partial constraint. There is reasonable agreement in relative terms, both experiment and theory indicating, for example, that the enhancement is most pronounced in steel and least in copper. From the uniform irradiation model, the reason for this is that of all the listed metals, steel produces the thinnest acoustic

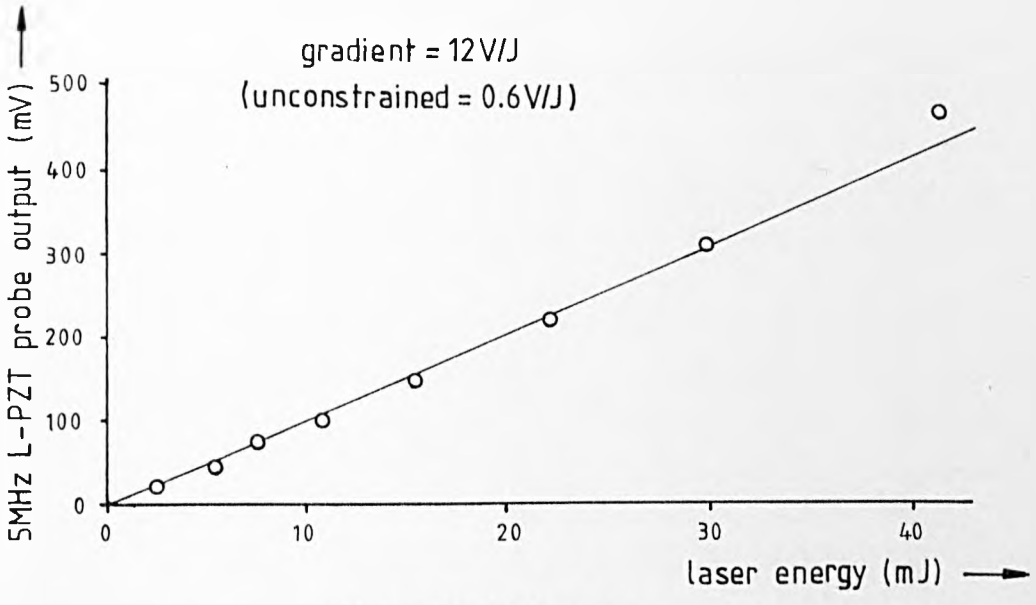

(a). Longitudinal pulse

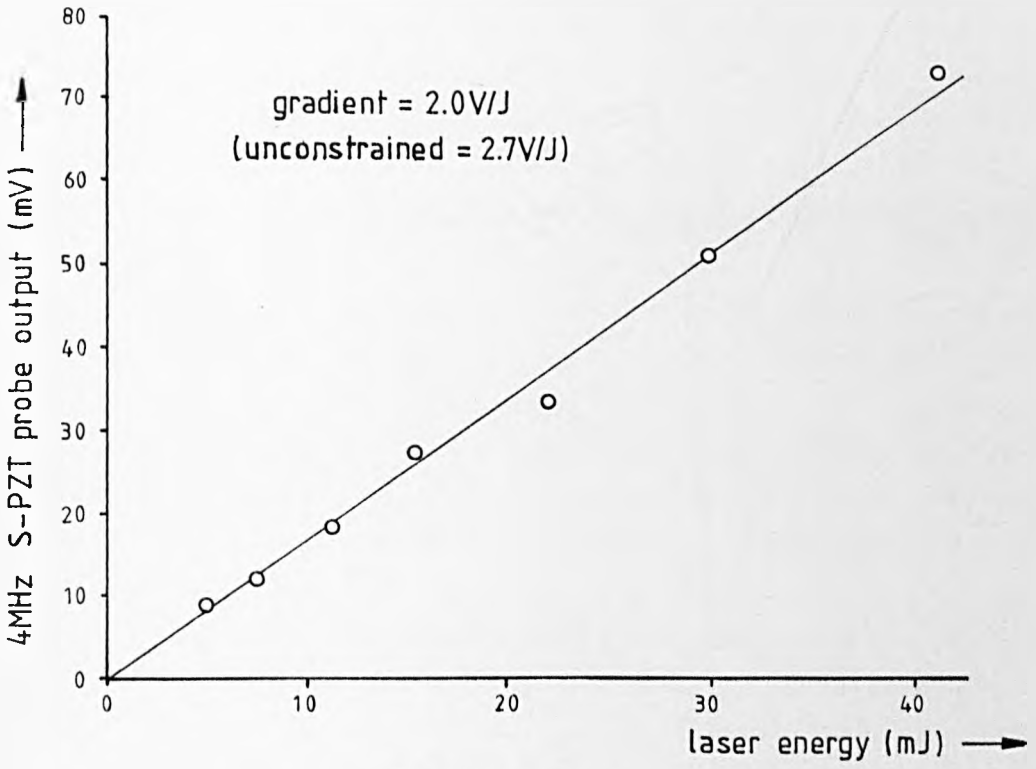

(b). Shear pulse

FIGURE 5.16: The variation of ultrasonic amplitude with laser energy at a constrained surface. Unfocused multimode pulses incident on aluminium submerged under ≈1.0cm deep water.

	Observed enhancement (± 1dB)	$\frac{C_L}{\sqrt{(2\pi\kappa f)}}$
Aluminium	27	42
Mild steel	31	47
Brass	23	42
Copper	21	38

TABLE 5.4 : Longitudinal enhancement produced by surface (water) constraint in dB.

source due to its exceptionally low thermal diffusivity while copper being an excellent diffuser produces the thickest. Consequently, the free surface source is relatively weak in steel and strong in copper, the former gaining most from constraint, the latter least. There is, however, an unexplained and serious discrepancy not in terms of magnitude of enhancement but rather of sign. The observed enhancement is in fact inverted in the sense that the polarity of the initial swing in the longitudinal signal is in the opposite direction to the main one in the free-surface waveform; Figure 5.4(a). The uniform irradiation theory, however, indicates essentially compressive generation at both a free and constrained surface. Clearly, constraint does more than enhance the generation process; it must change them in some fundamental way. It is interesting to note that the shear pulse is neither enhanced nor polarity inverted by constraint.

5.10 Finite thickness overlay

Figure 5.15 showed a thick constraining layer waveform in the sense that the water was sufficiently deep to ensure that any possible signals resulting from reflection off its upper surface, arrived after the time of interest. Shallower or thinner overlays may similarly be expected to enhance the initial direct pulse, and additionally to introduce a series of signals due to multiple internal reflections within the overlay, as described in Section 4.7. This proved to be the case as is demonstrated by the bulk waveform in Figure 5.17 which was produced on a standard aluminium sample the surface of which was covered with an oil film, nominally 1mm thick. The first signal, D_o, is thought to represent the longitudinal pulse which propagated from the vicinity of the irradiated interface and subsequent ones the multiple internal overlay reflections;

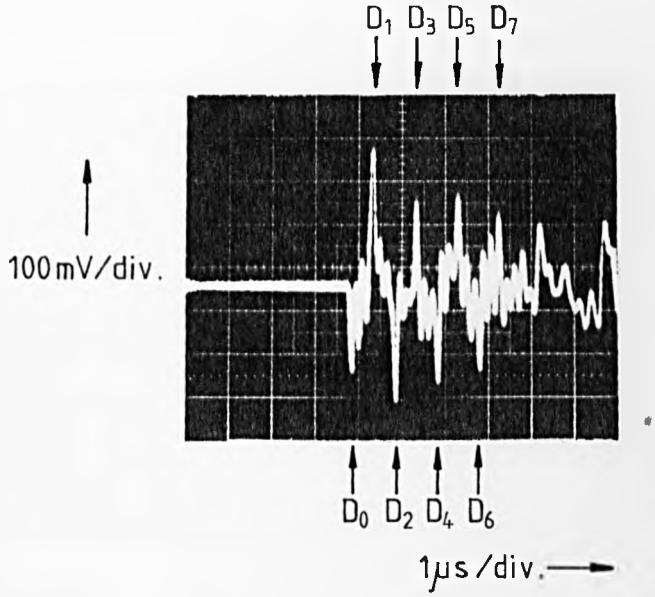

FIGURE 5.17: Constraining layer waveform showing multiple internal reflections of longitudinal pulses. Unfocused multimode laser pulse on an aluminium sample with a ≈1mm oil layer and 5MHz L-PZT.

Figure 5.18.

A notable feature of the waveform is that D_o is smaller in amplitude than the first reflected pulse D_1 and indeed at least the next two multiply reflected signals, D_2 and D_3. This may seem surprising since the pulses all originated from the same expansion and yet the oil-reflected pulses not only had to propagate further to reach the detector but also suffered further reduction in amplitude in being first transmitted and then reintroduced back across the impedance mismatch of the oil/metal interface.

The reason for this amplitude paradox is that the first detected signal is in fact composed of two unresolved components which interfere destructively with each other. Equation 4.32 has already expressed the boundary-distant thermoelastic displacement produced under a finite thickness overlay, as

$$U_1 = u_1 + u_3 + \sum_1^n u_g^n \qquad 5.1$$

where u_1 = direct wave

$$= \frac{\gamma}{2} \int_o^r \theta \left(z, t - \frac{r-z}{C_{1L}}\right) dz$$

u_3 = immediate boundary reflected wave

$$= \frac{\gamma}{2} R_{12} \int_o^\infty \theta \left(z, t - \frac{r+z}{C_{1L}}\right) dz$$

$\sum_1^n u_g^n$ = series of multiply reflected waves

$$= \frac{\gamma}{2} \sum_1^n T_{12} (R_{23})^n (R_{21})^{n-1} T_{21} \int_o^\infty \theta \left(z, t - \frac{2nD}{C_{2L}} + \frac{r+z}{C_{1L}}\right) dz$$

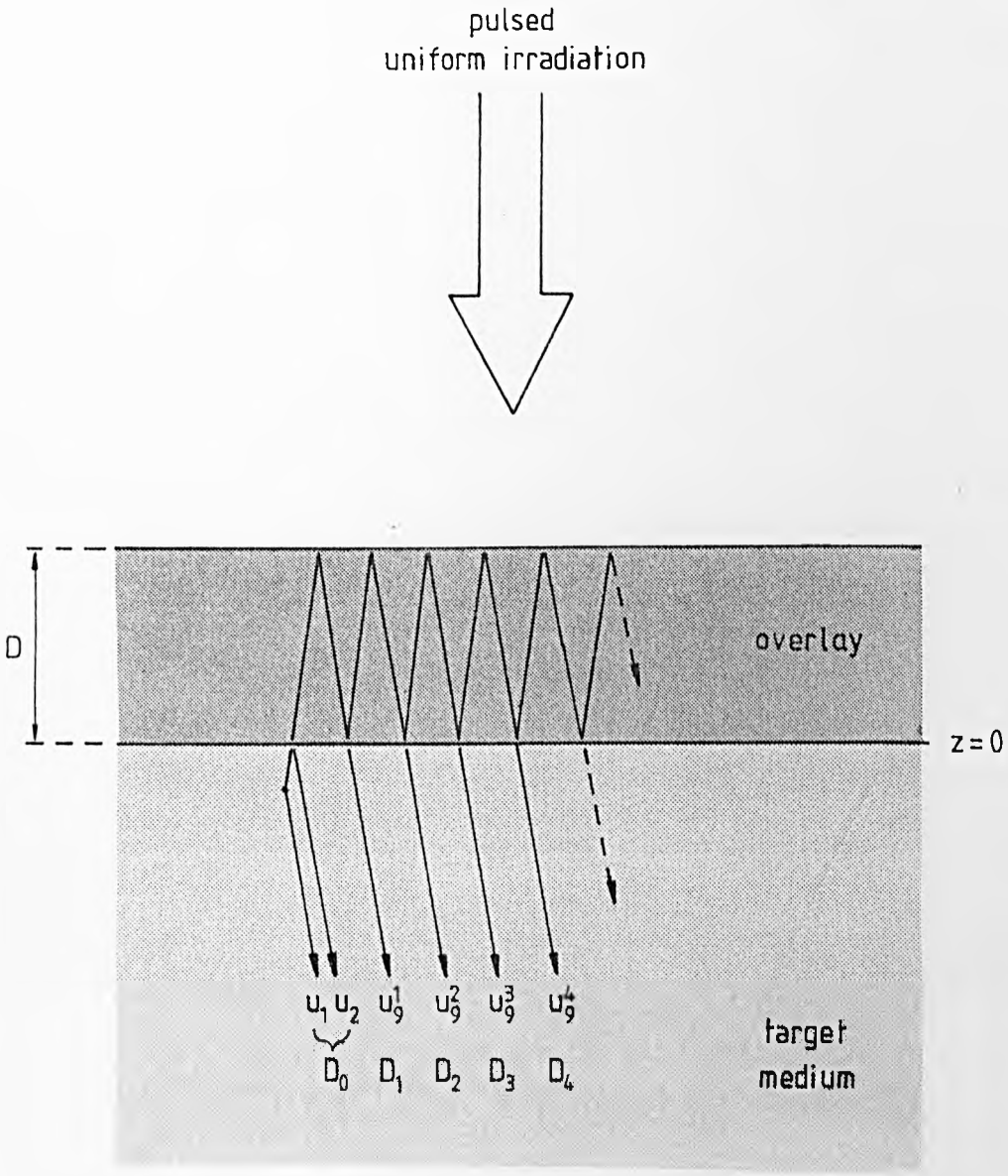

FIGURE 5.18: Wave groups contributing towards detected waveform under a finite thickness overlay (see Section 4.7).

Transmission back across target/overlay interface introduces a decaying wavetrain of acoustic pulses due to multiple internal reflections.

θ = temperature rise within target

C_{1L} = propagation velocity of longitudinal waves in target medium

C_{2L} = propagation velocity of longitudinal waves in overlying medium

D = overlay thickness

n = reflection order

Since the laser pulse duration of 25ns was much greater than 15ps, it follows from Figure 4.14 that the source remained acoustically thin for all times. Negligible time delays therefore existed across the heated region. This allows the delay-adjusted temperature integrals within the expressions for u_1 and u_3 to be satisfactorily approximated as

$$\int_0^\infty \theta\left(z,t - \frac{r-z}{C_{1L}}\right)dz \approx \int_0^\infty \theta\left(z,t - \frac{r}{C_{1L}}\right)dz$$

$$\int_0^\infty \theta\left(z,t - \frac{r+z}{C_{1L}}\right)dz \approx \int_0^\infty \theta\left(z,t - \frac{r}{C_{1L}}\right)dz$$

The propagation delays for these two boundary-close waves is effectively the same, both of them effectively arriving simultaneously as if generated at the very surface of the target.

These integrals are simply related to the absorbed energy density, E(t), as

$$\int_0^\infty \theta\left(z,t - \frac{r}{C_{1L}}\right)dz = \frac{1}{c\rho}\int_0^\infty E\left(t - \frac{r}{C_{1L}}\right)dz$$

$$= \frac{E_T}{c\rho} H\left(\tau - \frac{r}{C_{1L}}\right) \quad \text{(instantaneous pulse)}$$

where E_T = total absorbed energy density

c = specific heat

ρ = density

Similarly, the integrals involved with the multiply-reflected waves, u_9, approximate as

$$\int_0^\infty \theta\left(z, t - \frac{2nD}{C_{2L}} - \frac{r+z}{C_{1L}}\right)dz \approx \int_0^\infty \theta\left(z, t - \frac{2nD}{C_{2L}} - \frac{r}{C_{1L}}\right)dz$$

$$\approx \frac{E_T}{c\rho} H\left(t - \frac{2nD}{C_{2L}} - \frac{r}{C_{1L}}\right) dz$$

Substituting for the various integrals into equation 5.1, gives the initial signal, the sum of u_1 and u_3, as

$$D_0 = u_1 + u_3 = (1 + R_{12}) \frac{\gamma E_T}{2c\rho} H\left(t - \frac{r}{C_{1L}}\right)$$

and the subsequent multiply-reflected signals as

$$D_1 = u_9^1 = \frac{\gamma E_T}{2c\rho} [T_{12} R_{23} T_{21}] H\left(t - \frac{2D}{C_{2L}} - \frac{r}{C_{1L}}\right)$$

$$D_2 = u_9^2 = \frac{\gamma E_T}{2c\rho} [T_{12} (R_{23})^2 R_{21} T_{21}] H\left(t - \frac{4D}{C_{2L}} - \frac{r}{C_{1L}}\right)$$

$$D_n = u_9^n = \frac{\gamma E_T}{2c\rho} [T_{12} (R_{23})^n (R_{21})^{n-1} T_{21}] H\left(t - \frac{2nD}{C_{2L}} - \frac{r}{C_{1L}}\right)$$

The information about the relative amplitude of these step-like displacements is provided by the terms contained within square brackets,

and is related via the various transmission and reflection coefficients to acoustic impedances only. If the surface is not uniformly irradiated - as indeed was the case - all the waves would suffer from varying degrees of geometrical and material attenuation with the high order multiple reflections suffering the most. However, provided the overlay thickness is very much less than the distance to the detector, any such differences will be generally negligible and the relative amplitudes will be maintained.

If the square-bracket terms are evaluated and then normalised to the initial D_O term, a direct comparison can be made with the peak probe outputs; see Table 5.5. The agreement between experiment and theory is reasonable, and D_O is indeed expected to be smaller than D_1, D_2, D_3 or D_4. In this particular case, u_3 interfered destructively with u_1, $(1 + R_{12} = 0.16)$, so considerably reducing the amplitude of D_O. This is due to the comparatively low acoustic impedance of the oil overlay 1.4×10^6 $Pasm^{-1}$ compared with 17×10^6 $Pasm^{-1}$ for aluminium (Kaye and Laby 1973) which has inverted u_3 upon reflection. The wave driven into the overlay, u_8 in the terminology of Section 4.7, suffers no such interference and so reintroduces the subsequent series of comparatively strong multiply-reflected signals. The alternate polarity is due to successive inversion at the oil/free space (air) interface ($R_{23} = -1$).

Such results can be used to estimate two important parameters; first, the overlay thickness, and secondly, its acoustic impedance relative to the target medium. The thickness can be found from the interval between successive multiple reflections which simply gives the round trip delay within the overlay as

$$\Delta t = \frac{2\Delta D}{C_{2L}} \quad \text{or,} \quad \Delta D = \frac{\Delta t}{2} C_{2L}$$

	Uniform irradiation theory	Observed (Figure 5.17) ± 0.1
D_0	+ 1 (normalisation)	+ 1
D_1	- 1.85	- 1.7
D_2	+ 1.56	+ 1.4
D_3	- 1.34	- 1.1
D_4	+ 1.14	+ 0.9
D_5	- 0.95	- 0.8
D_6	+ 0.82	+ 0.8
D_7	- 0.69	- 0.7

TABLE 5.5 : Relative amplitudes of longitudinal pulses produced at an aluminium surface with an oil overlay.

On this basis, timing of the waveform in Figure 5.17 indicates an oil thickness of 0.70 ± 0.03mm assuming a value of C_{2L} =1400ms^{-1} typical of oils (Kaye and Laby 1973). Some caution is required if such results are analysed by Fourier techniques as the main spectral peak may not correspond to $1/\Delta t$ but rather $1/2\Delta t$, the reason being successive polarity inversion at the oil/air interface which doubles the apparent periodicity.

$$\tau = \frac{4\Delta D}{C_{2L}}$$

producing a spectral peak at

$$f = \frac{C_{2L}}{4\Delta D} \qquad 5.2$$

An account of the application of laser ultrasonics to measurements of this kind has been given previously (Dewhurst et al 1980).

The relative acoustic impedance of the overlay can be found by comparing the amplitudes of the signals. Substituting for R_{12} and T_{21} from equations 2.18 and 2.19 taking R_{23} = -1, gives

$$\frac{D_o}{D_1} = \frac{1 + R_{12}}{-T_{12}.T_{21}} = - \frac{z_1 + z_2}{2z_1}$$

or,

$$\frac{z_2}{z_1} = - \left(\frac{D_1 + 2D_o}{D_1}\right)$$

while division of successive multiple reflections yields

$$\frac{D_n}{D_{n+1}} \quad n \geq 2 = - \frac{1}{R_{21}} = \frac{z_2 + z_1}{z_2 - z_1}$$

or,

$$\frac{z_2}{z_1} = \frac{D_{n+1} + D_n}{D_n - D_{n+1}}$$

Given a knowledge of z_1, z_2 may thus be readily deduced. Substituting from Table 5.5 indicates $z_2 = 0.18 \pm 0.09\ Z_1$ from D_0/D_1, or, $0.12 \pm 0.06\ z_1$ from D_2/D_3. Both results are in agreement with a value of $z_2 = 0.08\ z_1$ calculated from accepted impedance values.

If the thickness of the film is reduced further, detector resonances may not have sufficient time to decay away between multiple reflections, and so the various pulses may not be fully resolved. Moreover, a resonance condition may be excited when the spectral peak described above corresponds to the resonant frequency of the detection probe. This is thought to have occurred in the waveform in Figure 5.19(a) where a thinner oil film was used. It shows a steady increase in the detected signal as successsive reflected pulses arrived in phase with the detector response, so building up the detected amplitude which then decayed away in an apparently extended resonance. The constraining layer reflections provided a resonant excitation wavetrain. Substituting f = 5MHz back into the equation 5.2 for the spectral peak, indicates a resonant film thickness of $\approx$ 70μm.

If the thickness was reduced further to a mere smear, all the waves effectively arrived within the initial stages of the detector response and so completely lost their individual identity. They still produced an enhancement but at a reduced level with a resultant waveform closely resembling that for the deep constraining layer; Figure 5.19(b). Under these conditions, it was also possible to obtain a surface Rayleigh waveform which was not perceptible with the thicker, highly damping oil layers. The resultant waveform in Figure 5.20 was obtained with the 3MHz

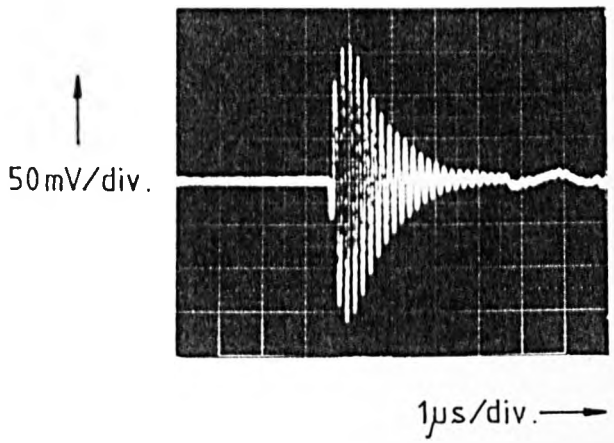

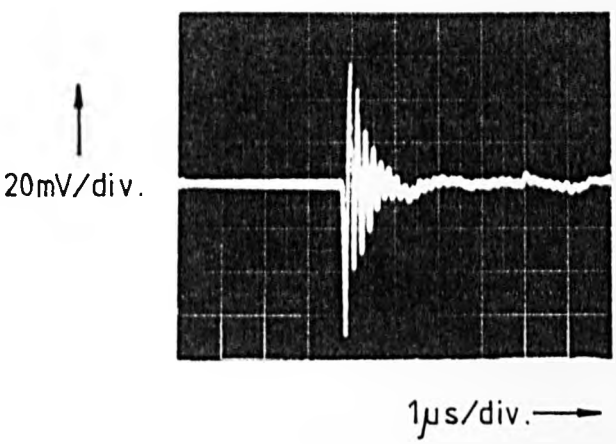

FIGURE 5.19: Bulk waveforms by thin constraining layers of oil. Multimode laser pulses on aluminium with 5MHz L-PZT detector.

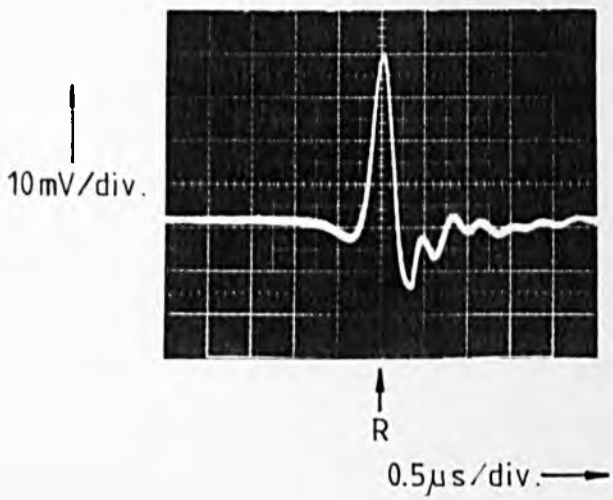

FIGURE 5.20: Details of the Rayleigh pulse produced by a thin constraining layer of oil ($D \ll 1mm$). 3MHz wedge probe on aluminium sample irradiated with multimode pulse.

Expanded time base.

wedge probe. It bears little resemblance to the free surface waveform in Figure 5.10, having lost its dipolar profile and instead become largely monopolar.

It should be noted that in the case of thin films producing the waveforms in Figures 5.19 and 5.20, the oil may be ablated during irradiation. This is not thought to be thermally driven but rather may be the result of mechanical or acoustic spallation due to the sudden upwards motion of the surface. In Chapter 7, it will be shown that the surface acceleration and subsequent deacceleration are in the order of $10^8 ms^{-2}$.

5.11 Directional beams of Rayleigh wave pulses

In general, an ultrasonic source with an extended geometry will have directional emission characteristics. The source shape produced by an unmodified laser beam is essentially a thin circular disc. This would be expected to impose some forward directivity on bulk wave emission but not the Rayleigh waves which would be emitted omnidirectionally. Highly-directional beams of Rayleigh pulses can, however, be generated by focusing the laser pulse in such a way as to form a line source.

The basic arrangement shown in Figure 5.21, comprised a standard metal target irradiated on axis with a multimode beam using a f = 50mm cylindrical lens, so forming a laser line approximately 4 × 0.1mm. In order to prevent surface vaporisation and keep the generation in the low intensity, non-destructive regime, the laser energy was filter-reduced to 5mJ. The metal target together with an integral 3MHz L-PZT edge probe, could be rotated as a unit about a pivot in the base, so providing a convenient means of studying the directional characteristics through a full 360° without incurring transducer bonding errors.

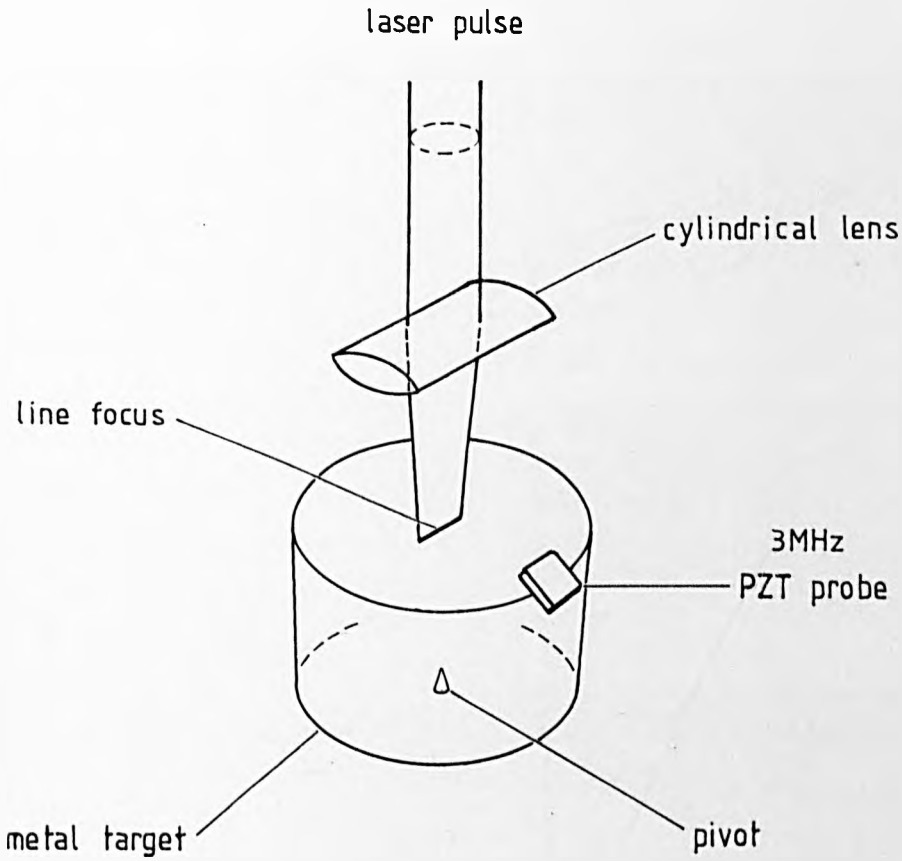

FIGURE 5.21: Experimental arrangement for generation and detection of directional beams of Rayleigh waves.

Broadside to the line source, in acoustic terms ≃ 4λ long × λ/10 wide, the Rayleigh pulse amplitude reached a well-defined maxima, as shown by the series of waveforms in Figure 5.22, detected at various angles, θ, to the line normal. The complete angular variation of the probe output expressed as the peak-to-peak amplitude, is presented as a directivity pattern in Figure 5.23. For comparison, the results are also given for a multimode beam partially focused down to a circular ≃ 1mm diameter spot using a spherical lens. Clearly, line focusing not only produces highly directional broadside beams but also enhances the maximum amplitude by ≃ ×3.

The transition between the two extremes of a long-line and point source is illustrated in Figure 5.24. These patterns were obtained by limiting the line length to 2.3mm (2.2λ), 1.1mm (1.1λ), and 0.8mm (0.8λ) using slotted stops.

Reducing the laser energy further whilst proportionally decreasing the Rayleigh amplitude, did not significantly affect the directional characteristics. This is demonstrated in Table 5.6 where the angular widths of directional beams produced by a 4mm long line source are apparently independent of laser energy.

Mild steel and brass targets produced similar directivities (Figure 5.25) though the beams were particularly directional in brass. In the case of an unstopped line, the angular widths (full-width half-height) were 17 ± 1° (steel) and 12 ± 1° (brass).

To understand these directional characteristics, the laser source may be considered as a linear array of instantaneous point sources. On this basis, it is clear that broadside to the line, all the component Rayleigh wavelets arrive at a distant point almost simultaneously. This produces a very brief, high amplitude δ(t)-type resultant pulse. End on, however,

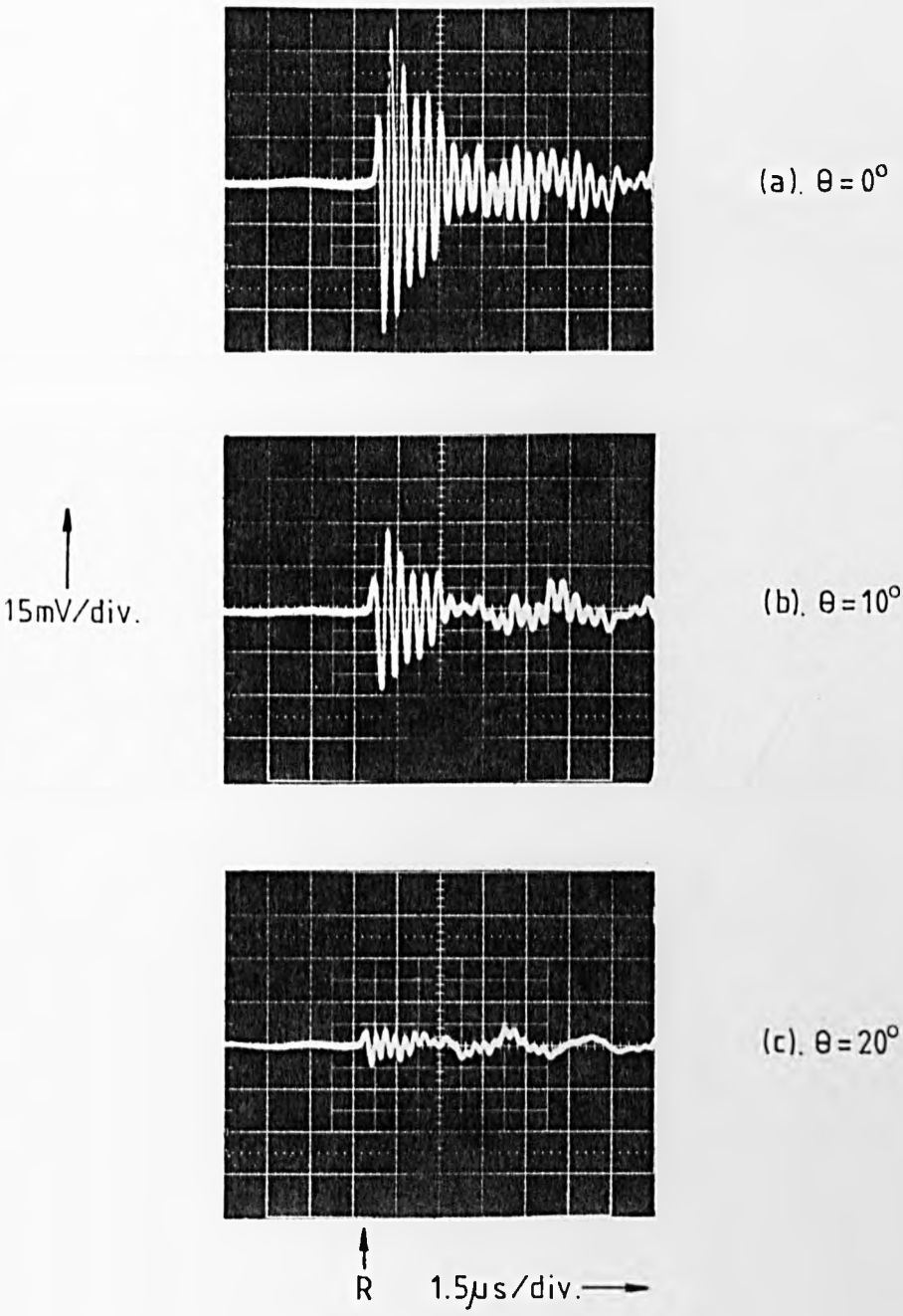

FIGURE 5.22: Output from a 3MHz surface wave probe at various angles, θ, normal to the axis of a 4 x 0.1mm laser line source.

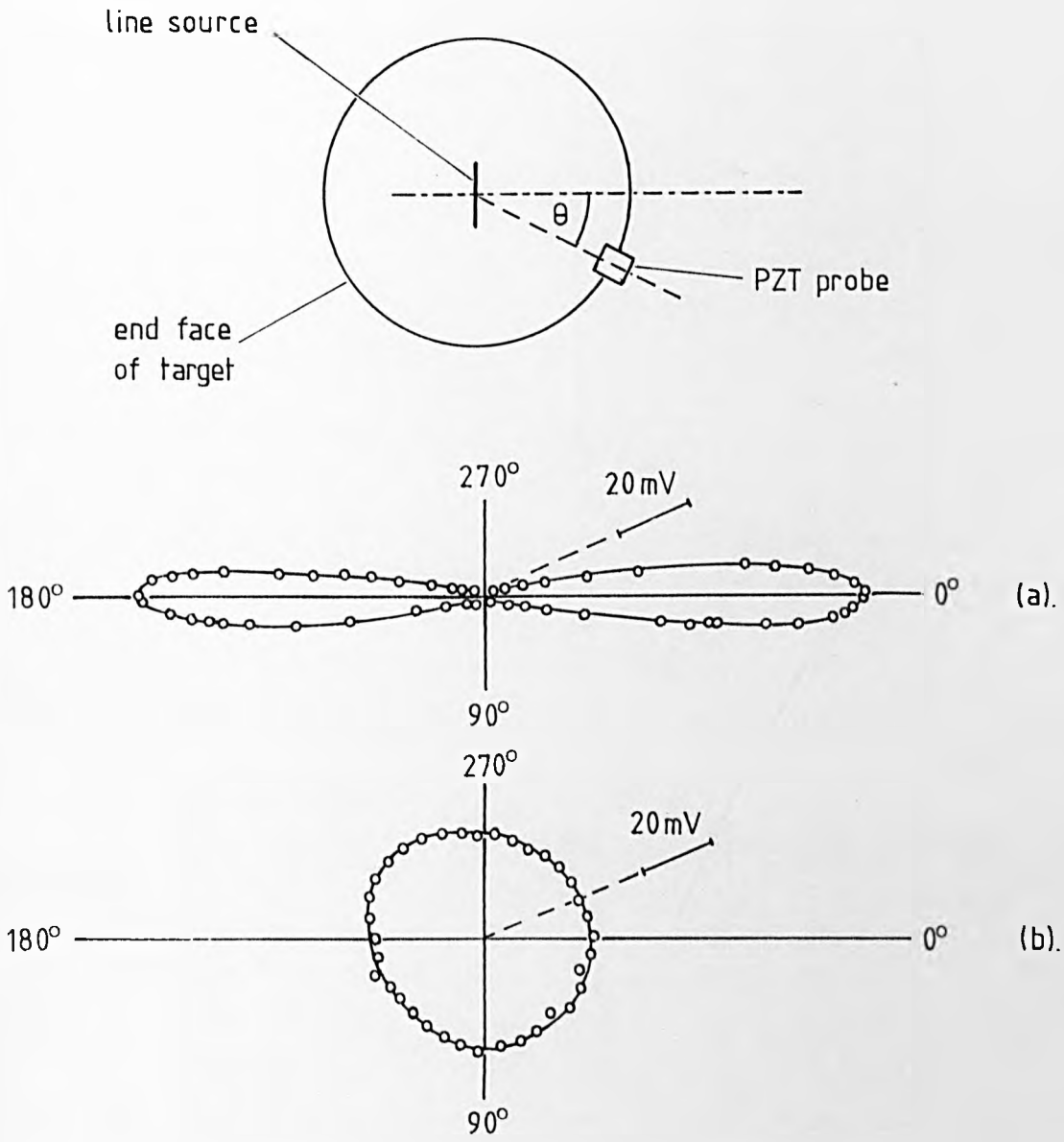

FIGURE 5.23: Directivity patterns in aluminium at 3MHz for

(a). 4 x 0.1mm line source (cylindrical lens)

(b). 1mm diameter spot (spherical lens)

Laser pulse energy ≈5mJ in both cases.

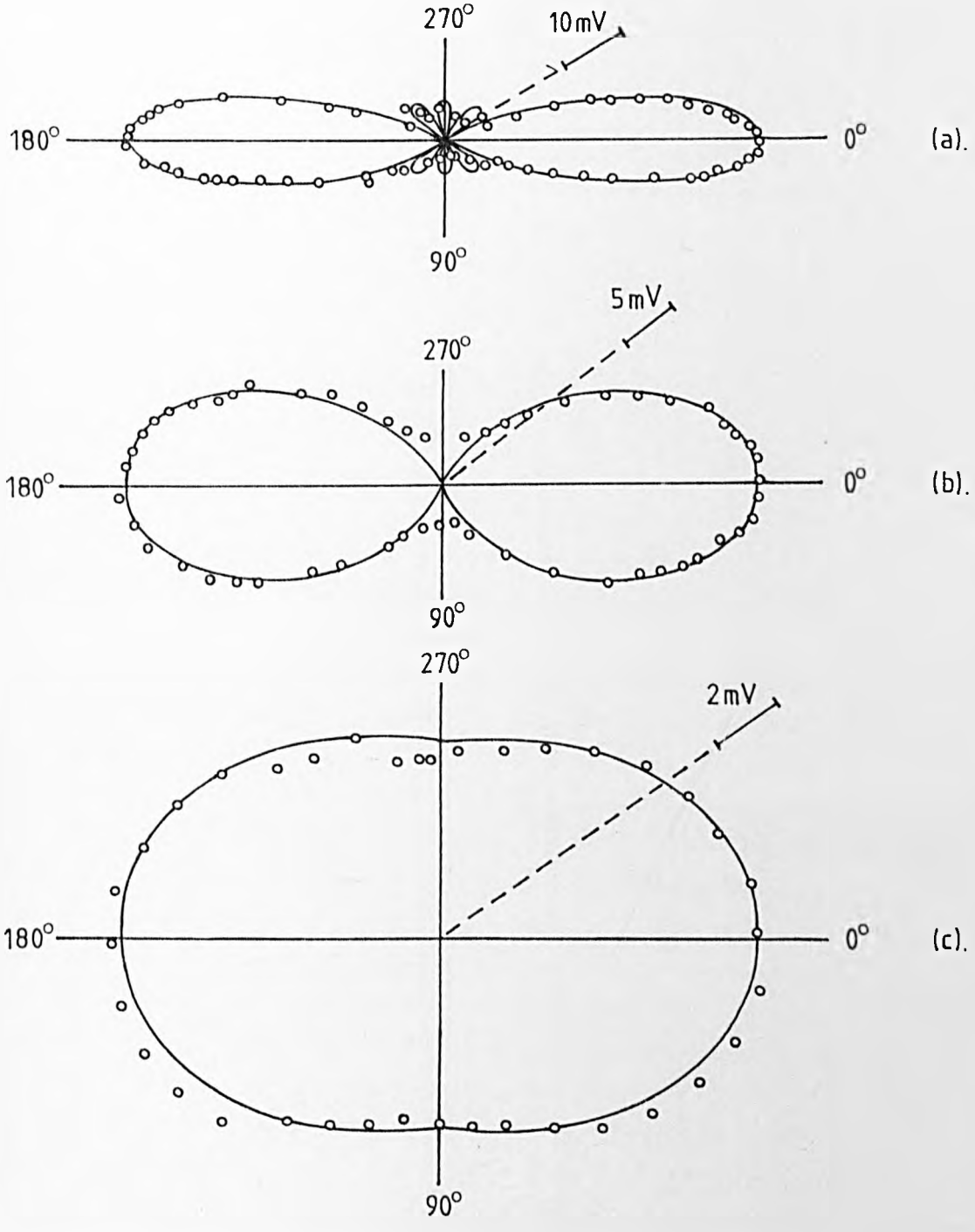

FIGURE 5.24: Directivity patterns in aluminium at 3MHz for different line lengths, l. The points are experimental for estimated line lengths of (a). l = 2.3mm, (b). l = 1.1mm and (c). l = 0.8mm produced by laser pulses containing ≤5mJ. The curves are best-fit theoretical patterns (see text) normalised to experiment at $\theta = 0^\circ$ using values of (a). l = 2.4mm, (b). l = 1.1mm and (c). l = 0.65mm.

Laser energy (mJ)	9	5	2	1	0.5
Beam width (± 1°)	17	19	18	17	18

TABLE 5.6 : Variation in Rayleigh wave beam width (full-width half-height) with laser energy.

4 × 0.1mm line source on an aluminium sample.

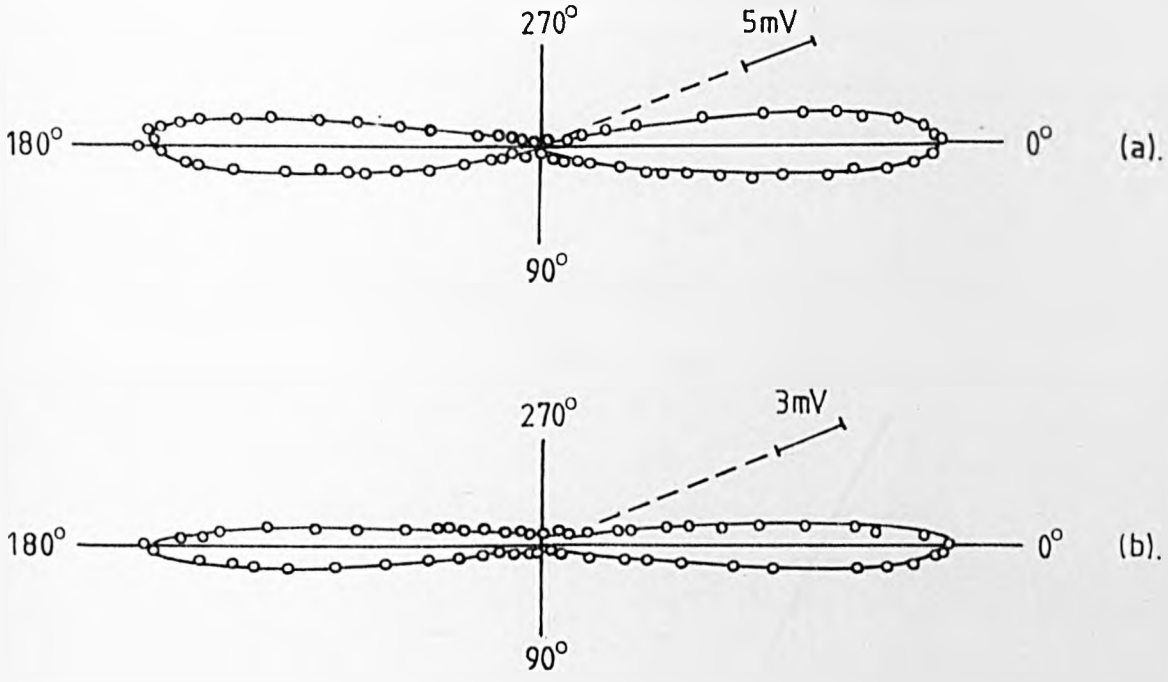

FIGURE 5.25: 3MHz directivity patterns produced by a 5mJ, 4x0.1mm line source in

(a). mild steel.

(b). brass.

there is a maximum of delay and the resultant pulse is both lower in amplitude and broadened in time, and consequently comparatively poor in the high frequency components, hence the directivity; Figure 5.26.

To a first approximation,the duration of the resultant pulse, Δt ,is given by the Rayleigh wave transit time of the line length projected in the detector direction

$$\Delta t = \frac{\ell \sin\theta}{C_R}$$

where ℓ = line length

Assuming the line is uniformly irradiated, the pulse amplitude is inversely related as

$$h = \frac{A}{\Delta t} = \frac{AC_R}{\ell \sin\theta}$$

where A = total area under all the wavelets, ie. a constant independent of θ.

The top hat function this defines, may be readily fourier transformed to show that the normalised angular variation in the amplitude of a frequency component, f, is given by

$$R_\theta = \frac{\sin\left((\pi \ell f/C_R)\ \sin\theta\right)}{\left((\pi \ell f/C_R)\ \sin\theta\right)}$$

This has the same form as the directivity for a cw acoustic line source in an infinite homogeneous medium (Olson 1974). This is expected since the pulsed and cw cases are fourier transforms of each other.

The expression for R_θ may be directly compared with the experimental results taking f = 3.0MHz, the resonant frequency of the probe. In Figure 5.27, R_θ has been calculated for the conditions encountered in

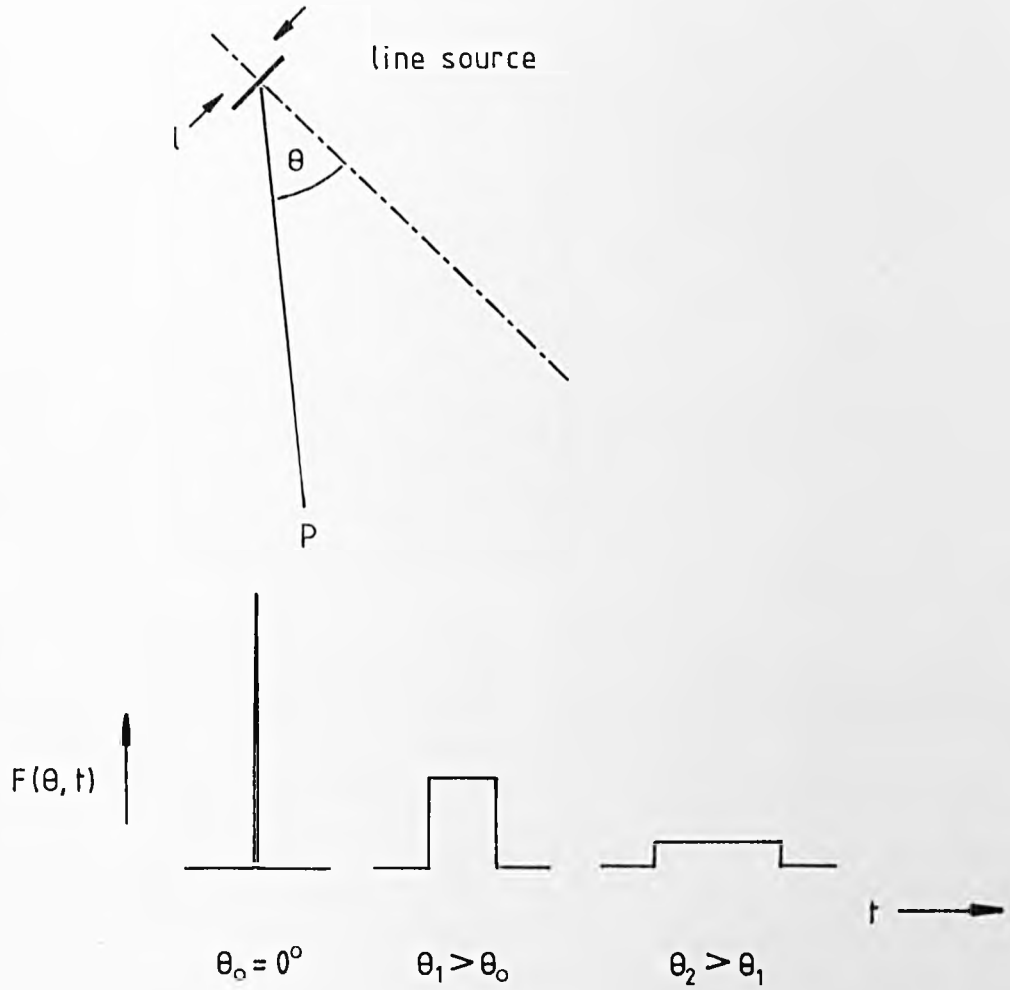

FIGURE 5.26: Idealised surface acoustic waveforms at various angles to a pulsed laser line source.

Broadside on, all the components arrive almost simultaneously producing a brief, high-amplitude pulse. End on, there is a maximum of delay resulting in a broad, low-amplitude waveform.

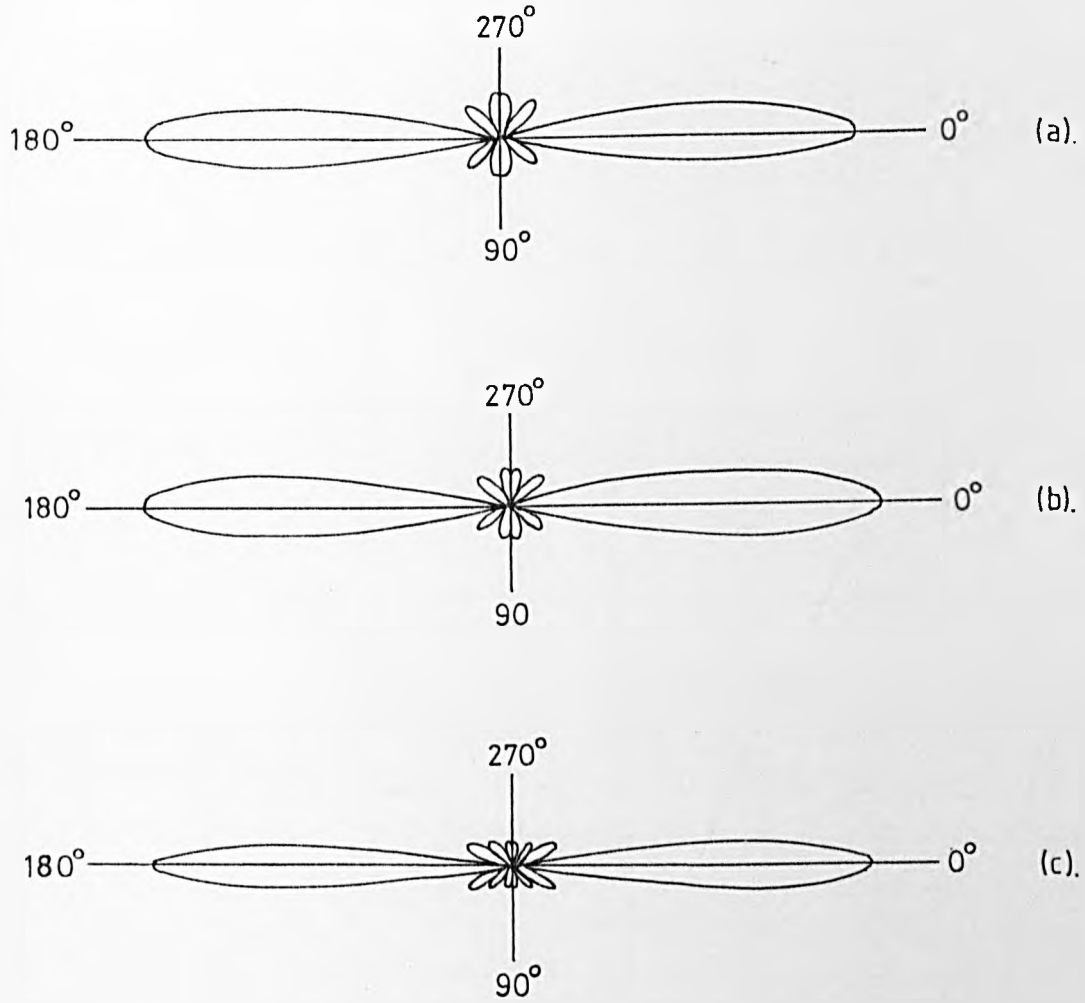

FIGURE 5.27: Theoretical directivity patterns (equation 5.6) for a 4mm line source at 3MHz in

(a). aluminium

(b). mild steel

(c). brass

Figures 5.23(a) and 5.25 assuming ℓ = 4.0mm and C_R = 2906ms^{-1} (aluminium), 2996ms^{-1} (mild steel) and 1964ms^{-1} (brass). The directivity is particularly narrow in brass due to the lower propagation velocity which extends the length of the line from $\simeq 4\lambda$ to 6λ. The theoretical curves defined by R_θ are directly compared with experimental points for different line lengths in Figure 5.24. The agreement is generally good. Any significant deviations are confined to secondary lobe regions. Figures 5.23(a) and 5.25, for example, show no side lobes whilst 5.24(a) does. The probable reason for this is that in the former cases, the beam was unstopped producing a source profile with tapered ends. Such an effect is well known to reduce side lobe amplitudes (Olson 1974).

5.12 Discussion

The low intensity (unfocused) laser source has been shown to generate a variety of both bulk and surface ultrasonic waveforms depending on spot diameter and surface conditions. The ultrasonic amplitudes vary linearly with laser intensity and are directly proportional to the optical absorptivity of the target surface, the hallmarks of being driven by thermal expansion. At a free surface, the source is characteristically shear but under surface constraint becomes strongly longitudinal. The uniform irradiation model which considers normal thermal expansion only, gives a good description of the constrained surface source. At a free surface, however, the model fails, predicting neither the dominant shear wave nor the polarity inversion of longitudinal pulse. It has also been shown how the source shape may be tailored by optical techniques so as to produce directional Rayleigh wave pulses.

To help explain the free surface source and the apparent failure of the uniform irradiation model, it is useful to introduce a known reference

source. This comes in the convenient form of the capillary breaking source (Beckenbridge 1975); Figure 5.28. The basic technique was to hold a capillary 0.5mm in diameter drawn from soda glass at ≈ 70° to the sample surface and gradually load it by hand until in a sudden release of stress, it fractured. Over ultrasonic time scales, this produced an approximate step stress-relieving surface pulse. The resultant ultrasonic waveforms are shown in Figures 5.29 (a) and (b) for the bulk (5MHz L-PZT) and Rayleigh pulse (3MHz wedge probe) respectively. As a polarity indicator, the bulk waveform may be considered in terms of the directional characteristics in Figure 5.30, which are for a point monopolar force acting within an extended solid bulk. From elementary considerations, it is clear that longitudinal waves are launched in the force direction as a compression and rearwards as a rarefaction whilst shear waves are radiated tangentially. This allows the longitudinal pulse in Figure 5.29(a) to be identified as a rarefaction. Moreover, in so doing, it has also established that in all waveforms obtained using L-PZT in this configuration, positive going pulses are associated with rarefactions and negative pulses with compressions.

Applying this guide to the laser waveforms and to the free surface source in particular, the longitudinal pulse in Figure 5.4(a) can now be identified as a rarefaction. This may seem surprising considering the essentially outward-compressive nature of thermal expansion. It is certainly not in accordance with the compressive-longitudinal uniform irradiation model. To explain this and the dominant shear character of this source, it can be seen from Figure 5.30 that to generate relatively strong shear waves the generating forces must be normal to the propagation direction. Clearly, in a free surface thermoelastic source, the principle forces must act tangentially to the surface, a view previously expressed by

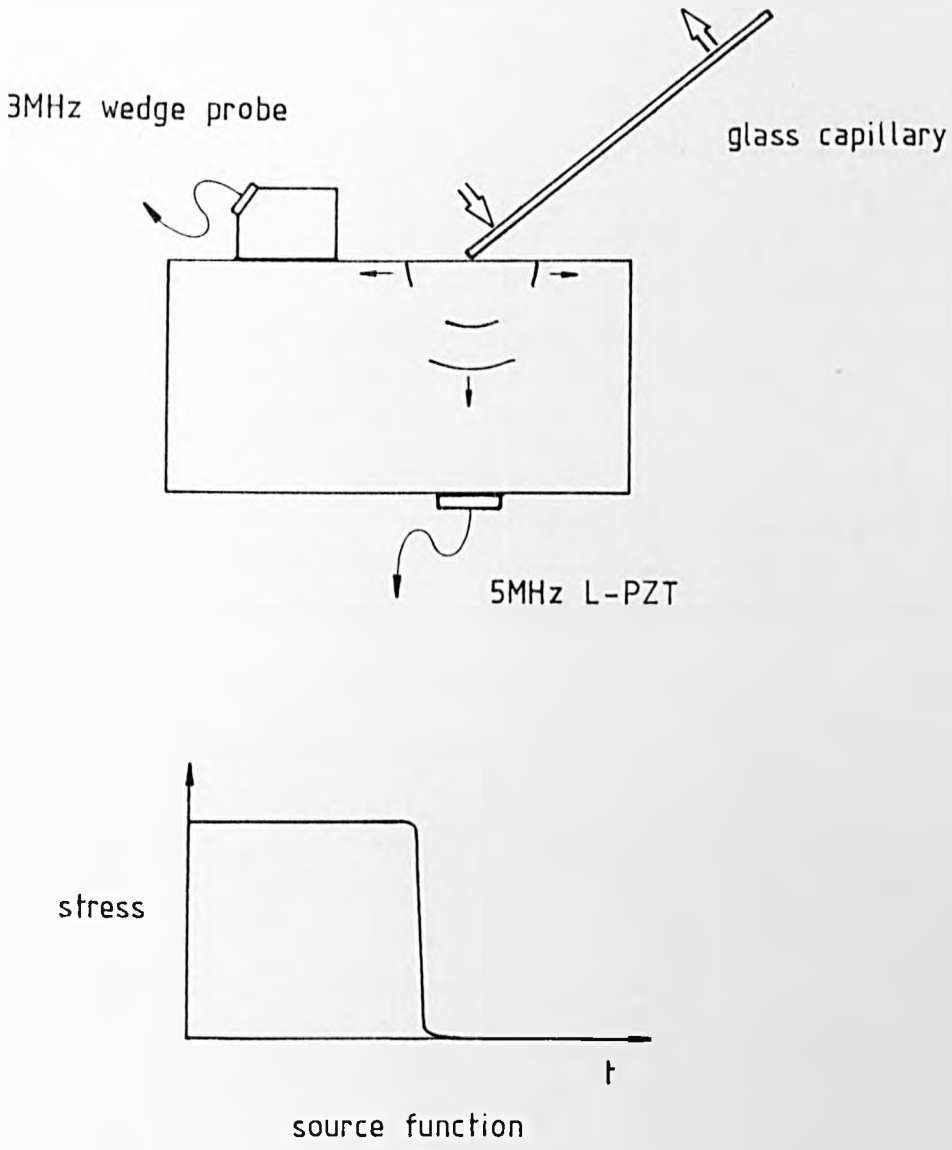

FIGURE 5.28: The capillary-breaking ultrasonic source. Gradual loading followed by fracture produces an approximate step stress-relieving pulse.

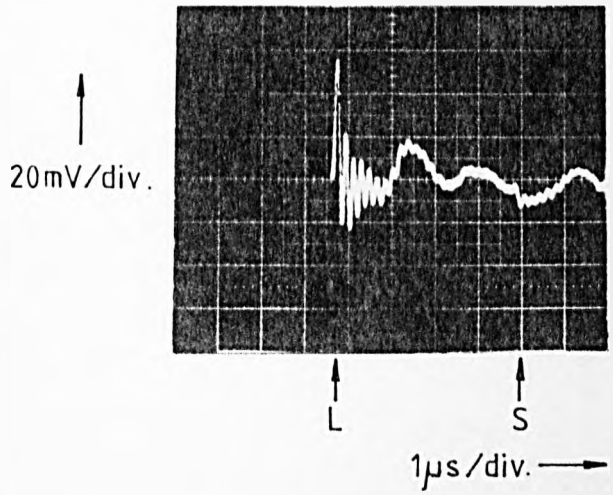

(a). Bulk waveform
(4MHz L-PZT)

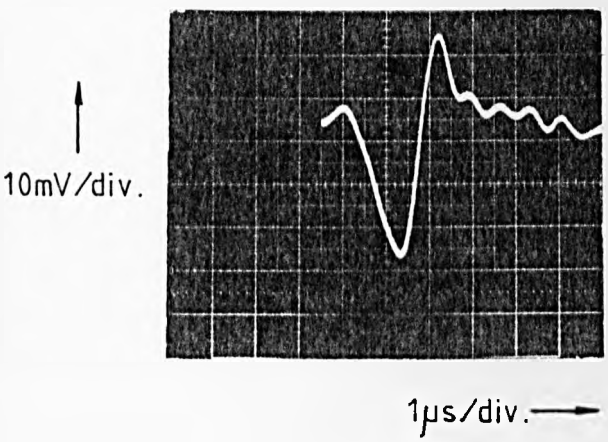

(b). Rayleigh waveform
(3MHz wedge probe)

FIGURE 5.29: Ultrasonic waveforms produced by the capillary-breaking source.

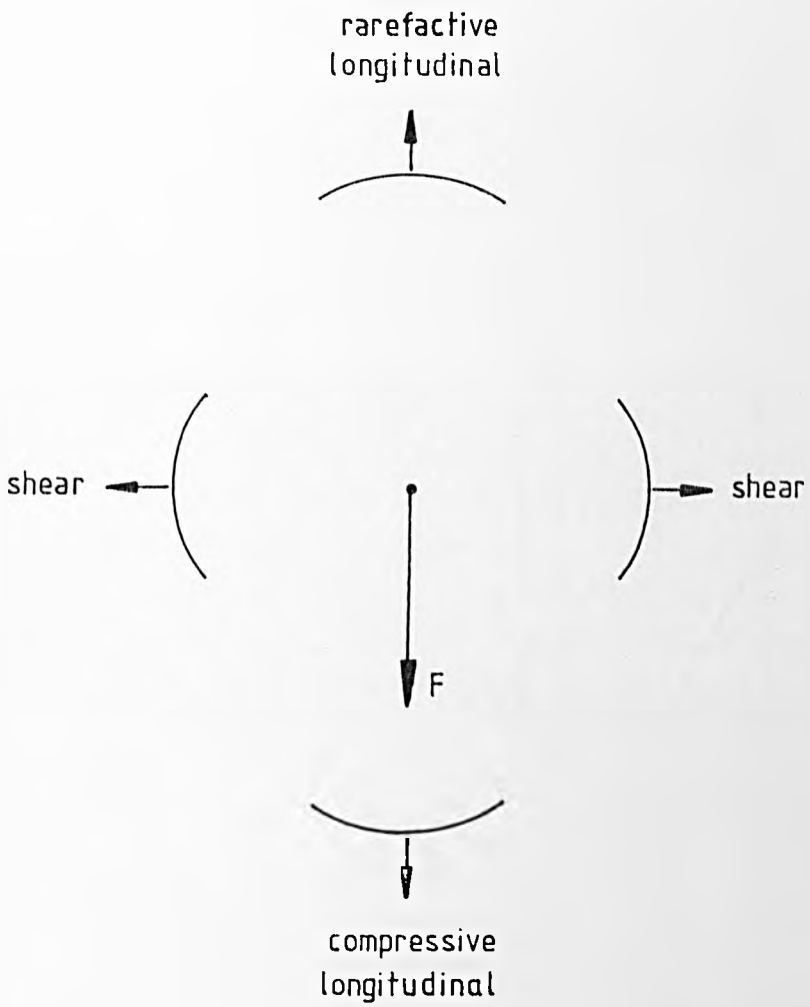

FIGURE 5.30: Directional emission of bulk waves due to a point force within an extended medium.

Scruby et al 1980. This is not unreasonable. The theory in Sections 4.8 and 4.9 showed precisely how weak normal thermal expansion was as an acoustic source at a free surface, and yet, lateral thermal stresses though relatively unaffected by the freedom to expand in normal directions, were not considered because no sidewards movement resulted due to symmetry. Over a finite source area, however, they may become active as expansion takes places against the constraint of surrounding cooler metal, so producing a shearing motion. The result will be a net outward force distribution giving the source a radial-shear character; Figure 5.31(a). Normal thermal expansion will take place virtually stress free upwards provided in the terms of Section 4.9, the laser pulse is not ultra short, $t_p >> \delta_{TP}/C_L$, typically >> 15ps. The resultant bulk ultrasonic waveforms will consequently possess a strong shear but weak longitudinal character. Furthermore, this shearing motion may be expected to launch a rarefactive longitudinal pulse into the bulk by a Poisson's ratio type effect. This understanding of the source is certainly borne out by the Rayleigh wave results which indicated a correlation with its width rather than thickness as emphasised by the uniform irradiation model. In this respect, it is tempting to suggest that of the two opposed pulses of which the Rayleigh waveform is composed, the earlier one is due to the net force acting tangentially outwards on the near side of the laser spot towards the detector, and the other to more distant forces acting on the far side in the opposite direction.

The physical origin of the dependence of ultrasonic pulse duration on spot diameter is perhaps now clearer. If the principle forces are taken as acting tangentially on or near the edges of the laser spot, it can be seen from Figure 5.32 that at a distant point, the duration of an ultrasonic pulse, or, in the case of a step waveform, the rise time, will

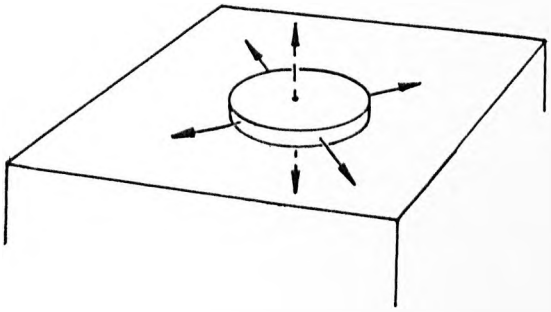

(a). Free surface; normal expansion takes place almost stress-free in an upwards mechanical motion whilst sidewards expansion is constrained by surrounding cooler metal, resulting in a radial-shear force distribution.

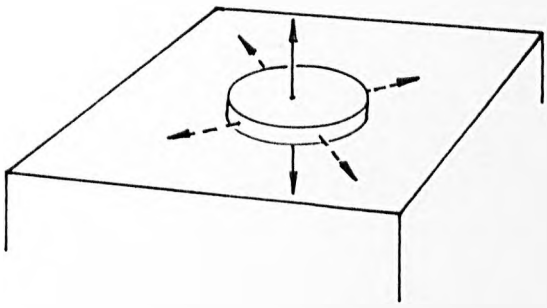

(b). Constrained surface; normal thermal stresses develop by expansion against overlying medium, producing a strongly longitudinal-compressive source.

FIGURE 5.31: Force distributions in the two basic forms of the thermoelastic laser acoustic source in metals.

In the case of ultra-short laser pulses, typically $t_p \leq 15ps$, normal thermal expansion may also become important at a free surface for reasons outlined in Section 4.9.

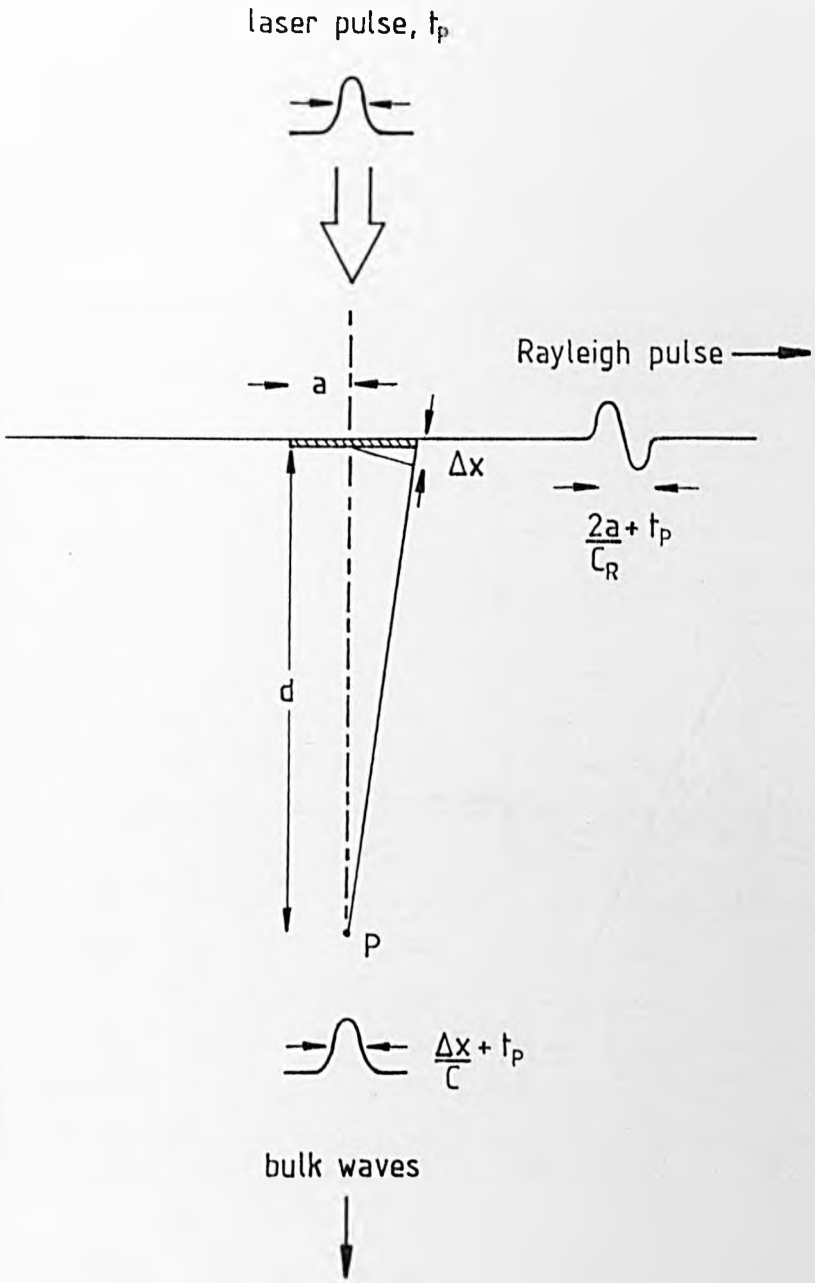

FIGURE 5.32: Approximate duration of acoustic pulses as given by a combination of geometrical delay and laser pulse duration.

If $d \gg a$, then $\Delta x \approx \frac{a^2}{d}$.

be given approximately by the summation of two terms; first, the geometrical acoustic delay due to the source's spatial extent, and secondly, the temporal duration of the driving mechanism behind the source, ie. the laser pulse duration,

$$\Delta t_R \simeq \frac{2a}{C_R} + t_p \qquad \text{Rayleigh wave}$$

$$\Delta t_L \simeq \frac{\Delta x}{C_L} + t_p \simeq \frac{a^2}{dC_L} + t_p \qquad \text{longitudinal wave}$$

$$\Delta t_S \simeq \frac{a^2}{dC_S} + t_p \qquad \text{shear wave}$$

where a = radius of laser spot

t_p = laser pulse duration

d = source/detector distance (sample thickness)

Under typical conditions, t_p = 25ns, $a = 10^{-3}$m, $C_R = 3{,}000\text{ms}^{-1}$, $C_L = 6000\text{ms}^{-1}$, $C_S = 3{,}000\text{ms}^{-1}$ and $d = 25 \times 10^{-3}$m, this gives

Δt_R = 690ns

Δt_L = 30ns

Δt_S = 38ns

In the case of Rayleigh pulses, the duration is largely determined by the spatial term ($t_p \ll 2a/C_R$); hence the strong direct correlation of the wave's physical length with spot diameter. In contrast, the duration of both types of bulk wave is limited by the laser pulse duration, spatial broadening being secondary. Moreover, for a typical PZT probe with a resonant frequency of 5MHz corresponding to a rise time of ≈ 50ns, the bulk waveforms will not be fully resolved. Despite a changing spot size, the source geometry, a point source in effect, remains approximately constant. The bulk waveforms would consequently be expected to be relatively independent of spot diameter.

At a constrained surface, the effect of the shear stresses will be reduced but significant normal thermal stresses may be developed as expansion in this direction becomes trapped between the overlay and underlying target bulk; Figure 5.31(b). The result is what can now be definitely identified as the strong compressive longitudinal/weak shear waveform in Figure 5.15. The uniform irradiation theory is now appropriate and gives the good source description as typified by the finite thickness overlay results.

Thus, two basic models of the laser thermoelastic source are suggested. In both, the ultrasonic pulses are generated by sudden thermal expansion due to transient laser heating but in one case against the self-imposed constraint of surrounding cooler metal (free surface) and in the other that externally provided by an overlying medium (constrained surface). The free surface source is discussed at greater length in Chapter 7.

CHAPTER 6

Resonant Probe Study of Ablation Generation in Metals

6.0 Introduction

A fundamentally different laser acoustic source may be generated by ablating surface material. This material may be either target material itself or some applied sacrificial coating.

6.1 Plasma-ablation generation

If the laser intensity is increased by focusing, the interaction with the metal surface undergoes a profound transformation. The local incident intensities may be so great as to cause surface metal not only to melt but also to vaporise and ionise. The result is a dense, hot plasma which while tending to shield the surface from further direct laser interaction, expands explosively away from the surface in a plume, leaving behind a small crater due to material ejection; Figure 6.1.

Bulk ultrasonic waveforms obtained under these plasma-ablation conditions, are typified by those in Figure 6.2 which were produced by a fully focused (f = 20mm) multimode pulse incident on a standard aluminium sample.

The first waveform was obtained at a filter-reduced pulse energy of 1.6mJ on the threshold of formation of a plume visible to the naked eye. The second waveform was produced by a full energy (45mJ) pulse resulting in an intense plasma plume. In both cases, the detector was 5MHz L-PZT. The dominant feature is the longitudinal pulse, shear generation being very secondary having all but disappeared from waveform (b). In this respect, the waveforms are similar to that for the constraining layer in

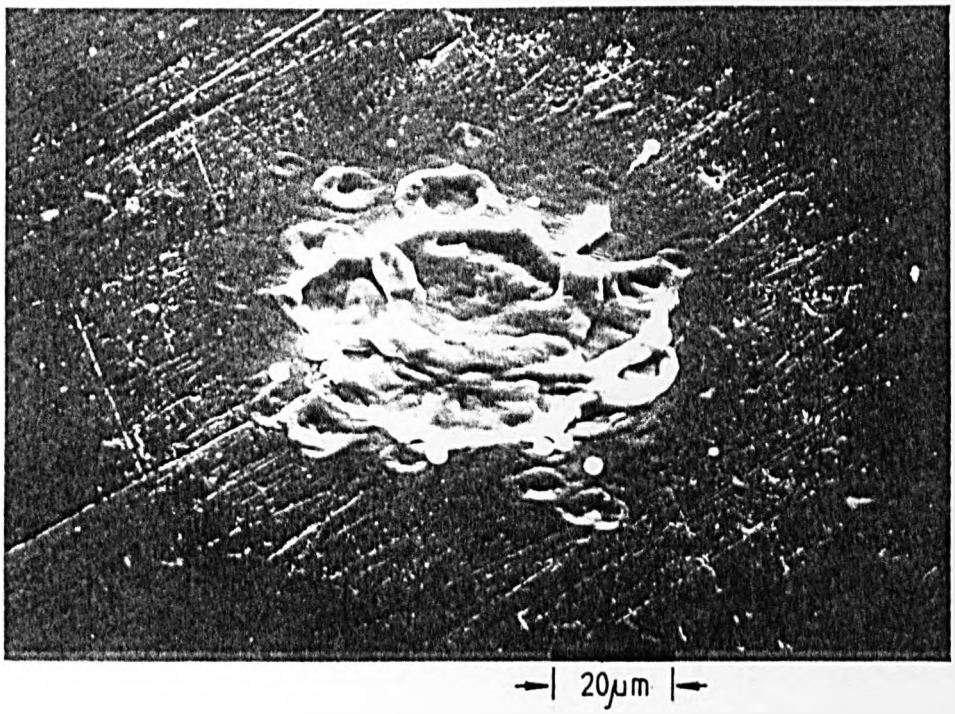

FIGURE 6.1: The melt-lipped crater produced on an aluminium surface by a by a focused (f=15mm) 3mJ single mode Nd:YAG laser pulse. An accompanying plasma forms and expands away from the surface in a plume.

Electron micrograph courtesy Department of Geology, University of Hull.

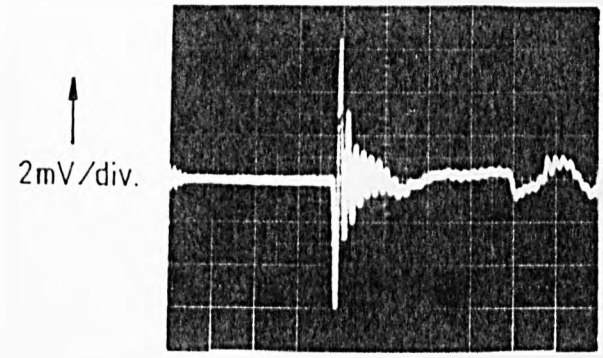

(a). 1.6mJ pulse
(ablation threshold)
5MHz L-PZT

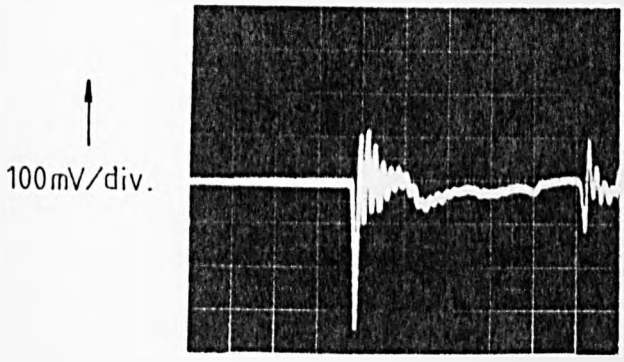

(b). 45mJ pulse
(intense plasma plume)
5MHz L-PZT

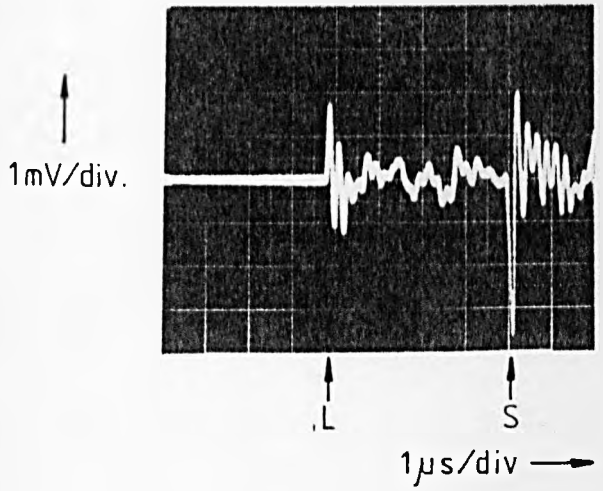

(c). 45mJ pulse
(intense plasma plume)
5MHz S-PZT

FIGURE 6.2: Bulk waveforms produced by a plasma-ablation laser source. Focused (f = 20mm) multimode Nd:YAG irradiation of a standard (25mm thick) aluminium sample.

Figure 5.15. Reducing the laser energy to 0.5mJ proved sufficient to return the waveform to the low intensity, unfocused profile in all respects.

The third bulk waveform (c) was produced under the same conditions as waveform (b) but the detector was 4MHz S-PZT. As expected, this enhances the relative amplitude of the shear signal. It is perhaps the most revealing of the three in that it bears a striking resemblance to the unfocused thermoelastic waveform in Figure 5.4(a) but detected with L-PZT. This directly implies some form of orthogonality exists between the forces acting under these different generating conditions.

The surface waveforms produced by plasma-ablation were also similar to the thin constraining layer waveforms; Figure 6.3. It is essentially a brief monopolar pulse.

6.2 Dependence of ultrasonic amplitude upon laser energy at constant focal diameter

The transition from thermoelastic generation to this plasma-ablation regime, is examined in Figure 6.4 which gives the variation of the bulk wave amplitudes with focused (f = 20cm) laser energy progressively attenuated by neutral density filters. Below the visible plume threshold, the acoustic generation is linear, being thermoelastic. Above the threshold, the longitudinal amplitude increases rapidly while the shear pulse does the opposite rapidly falling to very low comparative levels. The change in amplitudes is of such a magnitude that irradiation with, for example, a low-intensity, non-plasma forming pulse of 500μJ, produces a peak shear signal of 0.5mV, comparable to 0.3mV produced by a high-intensity plasma forming pulse of 45mJ. Over the same range, in contrast, the longitudinal amplitude increases a thousandfold. Clearly,

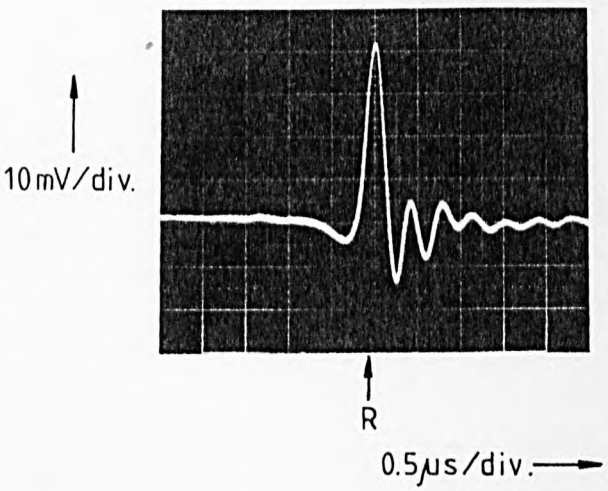

FIGURE 6.3: Details of Rayleigh pulse produced by the plasma-ablation source.

Focused (f=20cm) 45mJ multimode Nd:YAG pulse incident on an aluminium sample together with a 3MHz wedge probe detector. Approximately 10mm between source and front of detector shoe.

Expanded time base.

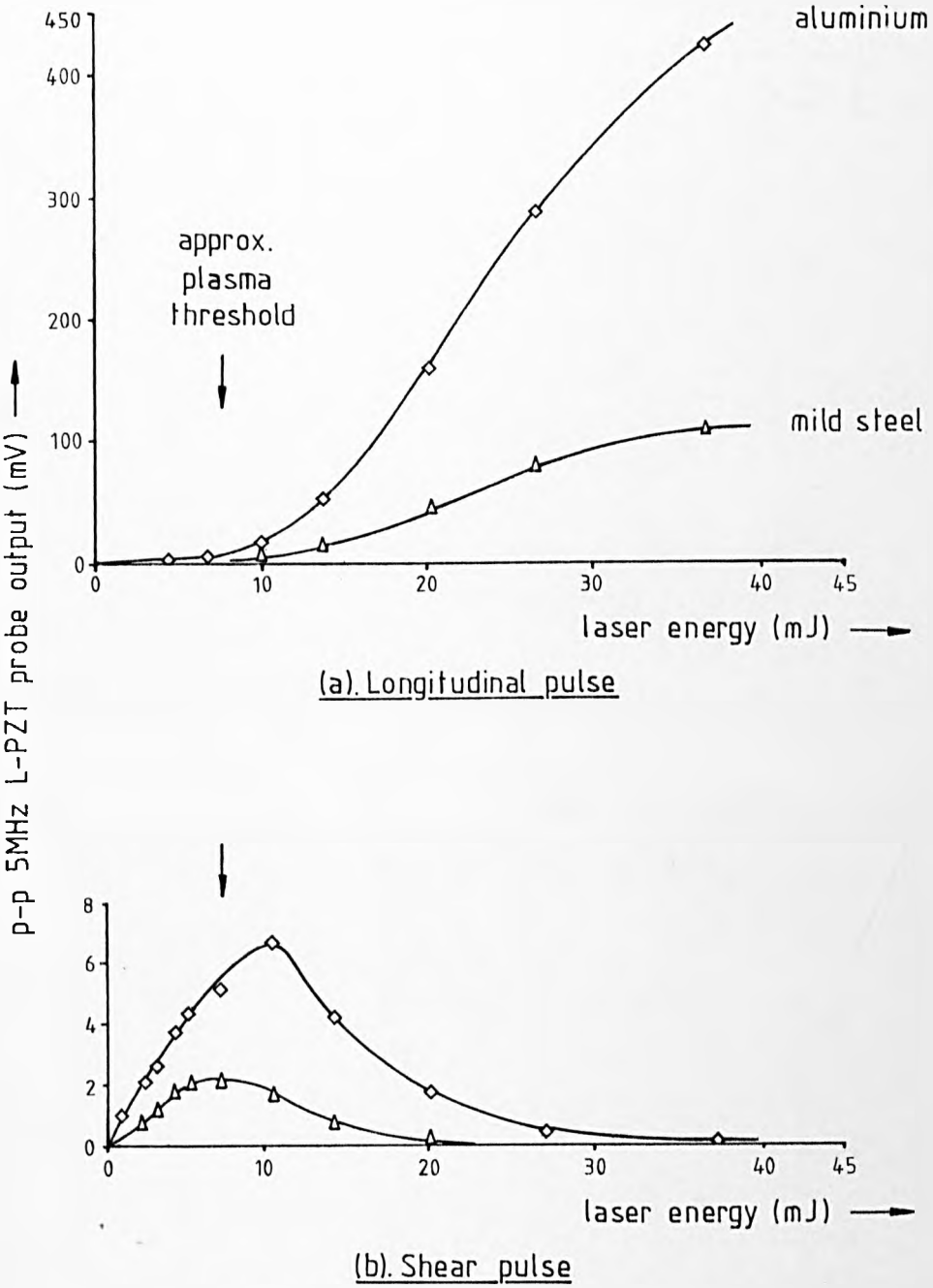

FIGURE 6.4: The variation of bulk wave amplitudes with laser energy at constant focal diameter. Standard (25mm thick) metal targets irradiated with focused (f=20cm) multimode Nd:YAG pulses.

Below the plasma threshold, the generation is linear and characteristically shear, being thermoelastic in nature; above non-linear and dominantly longitudinal.

the creation of a totally different acoustic source.

The amplitude of the surface waves does not show such strong variations with focused laser intesities; Figure 6.5. Both the longitudinal surface and Rayleigh waves show a comparatively steady increase in amplitude with laser intensity. As will be shown later, the longitudinal surface pulse does not even change polarity.

6.3 Ultrasonic amplitude versus spot diameter at constant total energy

An alternative method of studying the transition was to bring the laser gradually into focus by varying the distance, ℓ, between lens and sample, so allowing the intensity to be varied continuously rather than coarse filter-defined steps; Figure 6.6.

The bulk wave results are exemplified by the focused (f = 35mm) 2.5mJ single mode results in Figure 6.7 which gives the variation of the peak-to-peak output produced from 5MHz L-PZT on a standard aluminium sample. The accompanying values for the gaussian beam diameter were calculated assuming a linear reduction with distance to the focal point so

$$a(\ell) = \frac{\ell}{f} . a_o$$

where a_o = gaussian radius of unfocused beam

f = focal length of lens

Near the focus, the diameter will more realistically tend towards the diffraction-limited value of (Patek 1967)

$$2a(0) = f\phi$$

where ϕ = angular divergence of beam

Under present conditions ($\phi \approx 8 \times 10^{-4}$ rad), this indicates an on-focus gaussian diameter of $\approx$ 30μm which corresponds to a peak intensity of $\approx 10^{13}$ Wm^{-2}.

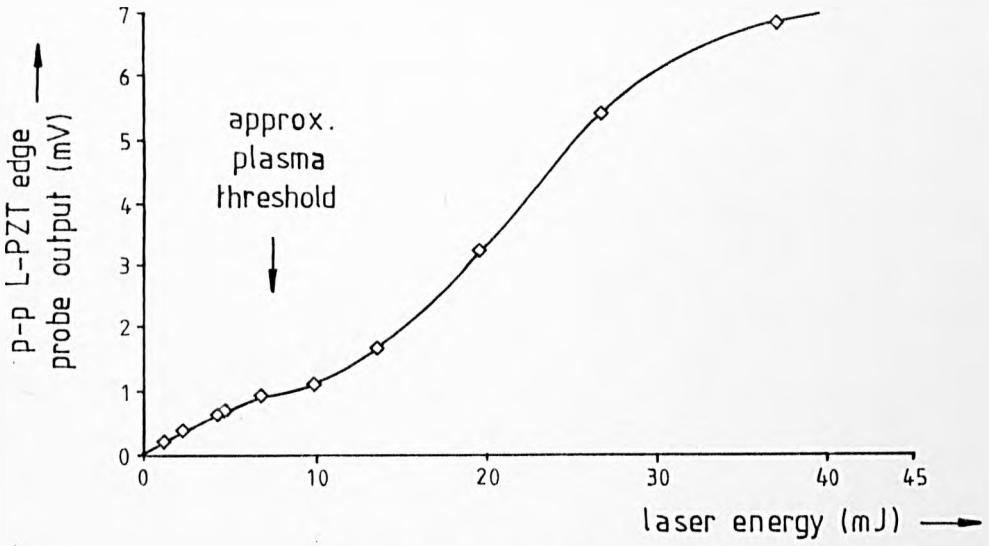

(a). Longitudinal surface pulse

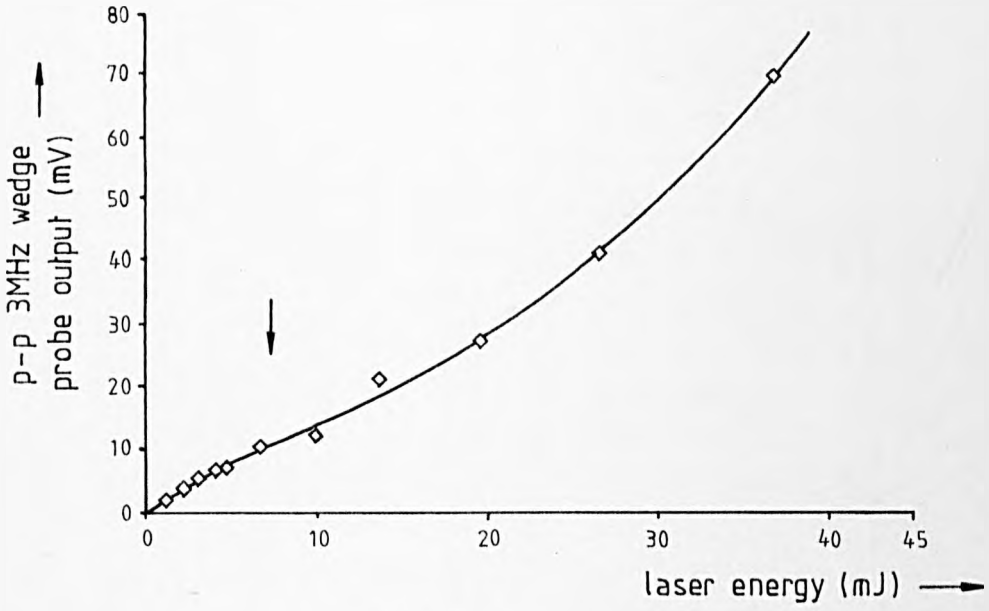

(b). Rayleigh pulse

FIGURE 6.5: The variation of surface wave amplitudes with laser energy at constant focal diameter. Aluminium target irradiated with focused (f = 20cm) multimode Nd:YAG pulses.

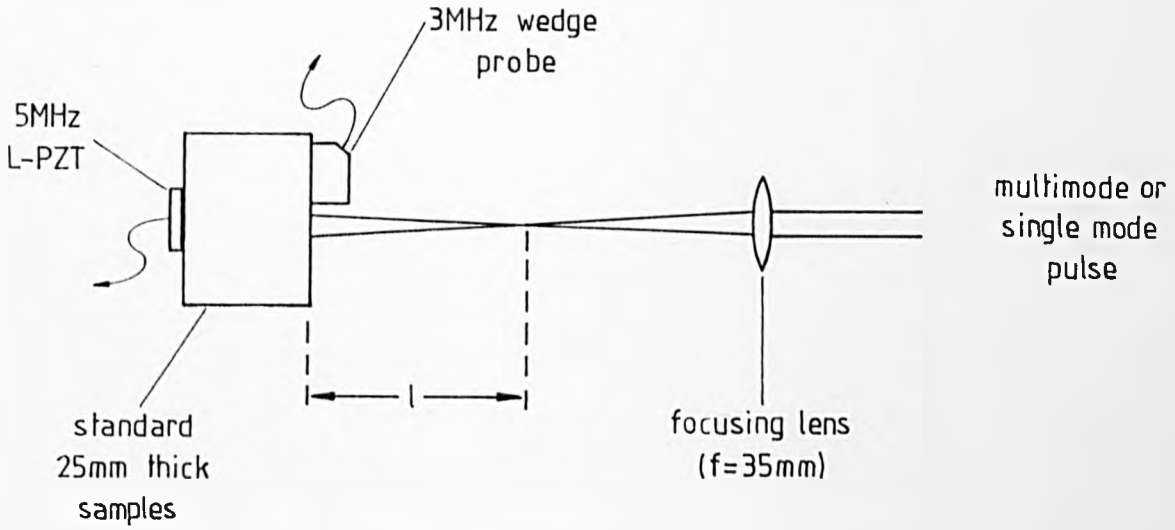

FIGURE 6.6: Arrangement for studying ultrasonic amplitudes versus spot diameter at constant energy ranging from thermoelastic (low intensity) to plasma ablation (high intensity) conditions.

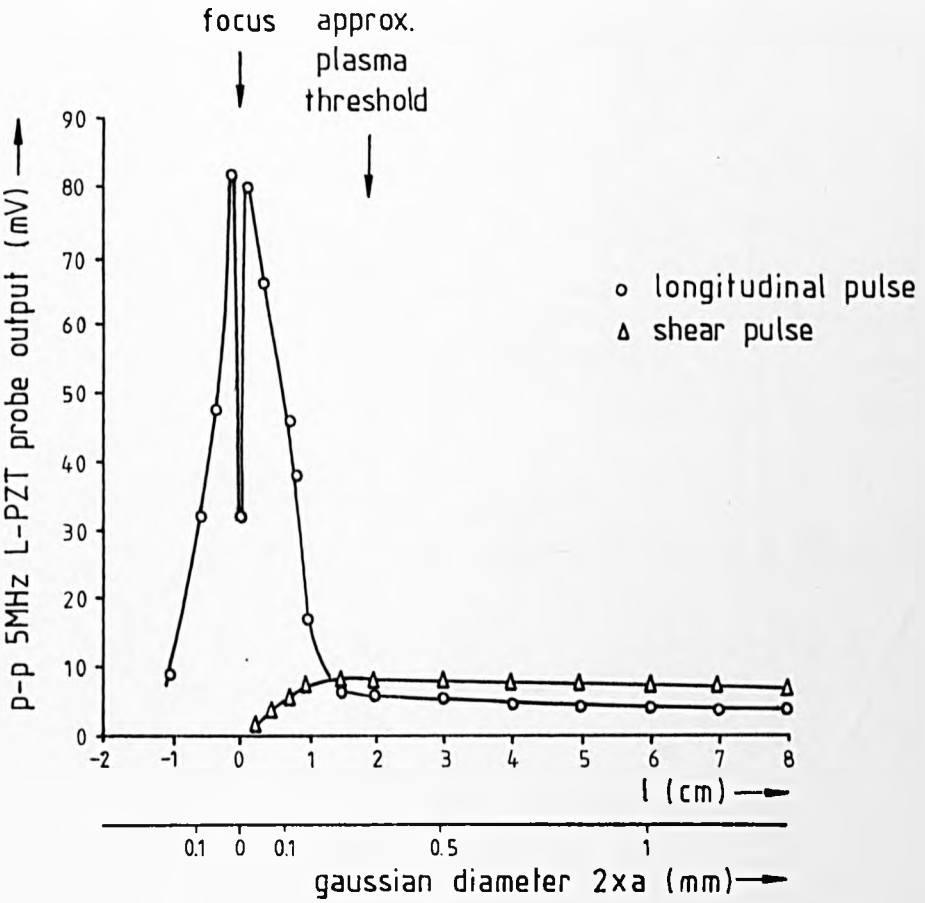

FIGURE 6.7: The variation in bulk ultrasonic amplitude in bringing 2.5mJ single mode pulses into focus (f=35mm) upon an aluminium sample.

Well away from the focus in the low-intensity thermoelastic region both the longitudinal and shear amplitudes are almost independent of ℓ or a. This is expected from Section 5.12 where it was indicated that the spatial extent of the source had little effect on the detected bulk waveforms. Once again, when the plasma threshold is reached, the shear pulse shows a rapid decrease in amplitude while the longitudinal amplitude increases markedly. At focus, however, a new high intensity feature is apparent in the form of a on-focus longitudinal minimum. This feature was fully reproducible and did not appear in Figure 6.4(a) because the required intensities were not reached, a longer focal length lens being used with a broader focus.

The corresponding results for the Rayleigh pulses are given for a multimode and single mode beam in Figures 6.8(a) and (b) respectively. In the low intensity thermoelastic region, the peak ultrasonic amplitude varies roughly as 1/d (1/a), a dependence which is associated with the variation of pulse duration with spot diameter as described in Section 5.8. Near the focus both sets of results are also similar in showing a marked increase in amplitude immediately prior to the previously observed on-focus minimum. In the vicinity of the transition region at $\ell \simeq 7$ mm , however, there is an obvious difference. The single mode plot reveals a well-defined minimum while the multimode results only show what is possibly a small corresponding plateau region. The origin of this difference is thought to lie in the different beam mode patterns and focusing properties. A single mode beam maintains its uniquely smooth gaussian profile, and has a well-defined focal point. The multimode beam by its nature is composed of a number of spatial modes, and so its profile consequently changes continually along the optic axis of the laser, giving a more extended focal region. Consequently, the resultant multimode

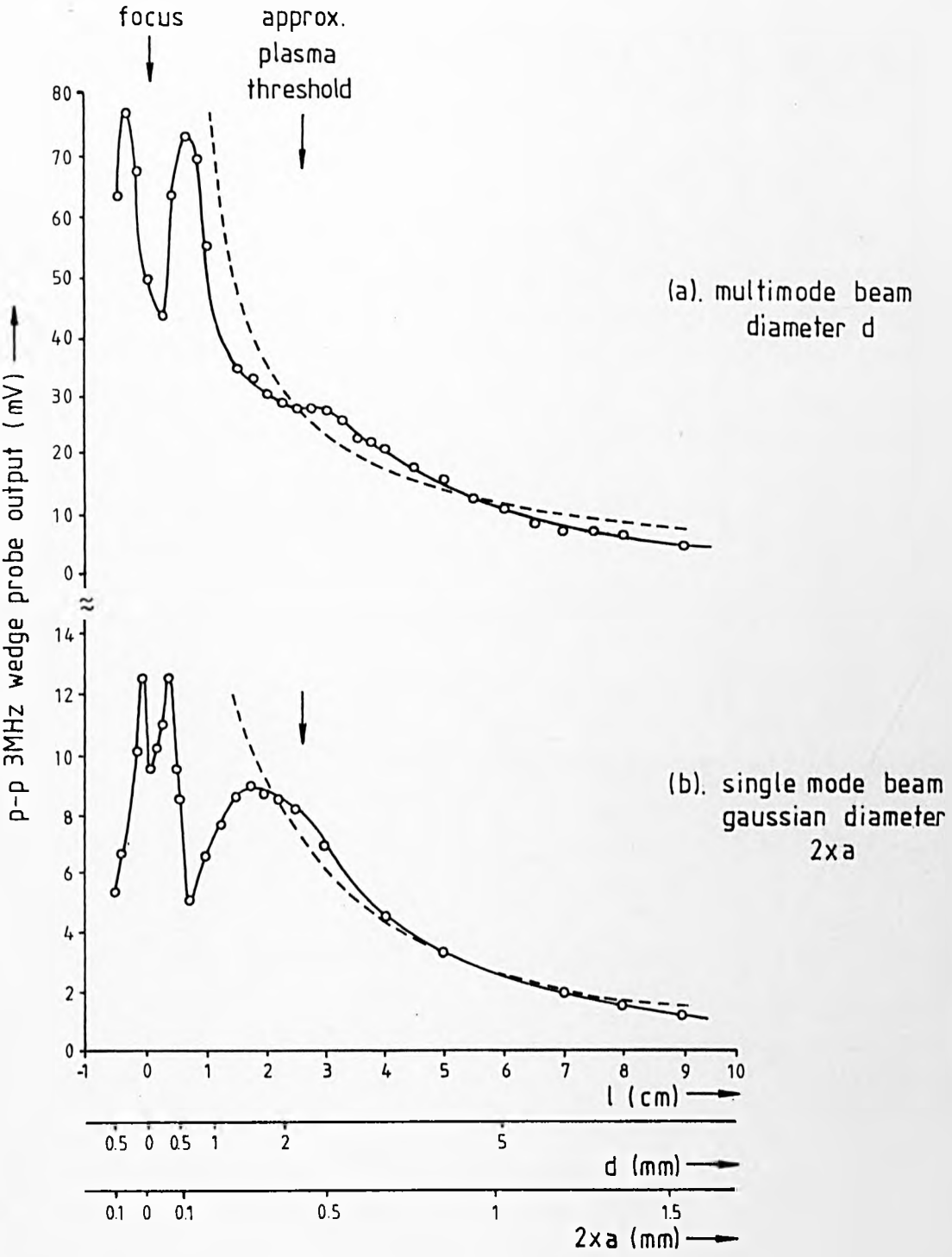

FIGURE 6.8: The variation in Rayleigh amplitude with focal position. 35mJ multimode and 2.5mJ single mode irradiation of an aluminium sample (f=35mm).

----- fitted 1/d, 1/a curves. (low-intensity, thermoelastic region only).

ultrasonic waveforms represent a broad average of generating conditions and so real, rapidly varying features revealed by a single mode beam, may well become intensity-averaged beyond recognition.

6.4 Discussion

The changes brought about in the laser ultrasonic sources by plasma formation, can be understood by comparing the resultant waveforms with those produced by the capillary breaking source. In particular, Figures 6.2(b) and 6.3 may be compared with Figures 5.29(a) and (b). The profiles are close inverses. This demonstrates that high intensity plasma formation produces the opposite surface force, namely, a roughly step-compressive surface force, confirming the earlier suggestion of an orthoganality shift. It also indicates that the dipolar - as opposed to monopolar - waveform in Figure 6.2(a) produced at the threshold of a visible plume, was generated by a force with a profile resembling the time differential of a step function ie. a brief vertical impulse.

Previous authors (Ledbetter and Moulder 1979) have suggested that ejection of hot surface material may aid thermoelastic generation by imparting to the surface an impulse due to momentum transfer. Ejection by direct laser-induced vaporisation, however, may be expected only to give a brief impulse over the time scale of the laser pulse, the possible origin of the threshold waveform. A sustained step-type force must stem from a source extended in time. At high laser intensities, the laser-produced plasma will absorb the laser radiation directly and rapidly heat. This will supply a subsequent resevoir of heat, some of which will vaporise more surface material by a combination of backwards thermal conduction and re-radiation of energy (Robin 1978). In addition, the plasma may directly exert a gas-dymanic over-pressure before it has expanded clear of the

surface, cooled and depressurised. In any case, such a vertically-directed source will be expected to launch a strong compressive-longitudinal pulse into the bulk but a weak shear component.

The cause of the high intensity, on-focus minima in Figures 6.7 (longitudinal pulse) and 6.8 (Rayleigh pulse) is not certain though they have a number of possible origins. The plasma driven by strong absorption may expand rapidly up the laser beam detaching itself from the surface (see, for example, Metz et al 1975, Robin 1978). Such detachment could have two effects; first, secondary vaporisation may be reduced, and secondly, the main plasma expansion will resemble more aerial-type blast rather than one detonated at zero level. Any contribution to the ultrasonic waveforms as a result of the gas-dynamic plasma expansion may therefore also be reduced, the pressure disturbance experienced by the surface possibly being both reduced in peak amplitude and distributed over a wider and hence more diffuse area.

The variation of target response with focused laser intensity has been investigated in a number of previous experiments (eg. Gregg and Thomson 1966, Jones 1971) though these have been largely confined to time-integrating ballistic measurements which yield only estimates of the total imparted momentum. The results have not necessarily indicated any direct drops in target response, though reduction in the rate at which momentum is imparted have been noted. In this respect, it is important to realise that ultrasonic measurements effectively resolve the form of the plasma surface forces, and so results may not be directly comparable. If, however, the surface forces could be deconvolved from ultrasonic waveforms, a correspondence would be expected upon integration with respect to time. This is discussed further in Chapter 7.

The minimum in the Rayleigh wave amplitude in Figure 6.8(b) at $\ell \simeq 7$mm is associated with the transition region and not with any changes in ablation processes. It is thought to result from the ablation component of the threshold ultrasonic source acting in part against remaining thermoelastic processes. This aspect of the target response is also described further in Chapter 7.

6.5 Paint-ablation source

There is another type of laser ultrasonic source which though operating at relatively low unfocused intensities, has some of the characteristics of the plasma-ablation source. This is the paint-ablation source in which the surface to be irradiated is first painted, usually matt black. During irradiation, some of this layer is ablated, probably by direct vaporisation, whilst some remains. The result is the bulk waveform in Figure 6.9 which was produced by an unfocused multimode pulse incident on an aluminium sample. The longitudinal pulse has been greatly enhanced by ×88 and to a lesser extent the shear pulse by ×4. In the latter respect, this source is different from either the constrained-surface thermoelastic or plasma-ablation source both of which led to reduced shear amplitudes.

This source may now be seen to be a hybrid between impulse-enhanced longitudinal generation due to partial paint-ablation, and thermoelastic-enhanced shear generation due to increased optical absorptivity; Figure 6.10. In this case, the impulse produced by ablation is expected to be a brief transient.

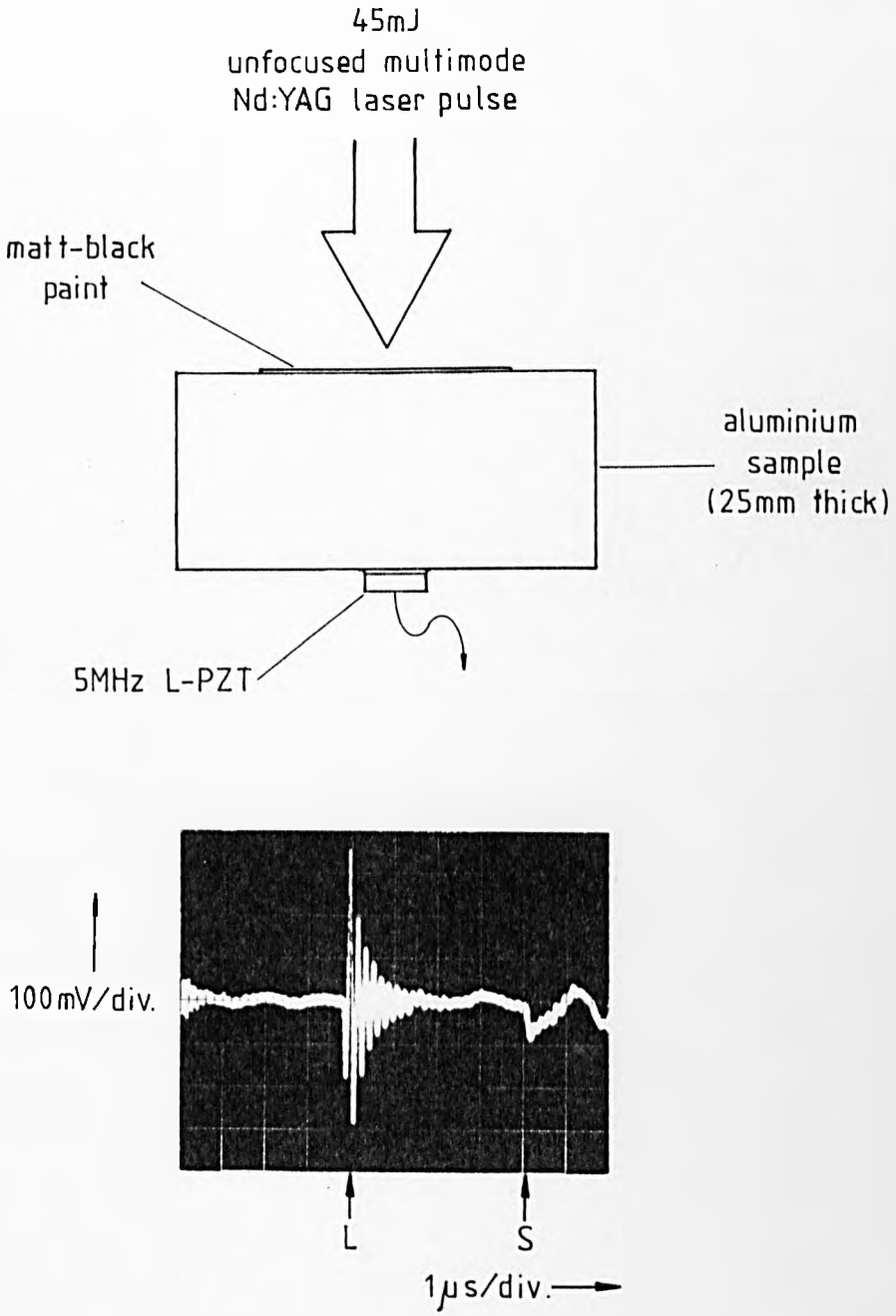

FIGURE 6.9: Bulk waveform produced by unfocused irradiation of a painted metal surface.

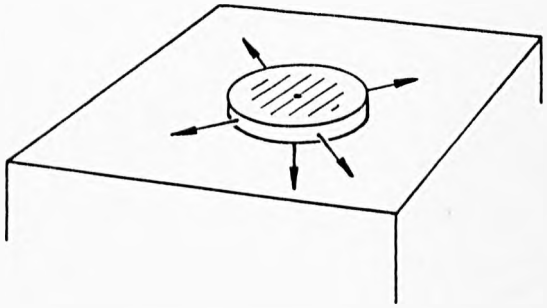

FIGURE 6.10: Model of the low-intensity (unfocused) laser ultrasonic source at a painted metal surface. Vertical forces are generated as a result of partial paint-ablation whilst increased optical absorptivity enhances horizontal thermoelastic stresses.

CHAPTER 7

Quantitative Study of the Surface Acoustic Response in Metals

7.0 Introduction

Chapters 5 and 6 identified the basic nature of both the thermoelastic and ablation laser ultrasonic sources but only in qualitative terms. This chapter aims to quantify the generation processes, relating in absolute terms the source mechanisms to the resultant target response. In particular, two aspects of the surface response are examined in detail; first, the motion of the source itself, and, secondly, the resultant surface acoustic waveforms. In the former case, a comparison is made with experimental traces recorded using a calibrated interferometer detector, and in the latter, with waveforms detected with broad bandwidth capacitance probes. The bulk acoustic response has been described in previous studies references to which may be found in Section 3.5.

7.1 Interferometer detection of the thermoelastic source motion

The interferometer, provided by the NDT Centre, Harwell UKAEA, was based on a Michelson arrangement described elsewhere (Moss 1982). Briefly, a 10mW cw He-Ne laser beam was beam split, 95% propagating towards the sample surface, the remaining 5% acting as a reference with which the return beam was recombined. The resultant interference was observed as an intensity fluctuation directly proportional to the vertical component of surface displacement. The interferometer and associated electronics had an overall frequency response ranging from 10KHz - 100MHz.

The experimental arrangement used to study the thermoelastic source motion is shown in Figure 7.1. By means of prisms, the probe beam was brought in normal to the target surface coincident with 3.5mm diameter 30ns 45mJ multimode pulses from a Nd:YAG laser acting as the source. The probe beam was aligned vertically to maximise the return signal, and also focused down to ≃ 0.5mm diameter spot to improve spatial resolution. The source beam was off-set by ≃ 4° to prevent direct breakthrough in the optical system of the interferometer. The detected source motion is typified by Figure 7.2(a) which reveals a step-like displacement produced in steel.

The accompanying theoretical trace was calculated from the uniform irradiation theory. This theory indicated that long laser pulses (t_p >> 15ps) produce acoustically thin sources, and as such cause the surface to rise in an almost stress-free, quasi steady-state motion. The expected upward displacement at any instant is (equation 4.59)

$$U_1(0,t) = \frac{\gamma}{c\rho} \int_0^t E(t)dt$$

where E(t) = absorbed laser energy density

γ = laminar coefficient of expansion

with a final upwards displacement of

$$U_1(0,t) \underset{t >> t_p}{=} \frac{\gamma E_T}{c\rho} \qquad \text{(uniform irradiation)}$$

where E_T = total absorbed energy density

Estimates of the final displacement in a variety of metals are compared with experimental values in Table 7.1. The observed results appear to be

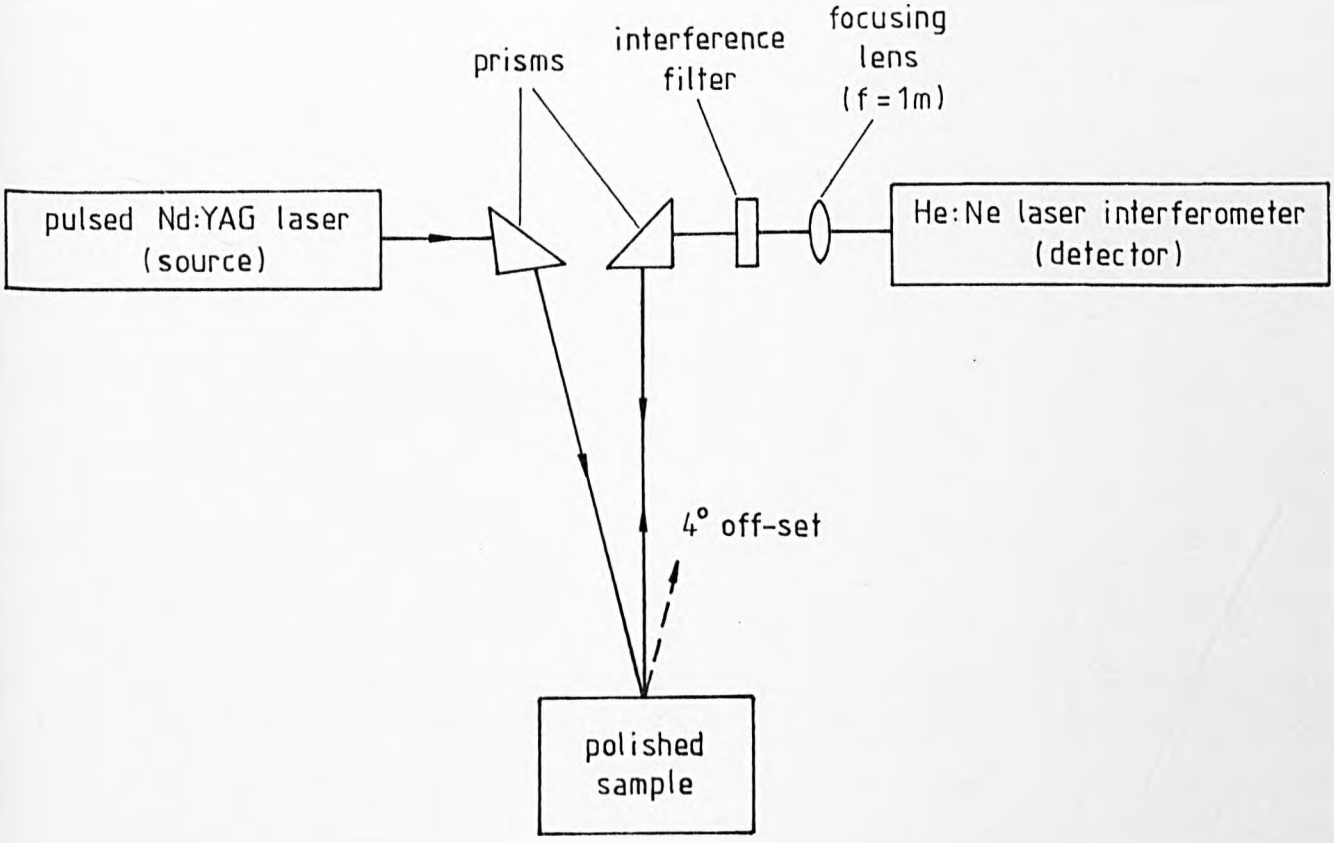

FIGURE 7.1: Arrangement for studying the vertical motion of the free-surface thermoelastic source.

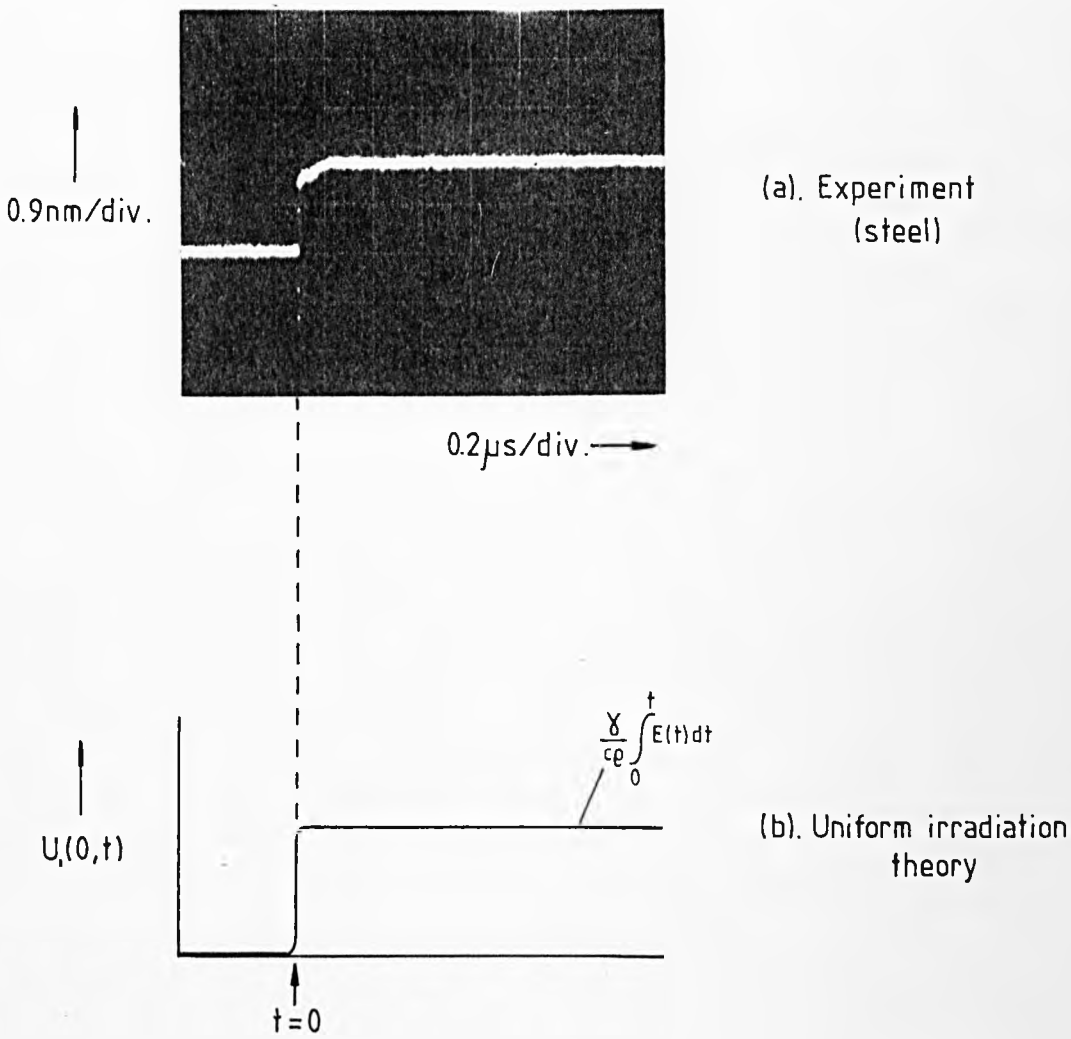

FIGURE 7.2: Normal component of displacement at the free-surface thermoelastic source. Experimental trace recorded by laser interferometer at a 3.5mm diameter 45mJ 30ns Nd:YAG source.

	Measured ± 20% (nm)	Uniform Irradiation Model $\gamma E_T/c\rho$ ± 15% (nm)
Brass	0.61	1.46
Aluminium	1.75	2.60
Copper	0.19	0.72
Steel	1.75	4.53

TABLE 7.1 : A comparison of experimental and theoretical values for the final surface rise at the thermoelastic source.

significantly lower. This may partly be due to radial stress relief over the finite source area which in practice may accommodate at least some of the expansion in lateral directions. Theory, however, implicitly assumed total radial constraint.

Both the experimental and theoretical traces show that the surface remains raised on time scales of a few microseconds. Eventually, the surface would be expected to sink back down but only when lateral flow of heat becomes significant, so transferring the heat away from the 1D geometry. This is a slow thermal effect, and would commence only when the thermal skin depth becomes comparable with spot diameter, ie. from Figure 4.1, only after ≃ 10ms.

It is interesting to note that the velocity and acceleration experienced by the surface may be estimated from the expressions

$$V(0,t) = \frac{\partial U_1}{\partial t} = \frac{\Upsilon}{c\rho} E(t)$$

$$a(0,t) = \frac{\partial^2 U_1}{\partial t^2} = \frac{\Upsilon}{c\rho} \frac{\partial E(t)}{\partial t}$$

with average values during irradiation of

$$\bar{V}(0,t) \simeq \frac{\Upsilon}{c\rho} \frac{E_T}{t_p}$$

$$\bar{a}(0,t) \simeq \frac{\Upsilon}{c\rho} \frac{E_T}{t_p^2}$$

Under present conditions, E_T = 3,500 Jm^{-2}, t_p = 30ns, $\Upsilon = 30 \times 10^{-6}$ K^{-1} indicating velocities in the order of $1ms^{-1}$ and accelerations of 10^8 ms^{-2}.

7.2 Design and construction of surface wave capacitance probes

To study the ultrasonic waveforms launched by the laser source, a convenient and more sensitive alternative to the interferometer is the broad bandwidth capacitance probe. The operating principle of such devices is well known eg. Breckenridge et al 1975. A detection element comprising a polished section of metal, is supported typically 2-10μm above the sample surface which is itself polished flat and metalised where necessary. Across the capacitor thus formed is applied a constant potential of usually +50 - 200V, using the sample surface as the earth side whilst feeding the detection element into a charge amplifier. Any changes in the gap dimension due to acoustic displacements induce a change in stored charge. Given a knowledge of the amplifier sensitivity, the resultant signal may be quantitatively related to the vertical component of surface displacement. Such devices are non-contact and have a frequency response ultimately limited only by phase differences of the incident acoustic wavefront across the detection area.

For present purposes, two surface wave probes were designed and constructed, the ring probe, and its derivative, the arc probe. The ring probe comprised the end section of a stainless steel ring, wall thickness Δa = 0.28mm, radius r_o = 12.4mm, set in epoxy resin; Figure 7.3. The entire assembly was polished flat to an optical quality finish, and supported by small area ($\simeq$ 4mm^2) spacers cut from 9 - 20μm melinex polyester film (ICI Ltd.). The degree of overlap was kept to a minimum to ensure the probe remained essentially an air-gapped device. The assembled probe was aligned concentrically with the laser pulses so that resultant circularly expanding surface acoustic wavefronts arrived in phase around the probe's inner perimeter. This design minimises phase incoherence and so maximises the frequency response, though at the expense of a

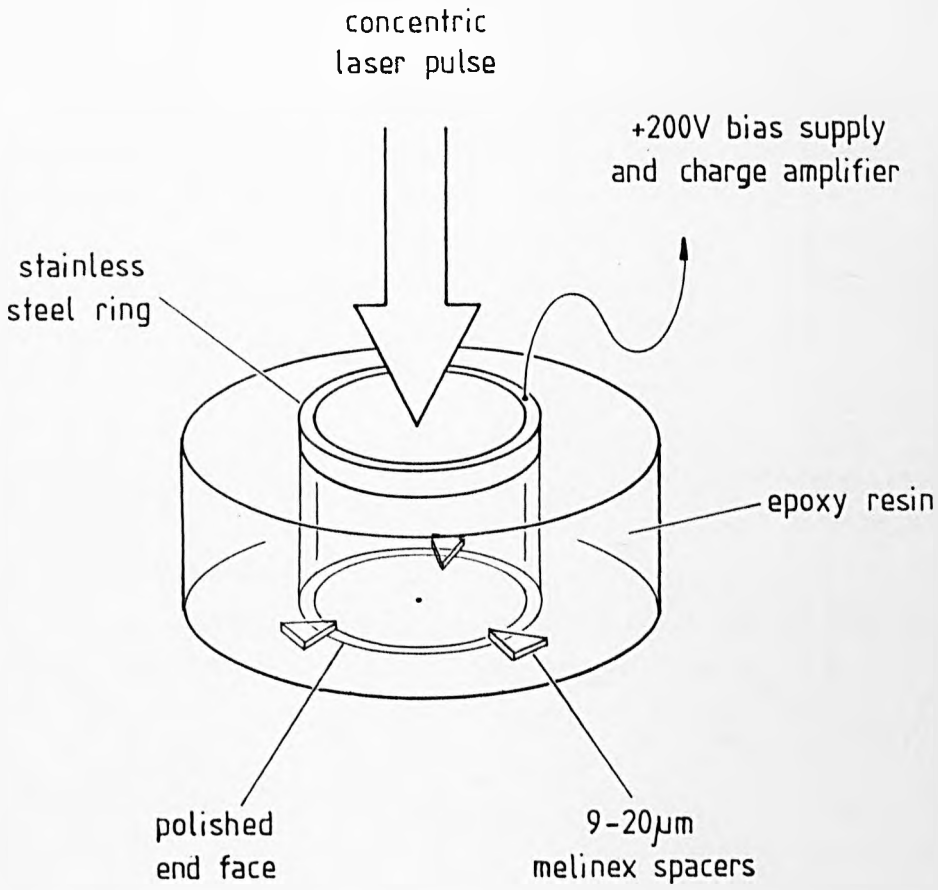

FIGURE 7.3: The ring capacitance probe for the detection of surface acoustic waves.

predetermined source/detector distance.

Since the wall thickness of such a probe is much greater than the gap dimension (≈ ×20), it effectively constitutes a plane parallel capacitor with negligible edge effects. As such, it has an approximate capacitance,

$$c \approx \frac{\xi_o A}{g} = \frac{2\pi\xi_o \, \Delta a \, r_o}{g}$$

where ξ_o = permittivity of free space

g = gap dimension

A = area

Any small uniform changes in g will consequently cause a change in capacitance

$$\delta c \approx \frac{\partial c}{\partial g} \cdot \delta g = - \frac{2\pi\xi_o \, \Delta a \, r_o}{g^2} \cdot \delta g$$

where δg = change in gap dimension

Under conditions of constant bias potential, V, a change in stored charge will be thus induced

$$\delta q = V \, \delta c = - \frac{2\pi\xi_o \, V \, \Delta a \, r_o}{g^2} \cdot \delta g \qquad 7.1$$

In other words, the probe has a sensitivity to spatially uniform (vertical) displacements of

$$\frac{\delta q}{\delta g} = - \frac{2\pi\xi_o \, V \, \Delta a \, r_o}{g^2} \qquad 7.2$$

Typical values of $\delta q/\delta g$ ranged from 4×10^{-5} to 2×10^{-4} Cm^{-1} depending on spacer thickness and bias voltage.

In the dynamic case of propagating wavefronts emergent from a laser source, the gap dimension will only change uniformly in the limit of the surface acoustic wavelength becoming much greater than the wall thickness, $\lambda >> \Delta a$. At shorter wavelengths, $\lambda \lesssim \Delta a$, the displacement will at any instant vary significantly across the active region. This will reduce the sensitivity due to spatial integration; Figure 7.4. In quantitative terms, if an emergent wavefront has the form

$$U(r,t) = A(r) \sin(\omega t - kr)$$

where $U(r,t)$ = vertical component of displacement,

$A(r)$ = amplitude variation with radial distance,

then the change in the mean gap dimension will be instantaneously reduced to

$$\overline{\delta g}\,(r,t) = \frac{1}{\Delta a} \int_{r_o}^{r_o+\Delta a} A(r) \sin(\omega t - kr)dr$$

Assuming the attenuation of the wave in propagating the small additional distance under the probe is negligible, ie. $A(r)$ remains approximately constant across the wall thickness, this gives

$$\overline{\delta g}(r,t) \approx \frac{A(r_o)}{\Delta a} \int_{r_o}^{r_o+\Delta a} \sin(\omega t - kr)dr$$

$$= \frac{2A(r_o)}{\Delta a} \cdot \frac{\sin\left(\frac{k\Delta a}{2}\right)}{k} \cdot \sin(\omega t - kr_o - \phi)$$

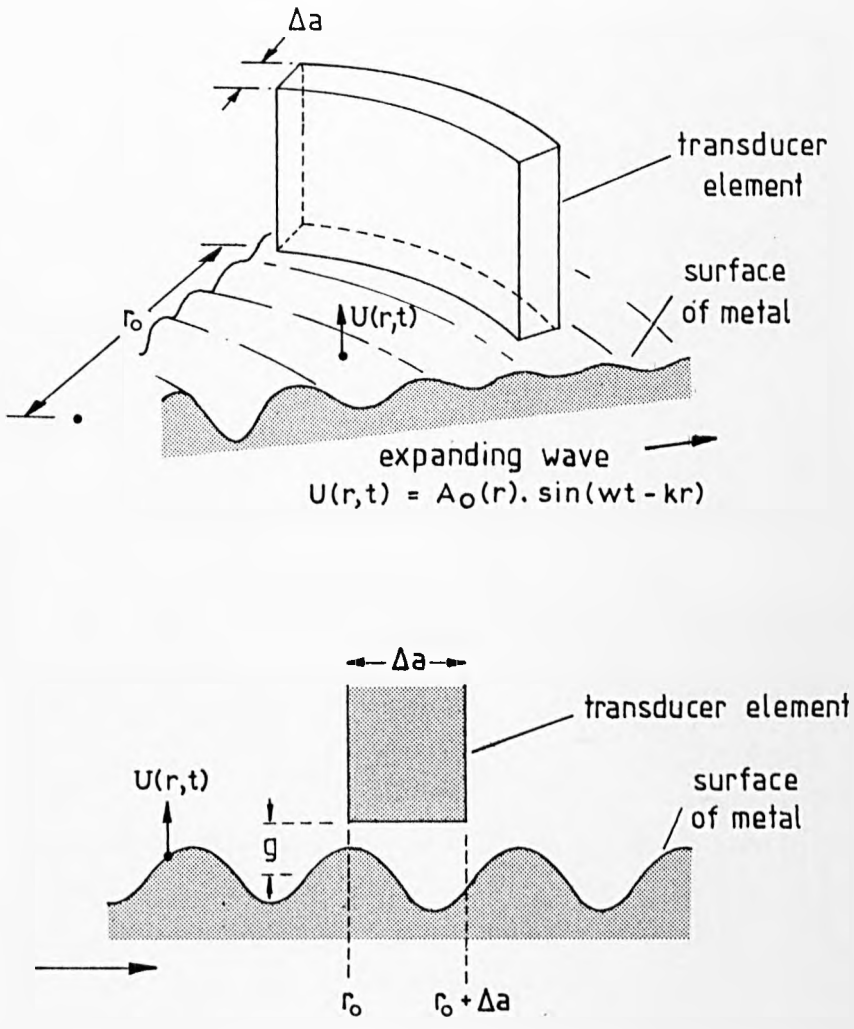

FIGURE 7.4: Response of the ring probe at high frequencies ($\lambda \lesssim \Delta a$).

Due to the effect of spatial integration, the change in the mean gap dimension, $\overline{\delta g}$, and hence sensitivity, are reduced.

where $\phi = \frac{k\Delta a}{2}$ = phase shift of detected signal.

Separating out the amplitude terms and substituting $\overline{\delta g}$ for δg in equation 7.1, gives an amplitude frequency response of

$$\frac{\delta q}{\delta g} = - \frac{4\pi\xi_o \, V \, r_o}{g^2} \cdot \frac{\sin(\frac{k\Delta a}{2})}{k} \qquad 7.3$$

This expression is plotted in Figure 7.5 for a propagation velocity of $3{,}000 ms^{-1}$ typical of Rayleigh waves on metal surfaces. The response extends to 6MHz at the -3dB point. Over this bandwidth, evaluation of θ indicates a phase coherence of $\leq 58°$. In the limit $k \to 0$ and hence $\sin(k\Delta a/2) \to k\Delta a/2$, the response can be seen to tend towards the expected uniform displacement sensitivity. The zeroes in the response occur where the wall thickness corresponds to an integral number of wavelengths $\Delta a = n\lambda$. At these points the wave passes undetected, at no time causing a change in the mean gap dimension.

The second detector, the arc probe, was essentially the same except only a segment of ring was employed with a longer acoustic focus of 50mm; Figure 7.6. Although this design reduced sensitivity, it had the specific advantage of allowing a metal case to be conveniently set around the active element thereby shielding it from any direct source illumination. This arrangement proved essential when studying the plasma-ablation source which tended to flood the detection element directly with UV-induced photoelectric charge. Both probes fed into a $250mV \, pC^{-1}$ charge amplifier (UKAEA type 0924-2) and were biased with a 0 - 200V supply. This gave the detection system an overall sensitivity typically ranging from $0.01mV \, pm^{-1}$ (arc probe) to $0.05mV \, pm^{-1}$ (ring probe).

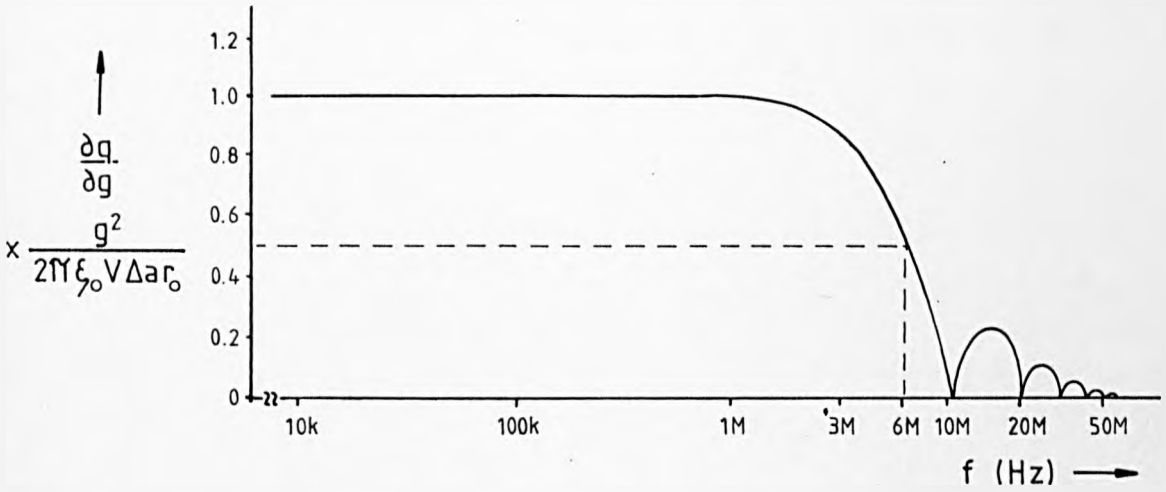

FIGURE 7.5: Amplitude frequency response of the ring probe for a surface wave propagation velocity of 3000ms^{-1}. Plotted by evaluation of equation 7.3.

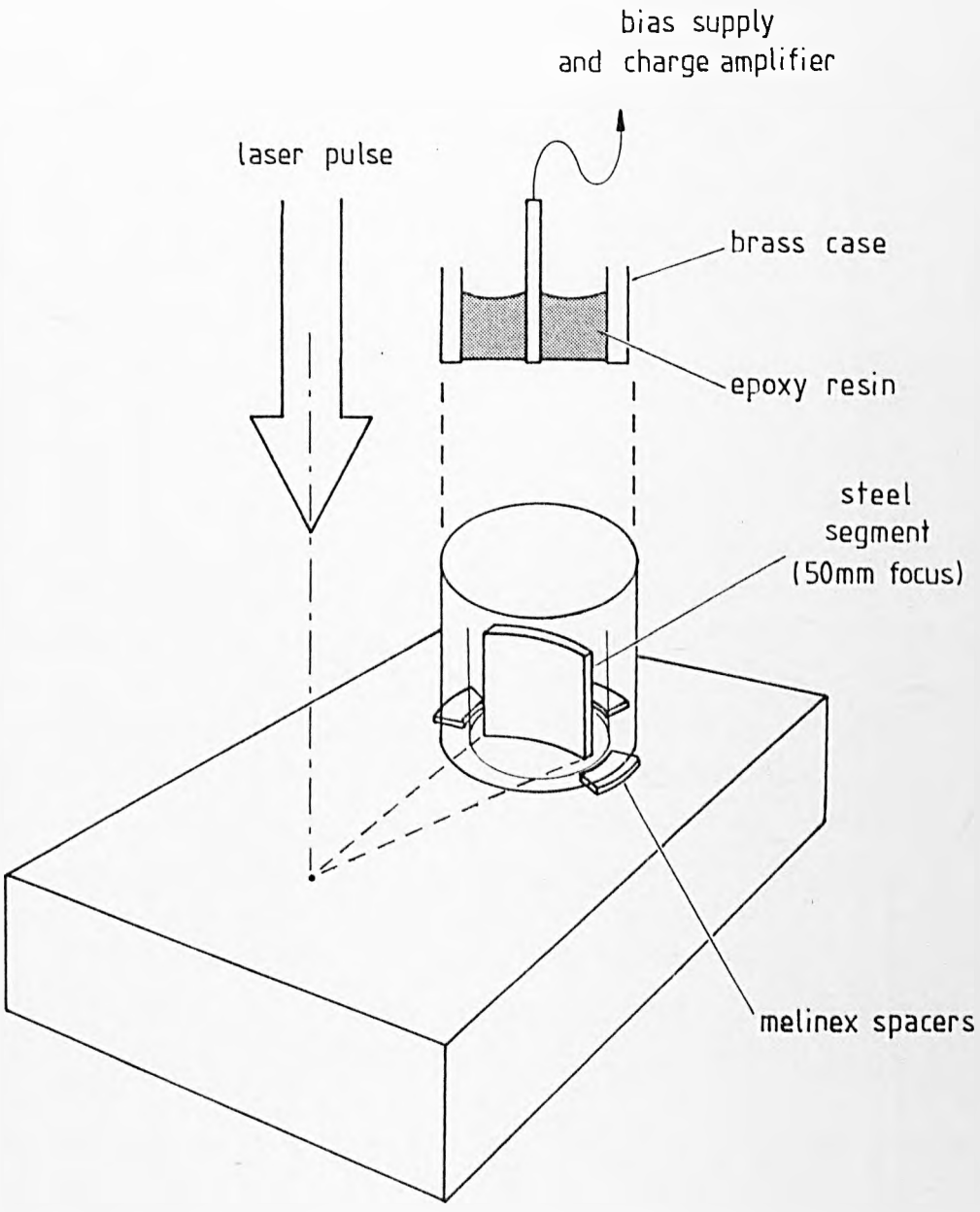

FIGURE 7.6 : The arc probe.

7.3 Capacitance probe results

The surface waveforms produced by the thermoelastic laser source are typified by the ring probe traces in Figure 7.7, captured with a Tektronix 466 oscilloscope. Both waveforms were produced at an aluminium surface by unfocused 30ns Nd:YAG pulses prealigned coaxially with the probe. The first waveform was produced by a single mode pulse, and reveals a brief Rayleigh pulse (R) comprising a surface fall followed by a lower amplitude rise, after which the surface returns to its original level. By calibration from equation 7.2, taking the parameter, g, as the nominal spacer thickness, the peak-to-peak amplitude is 260 ± 90pm. A small amplitude (20 ± 7pm) surface rising longitudinal pulse (SL) is also evident. The same general features are apparent in trace (b) produced by a multimode pulse, though much broadened by this source's greater spatial extent.

Focusing the pulses (f = 25mm) so as to form an intense plasma plume produced the higher-amplitude ablation waveform in Figure 7.8 recorded with a Tektronix 7912 AD digitizer. This waveform detected with the arc probe, likewise shows a bipolar Rayleigh pulse preceded by a longitudinal disturbance. There are two main differences; first, the Rayleigh pulse is inverted being a rise followed by a fall, and secondly, the surface remains depressed for some time after the immediate Rayleigh arrival, not returning to its original level for ≈ 8μs.

The transition between these two extremes is recorded in Figure 7.9 which gives arc probe waveforms obtained while bringing multimode laser pulses gradually into focus. The first waveform was produced below the threshold for visible plume formation and is characteristically thermoelastic. Its features are sharpened by the reduced beam diameter. At the threshold, the waveform begins to undergo a rapid but reversible

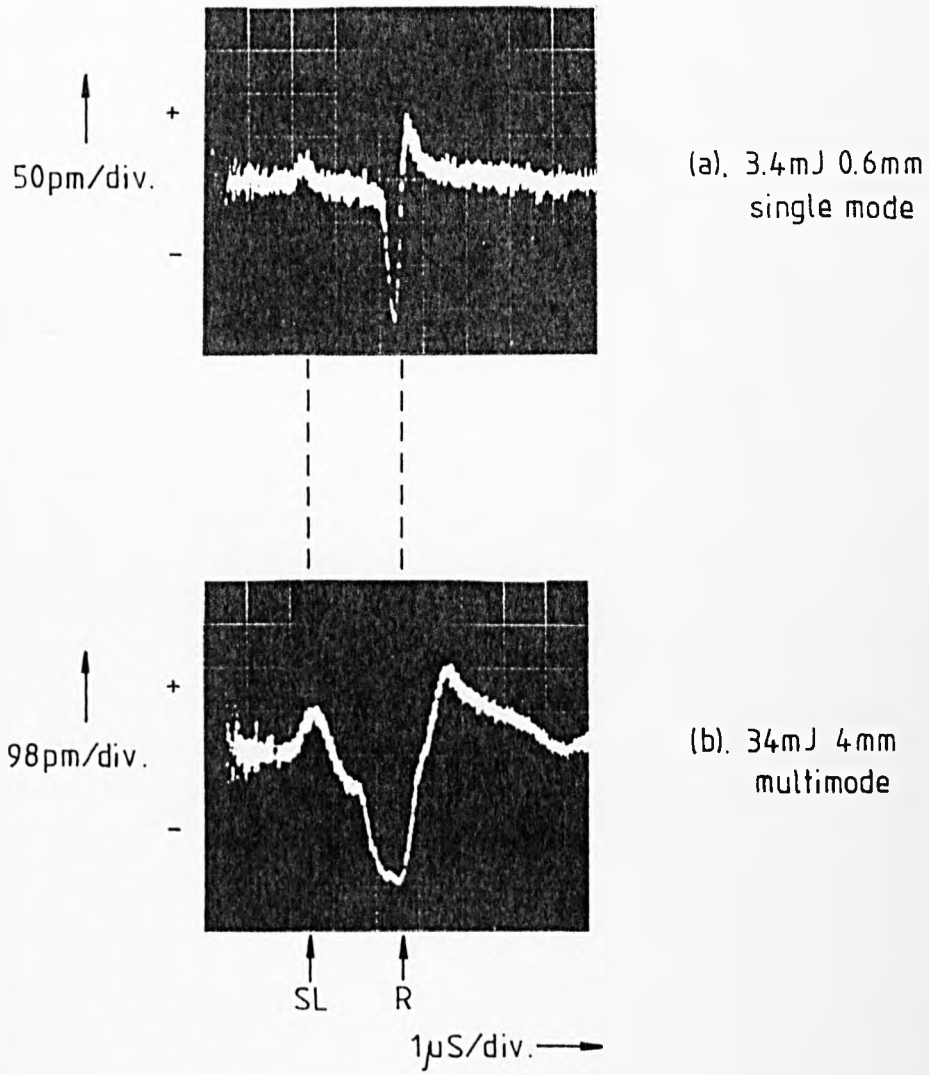

FIGURE 7.7: Thermoelastic surface acoustic waveforms produced in aluminium by 30ns Nd:YAG pulses. Ring capacitance probe.

+ indicates a surface rise
- surface fall.

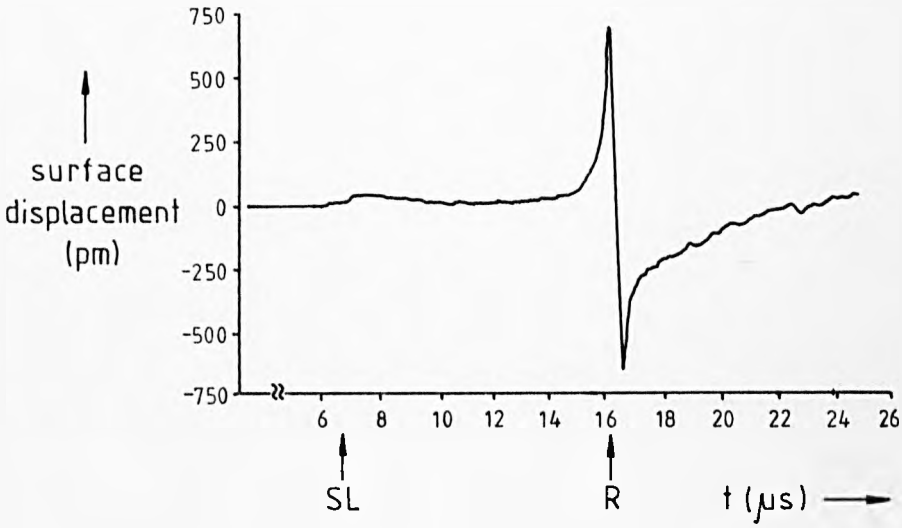

FIGURE 7.8: Plasma-ablation surface acoustic waveform produced in aluminium by focused (f=25mm) 30ns 34mJ multimode Nd:YAG pulse.

Arc capacitance probe.

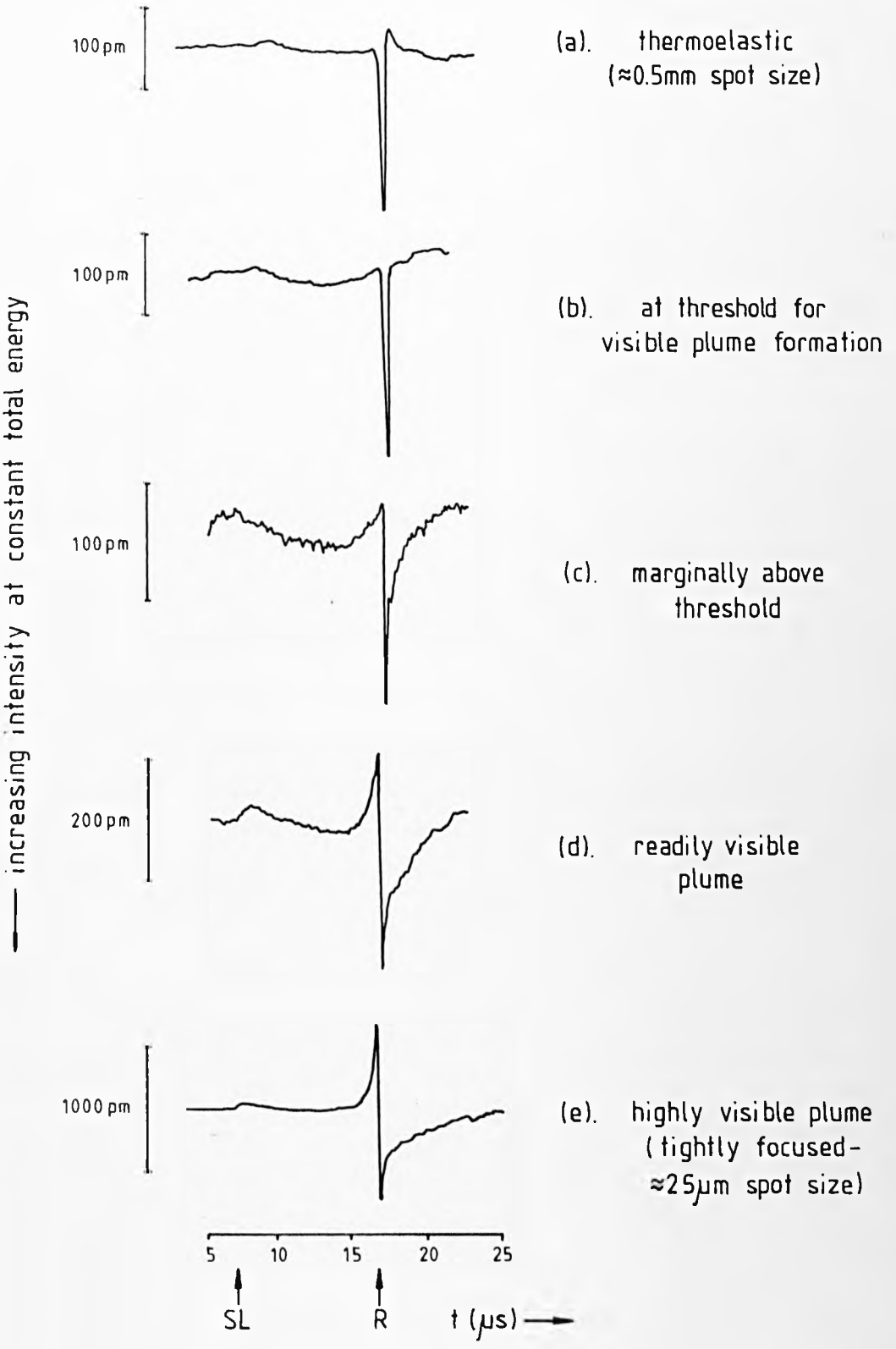

FIGURE 7.9: Transitional surface acoustic waveforms produced in aluminium by bringing multimode Nd:YAG pulses into focus (f=25mm).

Arc capacitance probe.

transformation. It commences with the cancellation of the surface rising component of the thermoelastic Rayleigh pulse resulting in an almost perfect monopolar $\delta(t)$-profile. As the spot diameter is further reduced, the source acquires a stronger ablation component, and the Rayleigh pulse develops a leading surface-rise. The surface remains depressed after the Rayleigh arrival for an increasing length of time until the waveform finally acquires its full plasma characteristics.

The ablation source could be greatly enhanced by applying a thin ($\simeq$ 0.2mm) layer of grease to the interaction area. The profile of resultant waveform in Figure 7.10, is intermediate between the plasma waveforms in Figures 7.9(c) and (d). In contrast to Figure 7.8, which was produced under otherwise identical conditions, the surface returns comparatively rapidly to its original level. The Rayleigh amplitude has been increased well into the nm range (3.7nm peak-to-peak). The grease is itself ablated as a result, and the plasma plume looses much of its luminosity.

7.4 Discussion

These various laser ultrasonic sources may be considered in terms of the forces created at the metal surface. The resultant acoustic waveforms may then be found by appropriate solution to the equation of motion (equations 4.16 and 2.20 for the thermoelastic and ablation source, respectively). In this respect, the simplest source geometry to analyse is the point source.

Consider first the thermoelastic source and in particular an elemental volume of metal dimension, Δr, assumed to contain all the absorbed laser energy; Figure 7.11. As a result of pulsed irradiation, it will rise in mean temperature by

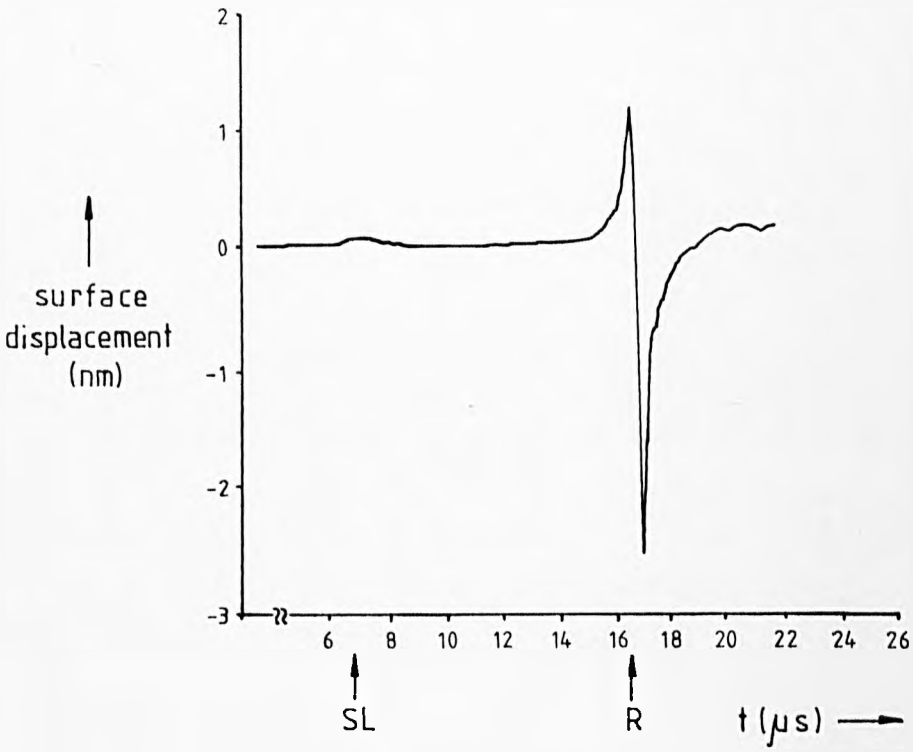

FIGURE 7.10: Surface acoustic waveform produced in aluminium by focused (f=25mm) multimode Nd:YAG ablation of a thin (≈0.2mm) layer of grease.

Arc capacitance probe.

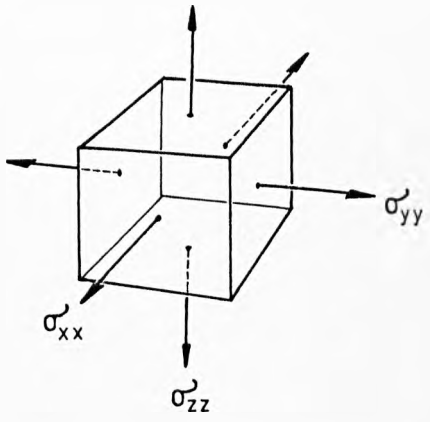

FIGURE 7.11: Point source model of thermoelastic laser source within a bulk medium. Elemental volume of metal dimension Δr assumed to contain all the absorbed laser energy.

$$\sigma_{xx} = \sigma_{yy} = \sigma_{zz} = -\alpha(3\lambda + 2\mu).\frac{E_T}{c\,\rho\,\Delta r^3}.H(t)$$

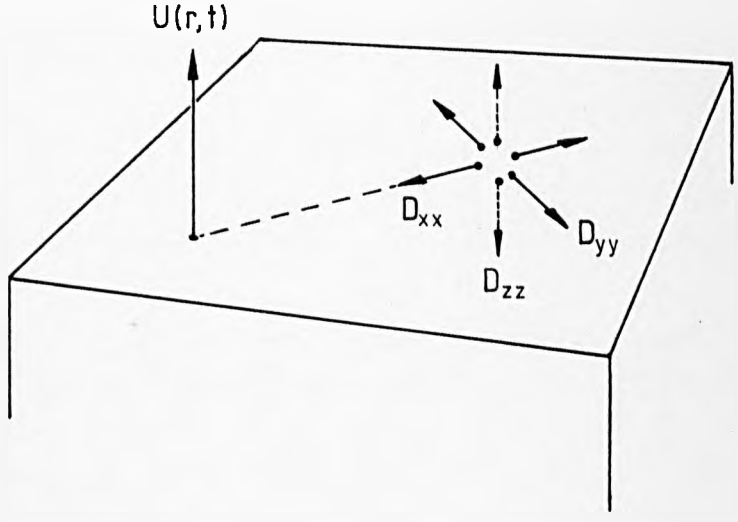

FIGURE 7.12: Representation of thermoelastic laser source at a free metal surface.

$$D_{zz} \approx 0$$

$$D_{xx} = D_{yy} = -\alpha(3\lambda + 2\mu).\frac{E_T}{c\,\rho}.H(t)$$

$$\bar{\theta}(t) = \frac{E_T}{c\rho\ \Delta r^3} \cdot H(t)$$

where E_T = total absorbed energy

c = specific energy

ρ = density

$H(t)$ = unit step function

If it were in an infinite medium, thermal stresses would be generated acting on each face

$$\sigma_{ii} = -K\frac{\Delta V}{V} = -3\alpha K\theta(t)$$

$$= -\alpha\,(3\lambda + 2\mu)\frac{E_T}{c\rho\ \Delta r^3} \cdot H(t)$$

where $K = \lambda + \frac{2}{3}\mu$ = bulk modulus

$i = x,y,z$

The total force acting on each face would thus be

$$F_{ii} = \sigma_{ii}.\Delta r^2 = -\alpha(3\lambda + 2\mu)\frac{E_T}{c\rho\ \Delta r} \cdot H(t)$$

equivalent to force dipoles acting across each pair of faces

$$D_{ii} = F_{ii} \cdot \Delta r = -\alpha(3\lambda + 2\mu)\frac{E_T}{c\rho} \cdot H(t) \qquad 7.4$$

The last result has been indirectly derived previously by Scruby et al 1980.

At a free surface, D_{zz} will be relieved in the limit of an acoustically thin source, typically $t_p >> 15$ps (see Section 4.9). D_{xx} and D_{yy},

however, will be largely unaffected. Thus the laser source reduces to two horizontal force dipoles (Figure 7.12), so forming the basis of the shearing source indicated in Chapter 5.

These in-plane dipoles may be considered as being composed of four orthogonal force monopoles acting tangentially to the surface, the response to which was described in Section 2.10 with reference to the work of Choa 1960. From equation 2.22 in particular, it is clear that D_{yy} in being normal to the detector direction ($\theta = 90°$), will make no significant contribution to the resultant component of displacement ($Q(r,t) = q(r,t) \cos\theta = 0$). Only D_{xx} is effective.

The displacement due to this remaining in-line dipole corresponds to the spatial derivative of Choa's solution. This is readily demonstrated by decomposing D_{xx} into its component forces

$$F_{xx} = \frac{D_{xx}}{\Delta r}$$

Taking one force to be positioned at r, and the other slightly more distance at $r+\Delta r$, gives the resultant vertical component of displacement as the superposition,

$$U(r,t) = \frac{D_{xx}}{\Delta r} \cdot q(r,t) - \frac{D_{xx}}{\Delta r} \cdot q(r-\Delta r,t)$$

Expanding $q(r-\Delta r,t)$ as the first two terms of a Taylor expansion, an accurate procedure since Δr is infinitesimal, gives

$$q(r-\Delta r,t) = q(r,t) - \Delta r \frac{\partial q}{\partial r}(r,t)$$

which on resubstitution yields

$$U(r,t) = \frac{D_{xx}}{\Delta r} q(r,t) - \left[\frac{D_{xx}}{\Delta r} q(r,t) - D_{xx} \frac{\partial q}{\partial r} (r,t) \right]$$

ie.

$$U(r,t) = D_{xx} \frac{\partial q}{\partial r} (r,t)$$

This expression has been evaluated numerically for a unit dipole, D_{xx} = 1Nm in Figure 7.13(a). The dominant feature is the double opposed discontinuity at the expected Rayleigh arrival.

To compare this function with experiment, it may be convolved with a suitable aperture function to simulate a finite source size. The results of such a procedure are shown in Figures 7.13(b) and (c), which give convolutions of U(r,t) to be compared with the experimental traces in Figure 7.7(a) and (b). The relevant computational procedures are outlined in an appendix together with further numerical evaluations. The profiles of both the Rayleigh and longitudinal pulses are well described. To make a quantitative comparison, the amplitude of the experimental and theoretical (D_{xx} = 1Nm) waveforms may be divided, so as to give an estimate of the total dipole moment. On this basis, a comparison of the Rayleigh pulse amplitudes indicates total dipole moments of

$D_{xx} = 9 \pm 3 \times 10^{-5}$ Nm single mode

$= 6 \pm 2 \times 10^{-4}$ Nm multimode

These estimates may be compared with the following expected values,

$D_{xx} = 29 \times 10^{-5}$ Nm single mode

$= 29 \times 10^{-4}$ Nm multimode

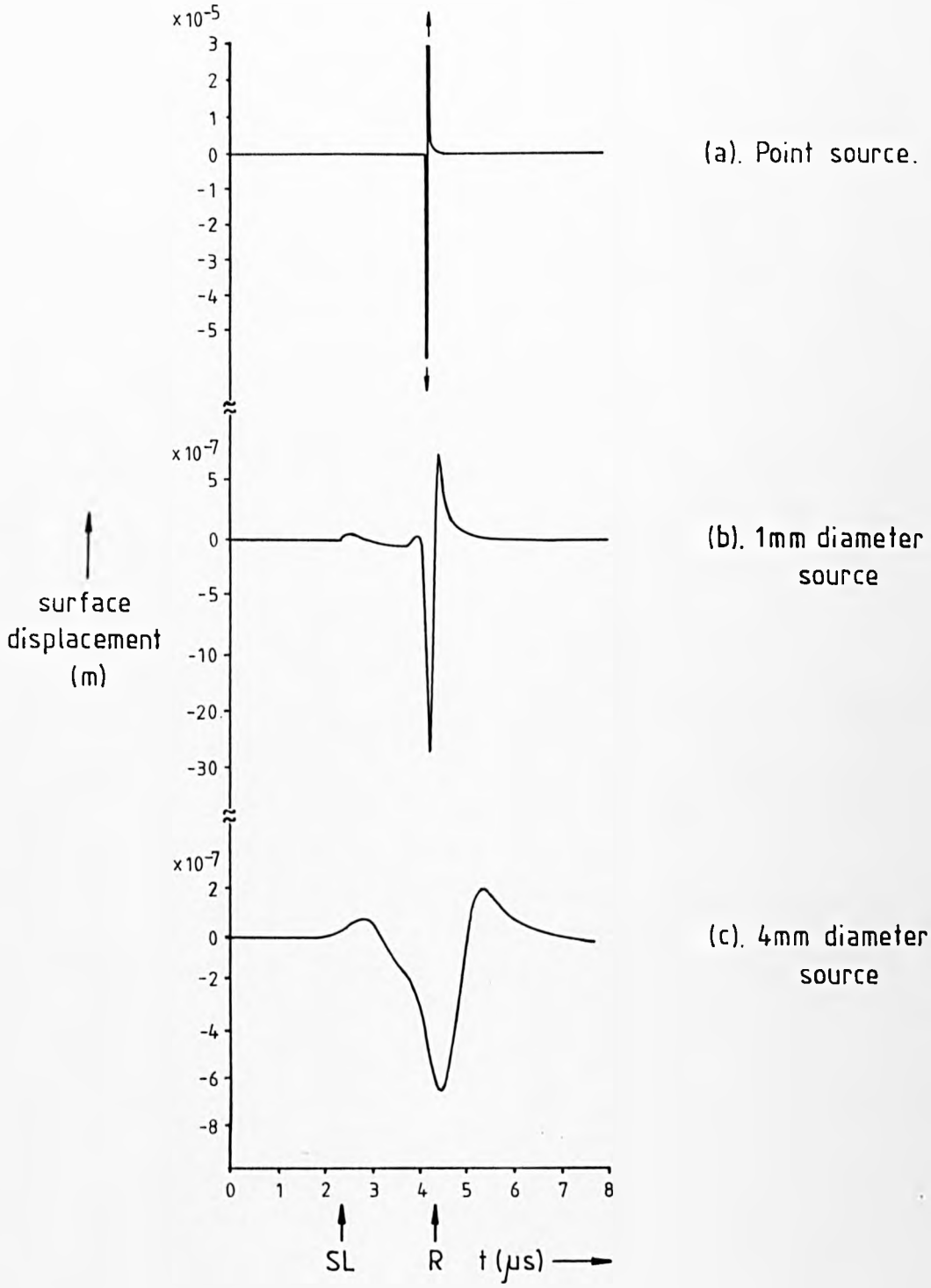

FIGURE 7.13: Theoretical surface displacements produced by a unit dipole (D_{xx} = 1Nm) thermoelastic source in aluminium at a distance r = 12mm. Waveforms (b) and (c) to be compared with Figures 7.7(a) and (b) respectively. The amplitudes may be divided so as to give an estimate of the total dipole moment

which were obtained by substituting into equation 7.4 the parameters: $\alpha = 23 \times 10^{-6}\ K^{-1}$, $\lambda \approx \mu = 26.5$ GPa, $c = 913\ J\ kg^{-1}K^{-1}$, $\rho = 2710\ kg\ m^{-3}$ and $E_T = 0.24$mJ (single mode), 2.4mJ (multimode).

The experimental values are of the same magnitude but appear to be significantly lower. This may be due to imperfect seating of the probe upon its spacers which would raise the mean gap dimension above the nominal spacer thickness, thereby reducing sensitivity and producing an unknown systematic error.

In the case of ablation generation, Section 6.4 showed that the resultant source may be represented as a vertical compressive force, F(t) with a time dependence determined by ablation and plasma processes. Assuming this force acts over an acoustically small area of surface, the resultant surface acoustic waveform will simply be the convolution of F(t) with the point surface impulse response. Since a $\delta(t)$ function is the derivative of the step function, H(t), the impulse response corresponds to the time differential of Pekeris' (1955) Heaviside solution, W(r,t), described in Section 2.9 (equation 2.21). Thus, the resultant vertical component of surface displacement may be written as (see Figure 7.14),

$$U(r,t) = F(t) * \frac{\partial W(r,t)}{\partial t}$$

where * denotes convolution.

The results of a numerical evaluation of $\partial W(r,t)/\partial t$ are shown in Figure 7.15, revealing a double Rayleigh discontinuity. The material parameters were chosen to approximate to aluminium.

In this case, the force function, F(t), may be empirically chosen to give close agreement with experiment. Examples are shown in Figures 7.16 and 7.17 which gives convolutions to be directly compared with Figures 7.8

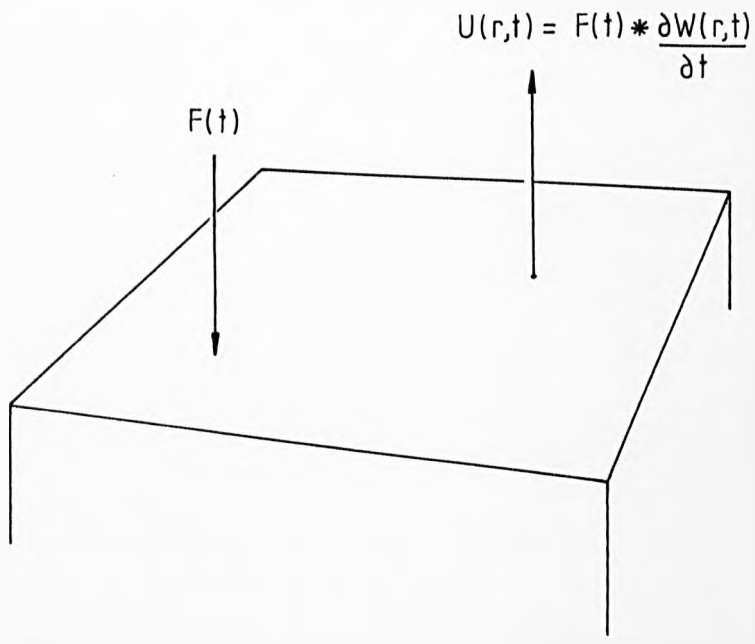

FIGURE 7.14: Surface displacement produced by ablation source.

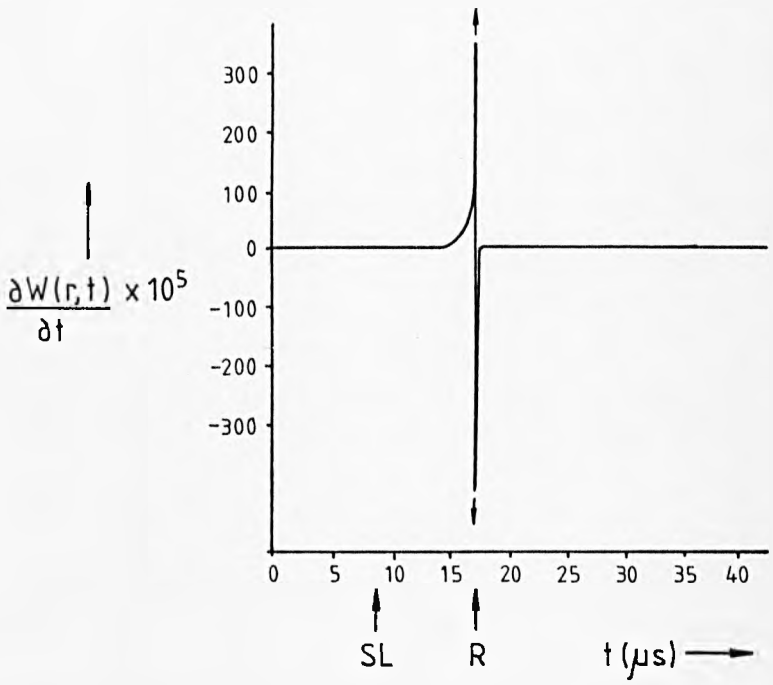

FIGURE 7.15: Theoretical surface impulse response in aluminium at r = 50mm.

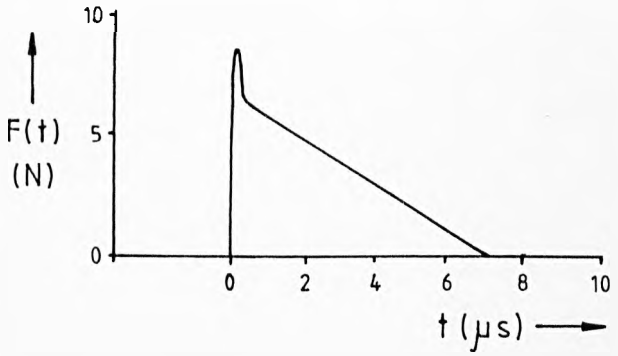

(a). Force function

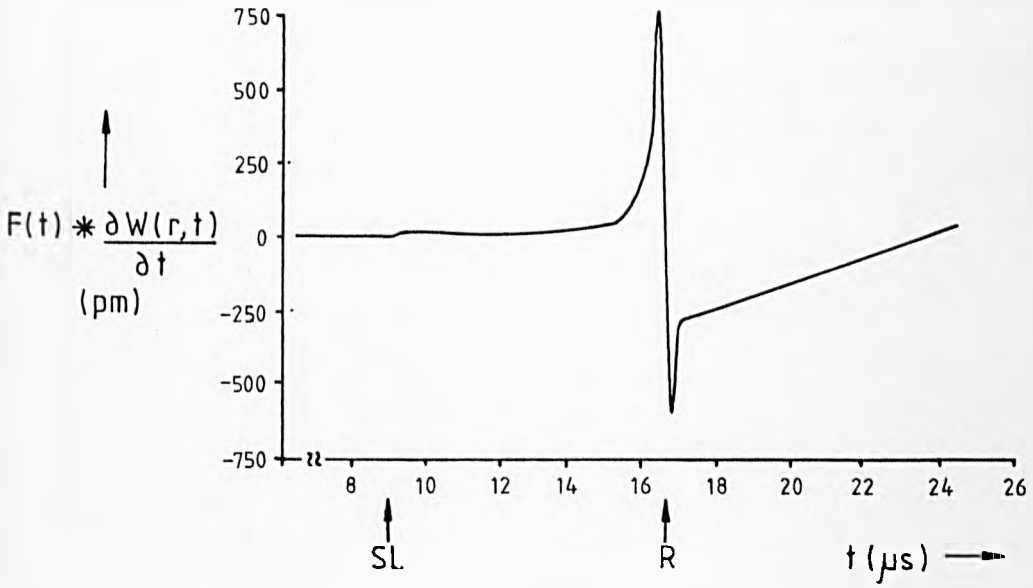

(b). Resultant surface acoustic waveform

FIGURE 7.16: Theoretical surface response produced in aluminium by plasma ablation at a distance r = 50mm. Force function has been adjusted to give a close fit to experimental waveform in Figure 7.8.

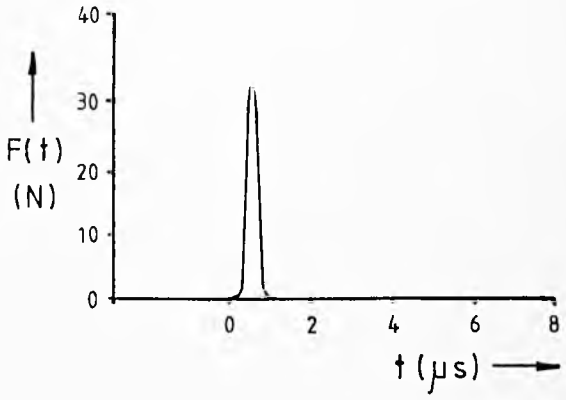

(a). Force function

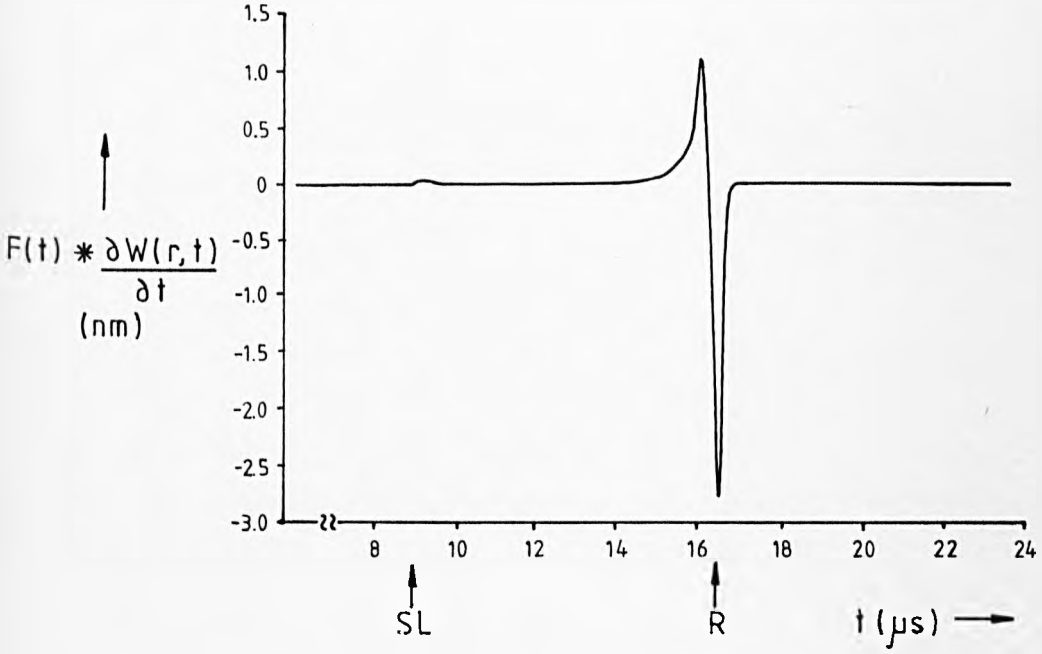

(b). Resultant surface acoustic waveform

FIGURE 7.17: Theoretical surface response produced in aluminium by grease ablation at a distance r = 50mm. Force function has been adjusted to give a close fit to experimental waveform in Figure 7.10.

and 7.10 respectively. The profile of F(t) in Figure 7.16(a) indicates that plasma-ablation produces a prolonged surface force as suggested in Chapter 6 though with a roughly triangular tail preceeded by an initial peak. The form of F(t) may be compared with the stress profile in Figure 3.4 obtained directly by Peercy et al 1970 at such a source. It is the triangular extension that is ultimately responsible for holding the surface down after the immediate Rayleigh arrival. This aspect of the response is essentially quasi-static and reflects the gradual rising of the surface in response to a steady slackening in the surface force. The initial peak is perhaps due to primary vaporisation and ionisation during the time of the laser pulse, and the extension to subsequent secondary vaporisation and gas-dynamic plasma expansion (see Chapter 6).

The theoretical waveforms have also been matched to experiment in terms of amplitude. From Figure 7.16(a), a peak plasma force of $\simeq$ 9N is thus indicated.

For the greased surface F(t) is shorter in duration and has no tail; Figure 7.17(a). The effect of the grease is probably to confine the plasma until in a sudden release of pressure it is lifted clear of the surface. In this case, cross correlation indicates a peak surface force of $\simeq$ 33N.

From these calibrated ablation force functions, it is possible to estimate the total momentum imparted to the target surface by the integration

$$I = \int F(t)dt$$

On this basis, integrating under F(t) indicates $I \simeq 2 \times 10^{-5}$ Ns for grease ablation increasing to $\simeq 3 \times 10^{-5}$ Ns for plasma-ablation.

Theoretical estimates of the impulse can also be made using the following, simple 1D model. Assuming all the absorbed energy, E_T, is ultimately carried off within ejected material as vertical kinetic energy, then the energy balance may be written approximately as

$$\frac{1}{2} \Delta m \, V^2 \simeq E_T$$

where Δm = mass of ejected material

V = ejection velocity

ie. $$V = \sqrt{\frac{2E_T}{\Delta m}}$$

The total imparted momentum is therefore

$$I = \Delta m \, V = \sqrt{2 \Delta m E_T}$$

or, for a disc of ejected material, radius r,

$$\Delta m = 2\pi r^2 \, \Delta d \, \rho$$

where Δd = depth of ejection

Hence

$$I = 2r\sqrt{\pi \, \Delta d \, \rho \, E_T}$$

This analysis may be compared with Jones' 1970 given in Section 3.3.

If it is assumed that the optical absorptivity of the target area remains constant during irradiation, then the following typical values can

be substituted for grease ablation,

$$r \simeq 5 \times 10^{-4} \text{ m}$$

$$\rho = 900 \text{ Kg m}^{-3}$$

$$E_T \simeq 3\text{mJ (7\% absorptivity)}$$

$$\Delta d \simeq 2 \times 10^{-4} \text{ m (oil film thickness)}$$

giving

$$I = 4 \times 10^{-5} \text{ Ns}$$

This is in an order of magnitude agreement with the experimental estimate.

In the case of plasma ablation, it is more difficult to make any such comparisons since the optical absorptivity may change significantly during irradiation due to laser/plasma interactions.

Thus, both the thermoelastic and ablation generation processes have been described in quantitative terms, and the source mechanisms related directly to the resultant surface acoustic response. It is likely that a combination of these primary source types could be used to model the transitional surface waveforms (see, for example, Scruby 1985).

CHAPTER 8

Generation in Non-Metals

8.0 Introduction

The thermoelastic generation of ultrasound by laser irradiation is markedly different in non-metals. This is principally due to the differing optical properties which allow the incident radiation to penetrate much deeper. The result is that the heating rather than being a surface phenomena, extends a significant distance into the bulk. The source is consequently produced sub-surface and so is naturally provided with a certain degree of constraint from overlying material. The result is a comparatively strong compressive-longitudinal source while surface boundary conditions, so important in metals, are reduced to playing a secondary role.

Above the threshold for plasma formation, the generation processes are dominated by surface plasma/laser interactions, and so closely resemble those in metals, this source being a vertical compressive surface force.

This study examines the bulk ultrasonic waveforms only. Previous work on generation in non-metals has been reviewed in Chapter 3.

8.1 Temperature rises

From electromagnetic theory (Longhurst 1974), light energy at normal incidence to a light absorbing dielectric is partially reflected

$$R_{op} = \frac{(n-1)^2 + n^2\chi^2}{(n+1)^2 + n^2\chi^2}$$

where R_{op} = intensity reflection coefficient

n = refractive index

χ = $\lambda_m \beta / 4\pi$ = optical extinction coefficient

λ_m = light wavelength in medium

β = optical absorption coefficient

The transmitted remainder is absorbed, and provided the medium is non-scattering, decreases exponentially in intensity with depth so

$$I(x,y,z,t) = I(x,y,0,t).e^{-\beta z}$$
$$= I_o.S(x,y).P(t).e^{-\beta z} \qquad 8.1$$

where I_o = maximum (surface) transmitted intensity

$S(x,y)$ = normalised laser spatial profile

$P(t)$ = normalised laser temporal profile

Typical values for the optical penetration depth as defined by $1/\beta$, range in the visible spectrum from many cms in a material such as glass to < 200μm in comparatively opaque materials such as ceramic.

These values which may be taken as a guide to the depth of heat production, are to be compared with the thermal skin depth (equation 4.2)

$$\delta_{TP} = \sqrt{4\kappa t}$$

Substituting a typical value for a non-metal of $\kappa = 6 \times 10^{-7}$ $m^2 s^{-1}$ indicates that even over relatively long time scales of $t \leq 100\mu s$ heat will diffuse over a distance $\delta_{TP} \leq 16\mu m$. In other words,

$$\delta_{TP} << 1/\beta$$

This implies that heat is not being significantly redistributed by thermal conduction but rather is largely remaining within the original absorption profile.

Under these conditions, the resultant temperature rises will simply integrate as

$$\theta(x,y,z,t) = \frac{\beta}{c\rho} \int_0^t I(x,y,z,t)\, dt \qquad 8.2$$

where c = specific heat

ρ = density

which by substitution from equation 8.1 gives

$$\theta(x,y,z,t) = \frac{\beta I_o}{c\rho} S(x,y)\, e^{-\beta z} \int_0^t P(t)dt \qquad 8.3$$

This equation has been evaluated in Figure 8.1 assuming the accompanying temporal profile. The time scale is arbitrary, the results being generally applicable provided the $\delta_{TP} << 1/\beta$ criterion is met. Over longer time scales, the surface will eventually begin to cool and the bulk warm as heat slowly diffuses in. However, this is a gradual process and so is not of interest in the case of ultrasonic generation.

The maximum temperature rise, $\hat{\theta}$, which will occur on axis at the surface as the laser pulse ends, can be calculated by setting $S(x,y) = 1$, $z = 0$ and letting the $P(t)$ integration tend to infinity, ie. from equation 8.3

$$\hat{\theta} = \frac{\beta I_o}{c\rho} \int_0^\infty P(t)\, dt$$

which for a laser beam with a uniform, cross-sectional area, A, reduces to

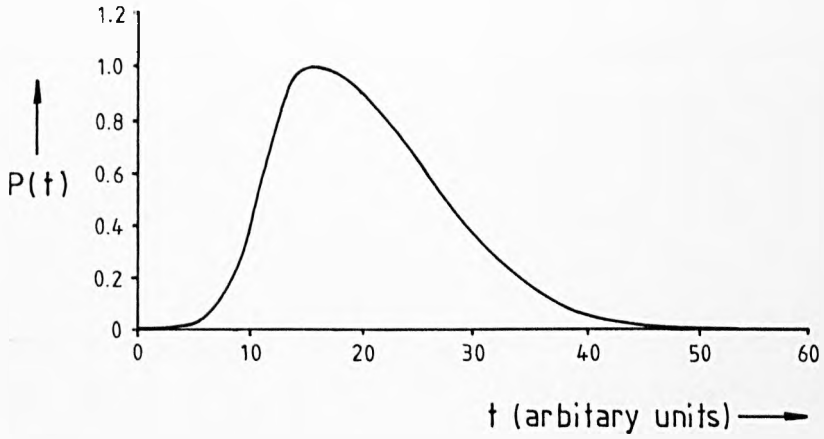

(a). Laser temporal profile

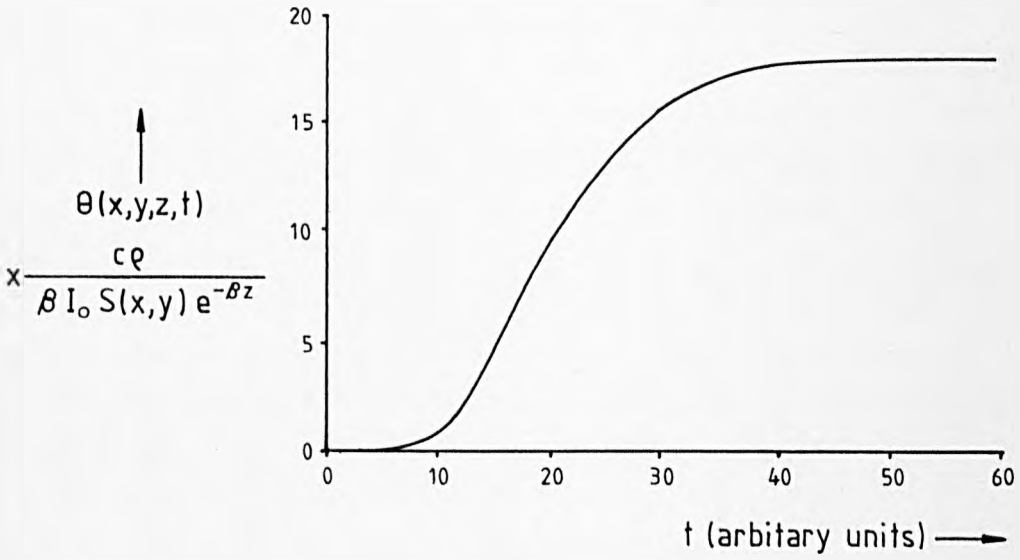

(b). Resultant temperature rise

FIGURE 8.1: Calculated temperature rise in a non-metal.

$$\hat{\theta} = \frac{\beta T_{op} E_I}{c\rho\ A} = \frac{\beta(1-R_{op})\ E_I}{c\rho\ A}$$

where T_{op} = optical intensity transmission coefficient

E_I = total incident pulse energy

This expression indicates that a 30mJ 4mm diameter pulse from a Nd:YAG laser, approximating to the multimode beam described in Section 5.1, would produce a maximum temperature rise of ≃ 3°C in darkened glass ($1/\beta = 5 \times 10^{-4}$m, $T_{op} = 0.92$, $c = 670 Jkg^{-1}K^{-1}$, $\rho = 2600 kgm^{-3}$) and ≃ 1°C in dyed water ($1/\beta = 10^{-3}$m, $T_{op} = 0.9$, $c = 4190 Jkg^{-1}K^{-1}$, $\rho = 1000 kgm^{-3}$).

These temperature rises are more than a magnitude lower than those estimated for metals under comparable conditions (see Section 4.1). This is due to the moderating effect of in-depth absorption which distributes the heat over a far greater volume of material.

8.2 Model of thermoelastic generation by uniform pulsed irradiation

In the case of uniform irradiation, $S(x,y) = 1$, by an instantaneous laser pulse, $P(t) = \delta(t)$, equation 8.3 reduces to

$$\theta(z,t) = \frac{\beta E_T}{c\rho} .e^{-\beta z}. H(t) \qquad 8.5$$

where E_T = absorbed energy density,

$H(t)$ = unit step function.

Substituting for $\theta(z,t)$ into equations 4.17 - 4.19 and summing together as indicated by equation 4.27, gives the longitudinal displacement produced anywhere within the target medium as

$$U_1 = \frac{\Upsilon\beta E_T}{2c\rho} [I_1 + I_2 + I_3]$$

where, I_1, I_2 and I_3 are the delay-adjusted temperature integrals for the u_1, u_2 and u_3 wave terms respectively,

$$I_1 = \int_0^r e^{-\beta z} . H(t - \frac{r-z}{C_L})dz$$

$$I_2 = - \int_r^\infty e^{-\beta z} . H(t - \frac{z-r}{C_L})dz$$

$$I_3 = R_{12} \int_0^\infty e^{-\beta z} . H(t - \frac{r+z}{C_L})dz$$

Taking I_1 as an example, these wave integrals may be conveniently split so

$$\int_0^r e^{-\beta z} . H(t - \frac{r-z}{C_L})dz = \int_0^{r-C_Lt} e^{-\beta z} . H(t - \frac{r-z}{C_L})dz + \int_{r-C_Lt}^r e^{-\beta z} . H(t - \frac{r-z}{C_L})dz$$

But

$$H(t - \frac{r-z}{C_L}) = 0 \quad z < r - C_Lt$$
$$= 1 \quad z > r - C_Lt$$

Hence

$$\int_0^r e^{-\beta z} . H(t - \frac{r-z}{C_L})dz = \int_{r-C_Lt}^r e^{-\beta z}\, dz$$

ie

$$I_1 = \frac{1}{\beta} [e^{\beta C_L t} - 1] e^{-\beta r} \qquad ; t < \frac{r}{C_L}$$

For $t \geq r/C_L$ when displacements from the surface itself have reached the level of interest, I_1 makes no further contribution but rather produces a constant displacement of

$$I_1 = [\frac{1}{\beta} [e^{\beta C_L t} - 1] e^{-\beta r}]_{t = \frac{r}{C_L}}$$

$$= \frac{1}{\beta}\left[1 - e^{-\beta r}\right] \qquad ; \; t > \frac{r}{C_L}$$

Similarly, I_2 and I_3 may be shown to be

$$I_2 = \frac{1}{\beta}\left[e^{-\beta C_L t} - 1\right] e^{-\beta r} \qquad ; \text{ all } t$$

$$I_3 = 0 \qquad ; \; t < \frac{r}{C_L}$$

$$= \frac{R_{12}}{\beta}\left[1 - e^{\beta(r - C_L t)}\right] \qquad ; \; t > \frac{r}{C_L}$$

Back substituting and summing gives the net displacement produced anywhere within a non-metal as

$$U_1 = \frac{\gamma E_T}{2c\rho} \begin{cases} 2(\cosh \beta t C_L - 1)e^{-\beta r} & ; \; t < \frac{r}{C_L} \\ \left[1 - 2e^{-\beta r} + e^{-\beta(r + C_L t)}\right. & \\ \left. + R_{12}\left(1 - e^{\beta(r - C_L t)}\right)\right] & ; \; t > \frac{r}{C_L} \end{cases} \qquad 8.6$$

This may be alternatively expressed in terms of stress by summing the elastic stresses with the original thermal stresses. The elastic stresses are related to the local strain through the longitudinal modulus, as

$$\sigma_{zz} = (\lambda + 2\mu)\frac{\partial U_1}{\partial r} \qquad 8.7$$

where $(\lambda + 2\mu)$ = longitudinal elastic modulus

while the original thermal stresses are (see equations 4.12 and 4.13).

$$\sigma_{zz}^{T} = 3\,\alpha\,K\,\theta(z,t) \qquad 8.8$$

where $K = \lambda + \frac{2}{3}\mu$ = bulk modulus

which by substitution from equation 8.5 gives

$$\sigma_{zz}^{T} = 3\,\alpha\,K\,\frac{E_T\beta}{c\rho}\,.\,e^{-\beta r} \qquad 8.9$$

Differentiating equation 8.6 with respect to r, substituting into 8.7, and summing with 8.9, gives the net stress as

$$\sigma_1(r,t) = \frac{3\alpha K\beta E_T}{2c\rho}\begin{cases} (4-2\cosh\,\beta tC_L)e^{-\beta r} & ;\quad t < \dfrac{r}{C_L} \\ [4e^{-\beta r} + e^{-\beta(r+C_L t)} & \\ + R_{12}\;\; e^{\beta(r-C_L t)}\;] & ;\quad t > \dfrac{r}{C_L} \end{cases} \qquad 8.10$$

Deep within the body well away from the heated region, equation 4.28 may be solved (the equivalent of summing the above I_1 and I_3 related terms only) to show that the boundary-distant waveforms produced in the case of the free surface ($R_{12} = -1$) and constrained surface ($R_{12} = +1$) are

$$U_1 = \frac{\gamma E_T}{2c\rho}\begin{cases} (e^{\beta tC_L} - 1)\,e^{-\beta r} & ;\quad t < \dfrac{r}{C_L} \\ [e^{\beta(r-C_L t)} - e^{-\beta r}] & ;\quad \text{free surface } t > \dfrac{r}{C_L} \\ [2 - e^{-\beta r} - e^{\beta(r-C_L t)}] & ;\quad \text{constrained surface } t > \dfrac{r}{C_L} \end{cases} \qquad 8.11$$

$$\sigma_1 = \frac{3\alpha K\beta E_T}{2c\rho} \begin{cases} (1 - e^{\beta t C_L})\, e^{-\beta r} & ; \quad t < \dfrac{r}{C_L} \\ [e^{-\beta r} + e^{\beta(r-C_L t)}] & ; \quad \text{free surface } t > \dfrac{r}{C_L} \\ [e^{-\beta r} - e^{\beta(r-C_L t)}] & ; \quad \text{constrained surface } t > \dfrac{r}{C_L} \end{cases} \qquad 8.12$$

The last result for stress may be compared to the expressions derived by Gournay 1966 or Carome et al 1964 for the case of irradiated liquids. The above results, however, apply equally to solids and liquids subject to the use of the appropriate elastic moduli and expansion coefficients.

The results are summarised in various forms in Figures 8.2 to 8.5. Figures 8.2 and 8.3 give the stress and displacement waveforms produced deep within the body for the free surface and fully constrained surface, respectively. In both cases, $n = \beta r$, ie. the higher the value of n, the optically denser the medium. In the case of the free surface, the stress pulse is dipolar and there is no steady state displacement. For the constrained surface, the stress pulse is purely compressive with a steady state inwards displacement of $\gamma E_T/c\rho$ into the bulk.

The physical origin of these characteristics can be understood by tracing the development of the waves as they make the transition from the heated region into the cooler bulk. This is shown in two forms in Figures 8.4 and 8.5. Figure 8.4 gives the displacement from various points across the transitions region as a function of time. If the surface is free, the surface itself rises continually upwards as the thermal expansion is accommodated up to the expected steady-state value of $\gamma E_T/c\rho$. Points deeper within the body first experience a displacement inwards and, if they are out of the heated region, then return to their original positions. In contrast, the surface of a constrained body is kept stationary while deeper

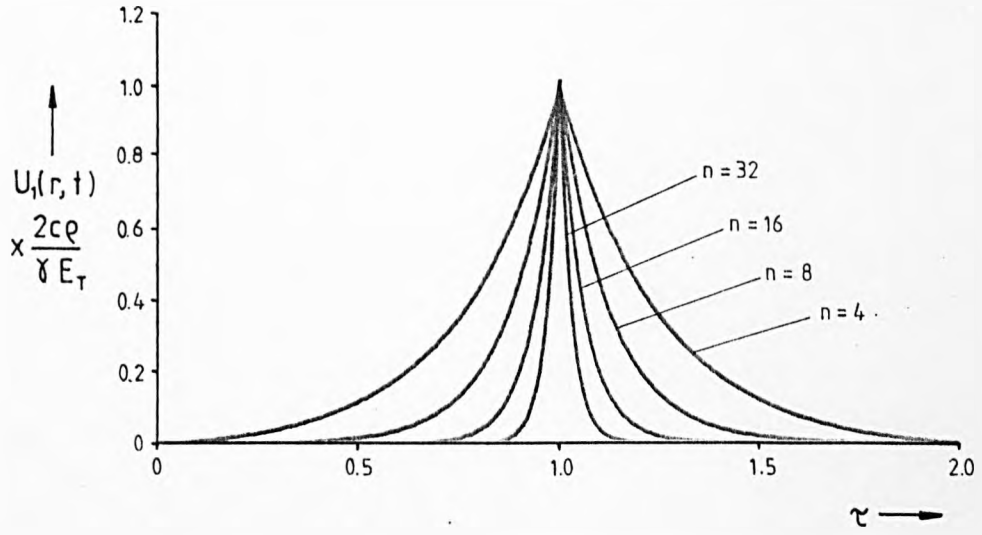

(a). Displacement

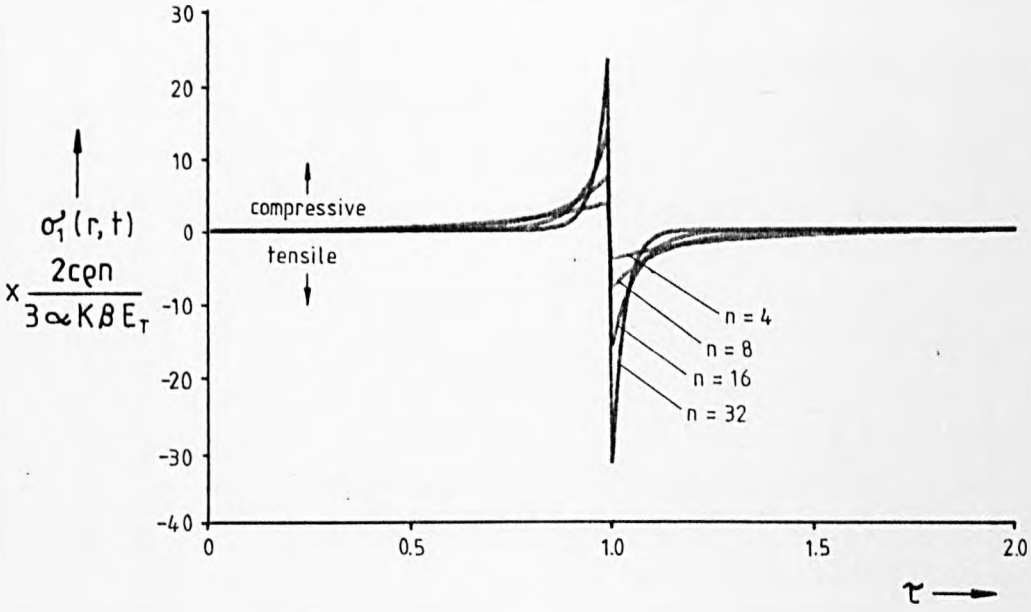

(b). Stress

FIGURE 8.2: Theoretical acoustic waveforms produced deep ($r \gg 1/\beta$) within a non-metal by pulsed irradiation at a stress-free surface. Obtained from equations 8.11 and 8.12.

$n = \beta r$ ie. the higher the value of n, the more optically dense the medium.

$\tau = \frac{c_L t}{r}$ ie. time normalised to longitudinal arrival from surface.

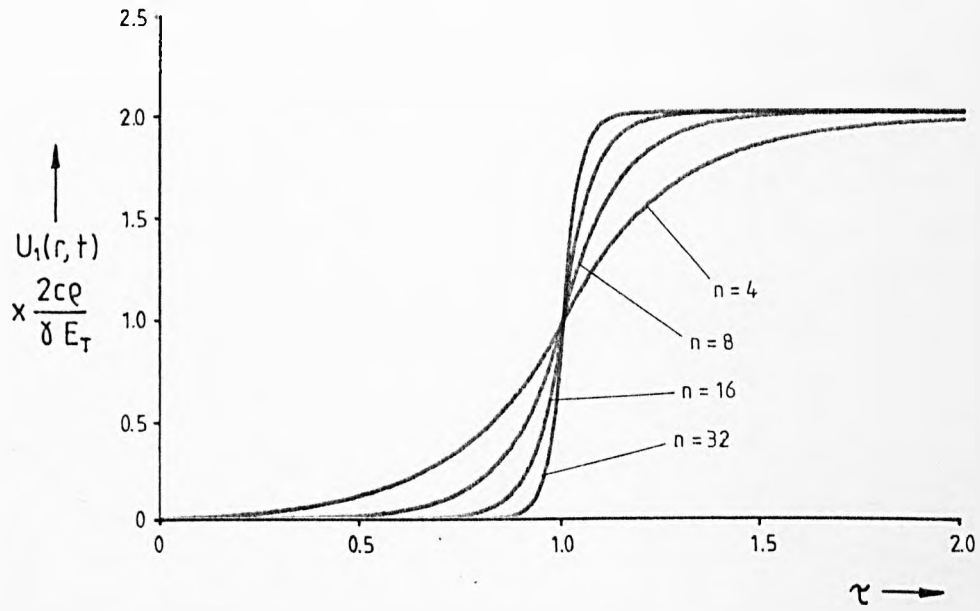

(a). Displacement

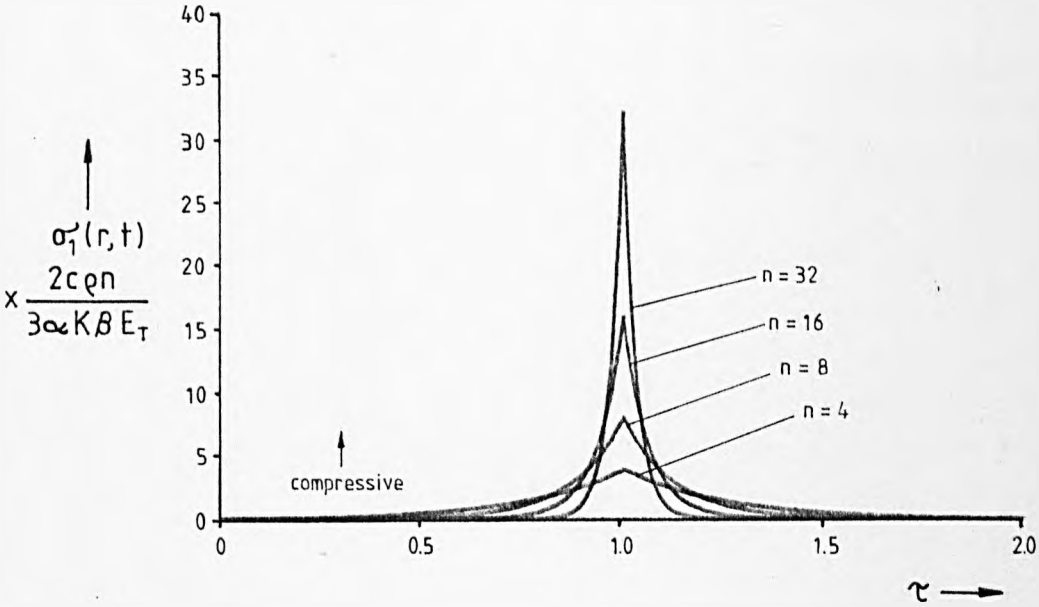

(b). Stress

FIGURE 8.3: Theoretical acoustic waveforms produced deep ($r \gg 1/\beta$) within a non-metal fully constrained at the surface. Obtained from equations 8.11 and 8.12.

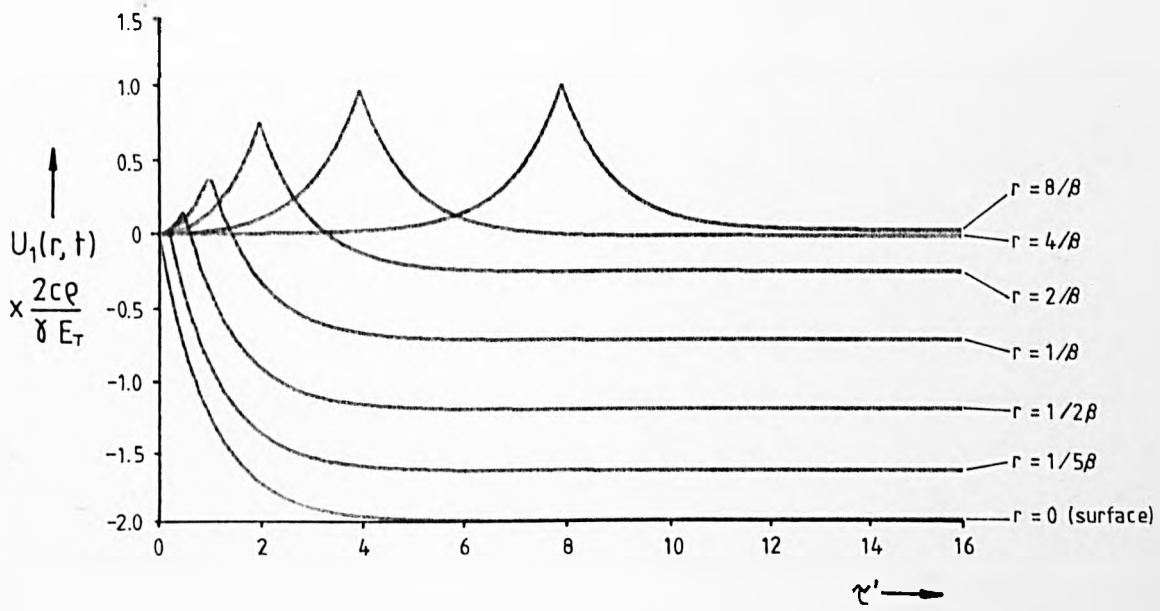

(a). Free surface

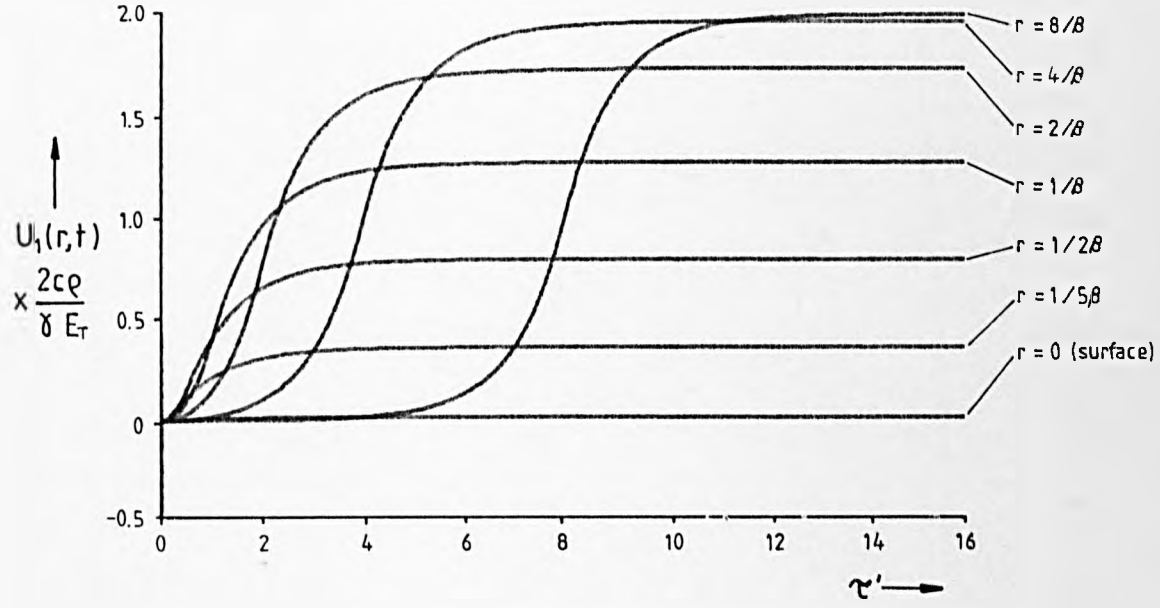

(b). Constrained surface

FIGURE 8.4: Theoretical displacement waveforms produced at various points near the surface ($r \lesssim 1/\beta$) of a non-metal.

$\tau' = \frac{\beta c_L}{t}$ ie. time normalised to longitudinal arrival at a point $z = 1/\beta$.

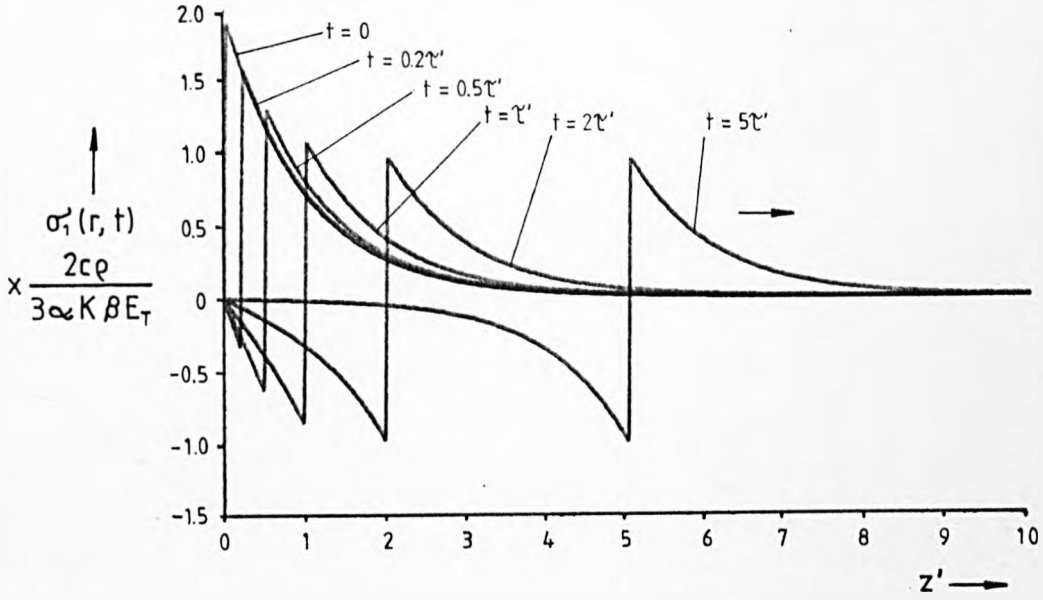

(a). Free surface

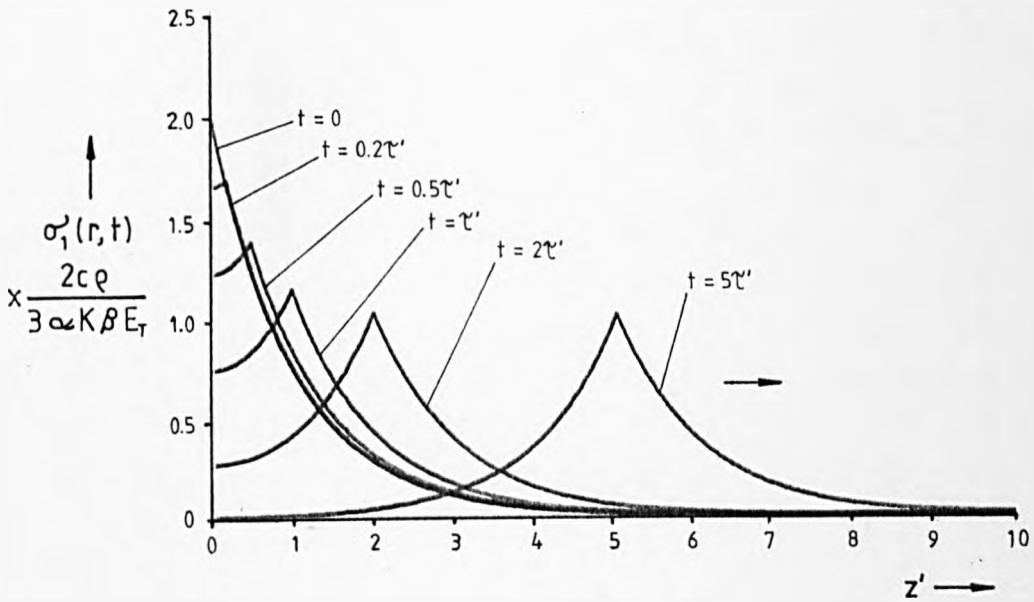

(b). Constrained surface

FIGURE 8.5: Theoretical stress profiles produced near the surface ($r \lesssim 1/\beta$) of a non-metal at various times after irradiation.

$z' = \frac{z}{\beta}$ ie. depth expressed in terms of optical penetration depths.

points are displaced inwards by successively increasing amounts up to the same maximum steady-state value. Figure 8.5, which is perhaps more revealing, gives the variation in stress across the transition region at various times from the onset of irradiation, $t = 0$, until the wave has propagated clear of the heated region, $t >> 1/\beta C_L$. If the surface is free, stress is immediately relieved at the very surface but a compressive pulse is launched into the bulk by deeper heated regions reacting against the overlying regions. Soon this constraint is overcome as the stress-relieving effect of the surface reaches deeper into the body. The result is the development of the tensile tail which ultimately becomes a perfect reflection of the initial compressive half of the waveform, this feature being essentially an inverted surface reflection. If the surface is constrained, the heated region can be seen to launch a purely compressive pulse into the bulk as it expands against the rigidly constrained surface.

Although all these results have been derived for a laser pulse with a $\delta(t)$ temporal profile, they can be adapted to a prolonged laser pulse by convolution. They can, however, be applied directly with no such modification provided the acoustic waves have not begun to propagate a significant distance out of the heated region before the laser pulse ends, ie. when

$$t_p << \frac{1}{\beta C_L} \qquad \text{or} \quad \frac{1}{\beta} >> C_L.t_p$$

where t_p = laser pulse duration

For $t_p \approx 30\text{ns}$ and $C_L \approx 3000\text{ms}^{-1}$, convolution is therefore necessary if $1/\beta >> 90\mu\text{m}$; this is often the case.

Under this condition, the results can be summarised by noting the peak stress, $\hat{\sigma}_i$ and peak displacement, $\hat{U}_i$ produced deep with the body are

$$\hat{\sigma}_1 = \frac{3\alpha K\beta E_T}{2c\rho} \qquad \text{(free and constrained surface)}$$

$$\hat{U}_1 = \frac{\gamma E_T}{2c\rho} \qquad \text{(free surface)}$$

$$\hat{U}_1 = \frac{\gamma E_T}{c\rho} \qquad \text{(constrained surface)}$$

while the pulse duration is approximately given by the acoustic transit time of the heated region

$$\Delta t \simeq \frac{1}{\beta C_L}$$

8.3 Experimental study of bulk wave thermoelastic generation

Generation has been studied in a limited number of non-metals, namely, darkened glass (neutral density filter), ceramic (white, unglazed domestic tile) and tufnol (a composite, machinable plastic laminate).

The ultrasonic detector, a broadband capacitance probe, was designed and constructed by the NDT Centre, Harwell, UKAEA. This device, described fully elsewhere (Scruby and Wadley 1978), comprised a 6mm diameter, polished metal disc supported by a differential micrometer mechanism approximately 5-10μm above the sample surface, and maintained at DC potential of +100v; Figure 8.6. The operating principle is the same as that described in Section 7.2. The sample surfaces were necessarily vacuum aluminised so as to complete the detection capacitor. The probe was sensitive to normal displacements over a band width of ≃ 4MHz at approximately 0.05mV pm^{-1}.

The free surface thermoelastic waveforms are typified by those in Figures 8.7, 8.8 and 8.9 which were produced by unfocused 30mJ 30ns multimode Nd:YAG pulses incident on darkened glass, ceramic and tufnol

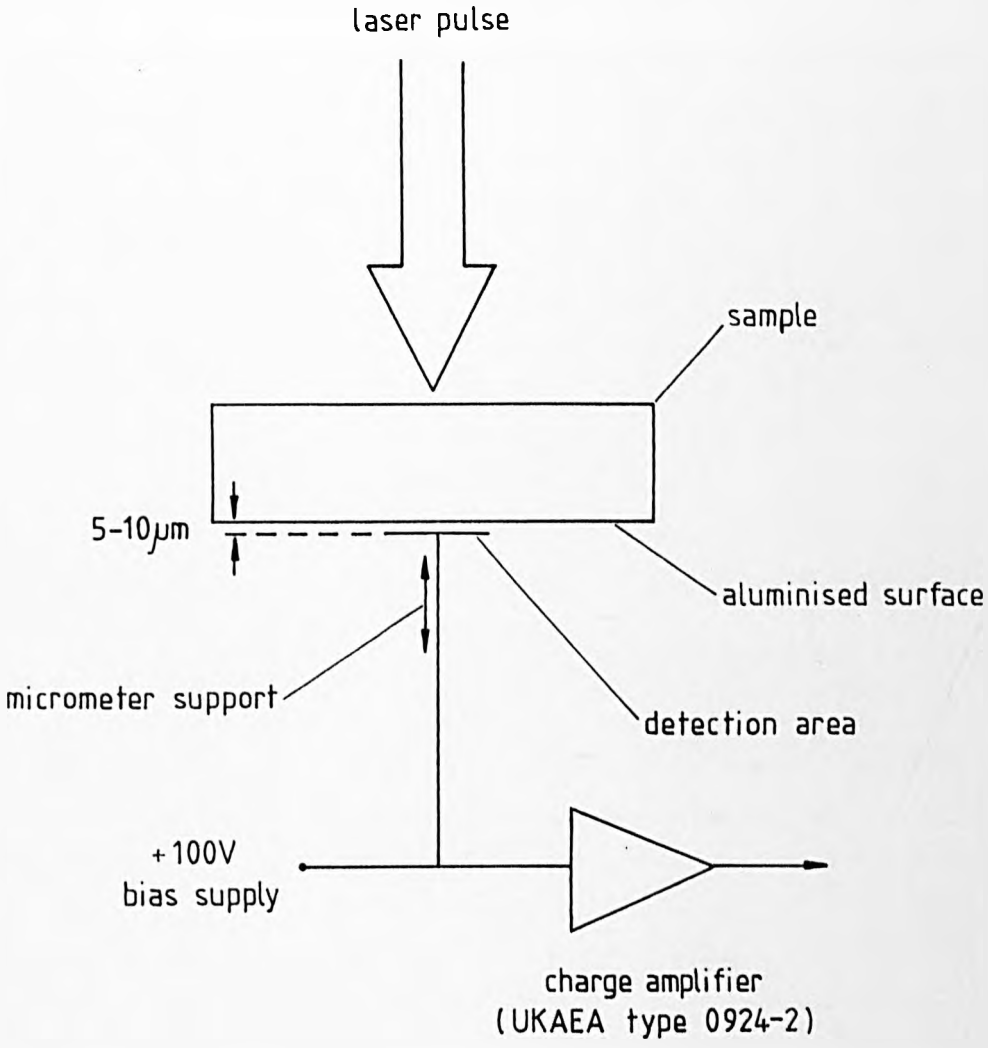

FIGURE 8.6: Experimental arrangement for the study of laser-generated bulk acoustic waveforms in non-metals.

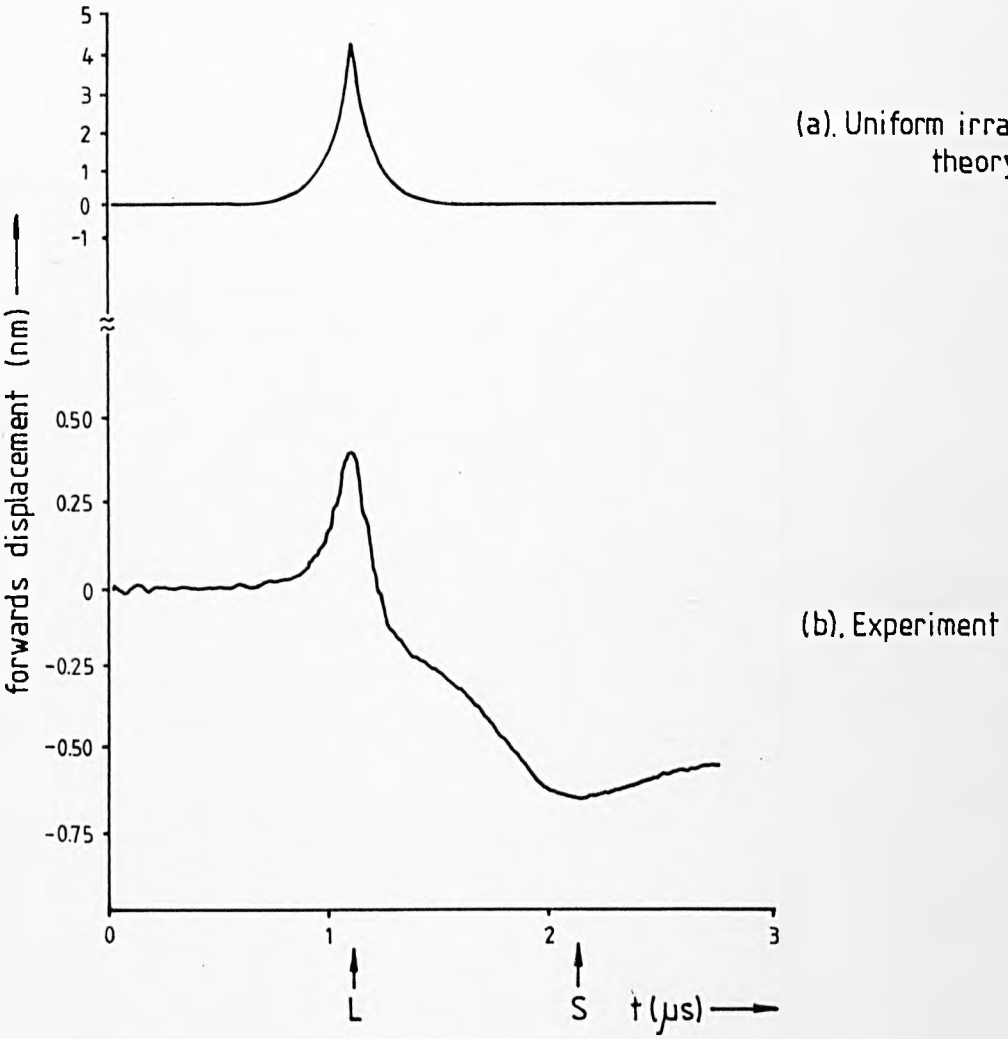

FIGURE 8.7: Thermoelastic bulk waveform produced in darkened glass by pulsed multimode Nd:YAG irradiation. Harwell capacitance probe.

Material parameters used to obtain theoretical waveform:

$C_L = 5300\,ms^{-1}$, $\beta = 1860\,m^{-1}$, $T_{OP} = 0.9$, $c = 500\,J\,kg^{-1}K^{-1}$, $\rho = 4200\,kgm^{-3}$ and $\alpha = 7 \times 10^{-6}K^{-1}$.

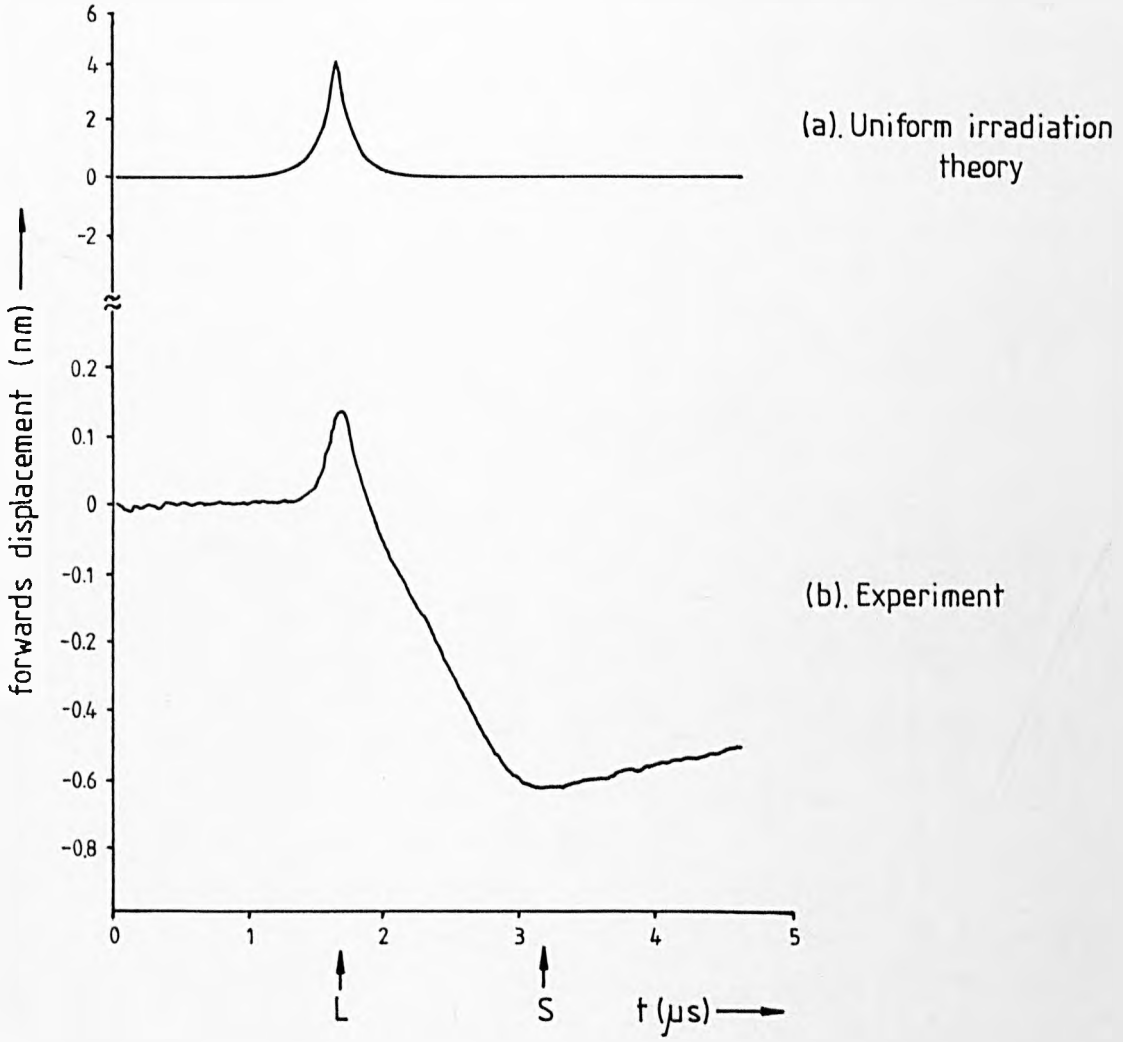

FIGURE 8.8: Thermoelastic bulk waveform produced in white unglazed ceramic by pulsed multimode Nd:YAG irradiation. Harwell capacitance probe.

Material parameters used to obtain theoretical waveform:

$C_L = 3360\,m s^{-1}$, $\beta = 2600\,m^{-1}$, $T_{OP} = 0.2$, $c = 800\,J kg^{-1}K^{-1}$, $\rho = 3800\,kg m^{-3}$ and $\alpha = 9 \times 10^{-6}K^{-1}$.

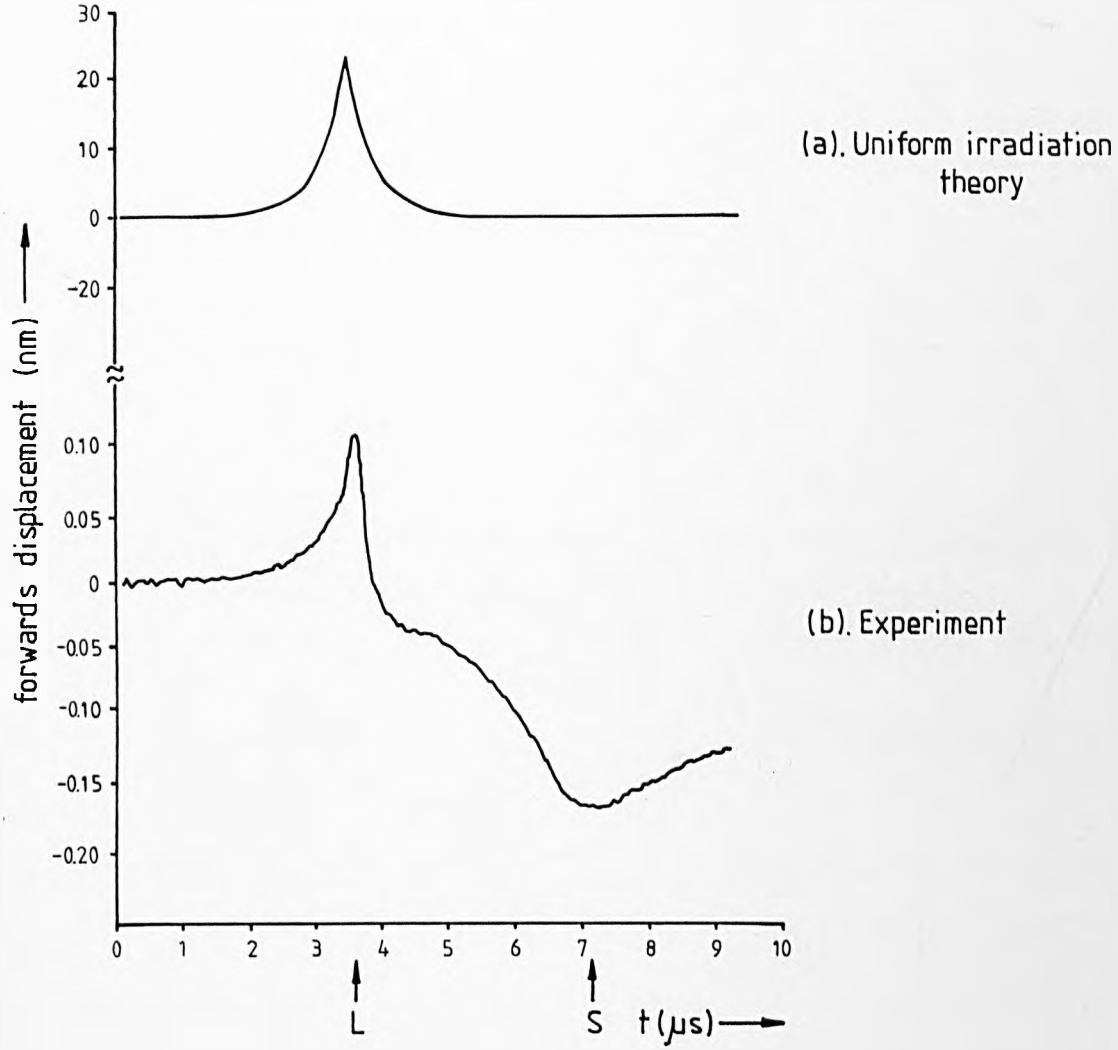

FIGURE 8.9: Thermoelastic bulk waveform produced in tufnol by pulsed multimode Nd:YAG irradiation. Harwell capacitance probe.

Material parameters used to obtain theoretical waveform:

$C_L = 2870\,ms^{-1}$, $\beta = 760\,m^{-1}$, $T_{OP} = 0.6$, $c = 1000\,J\,kg^{-1}K^{-1}$, $\rho = 2000\,kgm^{-3}$ and $\alpha = 5 \times 10^{-6}K^{-1}$

samples, 6.3, 5.4 and 9.8mm thick, respectively. All the waveforms consist of a longitudinal pulse with a displacement forwards, ie. in the direction of propagation, followed by a less well defined rearwards displacement reaching a maximum near the expected shear arrival. The profiles of the longitudinal pulses are well described by the accompanying theoretical waveforms calculated from equation 8.11 assuming the given material parameters. The amplitudes, however, are considerably lower than expected. This is due partly to the wavefront speading out in 3D away from the normal defined by the uniform irradiation model, resulting in significant geometrical attenuation. In addition, granular or composite materials such as ceramic and tufnol may be expected to suffer from considerable material attenuation and scattering. The subsequent motion leading to the shear arrival likewise demonstrates the limitations of this model which only indicates a return to the original level. This additional displacement is probably due to thermal stresses acting radially outwards from the finite size laser spot, producing more complicated shear propagation. In the latter respect, a comparison may be made with the previous free-surface thermoelastic waveform for a metal surface in Figure 3.6 where a similar but more sharply defined motion is observed but without the initial forwards-displacing longitudinal pulse.

The effect of surface layers on thermoelastic generation is shown in Figures 8.10 (a) and (b). Both waveforms were produced in darkened glass, the first with a 2mm thick surface layer of grease, the second through a 10mm thick block of clear soda glass coupled with water. In the case of a metal surface, both arrangements would have led to a greatly enhanced longitudinal pulse (for example, compare with Figure 5.15). In the present case, there is no such effect rather the opposite, a moderated reduction in amplitude. Surface boundary conditions are clearly not so

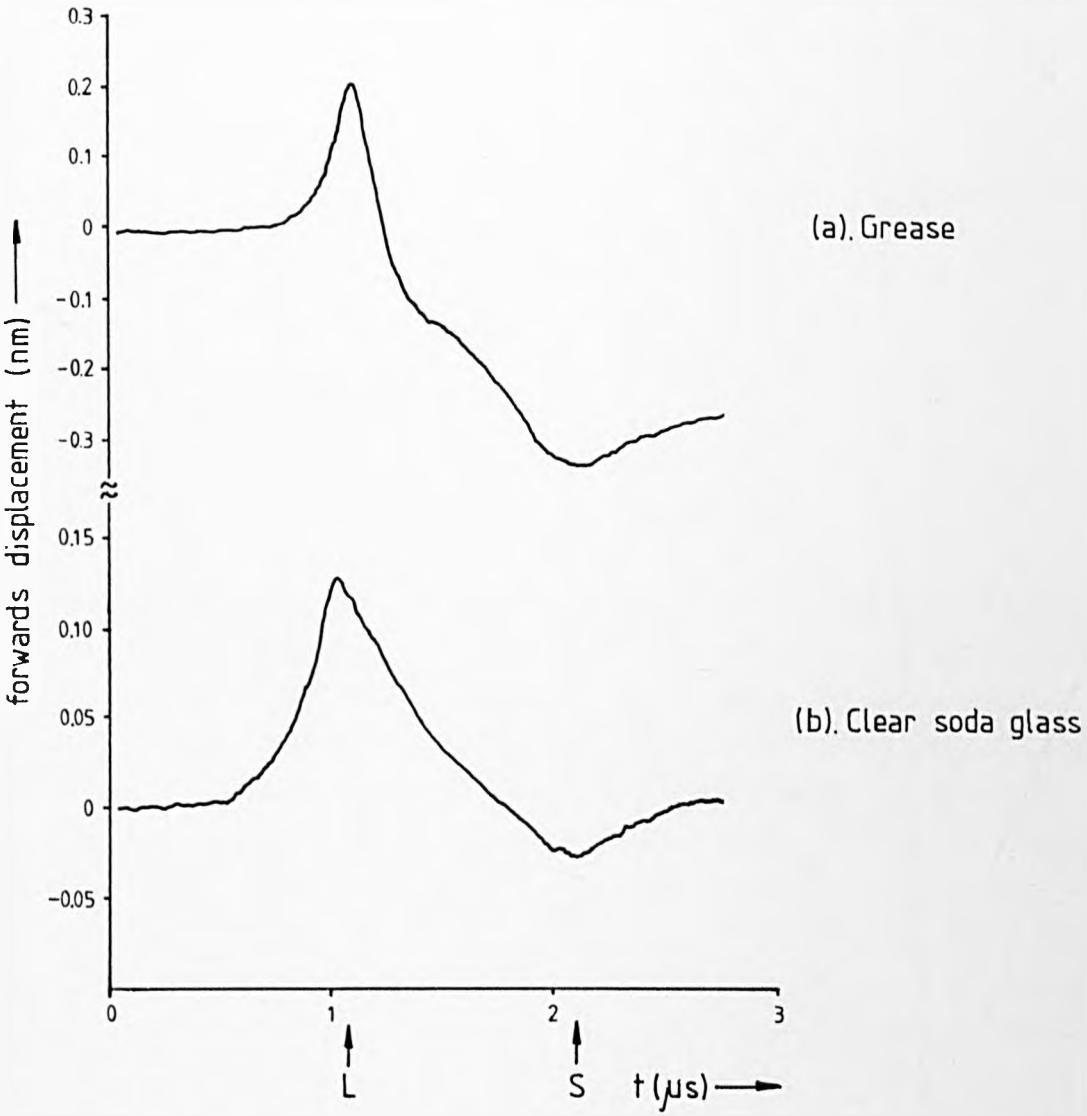

FIGURE 8.10: The effect of surface constraing layers on thermoelastic bulk-wave generation in darkened glass.

important but instead play a secondary role as emphasised by the uniform irradiation model of in-depth absorption.

The grease waveform in particular is very similar to that for the free surface, the main effect of the grease apparently being to reduce the intensity of laser radiation reaching the glass surface and hence to decrease the waveform's overall amplitude (× 0.6). The clear glass block has a stronger effect especially on the subsequent shear motion which is largely absent. This is presumably due to the clear glass having comparable acousto-mechanical properties which will tend to contain the effect of the radial thermal stresses.

8.4 Plasma-ablation generation

Above the threshold of plasma-ablation, the waveforms undergo a transformation similar to that in metals described in Sections 6.1 - 6.4. This is shown in Figure 8.11(a) which gives the bulk waveform produced by a focused ($f \simeq 100$mm) 30mJ multimode Nd:YAG pulse incident on darkened glass. The waveform is a general motion forwards, ie. away from the plasma with step-like or discontinuous displacements corresponding to longitudinal and shear arrivals and cross-sample reflections. A revealing comparison may be made with the accompanying theoretical waveform which is for a step point compressive force after Knopoff 1979. There is an approximate waveform correspondence confirming that plasma formation exerts a roughly step compressive surface force.

In the experimental waveform, there is a tendency for the rear surface to pull back between successive arrivals rather than being driven continually in the force direction. This probably reflects a slackening off of the surface plasma force. The effect is even more pronounced in the ceramic and tufnol waveform; Figures 8.12 (a) and (b). In general, it is

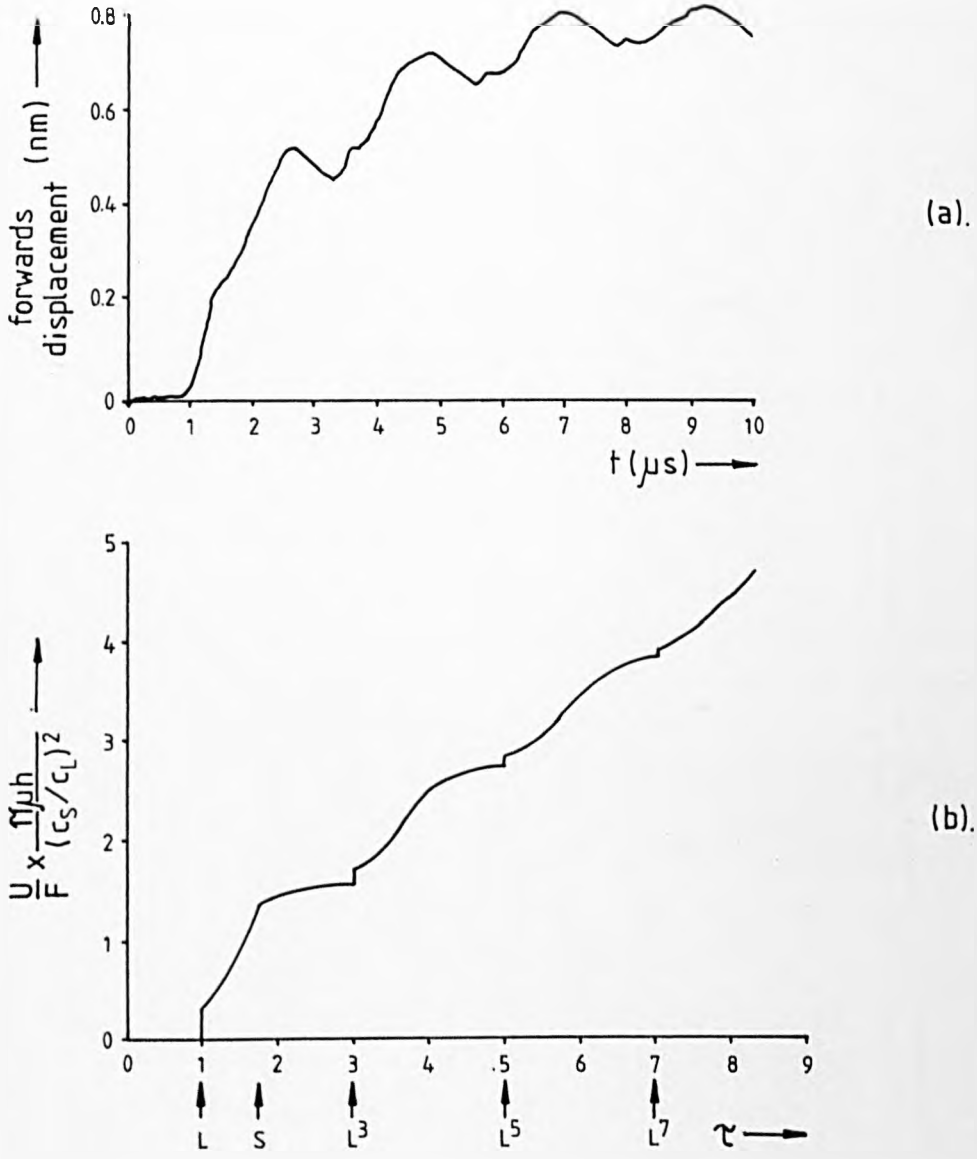

FIGURE 8.11: A comparison between:

(a). plasma-ablation bulk waveform produced in darkened glass by focused Nd:YAG irradiation. (Harwell capacitance probe).

(b). theoretical epicentral displacement, U, produced in a plate, thickness, h, due to a step compressive force, F, acting vertically at a point on the surface. (After Knopoff 1979).

$\tau = \frac{c_L t}{h}$ ie. time normalised to first longitudinal arrival.

Superscripts on arrival markers indicate cross-sample reflections.

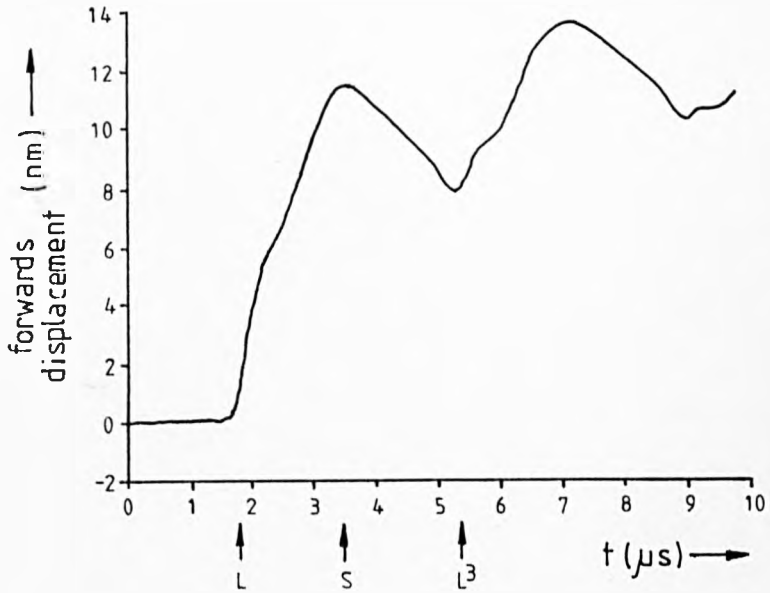

(a). Ceramic

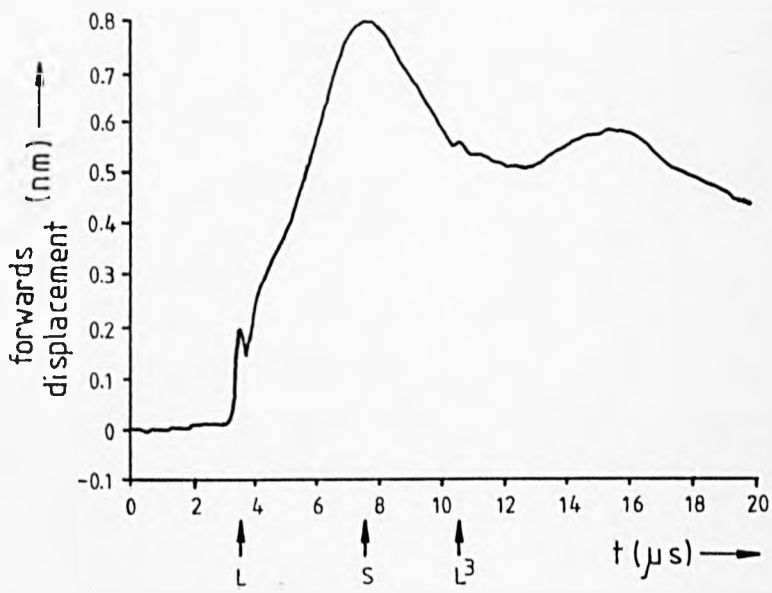

(b). Tufnol

FIGURE 8.12: Plasma-ablation bulk waveforms produced by focused (f=100mm) Nd:YAG irradiation. Harwell capacitance probe.

to be expected that for a given pulse energy, the plasma will reach differing stages of development depending on the target material properties. Non-metals in particular with extended pentration depths, may have a delayed plasma development due to moderation of the initial rate of temperature rise.

By means of a summary, a number of cases of both thermoelastic and plasma-ablation generation are shown in Figure 8.13. All the bulk waveforms were detected with resonant 2MHz L-PZT on the tufnol sample. Despite the wide variety of surface conditions and range of laser intensities, the waveforms show similar characteristics, notably the constant polarity longitudinal pulse. The shear pulse is indistinct even in the case of thermoelastic generation at a free surface where, in metals, it was characteristic. The laser ultrasonic source in non-metals is invariably longitudinal-compressive irrespective of generating conditions.

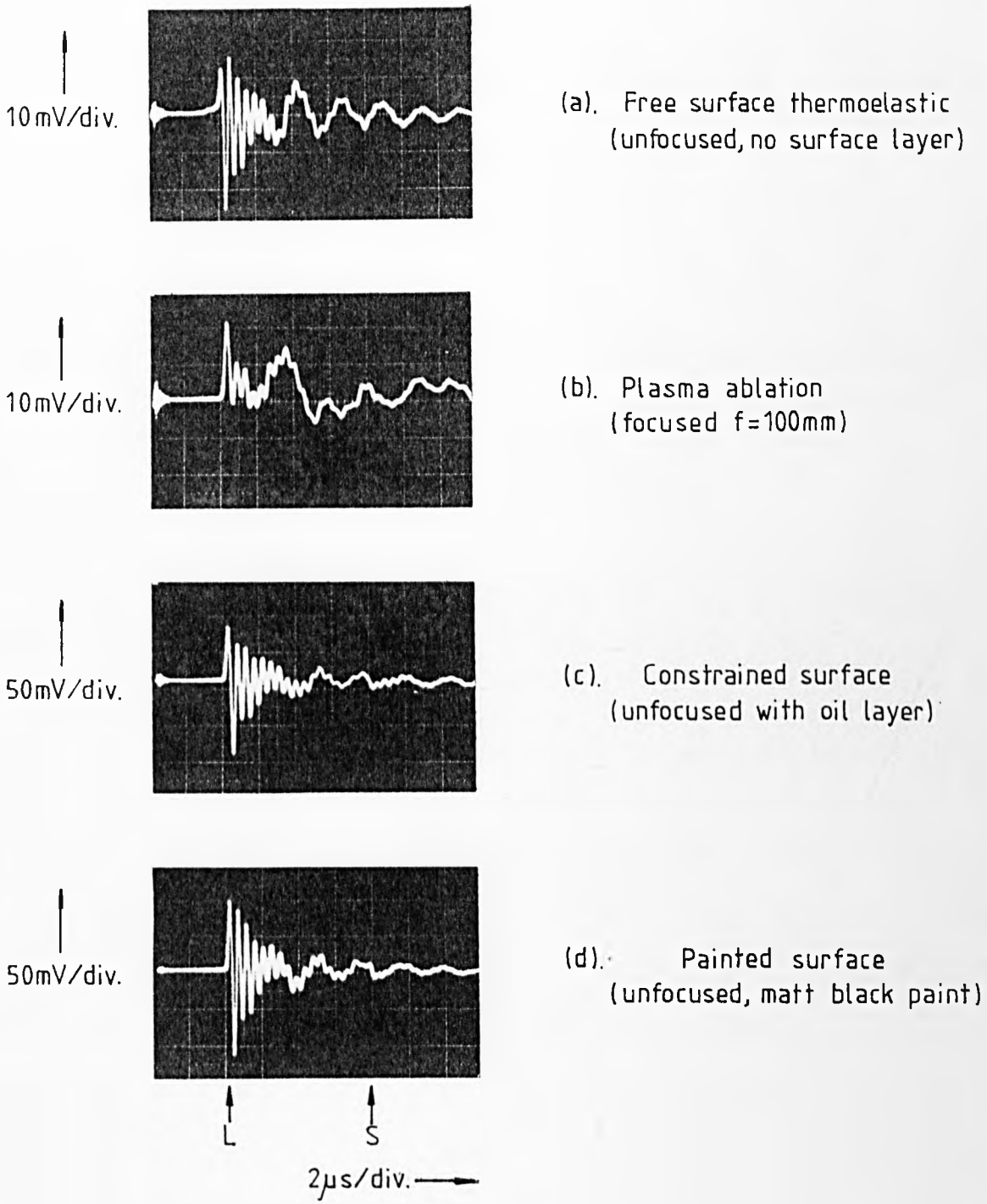

FIGURE 8.13: Bulk ultrasonic waveforms generated under a variety of conditions in tufnol by 50mJ 50ns Nd:YAG irradiation. 2MHz resonant L-PZT detector.

CHAPTER 9

Conclusion

9.0 Summary

The laser ultrasonic source is a multifarious phenomena, manifesting itself in a number of different forms depending on laser intensity, target medium and surface conditions. There are two basic source types, the thermoelastic and the ablation source. The former operates at comparatively low laser intensities, typically $< 3 \times 10^{12}$ Wm^{-2}, and is driven by the dynamic thermal expansion due to a transient surface heating. The latter source rapidly takes over at higher absorbed intensities, and results from surface impulse and pressure associated with the removal of surface material and plasma formation. Both sources have been described in qualitative (Chapters 5 and 6) and quantitative terms (Chapters 4, 7 and 8). In addition, thermoelastic generation has been related to the photoacoustic effect in a generalised 1D model (Chapter 4).

A crucial parameter controlling thermoelastic processes is the acoustic thickness of the source. In metals, the heating is superficial, producing an acoustically thin source. As a result, the expanding source metal reacts against its surroundings almost instantaneously and uniformly across its thickness. This has two contrasting effects depending on surface conditions. First, at a constrained surface, it ensures that the source trapped between the overlay and sample, expands in an efficient piston-like manner against both. The result is the generation of comparatively strong, compressive longitudinal waves. Secondly, at a free surface where no effective constraint exists, the result is that the heated region possesses negligible longitudinal inertia, and so expands smoothly

upwards without exerting any significant compressive stresses against the bulk. If irradiation is over a finite area only, radial thermal stresses dominate, producing a characteristically shear source.

In non-metals, the incident laser radiation penetrates much deeper into the target bulk. This produces a distributed thermoelastic source, acoustically thick and physically removed from the effect of surface boundary conditions. The resultant sub-surface expansion launches strong longitudinal compressive waves irrespective of boundary conditions.

The ablation source comes in two forms, the plasma-ablation and the surface-coat ablation sources. Both are characteristically longitudinal-compressive. The plasma-ablation source is produced by focusing, and results from the vaporisation and ionisation of surface material. Immediately above the ablation threshold, simple vaporisation imparts a brief vertical impulse to the surface due to recoil through momentum transfer. At higher intensities, this mechanism is supplemented by the effects of ionisation and plasma formation which produce an extended surface force outlasting the actual period of irradiation. Since laser/plasma interactions dominate such processes, the physical properties of the original target material are not critical. The resultant ultrasonic waveforms are consequently very similar in both metals and non-metals. In the surface-coat ablation source, a specially applied surface material is preferentially vaporised, so imparting a brief vertical impulse to the target. There may also be an accompanying enhancement of thermoelastic processes due to increased optical absorption resulting in a hybrid source. In this respect, there probably exists a continuum between this source and the thin-film, constrained thermoelastic source where comparatively transparent coats may be also ablated due to acoustic spallation.

Both the thermoelastic and ablation sources launch a variety of bulk

(shear and longitudinal) and surface (Rayleigh and longitudinal) acoustic pulses. These have been studied over a wide range of surface conditions using both resonant piezoelectric probes (Chapters 5 and 6) and absolute displacement probes (Chapters 7 and 8). They come typically in the form of brief transients or sharp discontinuities and, as a comparison with acoustic theory reveals, are characteristic of the forces producing them.

9.1 Future work

One area yet to be studied in detail is generation in bulk metals in the hypersonic region, 1GHz+, using mode-locked ps laser pulses. Some relevant experiments have been carried out, for example, Brienza and De Maria 1967 (Section 3.2). Theory, however, appears to be lacking. In this respect, the 1D model in Chapter 4 and Section 4.9 in particular, indicates that at a free surface normal thermal stresses though generally insignificant, should become increasingly important as the pulse duration is shortened and the source becomes acoustically thicker. In the hypersonic region where the thermal front velocity approaches the acoustic propagation velocity, the resultant longitudinal-compressive source should become comparable to that produced under constrained surface conditions. Strong compressive-longitudinal generation should result. In addition, the effects of shear stresses which dominate at lower frequencies, should become progressively insignificant. To model these generation processes, it may prove necessary to modify the original temperature rise expressions. Classical heat flow theory from which they were derived, implicitly assumes that the thermal front velocity can increase over shortening time scale without limit as, for example, $t^{-1/2}$ in 1D geometry, which is a physical absurdity. In this respect, a reformulation combining heat flow and acoustic theory may be required (see Tavernier 1962, Achenbach 1968).

A growing area of current laser ultrasonics is its application to remote NDT. In this respect, the laser represents an ultrasonic source of almost incomparable finesse; it is remote, scannable, has a physically small source area, and produces brief ultrasonic pulses free from unwanted resonances. However, as Section 3.6 indicated, there are problems with low sensitivity, particularly when relying on the thermoelastic source to avoid damage. In this respect, there are a number of possible methods of increasing the amplitude which are essentially damage-free. First, laser pulses could be optimally profiled to put in the maximum amount of energy while keeping the surface below any critical temperature. Given that the thermal skin depth increases as $t^{1/2}$, the optimum pulse profile would approximately scale as the complimentary function, $t^{-1/2}$. On this basis, irradiation with a 1μs pulse could produce ≃ 7× the amplitude of a 25ns pulse without raising the maximum (surface) temperature. The accompanying increase in the acoustic pulse duration and fall in bandwidth, would also have to be acceptable. Another method would be to scan the laser beam during irradiation. If, for example, a laser beam is tracked across a surface at the Rayleigh wave velocity, it would continuously feed energy into the surface acoustic wavefront whilst covering new areas of surface. For a track of say 50mm, an amplitude increase of ×25 could be expected over a stationary 2mm diameter source. The pulses would also be produced in end-fire beams. By scanning at different speeds, different types of wave could be generated both on the surface and in the bulk, propagating in any desired direction. Similar ideas have been expressed previously for harmonic generation in liquids by Bozhkov et al 1980.

A third and completely different technique of increasing the acoustic amplitude could be to use a TEA CO_2 laser to provide multi-joule pulses in the infra-red (λ = 10.3μm). Such pulses readily form intense plasma when

focused onto metal surfaces but without necessarily removing any surface material. The reason for this is that metals reflect strongly at these wavelengths and so it is difficult to couple any radiation in. As a result, upon focusing, breakdown tends to occur first in the air immediately above the surface. The metal itself may not be directly involved but instead act as a nearby blast-receiving area of surface. The resultant ultrasonic source would result solely from the over-pressure exerted by the plasma, resembling a small scale air-borne detonation. An experiment of this kind was performed using a similar arrangement to Figure 5.4(a) but with a focused 4J 1μs TEA CO_2 laser. Preliminary results indicate that longitudinal enhancements of ≃ 500× can be achieved over the Nd:YAG thermoelastic source without causing any visible damage. By calibration against the thermoelastic study of Scruby et al 1980, this suggests longitudinal amplitudes in the order of 10nm+ developed at distances of ≈ 25mm. By current standards, that is an intense source of ultrasound, and should increase the viability of damage-free laser NDT.

Another application of laser ultrasonics could be to test the optical homogeneity of non-metallic samples. From the solution of the 1D model in Chapter 8 (equation 8.11), it may be shown that if, for example, the bulk epicentral waveform is reversed in time from the surface longitudinal arrival back to t = 0, it has the same form as the original optical attenuation curve. Thus, in-depth optical characteristics could be readily resolved from single-shot measurements.

APPENDIX

Notes on the numerical evaluation of the surface acoustic waveforms

In the case of plasma ablation, the surface response due to a momentary, $\delta(t)$, vertical force was obtained by numerical differentiation of the unit step solution, $W(r,t)$, derived by Pekeris (equation 2.21). This was achieved by representing $W(r,t)$ as an array $A[n]$ and subtracting adjacent points normalised to the time interval, Δt,

$$I[n] = \frac{A[n+1] - A[n]}{\Delta t}$$

This is ploted as the waveform in Figure 7.15.

For prolonged surface forces (Figures 7.16 and 7.17), $I[n]$ was convolved with the appropriate force function, $F[n]$, by the following step-and-sum procedure, expressed in BASIC

```
FOR n = 1 TO 500
    FOR m = n TO 500
        U[m] = U[m] + F[n].I[m-n].Δt
    NEXT
    PRINT U[n]
NEXT
```

In the case of thermoelastic generation, the surface response was first calculated for a dipolar source comprising two unit step forces, $F_{xx} = 1N$, acting tangentially to the surface. One force was positioned at, r, acting towards the detection point, the other in the opposite direction at a marginally greater distance, $r + \Delta r$, where typically $\Delta r = r/500$ (see Section 7.4). The displacement for each force component was then

evaluated directly from Chao's solution (equation 2.22) and stored as two arrays, $A_1[n]$ and $A_2[n]$. The displacement due to a point unit dipole ($D_{xx} = F_{xx}.\Delta r = 1Nm$), could thus be approximated as

$$U[n] = \frac{A_1[n] + A_2[n]}{\Delta r}$$

This is the waveform shown in Figure 7.13(a).

For a finite source area (Figures 7.13(b) and (c)), the above solution was convolved with aperture functions using the program, A5, developed by Cooper (1985).

REFERENCES

Achenbach, J.D. (1968) J. Mech. Phys. Solids, 16, 273

Achenbach, J.D. (1973) "Wave Propagation in Elastic Solids", 187-194. North-Holland Publishing Co., Oxford.

Aindow, A.M., Cooper, J.A., Dewhurst, R.J. and Palmer, S.B. (1983a). In "Quantum Electronics and Electro-Optics" (P.L. Knight, ed.) 427-43 . Wiley

Aindow, A.M., Cooper, J.A., Dewhurst, R.J. and Palmer, S.B. (1983b). In "Proceedings of Ultrasonics International '83", Halifax, 20-24.

Aindow, A.M., Cooper, J.A., Dewhurst, R.J. and Palmer, S.B. (1983c). In "Technical Digest on CLEO '83", 238-239.

Aindow, A.M., Dewhurst, R.J., Hutchins, D.A. and Palmer, S.B. (1979). In "Proceedings of the 4th National Quantum Electronics Conference", Edinburgh, UK, 255-258.

Aindow, A.M., Dewhurst, R.J., Hutchins, D.A. and Palmer, S.B. (1980). In "Proceedings of 1980 European Conference on Optical Systems and Applications", SPIE 236, 478-484.

Aindow, A.M., Dewhurst, R.J., Hutchins, D.A. and Palmer, S.B. (1981). J. Acoust. Soc. Am., 69, 449-455.

Aindow, A.M., Dewhurst, R.J. and Palmer, S.B. (1982). Opt. Commun. 42, 116-120.

Aindow, A.M., Dewhurst, R.J., Palmer, S.B. and Scruby, C.B. (1984). NDT Int., 17, 329-335.

Ameri, S., Ash, E.A., Newman, V. and Petts, C.R. (1981). Electron. Lett., 17, 337-338.

Anderholm, N.C. (1970). Appl. Phys. Lett., 16, 113-115.

Ash, E.A., Dieulesaint, E. and Rakouth, H., (1980). Electron. Lett. 16, 470-472.

Askar'yan, A., Prokhorov, A.M., Chanturiya, G.F. and Shipulo, M.P. (1963). Sov. Phys. JETP, 17, 1463-1465.

Bar-Cohen, Y. (1979). J. NDT, 21, 76-78.

Beckenbridge, F.R., Tschiegg, C.E. and Greenspan, M. (1975). J. Acoust. Soc. Am. 57, 626-631.

Bell, A.G. (1881). Phil. Mag. 2, 510-528.

Brinbaum, G. and White, G.S. (1984). In "Research Techniques in Non-Destructive Testing" (R.S. Sharpe, ed.) VII, 259-365. Academic Press, London.

Bleaney, B.I. and Bleaney, B. (1976). "Electricity and Magnetism". Oxford Press.

Bondarenko, A.M., Drobot, B. and Kruglov, S.V. (1976). Sov. J. NDT, 12, 655-658.

Bourne, O. (1980). Ph.D. Thesis, University of Hull, England.

Bozkhov A.I., Bunkin, F.V., Esipov, I.B., Malyarouskii, A.I. and Mikhalevich, V.G. (1980). Sov. Phys. Acoust., 25(2), 100-104.

Breinza, M.J. and De Maria, A.J. (1967). Appl. Phys. Lett. 11, 44-46.

Budenkov, G.A. and Kaunov, A.D., (1979). 9th World Conference on NDT. paper 4A-14.

Burridge, R. and Knopoff, L. (1964). Bulletin Siesmol. Soc. USA, 54, 1875.

Bushnell, J.C. and McCloskey, D.J. (1968). J. Appl. Phys. 39, 5541-5546.

Cachier, G. (1971). J. Acoust. Soc. Am. 49, 974-978.

Calder, C.A. and Wilcox, W.W. (1978). In "Characterisation of Materials for Service at Elevated Temperatures" (G.V. Smith, ed.) 169-181. ASME Series MPC-7.

Carome, E.F., Clark, N.A. and Moeller, C.E. (1964). Appl. Phys. Lett. 4, 95-97.

Carslaw, H.S., and Jaeger, J.C. (1959). "Conduction of Heat in Solids", 2nd edition, Oxford University Press, London.

Chao, C.C. (1960). J. Appl. Mech., 27, 559-567.

Chiao, R.Y., Townes, C.H. and Stoicheff, B.P. (1964). Phys. Rev. Lett., 12, 592-597.

Cielo, P. (1984). Appl. Phys. Lett., 56, 230-234.

Condon, E.U. (1958a). In "Handbook of Physics" (E.U. Condon and H. Odishaw, eds.), Chp. 3-1. McGraw-Hill, New York.

Condon, E.U. (1958b). In "Handbook of Physics" (E.U. Condon and H. Odishaw, eds.) Chp. 5-64. McGraw-Hill, New York.

Cooper, J.A. (1985). Ph.D. Thesis. University of Hull, England.

Couchman, J.C. and Bell, J.R. (1978). Ultrasonics, 16, 272-274.

Davidson, G., Emmony, D.C. and Maloney, T. (1976). In "Proceedings of the 2nd Acoustic Emission Conference", AML, Dorset, UK.

Dewhurst, R.J., Hutchins, D.A., Palmer, S.B. and Scruby, C.B. (1982). J. Appl. Phys., 53, 4064-4071.

Egle, D.M. and Brown, A.E. (1976). J. Test and Eval., 4, 196-199.

Fairand, B.P. and Claver, A.H. (1979). J. Appl. Phys., 50, 1497-1502.

Fairand, B.P. and Claver, A.H., Jung, R.G. and Wilcox, B.A. (1974). Appl. Phys. Lett., 25, 431-433.

Favro, L.D., Kuo, P.K., Puch, J.J. and Thomas, R.L. (1980). Appl. Phys. Lett. 36, 953-954.

Felix, M.P. (1974). Rev. Sci. Instr., 45, 1106-1108.

Fox, J.A. (1974). Appl. Phys. Lett., 24, 461-464.

Garmire, E. and Townes, C.H. (1964). Appl. Phys. Lett., 5, 137-139.

Gournay, L.S. (1966). J. Acoust. Soc. Am., 40, 1322-1330.

Gregg, D.W. and Thomson, S.J. (1966). J. Appl. Phys., 37, 2787-2789.

Hutchins, D.A. (1986). In "Physical Acoustics" (W.P. Mason and R.N. Thurston, eds.) Academic Press, London. To be published.

Hutchins, D.A., Dewhurst, R.J. and Palmer, S.B. (1981a). Ultrasonics, 19, 103-108.

Hutchins, D.A., Dewhurst, R.J. and Palmer, S.B. (1981b). J. Acoust. Soc. Am. 70, 1362-1369.

Hutchins, D.A., Dewhurst, R.J. and Palmer, S.B. (1981c). Appl. Phys. Lett., 38, 677-679.

Hutchins, D.A. and Nandeau, F. (1983). In "Proceedings of the 1983 IEEE Ultrasonics Symposium", Atlanta, 1175-1177.

Hutchins, D.A. and Wilkins, D.E. (1985). J. Appl. Phys., 58, 2469-2477.

Hutchins, D.A., Wilkins, D.E. and Luke, G. (1985). Appl. Phys. Lett., 46, 634-635.

Jen, C.K., Cielo, P., Nandeau, F., Bussiere, J. and Farnell, F. (1980). In "Proceedings 1984 IEEE Ultrasonics Symposium", 660-665.

Johns, D.J. (1965). "Thermal Stress Analysis", 8, Pergamon Press, New York.

Kaule, W. (1978). 8th World Conference on NDT, Cannes, France, 1-7.

Kaye, G.W.C. and Laby, T.H. (1973). "Tables of Physical and Chemical Constants". Longman, London and New York.

Knopoff, L. (1979). J. Appl. Phys., 29, 661-670.

Krautkramer, J. (1979). 9th World Conference on NDT. Plenary Lecture, Melbourne, Australia.

Kubota, K. and Nakatoni, Y. (1973). Jap. J. Appl. Phys., 12, 888-894.

Lamb, H. (1904). In "Proceedings of the Cambridge Philosophical Society", 1-42.

Ledbetter, H.M. and Moulder, J.C. (1979). J. Acoust. Soc. Am., 65, 840-842.

Lee, R.E. and White, R.M. (1968). App. Phys. Lett., 12, 12-14.

Longhurst, R.S. (1973). "Geometrical and Physical Optics", 3rd edition. Longman, London and New York.

Luukkata, M. and Penttinem, A., (1979). Electron. Lett., 15, 325-326.

Martin, Y. and Ash, E.A. (1984). In "Proceedings of the 1984 IEEE Ultrasonics Symposium", 647-650.

McDonald, F.A. and Wetsel, G.C. (1977). J. Appl. Phys., 49, 2313-2322.

Metz, S.A., Hettche, L.R., Stegman, L. and Schriempf, J.T. (1975). J. Appl. Phys., 46, 1634-1642.

Moss, B.C. (1982). "The Harwell Interferometer", AERE Report - R10417, Harwell UKAEA.

Mozina, J. (1981). In "Proceedings of Ultrasonics International 1981 Conference", 372-377, IPC Press, UK.

Nadeau, F. and Hutchins, D.A. (1984). In "Proceedings of the 1984 IEEE Ultrasonics Symposium", 921-925.

Nelson, K.A. Dwayne-Miller, R.J. Lutz, D.R. and Fayer, M.D. (1982). J. Appl. Phys., 53, 1144-1149.

Officer, C.B. (1958). "Introduction to the theory of sound and transmission", Chp. 1, McGraw-Hill.

O'Keefe, J.D. and Skeen, C.H. (1972). Appl. Phys. Lett., 21, 464-466

Olson, H.F. (1947). "Elements of Acoustical Engineering", 2nd edition, Chp. 2. Van Nostrand Co., New York.

Palmer, A.J. and Asmus, J.F. (1970). Appl. Opt., 9, 227-229.

Pao, Y.H. (1977). "Optoacoustic Spectroscopy and Detection". Academic Press, New York.

Parker, J.G. (1973). Appl. Opt., 12, 2974-2977.

Patek, K. (1967). "Lasers", 131, Iliffe, London.

Patel, C.K.N. and Tam, A.C. (1980). Appl. Phys. Lett., 36, 7-9.

Peercy, P.S., Jones, E.D., Bushnell, J.C. and Gobeli, G.W. (1970). Appl. Phys. Lett., 16, 120-122.

Pekeris, C.L. (1955). Geophys. Proc. NAS, 41, 469-480.

Penner, S.S. and Sharma, O.P., (1966). J. Appl. Phys., 37, 2304-2308.

Percival, C.M. (1967). J. Appl. Phys., 38, 5313-5315.

Petts, C.R. and Wickramasinghe, H.K. (1980). In "Proceedings of the 1980 IEEE Ultrasonics Symposium", 636.

Lord Rayleigh (1881). Nature, 23, 274-275.

Ready, J.F. (1971). "Effects of High Power Laser Radiation", Academic Press, New York.

Robin, J.E. (1978). J. Appl. Phys., 49, 5300-5310.

Rose, L.R.F. (1984). J. Acoust. Soc. Am., 75, 723-732.

Rosen, M., Wadley, H.N.G. and Mehrabian, R. (1981). Scripta Metallurgica, 15, 1231-1236.

Rosencwaig, A. and Gersho, A. (1976). J. Appl. Phys., 47, 64-69.

Rosencwaig, A. (1980). In "Scanned Image Microscopy" (E.A. Ash, ed). Academic Press, New York, 291-317.

Royer, D. and Dieulesaint, E. (1983). In "Proceedings of '83 Ultrasonics Symposium", Atlanta, 664-667.

Scruby, C.B. (1985). In "Rayleigh Wave Theory and Application" (E.A. Ash and E.G.S. Paige, eds.) Springer-Verlag, Berlin.

Scruby, C.B., Dewhurst, R.J., Hutchins, D.A. and Palmer, S.B. (1980). J. Appl. Phys., 51, 6310-6216.

Scruby, C.B., Dewhurst, R.J., Hutchins, D.A. and Palmer, S.B. (1982). In "Research Techniques in Non-Destructive Testing" (R.S. Sharpe, ed.) Vol. V, 281-327. Academic Press, New York.

Scruby, C.B. and Wadley, H.N.G. (1978). J. Phys. D., 11, 1487.

Sessler, G.M., Gerhard-Multhaupt, R. and West, J.E. (1983). Polymer Bull., 6, 109-111.

Skeen, C.H. and York, C.M. (1968). Appl. Phys. Lett., 12, 369-371.

Smith, J.J., Rosen, M. and Wadley, H.N.G. (1983). In "Proceedings of the Symposium on Applications and Development of Non-Destructive Evaluation for use in Materials Processing", 1-9, AMS, USA.

Tam, A.C. (1983). In "Ultrasensitive Laser Spectroscopy" (D. Kliger, ed.), 1-108. Academic Press, New York.

Tam, A.C. and Confal, H. (1983). J. de Phys. (Paris) Coll., C6, 9.

Tam, A.C., Patel, C.K.N. (1979). Appl. Opt., 18, 3348-3358.

Tavernier, J. (1962). L'Onde Electrique, 42, 541.

Tilley, D.R. (1974). "Waves", 159-161. MacMillan.

Viktorov, I.A. (1967). "Rayleigh and Lamb Waves". Plenum Press, New York.

Von Gutfield, R.J. and Melcher, R.L. (1977). Appl. Phys. Lett., 30, 257-259.

Wadley, H.N.G., Simmons, J.A. and Stockton, C.K. (1982). Report No. AERE-R1041, AERE, Harwell, UK.

Wellman, R.J. (1980). Report No. HDL-TR-1902. Harry Diamond Laboratories.

White, R.M. (1963). J. Appl. Phys., 34, 3559-3567.

Wickramasinghe, H.K., Bray, R.C., Jipson, V., Quate, C.F. and Salced, J.R. (1978). Appl. Phys. Lett., 33, 923-925.

Winfield, R.J. Ph.D. Thesis, 1982. University of Hull, England.

Yang, L.C. (1974). J. Appl. Phys., 45, 2601-2608.